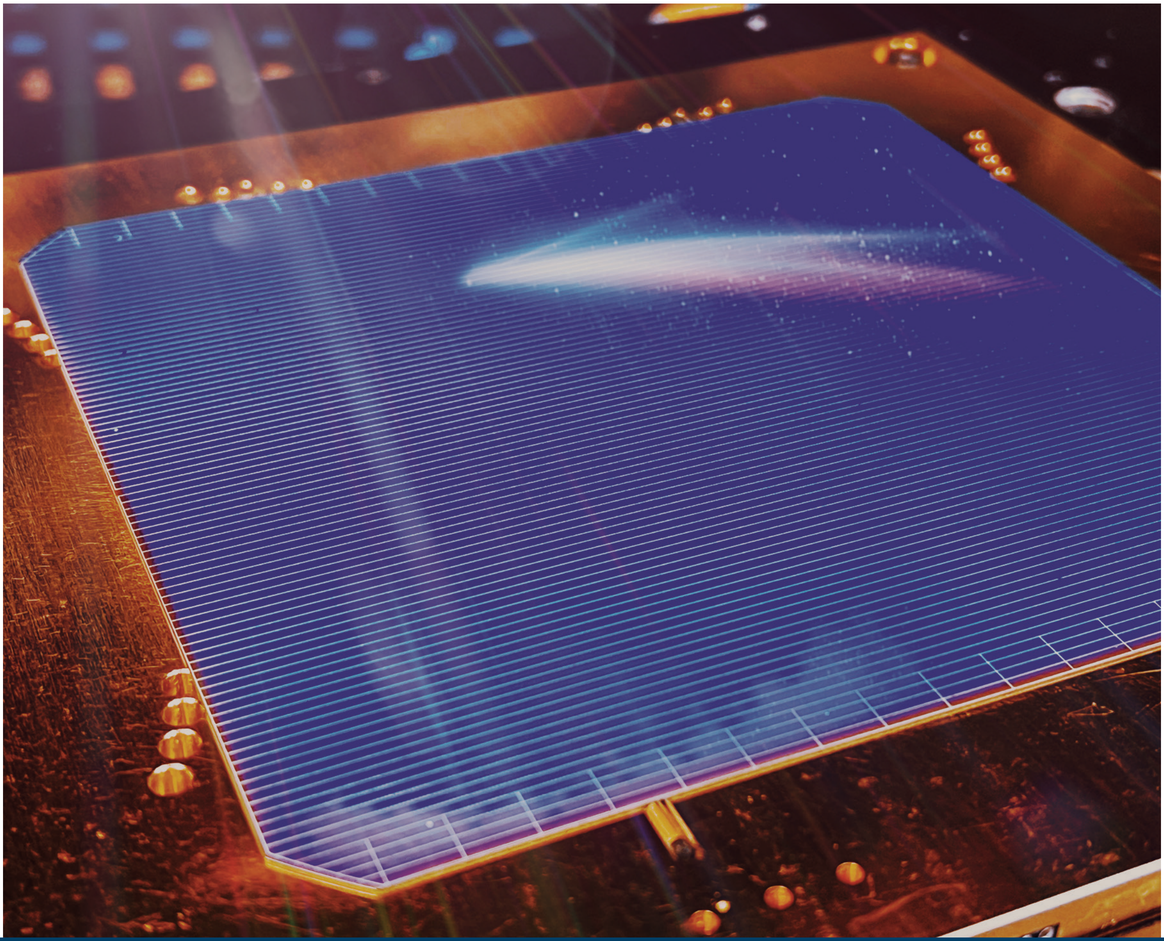

Development of industry-scalable processes for nanocrystalline silicon oxide in silicon heterojunction solar cells

Depeng Qiu

Energie & Umwelt / Energy & Environment
Band / Volume 619
ISBN 978-3-95806-734-9

Mitglied der Helmholtz-Gemeinschaft

JÜLICH
Forschungszentrum

Schriften des Forschungszentrums Jülich
Reihe Energie & Umwelt / Energy & Environment Band / Volume 619

Forschungszentrum Jülich GmbH
Institut für Energie- und Klimaforschung (IEK)
Photovoltaik (IEK-5)

Development of industry-scalable processes for nanocrystalline silicon oxide in silicon heterojunction solar cells

Depeng Qiu

Schriften des Forschungszentrums Jülich
Reihe Energie & Umwelt / Energy & Environment Band / Volume 619

ISSN 1866-1793 ISBN 978-3-95806-734-9

Bibliografische Information der Deutschen Nationalbibliothek.
Die Deutsche Nationalbibliothek verzeichnet diese Publikation in der
Deutschen Nationalbibliografie; detaillierte Bibliografische Daten
sind im Internet über http://dnb.d-nb.de abrufbar.

Herausgeber und Vertrieb: Forschungszentrum Jülich GmbH
Zentralbibliothek, Verlag
52425 Jülich
Tel.: +49 2461 61-5368
Fax: +49 2461 61-6103
zb-publikation@fz-juelich.de
www.fz-juelich.de/zb

Umschlaggestaltung: Grafische Medien, Forschungszentrum Jülich GmbH

Druck: Grafische Medien, Forschungszentrum Jülich GmbH

Schriften des Forschungszentrums Jülich
Reihe Energie & Umwelt / Energy & Environment, Band / Volume 619

D 82 (Diss. RWTH Aachen University, 2023)

ISSN 1866-1793
ISBN 978-3-95806-734-9

Contents

Abstract

Thanks to the excellent passivation of hydrogenated amorphous silicon (a-Si:H) to wafer surface, high open circuit voltage (V_{oc}) as well as power conversion efficiency (η) have been achieved by the silicon heterojunction (SHJ) solar cell technology in the recent decades. However, a significant parasitic absorption in doped a-Si:H results in a low short circuit current density (J_{sc}), limiting the cell performance of SHJ solar cells. Doped hydrogenated nanocrystalline silicon oxide (nc-SiO$_{\mathrm{x}}$:H), consisting of conductive silicon crystallites (nc-Si:H) embedded in transparent hydrogenated amorphous silicon oxide (a-SiO$_{\mathrm{x}}$:H) matrix, is an attractive alternative material to the commonly used a-Si:H in SHJ solar cells to further improve the cell performance. A trade-off between the optical and the electrical properties always need to be taken into account when applying the nc-SiO$_{\mathrm{x}}$:H(n) films in SHJ solar cells. The goal of this thesis is to systematically investigate the implementation of nc-SiO$_{\mathrm{x}}$:H(n) in SHJ solar cells, to find the correlation between the material properties and the device performance, and to demonstrate the industrial applicability of nc-SiO$_{\mathrm{x}}$:H in SHJ solar cells.

In the first part of this work, n-type nc-SiO$_{\mathrm{x}}$:H and hydrogenated nanocrystalline silicon (nc-Si:H) (x equals zero) layers were developed and compared in an industrial multi-substrate plasma enhanced chemical vapor deposition (PECVD) system for the application in full-sized ($>156\times156$ mm^2) SHJ solar cells. By means of optical, electrical and structural material characterizations, the influence of deposition parameters, such as deposition power density (P), deposition pressure (p) and gas compositions, was investigated. It was found that the response of nc-SiO$_{\mathrm{x}}$:H to the variation of deposition parameters is different from that of nc-Si:H layers. Moreover, a synergistic effect of CO_2 and PH_3 or SiH_4 on the material properties of nc-SiO$_{\mathrm{x}}$:H films was observed. To acquire the nc-SiO$_{\mathrm{x}}$:H films with high transparency and sufficient conductivity, high volume fraction of a-SiO$_x$:H ($F_{\text{a-SiO}_2}$) and nc-Si:H (F_c), but low a-Si:H volume fraction ($F_{\text{a-Si:H}}$) are required. Furthermore, a very good homogeneity of the nc-SiO$_x$:H(n) films prepared in this large-area system was demonstrated.

In the second part of this work, the nc-SiO$_x$:H layers at thickness of 15 nm were integrated in the rear-junction SHJ solar cells as electron transport layer (ETL) on n-type quarter-M2-sized c-Si wafers. It was demonstrated that the variation of material properties of nc-SiO$_x$:H(n) does not affect the V_{oc} but has a big influence on the J_{sc} and the fill factor (FF) of SHJ solar cells as well as the contact resistivity (ρ_c) of indium tin oxide (ITO) / nc-SiO$_x$:H(n). It was found that the ρ_c of ITO / nc-SiO$_x$:H(n) can be reduced by increasing the dark conductivity (σ) and the F_c, or reducing the optical band gap (E_{04}) of nc-SiO$_x$:H(n). In total, the best performed cell in the preliminary development shows V_{oc} of 728 mV, FF of 76.7%, J_{sc} of 39.1 mA/cm^2 and η of 21.83%. To have a comprehensive knowledge on efficiency limit of the solar cell, a highly predictive model was built in Quokk3 simulator and a power loss analysis was carried out. It was found that the bottleneck to the cell performance is the properties of the front layer stacks. Then, a road map to 24% of power conversion efficiency was put forward.

In the third part of this work, a systematical optimization has been done to improve the cell performance. The solar cells with different ETL structure at various thickness were fabricated. Significantly deteriorated contact property of nc-SiO$_x$:H(n) / ITO was observed when reducing the nc-SiO$_x$:H thickness from 20 to 5 nm, which can not be compensated by the decreased parasitic absorption on the front. By inserting the a-Si:H(n) or the highly conductive nc-Si:H(n) between nc-SiO$_x$:H(n) and ITO an enhancement of the contact property can be achieved. Besides, it was demonstrated that a rapid nucleation and a thinner incubation layer can be obtained by depositing nc-Si:H(n) seed layer prior to the nc-SiO$_x$:H(n). Compared to the cells with nc-SiO$_x$:H(n) single layer, around 3% relative gain of η is achieved for the cells with nc-Si:H(n) / nc-SiO$_x$:H(n) multi-layer. To enhance the surface passivation, the hydrogen plasma treated a-Si:H(i) layers were deposited as the passivating layer on both side, yielding about 1%$_{\text{abs}}$ increase of η. Additionally, the devices with various transparent conductive oxide (TCO) upon nc-SiO$_x$:H(n)

single layer were prepared and their IV parameters were compared. It was found that lower contact resistivity of nc-SiO$_x$:H(n)/TCO and nc-SiO$_x$:H/Ag are reached for the cells with titanium doped indium oxide (ITiO) compared to the devices with ITO. Besides, we identified the optimal thickness of the magnesium fluoride (MgF$_2$) and ITO for the cells with 10 nm nc-SiO$_x$:H(n) single layer by OPAL 2 simulation to maximize the generate current. More than 0.6 mA/cm^2 gain of J_{sc} and 0.3%$_{\mathrm{abs}}$ increase of η were observed without compromising to FF and V_{oc}, achieving 40.06 mA/cm^2 of J_{sc} and 22.8% of η. Furthermore, the perimeter recombination in the devices with four 1.9×1.9 cm^2 cells embedded in a quarter-M2-sized wafer was studied by means of Quokka3 simulation. About 9 mV reduction of V_{oc} was found for the small size cells compared with the full-size cells. Then we applied the optimized ETL, ITO, a-Si:H(i) and a-Si:H(p) in the full-sized M2 wafers to totally omit the perimeter recombination. To further improve the device performance, ultra-thin (5nm) nc-Si:H(n) film was utilized and optimized in the full-sized SHJ solar cells. A TCO sputter damage was observed for the cells with porous nc-Si:H(n) and proved to be related to the ion bombardment and the microstructure of nc-Si:H(n). By using a denser nc-Si:H(n), a decreased sputter damage and an enhancement of η from 22.4% to 23.6% were demonstrated. The best solar cell exhibits V_{oc} of 741.8 mV, FF of 82.2%, J_{sc} of 39.27 mA/cm^2 and η of 23.95% on an M2-sized wafer (244.3 cm^2).

Zusammenfassung

Dank der hervorragenden Passivierung von hydriertem amorphem Silizium (a-Si:H) auf der Wafer-Oberfläche wurden in den letzten Jahrzehnten mit der Silizium-Heteroübergangs-Solarzellentechnologie (SHJ) eine hohe Leerlaufspannung (V_{oc}) und ein hoher Wirkungsgrad (η) erreicht. Allerdings führt eine erhebliche parasitäre Absorption in dotiertem a-Si:H zu einer niedrigen Kurzschlussstromdichte (J_{sc}), wodurch die Zellleistung von SHJ-Solarzellen eingeschränkt wird. Dotiertes hydriertes nanokristallines Siliziumoxid (nc-SiO$_{\mathrm{x}}$:H), das aus leitfähigen Siliziumkristalliten (nc-Si) besteht, die in eine transparente Matrix aus hydriertem amorphem Siliziumoxid (a-SiO$_{\mathrm{x}}$:H) eingebettet sind, ist ein attraktives Alternativmaterial zum üblicherweise in SHJ-Solarzellen verwendeten a-Si:H, um die Zellleistung weiter zu verbessern. Bei der Anwendung von nc-SiO$_{\mathrm{x}}$:H(n) in SHJ-Solarzellen muss immer ein Kompromiss zwischen den optischen und elektrischen Eigenschaften berücksichtigt werden. Ziel dieser Arbeit ist es, die Implementierung dieser Schicht in SHJ-Solarzellen systematisch zu untersuchen, die Korrelation zwischen Materialeigenschaften und Geräteleistung zu ermitteln und die industrielle Anwendbarkeit von nc-SiO$_{\mathrm{x}}$:H in SHJ-Solarzellen zu demonstrieren.

Im ersten Teil dieser Arbeit wurden n-Typ nc-SiO$_{\mathrm{x}}$:H und hydriertes nanokristallines Silizium (nc-Si:H) Schichten entwickelt und in einer industriellen Multisubstrat plasmaunterstützten chemischen Gasphasenabscheidung (PECVD) Anlage für die Anwendung in vollflächigen ($>$156×156 mm^2) SHJ Solarzellen verglichen. Mittels optischer, elektrischer und struktureller Materialcharakterisierungen wurde der Einfluss der Depositionsparameter, wie Depositionsleistungsdichte (P), Depositionsdruck (p) und Gaszusammensetzungen, untersucht. Es wurde festgestellt, dass die Reaktion von nc-SiO$_{\mathrm{x}}$:H(n) auf die Variation der Abscheidungsparameter anders ist als die von nc-Si:H(n)-Schichten. AuSSerdem wurde ein synergistischer Effekt

von CO_2 und PH_3 oder CO_2 und SiH_4 auf die Materialeigenschaften von nc-SiO$_x$:H-Schichten beobachtet. Um nc-SiO$_x$:H mit hoher Transparenz und ausreichender Leitfähigkeit zu erhalten, ist ein hoher Volumenanteil von a-SiO$_x$:H ($F_{\text{a-SiO}_2}$) und nc-Si (F_c), aber ein geringer Volumenanteil von a-Si:H ($F_{\text{a-Si:H}}$) erforderlich. AuSSerdem wurde eine sehr gute Homogenität der in diesem groSSflächigen System hergestellten nc-SiO$_x$:H(n)-Schicht nachgewiesen.

Im zweiten Teil dieser Arbeit wurden die nc-SiO$_x$:H-Schichten mit einer Dicke von 15 nm in SHJ-Solarzellen mit rückseitigem Übergang als ETL auf n-Typ c-Si-Wafern der GröSSe M2 integriert. Es wurde gezeigt, dass die Variation der Materialeigenschaften von nc-SiO$_x$:H(n) keinen Einfluss auf das V_{oc} hat, aber einen groSSen Einfluss auf den J_{sc} und den Füllfaktor (FF) der Solarzellen sowie den Kontaktwiderstand (ρ_c) von Indium-Zinn-Oxid (ITO) / nc-SiO$_x$:H(n). Es wurde festgestellt, dass der ρ_c von ITO / nc-SiO$_x$:H(n) durch Erhöhung der Dunkelleitfähigkeit (σ) und des F_c oder durch Verringerung der optischen Bandlücke (E_{04}) von nc-SiO$_x$:H(n) verringert werden kann. Insgesamt zeigt die beste Zelle in der Vorentwicklung V_{oc} von 728 mV, FF von 76,7%, J_{sc} von 39,1 mA/cm^2 und η von 21,83%. Um ein umfassendes Wissen über die Wirkungsgradgrenze der Solarzelle zu erhalten, wurde ein hochgradig vorhersagendes Modell im Quokk3-Simulator erstellt und eine Verlustleistungsanalyse durchgeführt. Es wurde festgestellt, dass der Engpass in den Eigenschaften der Frontschichtstapel liegt. AnschlieSSend wurde ein Fahrplan zur Erreichung eines Wirkungsgrads von 24% aufgestellt.

Im dritten Teil dieser Arbeit wurde eine systematische Optimierung durchgeführt, um die Zellleistung zu verbessern. Es wurden Solarzellen mit verschiedenen ETL-Strukturen und unterschiedlichen Dicken hergestellt. Eine deutliche Verschlechterung der Kontakteigenschaften von nc-SiO$_x$:H(n) / ITO wurde bei einer Verringerung der nc-SiO$_x$:H-Dicke von 20 auf 5 nm beobachtet, was nicht durch die verringerte parasitäre Absorption auf der Vorderseite kompensiert werden kann. Durch Einfügen von a-Si:H(n) oder hochleitfähigem nc-Si:H(n) zwischen nc-SiO$_x$:H(n) und ITO kann eine Verbesserung der Kontakteigenschaften erreicht werden. AuSSerdem wurde gezeigt, dass eine schnelle Keimbildung und eine dünnere Inkubationsschicht erreicht werden kann, wenn die nc-Si:H(n)-Saatschicht vor dem nc-SiO$_x$:H(n) aufgebracht wird. Im Vergleich zu den Zellen mit einer einzelnen nc-SiO$_x$:H(n)-Schicht wird bei den Zellen mit einer nc-Si:H(n)/ nc-SiO_x:H(n)-Mehrschicht ein relativer Zuwachs von etwa 3% erreicht. Um die Oberflächenpassivierung zu verbessern, wurden die mit Wasserstoffplasma behandelten a-Si:H(i)-Schichten als Passivierungsschicht auf beiden Seiten abgeschieden, was zu einer Erhöhung des η um etwa $1\%_{abs}$ führte. Zusätzlich wurden Bauelemente mit verschiedenen transparenten leitfähigen Oxiden (TCO) auf nc-SiO_x:H(n)-Einzelschichten hergestellt und deren IV-Parameter verglichen. Es wurde festgestellt, dass der Kontaktwiderstand von nc-SiO_x:H(n)/TCO und nc-SiO_x:H/Ag für Zellen mit titandotiertem Indiumoxid (ITiO) niedriger ist als für Zellen mit ITO. AuSSerdem haben wir die optimale Dicke von MgF_2 und ITO für die Zellen mit 10 nm nc-SiO_x:H(n)-Einzelschicht durch OPAL 2-Simulation ermittelt, um den erzeugten Strom zu maximieren. Mehr als 0,6 mA/cm^2 Gewinn von J_{sc} und $0,3\%_{abs}$ Erhöhung von η wurden beobachtet, ohne FF und V_{oc} zu beeinträchtigen, wobei 40,06 mA/cm^2 von J_{sc} und 22,8% von η erreicht wurden. Darüber hinaus wurde die Randrekombination in den Bauelementen mit vier 1,9 mal 1,9 cm^2 groSSen Zellen, die in einen Wafer der GröSSe eines Viertel-M2 eingebettet sind, mit Hilfe der Quokka3-Simulation untersucht. Es wurde eine Verringerung des V_{oc} um etwa 9 mV für die kleinen Zellen im Vergleich zu den Zellen in voller GröSSe festgestellt. Dann haben wir die optimierten ETL, ITO, a-Si:H(i) und a-Si:H(p) in den M2-Wafern in voller GröSSe eingesetzt, um die Rekombination am Rand vollständig zu vermeiden. Zur weiteren Verbesserung der Bauelementleistung wurde eine ultradünne (5 nm) nc-Si:H(n)-Schicht verwendet und in vollflächigen SHJ-Solarzellen optimiert. Bei Zellen mit porösem nc-Si:H(n) wurde ein TCO-Sputterschaden beobachtet, der nachweislich mit dem Ionenbeschuss und der Mikrostruktur von nc-Si:H(n) zusammenhängt. Die Verwendung eines dichteren nc-Si:H(n) führte zu einer Verringerung des Sputterschadens und zu einer Erhöhung von η von 22,4% auf 23,6%. Die beste Solarzelle weist einen V_{oc} von 741,8 mV, FF von 82,2%, J_{sc} von 39,27 mA/cm^2 und einen Wirkungsgrad η von 23,95% auf einem Wafer der GröSSe M2 (244,3 cm^2) auf.

1. Introduction

Energy is the cornerstone of the human society and the main energy source to satisfy the highly and ever-increasing energy demand is still the fossil fuel, the continues use of which causes excessive carbon emissions and is responsible for global warming and climate anomalies. Besides, the fossil fuel is derived from solar energy and it's generation is so complex and time-consuming that can be ranked as miracle on the earth, but at current consumption rates it will be exhausted sooner or later. Therefore, it is a task which brooks no decay for mankind to develop clean and renewable energy to share the energy demand or even to replace the fossil fuel. Solar cell is a physical device that transforms the solar energy to the electric energy which can be used directly in our life. More and more people focus on solar cell and install the solar modules on the roof of their buildings, which are just like the household appliance and are making a difference around the world. Large-scale photovoltaic (PV) power stations have started appearing in many countries, and the globalization of the PV market is growing ever more noticeable year by year. According to the Sustainable Development Scenario, solar PV generation increased a record of 156 TWh (23%) in 2020 to 821 TWh and becomes the second-largest absolute generation growth of all renewable technologies [1]. Furthermore, the announcement of the target for carbon neutrality and net-zero in more and more countries spurs an unprecedented boom in PV industry and boosts the development of PV technologies.

Over the past decades, the silicon PV industry has devoted a continuous effort to the power conversion efficiency (η) improvement ($0.5{\sim}0.6\%_{\mathrm{abs}}$ per year) and the cost reduction ($> -15\%$ per year in average) [2, 3]. Currently, Passivated Emitter and Rear Cell (PERC) are the actual workhorse of the PV industrial and hold a dominant market share due to its mature supply chain (equipment, materials, chemicals), standardized cell (and module) design or process, low levelized cost of electricity (LCOE) and high efficiency (22%∼23.4% in production) [2]. However, the practical efficiency limit of this concept is about 24.5% while the efficiency in mass production has reached 23.3% already, making it very difficult to further improve the cell performance [4]. Therefore, new technologies have to be implemented if industry wants to stay on the 0.5∼0.6%$_{\mathrm{abs}}$ annual efficiency improvement.

The silicon heterojunction (SHJ) solar cell combining the high efficiency of crystalline silicon (c-Si) with the low temperature deposition technology of thin-film silicon (< 200 °C) has progressed rapidly over the past few years [5]. Its production is expected to gain about 10% market shares in 2024 and 17% by 2030, as predicted by the International Technology Roadmap for Photovoltaic (ITRPV) in 2019 [6]. The SHJ concept is able to exceed the efficiency limit of PERC and will be the next generation high-efficiency PV production after PERC due to its low thermal coefficient ($< 0.3\%/°\mathrm{C}$), lean fabrication process and high bifaciality ($> 90\%$) [2,4,7]. Intrinsic hydrogenated amorphous silicon (a-Si:H(i)) layer is used to passivate the c-Si surface and the doped a-Si:H film acts as carrier selective layer in SHJ solar cells [5, 8, 9]. Thanks to the excellent surface passivation quality of a-Si:H(i), SHJ solar cells hold the record for open circuit voltage (V_{oc}) at one sun (750 mV) and achieve more than 25% of efficiency on both-side contact structure [8, 9]. The main challenge of SHJ solar cells is the high absorption coefficient of a-Si:H films. Although the front doped a-Si:H layer is only several nanometers thin (5∼10 nm), it does absorb a significant amount of incoming light, leading to a reduction of the short circuit current density (J_{sc}) by 1.6 mA/cm^2 and much lower J_{sc} than PERC [10, 11]. This disadvantage can be overcome by using the interdigitated back contact (IBC) design to eliminate the shading of front electrodes and reduce the parasitic absorption in a-Si:H layers, leading to a world-record efficiency of 26.7% in 2017 [12]. However, the fabrication process of IBC cells is much more complex than the conventional two-side contact structure, making it expensive and unsuitable for the mass production. Another solution to tackle the optical issue in SHJ solar cells is the usage of a wide band-gap material on the front side. The hydrogenated nanocrystalline silicon oxide (nc-SiO$_{\mathrm{x}}$:H) consists of highly conductive nanocrystalline silicon (nc-Si) and highly transparent amorphous silicon oxide (a-SiO$_{\mathrm{x}}$:H) phases [13, 14]. Such a unique structure opens another degree of freedom for finding an optimum between electrical and optical properties that can be tuned over a wide range by varying growth conditions, yielding a highly promising alternative to the commonly used doped a-Si:H film [13–16].

This thesis deals with the development of the large area up-scaling of nanocrystalline silicon oxide thin-films as highly transparent and highly conductive front side layers in the industrial sized 156×156 mm^2 SHJ solar cells. The aim of this work is at the demonstration of the industrial applicability of this material in SHJ solar cells and the finding of the correlation between the material properties and the cell performance on the basis of reliably large statistics. From material preparation to solar cell prototype, power loss analysis to parameters optimization, light management to contact formation and surface passivation, every aspect which may result in the up-scaling solar cell performance improvement has been studied. At the beginning of this work, n-type nc-SiO$_x$:H(n) films are developed in a industrial multi-substrate plasma enhanced chemical vapor deposition (PECVD) system by tuning the deposition parameters. Then the nc-SiO$_x$:H (n) films with different material properties are integrated in the rear-junction SHJ solar cells to link the material properties to the cell performance and to establish a standard nc-SiO$_x$:H(n) recipe for SHJ devices. Meanwhile, a power loss analysis is conducted by Quokka3 simulator to find the cell performance bottleneck and to build a roadmap to the high-efficient solar cells ($\eta >$ 24%). Afterwards, a systematic optimization of the devices is followed to improve the cell performance and to acquire a deep understanding of the physical working principle of SHJ solar cells.

Chapter 2 presents a literature review on SHJ solar cells and nc-SiO$_x$:H material. Sec. 2.1 describes the development history of SHJ solar cells and its specific features. Sec. 2.2 gives a brief introduction of nc-SiO$_x$:H or hydrogenated nanocrystalline silicon (nc-Si:H) films and their growth models in PECVD system.

Chapter 3 describes the experiment and material characterization methods employed in this thesis. Sec. 3.1 presents the principle of the technology for material and solar cell preparation. Sec. 3.2 and Sec. 3.3 shows the details on characterization methods for the silicon thin-films and the silicon based solar cells, respectively. Sec. 3.4 introduces software for numerical device simulations and power loss analysis.

Chapter 4 focuses on the development of nc-SiO$_x$:H (n) layers in an industrial multi-substrate PECVD system. Sec. 4.1 reports the effect of power density and process pressure on the opto-electrical properties of nc-Si:H(n) or nc-SiO_x:H(n) layers. In Sec. 4.2, the influence of the gas composition used in PECVD process, including the total gas flow (f_{total}), the CO_2 gas flow fraction (f_{CO_2}), the PH_3 gas flow fraction (f_{PH_3}) and the SiH_4 gas flow fraction (f_{SiH_4}), is investigated. Sec. 4.3 presents a overview of the material properties, the relationship between the material structure properties and opto-electrical properties, and the homogeneity of nc-SiO_x:H(n) layers prepared in this industrial PECVD system.

Chapter 5 describes a preliminary development of the rear-junction SHJ solar cells with nc-SiO_x:H(n) as window layer on quarter-M2-sized wafer. Sec. 5.1 introduces the fabrication process of the SHJ solar cells in this thesis. In Sec. 5.2.1, the effect of the intrinsic and the doped silicon layer stack on passivation quality is presented. In Sec. 5.2.2, the influence of nc-SiO_x:H material properties on the passivation quality and the performance of the SHJ solar cells are investigated by varying f_{CO_2} and f_{PH_3}. Sec. 5.3 reports a detailed power loss analysis for the best solar cell in this chapter and a road map to reach >24% of power conversion efficiency.

Chapter 6 introduces a systematic optimization of the rear-junction SHJ solar cells. In Sec. 6.1, the SHJ solar cells with nc-SiO_x:H(n) single layer, a-Si:H(n) / nc-SiO_x:H(n) or nc-SiO_x:H(n)/nc-Si:H(n) multi-layer at different thickness are fabricated and the influence of those structures on the cell performance is presented. Sec. 6.2 describes the optimization of a-Si:H(i) layer by applying H_2 plasma treatment during the depositions and reducing the layer thickness. In Sec. 6.3, different kinds of transparent conductive oxide (TCO) layers are integrated in the devices with nc-SiO_x:H single layers. Sec. 6.4 presents a detailed Quokka3 simulation on the perimeter recombination in the quarter-M2-sized solar cells and a strategy to reduce this effect. In Sec. 6.5, an optimization of full-size (244.3 cm^2) solar cells with 5 nm nc-Si:H(n) is carried out by increasing the crystalline volume fraction (F_c) of nc-Si:H. Meanwhile, the effect of sputtering process on passivation quality and performance of these cells are investigated.

Chapter 7 summarizes all key results and conclusions of this thesis, and gives a outlook of the topic on the industrial SHJ solar cells with nc-SiO_x:H layers.

2. Literature review

This chapter reports a literature review on SHJ solar cells and nc-SiO_x:H or nc-Si:H films. Firstly, the development history and the specific features of SHJ solar cells are described. Secondly, an introduction of the nc-SiO_x:H films and their growth models in PECVD system is presented.

2.1. Silicon heterojunction solar cell

Silicon heterojunction solar cells represents a very promising technology for highly efficient solar cells with fairly low manufacturing cost and predicted to be the next mainstream production in PV industry after PERC [2, 4, 6, 7]. The heterojunction approach applied to solar cells is inspired by the heterojunction transistor proposed by Shockley in 1948 [17]. Fuhs et al. reported the first investigation on the heterojunction formed between a doped a-Si:H thin-film and a crystalline silicon (c-Si) in 1974 [18]. A few years later, remarkable passivated c-Si surfaces were obtained by the usage of a-Si:H(i) films [19]. In 1983, the silicon heterojunction (a-Si:H/poly-Si) was integrated for the first time in a tandem junction solar cell, the so-called Honeymoon cell by Hamakawa et al [20, 21]. At about the same time, the electronic junction between the doped a-Si:H and c-Si drew extensive attention [22, 23]. In the late 1980s, Sanyo was devoted into this research field and applied a p-type a-Si:H(p) layer onto a c-Si(n) directly to form the heterojunction solar cell, achieving an efficiency of 12.3% [24, 25]. In 1992, Sanyo incorporated a thin a-Si:H(i) layer between the c-Si(n) and the a-Si:H(p) to passivate the dangling bonds on the c-Si surface, which brought the efficiency up to 14.8% [25]. This cell structure was named heterojunction with intrinsic thin layer (HIT®) solar cell and the related patent was filed in 1993 [26]. In the next, a back surface field (BSF) induced by a-Si:H(n) on textured wafer was introduced into the HIT® solar cells to reduce the carrier recombination on the backside of the wafer and to increase the average optical light path length inside the wafer, enabling the HIT® solar cell efficiency as high as 18.1% [25]. In 1997, the first industrialization of a-Si:H/c-Si hybrid solar cells was started by Sanyo. An efficiency in excess of 20% was reported for large area (>100cm^2) devices in 2000 [5]. Using a similar a-Si:H(i) film as a passivating layer on the backside boosted the cell efficiency to 21.3% [5, 27]. By 2009, Sanyo had achieved HIT® solar cell efficiency as high as 23% with a thin wafer of 98 μm after further optimization of materials and processing [28]. The high performance and low-temperature process of Sanyo HIT® solar cells have attracted the interest of companies and researches all over the world [29–33]. This concept laid the foundation for the commercialization and the current success of SHJ cells. Panasonic announced an efficiency of 24.7% for both side contacted cells and 25.6% using the interdigitated back contact (IBC) structure in 2014 [8, 34]. At the same time, a rear emitter concept of the SHJ solar cells was gaining more and more attention. The c-Si(n) wafer was used as absorber in this concept and a front surface field (FSF) was induced by the a-Si:H(n) film. The doped layer on the front side underlies more restrictions and the a-Si:H(n) can fulfill the requirements more easily than the a-Si:H(p), making the rear emitter concept attractive [35, 36]. Another company with a strong background in silicon thin-film solar cell (Kaneka Corp) demonstrated an efficiency of 25.1% for both side contacted cells in 2015, surpassing the champion efficiency of the homojunction PERC [37]. Two years later, Kaneka improved the IBC efficiency to the world record of silicon solar cells of 26.7% [12] by integrating the SHJ concept. This world record was broken in 2022 by LONGi company and the efficiency reached 26.81% for the two-side contacted SHJ solar cells [38].

Fig. 2.1 shows a sketch of a typical SHJ solar cell and its band diagram under equilibrium condition. An n-type crystalline wafer is used as absorber and a random surface texture provides effective light trapping. Intrinsic hydrogenated amorphous silicon films are deposited on both sides of the wafer by plasma enhanced chemical vapor deposition (PECVD) to provide chemical passivation of the absorber surface and to achieve a low defect density. An a-Si:H(p) emitter layer is utilized on the front side to extract holes, and an a-Si:H(n) is deposited on the rear side to create a BSF that repels the minority charge carriers and extracts the electrons. A transparent

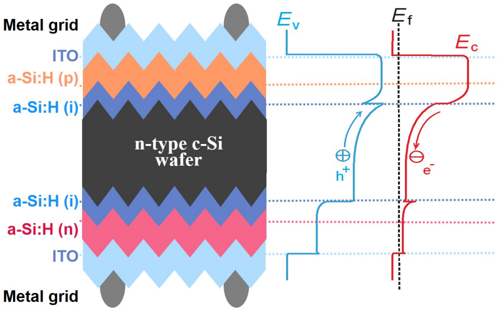

Figure 2.1.: *Sketch of a typical SHJ solar cell and its band diagram under equilibrium condition with indicated direction of hole* (h^+) *and electron* (e^-) *transport.* E_v, E_c *and* E_f *is the valence band edge, conduction band edge, and Fermi level, respectively.*

conductive oxide (TCO) layer is deposited above the doped a-Si:H layers by physical vapor deposition (PVD) to collect the carriers on the lateral direction and to ensure a good contact to the metal grid prepared by screen printing. Due to the difference of the band gap and the electron affinity of c-Si and a-Si:H, the conduction and the valence band offsets are induced on the c-Si/a-Si:H interfaces of both sides. They act as energy barriers for the charge carriers, minimizing the injection of minority carriers from the absorber into the doped layers. For the majority carriers the narrow 'spike' barrier can be overcome by band-to-band tunneling, trap-assisted tunneling or thermionic emission [39]. Details on the working principle of the heterojunction solar cells can be found in Ref. [40, 41].

Thanks to the smart design, the SHJ solar cells have several advantages over the conventional silicon homojunction solar cells. First, the thermal budget during the heterojunction formation is considerably lower than the homojunction formation (Fig. 2.2 (a)), resulting in a lower energy consumption during the production [40]. The deposition temperature of a-Si:H and TCO is usually less than 250°C, while that of the phosphorous or the boron diffusion in the homojunction devices is more than 850°C [40]. Second, the process time required to form the junction and to deposit the contact layers is also shorter for the heterojunction than the conventional homojunction solar cells (Fig. 2.2 (a)), allowing a high-throughput production machinery for the SHJ devices [40]. Third, the SHJ device features a symmetrical structure and can reach high bifaciality (>90%) naturally [5, 27]. Therefore, more than 3%

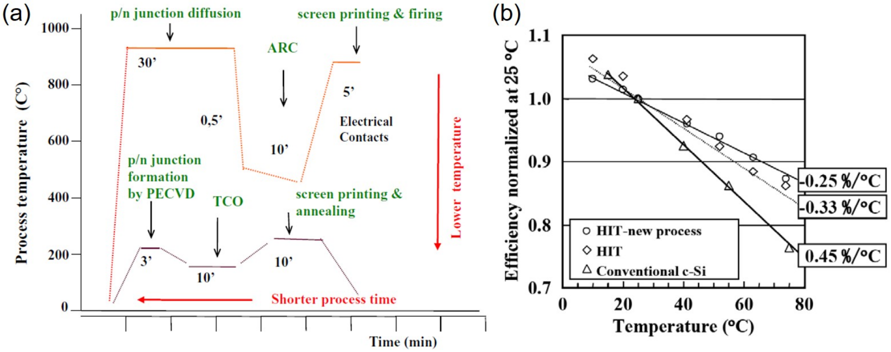

Figure 2.2.: *(a) Estimated thermal budget and process time for the conventional c-Si technology (top curve) and SHJ technology (bottom curve) [40]. (b) Stability of SHJ solar cells regarding temperature dependence [42].*

higher power output for the SHJ bifacial modules was obtained under the realistic operation condition, compared with the PERC modules [2, 43]. Fourth, due to the low process temperature of the SHJ solar cells and their symmetric structure, less warping effects take place, making it possible to use a thinner silicon wafer (<100 μm). This is beneficial for bringing the production cost down by reducing the silicon material consumption [28]. Fifth, the efficiency of the SHJ solar cells has a less temperature dependence than the conventional diffused cells (see Fig. 2.2(b)), giving rise to 8.8% higher power output during the high temperature usage [42]. Sixth, a high stability is observed for the SHJ devices [44], owing to the absence of the Staleber-Wronski effect, which is seen in a-Si based thin-film solar cells [45, 46], and no boron-oxide complex in c-Si(n), which is responsible for the minority carrier lifetime degradation in PERC prepared on p-type wafer [47].

2.2. Hydrogenated nanocrystalline silicon oxide

These advantages mentioned previously makes SHJ solar cell a suitable candidate for the large-volume production after PERC in the future. One of the challenges to further improve the SHJ cell performance is the parasitic absorption in the a-Si:H layers on the front [10, 11]. Replacing the a-Si:H(n) with a wide-band material,

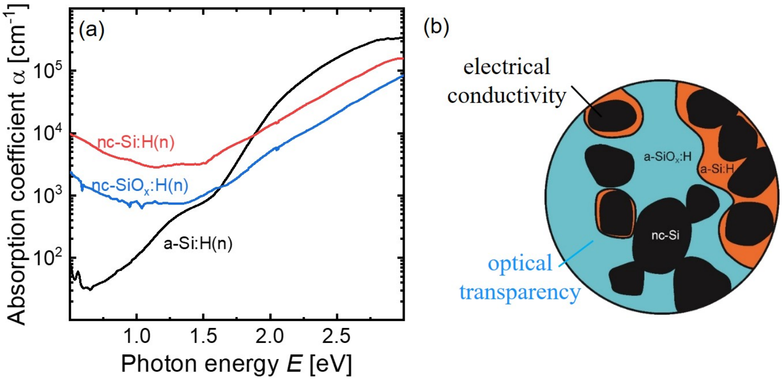

Figure 2.3.: *(a) Absorption coefficient (α) of n-type doped silicon alloys. (b) Sketch of the microstructure of nc-*SiO_x*:H films consisting of an a-Si:H, a-*SiO_x*:H and nc-Si:H phase [13].*

such as hydrogenated nanocrystalline silicon (nc-Si:H)(n) or hydrogenated nanocrystalline silicon oxide (nc-$\mathrm{SiO_x}$:H)(n), is a possible strategy to overcome this challenge. Fig. 2.3 shows the absorption coefficient (α) of different silicon alloys. A reduced α in the blue part of the spectrum is observed for nc-Si:H(n) and nc-$\mathrm{SiO_x}$:H(n) in comparison with a-Si:H(n). Hydrogenated nanocrystalline silicon is a biphasic material, where the nanocrystalline phases (nc-Si:H) are embedded in the amorphous silicon matrix (a-Si:H) [48–51]. The size of crystallites in nc-Si:H layers is in the range of 1 $\sim$ 100 nm, resulting in a wider band gap than a-Si:H due to quantum size effects [52]. The first paper on the deposition of nc-Si:H, which was named hydrogenated microcrystalline silicon (μc-Si:H) at that time, by PECVD was reported by Usui and Kikuchi in 1979 [53]. The first successful application of the doped nc-Si:H layers in the thin-film solar cells was demonstrated by Guha et al. in 1986 [54]. The nc-$\mathrm{SiO_x}$:H films were deposited via PECVD for the first time by adding carbon dioxide (CO_2) during the deposition of nc-Si:H films in 1993 [55]. The nc-$\mathrm{SiO_x}$:H films consist of three phases: nc-Si:H, a-Si:H and hydrogenated amorphous silicon oxide (a-$\mathrm{SiO_x}$:H), as shown in Fig. 2.3(b) [13, 15, 56–60]. It was reported that the conductivity of the nc-Si:H phases is around several orders of magnitude larger than those of the amorphous phases due to its higher doping efficiency [61]. Thus, the nc-Si:H phase is responsible for the conductivity of the nc-SiO_x:H layers, while the optical property of nc-SiO_x:H is assigned to the highly transparent a-SiO_x:H phase [13, 51, 58]. The first application of nc-SiO_x:H in the thin-film solar cell was reported by Sichanugrist et al. in 1994 [62]. Few years later, Yamamoto et al. integrated this film as an intermediate reflector in a-Si:H/nc-Si:H tandem cells [63]. Since then, many studies on the nc-SiO_x:H layer and its application on the thin-film silicon solar cells were published [59, 60, 64, 65]. In 2007, the first silicon heterojunction solar cell with nc-SiO_x:H as emitter layer was fabricated by Sritharathikhun et al [66, 67]. Thanks to its combination of the highly conductive nc-Si:H phases with the highly transparent a-SiO_x:H matrix, nc-SiO_x:H is very suitable for being an emitter or window layer in SHJ devices. However, the material properties need to be carefully tuned to achieve highly transparency with sufficient conductivity.

The PECVD method is widely used for the preparation of uniform and high-quality nc-SiO_x:H films at a low substrate temperature. A silicon containing gas, usually silane (SiH_4), hydrogen (H_2) and oxygen source gas, CO_2, are admitted to a vacuum reactor chamber for the deposition of nc-SiO_x:H films. Then a gas discharge is initiated and maintained by an electric field between two parallel plates, using either a direct current (DC) voltage or a voltage in the radio frequency domain (13.65 $\sim$ 200 MHz) [68, 69]. In the glow discharge plasma, reactive molecules are excited to higher electronic states due to inelastic collisions with energetic electrons and dissociated to silanide (SiH_3), silylene (SiH_2), mono-hydride (SiH), Si, carbon oxide (CO), oxygen (O), H_2 and H spontaneously via following reactions Ref. [70,71]:

$$\mathrm{SiH_4 + e^- \Longrightarrow SiH_3 + H + e^-} \tag{2.1}$$

$$\mathrm{SiH_4 + e^- \Longrightarrow SiH_2 + H_2 + e^-} \tag{2.2}$$

$$\mathrm{SiH_4 + e^- \Longrightarrow SiH + H + H_2 + e^-} \tag{2.3}$$

$$\mathrm{SiH_4 + e^- \Longrightarrow Si + 2H_2 + e^-} \tag{2.4}$$

$$\mathrm{SiH_4 + H \Longrightarrow SiH_3 + H_2} \tag{2.5}$$

$$\mathrm{CO_2 + e^- \Longrightarrow CO + O + e^-} \tag{2.6}$$

Additionally, these reactive species produced in the plasma experience secondary reactions with SiH_4 and H_2 molecules, resulting in a steady state [69, 70]. The relative importance of each reactions depends on the energy of the electrons, which is a function of the electric field and their mean free path, depending on the total pressure. The reactivity of SiH_3 along with SiH_4 and H_2 (long-time species) is lower than SiH_2, SiH and Si (short-lifetime species), making SiH_3 radicals be the dominant chemical species for the deposition of nc-SiO_x:H materials. Hydrogen molecules are also decomposed to atomic hydrogen, which reach the film-growing surface and play an important role in the formation of the nc-Si:H phases. To explain the growth processes of nc-Si:H or nc-SiO_x:H, three different growth models had been proposed: i) the surface diffusion model [72], ii) the etching model [73], iii) the chemical annealing model [74].

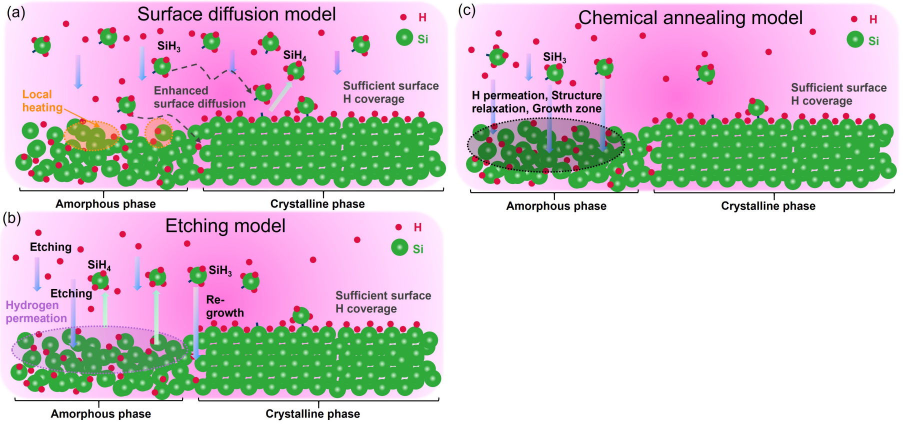

Figure 2.4.: *Schematic representation of (a) the surface diffusion model, (b) the etching model and (c) the chemical annealing model for the growth process of nc-Si:H or nc-SiO_x:H films [69].*

The surface diffusion model is depicted schematically in Fig. 2.4(a). A full coverage of the dangling bonds on the film-growing surface is acquired by a high atomic H flux from the plasma. On one hand, the SiH_3 radicals are adsorbed on the surface and interact with the hydrogen at its landing site, forming SiH_4 and leaving dangling bonds on the surface, which is known as growth-site formation. Afterwards, other adsorbed SiH_3 radicals diffuse across the surface to find the site containing the dangling bonds, where the Si-Si bond formation occurs [72]. On the other hand, the local heating on the film-growth surface through hydrogen exchange reactions enhances the surface diffusion of SiH_3, which is beneficial for the nucleus formation and the epitaxial-like crystal growth in the incubation layer [72, 75, 76].

The concept behind the etching model is shown schematically in Fig. 2.4(b). It was developed to interpret the decline of the deposition rate when increasing the hydrogen dilution [75]. The atomic hydrogen reach the film-growing surface and break Si-Si bonds, preferentially weak bonds involved in the amorphous network structure, where the formation of a stronger Si-Si bond with SiH_3 takes place [75]. The continuous iterations of these processes improve the stability of the network and boost the crystalline growth with a compromising to the deposition rate [75].

A schematic drawing of the chemical annealing model is illustrated in Fig. 2.4(c). The atomic hydrogen from the plasma permeates through the subsurface (the growth zone) and reacts with Si-H or strained Si-Si bonds, leading to the crystallization of an amorphous network without any significant removal of Si atoms [76]. This model was proposed to explain the transformation of the a-Si:H phases to the nc-Si:H phases during the hydrogen plasma treatment [76, 77].

The crystallites in nc-SiO_x:H films typically grow in a columnar structure in the direction of the growth, enabling the transport of the charge carriers in the growth direction. The growth direction of crystallites is the same as the current flow direction through the doped layer in SHJ solar cells [51]. Furthermore, a lower conductivity of the nc-SiO_x:H layer in the horizontal direction was demonstrated compared to the vertical one [78, 79]. The growth of nc-SiO_x:H layer can be differentiated into four kinds of status: incubation, nucleation, growth and steady-state [80]. The first few nanometers layer in which crystalline growth has not yet appeared is named incubation layer, followed by the onset of the nucleation of crystallites. Thereon the mixed phases of a-Si:H, nc-Si:H and a-SiO_x:H grow epitaxially and the size of the crystal phases become large until the growth reaches stationary stage. The thickness of the incubation layer is associated with the deposition conditions and can be reduced by inserting a soft CO_2 plasma treatment [81, 82], performing a hydrogen plasma treatment [83], depositing a hydrogenated amorphous silicon oxide buffer layer [84], replacing the silane by the disilane for the deposition [85], and using a high excitation frequency [86]. The microstructure of nc-SiO_x:H can be controlled from highly crystalline to almost amorphous by varying the PECVD conditions, investigation on which is presented in Chapter 4.

3. Experimental methods

This chapter describes details of the samples prepared for material characterization, the tools used for thin-film deposition and solar cell fabrication, the measurements conducted for the characterization of material properties and solar cell performance, and the software for numerical device simulations and power loss analysis.

3.1. Technology for material and solar cell preparation

Plasma enhanced chemical vapor deposition (PECVD) PECVD is a widely used technique to obtain device-quality thin films at lower substrate temperature than that of standard chemical vapor deposition (CVD). In PECVD, source gases are decomposed in the plasma by the collisions between high-energetic electrons and gas molecules. The reactive species then reach the surface of the substrate via drift- and diffusion processes and react with each other or with surface atoms, forming the thin-films from islands to a complete layer. Detailed information on the method can be found in Ref. [68].

In this study, an industrial multi substrate PECVD system (AK 1000 Inline) from Meyer Burger Technology AG was used to produce nc-SiO$_x$:H and a-Si:H films. A sketch of the equipment is illustrated in Fig. 3.1. The tool consists of five chambers, including three process modules (PM1, PM2 and PM3) and two loading modules (LM1 and LM2). Carriers with dimension of $50 \times 50\,\mathrm{cm}^2$ can be loaded into the system via LM1 or LM2, and then transported to the process chambers. This system is capable of preparing 9 wafers of M2 size or glass substrates of equivalent area in one processing run. To avoid cross-contaminations on devices, the p-type

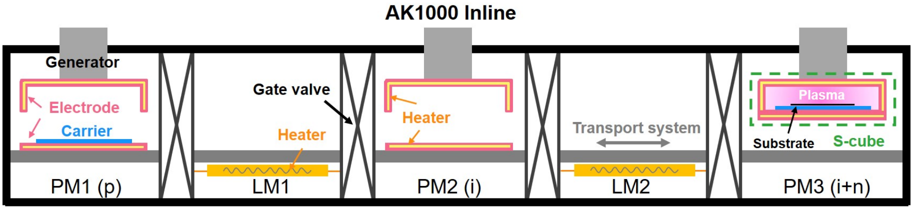

Figure 3.1.: *A top view sketch of the AK 1000 Inline PECVD deposition system. The types of layers prepared in the deposition chambers are indicated. The chambers are connected via evacuated transfer locks and load locks to move the substrate without breaking the vacuum. The transfer valves separate the chambers from each other.*

material, the intrinsic material below p-layer, the n-type material and the intrinsic material below n-layer were prepared in PM1, PM2, PM3 and PM3, respectively. Fig. 3.2 shows a schematic cross-section of one process chamber. A base pressure of at least 10^{-6} Pa was targeted within the chamber before deposition. The gas distribution is integrated in the upper electrode which is powered by an generator at radio frequency (RF, 13.56 MHz) via a matchbox. The carrier with substrates was placed on the lower electrode grounded by the rails. Both electrodes are made of aluminum and can be heated up separately. The temperature of the heaters was set to 200°C. To realize the plasma process the substrate electrode will be lifted up and contact with the RF electrode, forming a separate plasma discharge chamber (S-Cube), which is evacuated by an additional backing pump while the vacuum pressure is controlled by a butterfly valve. In this work, the process gases for hydrogenated amorphous silicon (a-Si:H) (i) were silane (SiH_4) and hydrogen (H_2), whereas carbon dioxide (CO_2) was added for nc-SiO_x:H films. In addition, phosphine (PH_3) and trimethylborane ($B(CH_3)_3$) or diborane (B_2H_6), diluted to 1 % in H_2, were supplied for n-type and p-type doping, respectively. The gas flows were controlled via mass flow controllers and measured in standard cubic centimeters (sccm).

All nc-SiO_x:H(n) layers in this work were prepared in PM3 and the detailed development of this material will be presented in Chapter 4. The material properties are strongly dependent on the deposition parameters, such as the power density of the generator (P), the process pressure (p) of the S-cube and the composition of the precursor gases. We defined CO_2, SiH_4, PH_3 and H_2 gas flow fractions via following

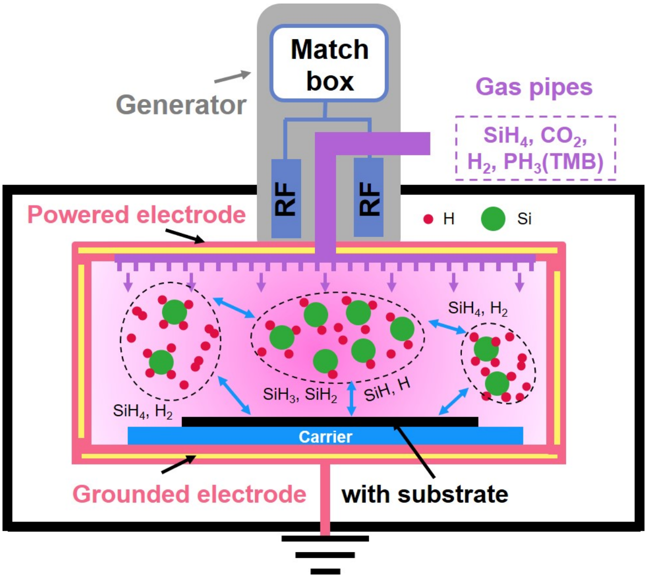

Figure 3.2.: *A schematic view of one of PECVD chambers used in the present study for the film and solar cell preparation.*

equations:

$$f_{\mathrm{CO2}} = \frac{[\mathrm{CO_2}]}{[\mathrm{CO_2}] + [\mathrm{SiH_4}]}, \tag{3.1}$$

$$f_{\mathrm{SiH4}} = \frac{[\mathrm{SiH_4}]}{[\mathrm{SiH_4}] + [\mathrm{H_2}]}, \tag{3.2}$$

$$f_{\mathrm{PH3}} = \frac{[\mathrm{PH_3}]}{[\mathrm{PH_3}] + [\mathrm{SiH_4}]}, \tag{3.3}$$

$$f_{\mathrm{H2}} = \frac{[\mathrm{H_2}]}{[\mathrm{PH_3}] + [\mathrm{SiH_4}] + [\mathrm{CO_2}] + [\mathrm{H_2}]}, \tag{3.4}$$

where the f_{CO2}, f_{SiH4}, f_{PH3} and f_{H2} are the gas flow fraction of CO_2, SiH_4, PH_3 and H_2, respectively; $[CO_2]$, $[SiH_4]$, $[PH_3]$ and $[H_2]$ are the gas flow of CO_2, SiH_4, PH_3 and H_2, respectively. Since the PH_3 is 1 % diluted in H_2, $[PH_3]$ is the net gas flow of the dopant gas and $[H_2]$ includes the dilution gas flow of the dopant gas.

Magnetron sputtering Magnetron sputtering is a deposition technology involving a gaseous plasma, generated and confined to a space near a solid target, which contains the material to be deposited. To initiate the plasma generation, a high voltage is applied between the cathode, commonly located directly behind the sputtering target, and the anode, commonly connected to the chamber as electrical ground. Electrons in the sputtering gas are accelerated away from the cathode, causing collisions with the nearby atoms of the sputtering gases. The collisions result in a electrostatic repulsion to the electrons and make the ionization happen. Afterwards, the surface of the target is eroded by these high-energy ions within the plasma, and the liberated atoms with enough kinetic energy travel through the vacuum environment and deposit onto a substrate to form a thin film. To confine the electrons in the plasma at or near the surface of the target, a very strong magnetic field is applied during the sputtering process. With this technique the ionization of the inert gas is enhanced, leading to a higher density plasma and a increase in deposition rates. Meanwhile, the damage related to the direct impact of these electrons on the substrate or growing film can also be reduced, yielding less porous films. Ref. [87] is recommended for further readings.

In this work, magnetron sputtering was used to prepare transparent conductive oxide (TCO) materials, such as indium tin oxide (ITO), tungsten doped indium oxide (IWO), titanium doped indium oxide (ITiO) and Al-doped zinc oxide (AZO). The ITO films were sputtered from a cylindrical 97:3 wt. % In_2O_3:SnO_2 target with a substrate temperature of 200°C, IWO from a 99:1 wt. % In_2O_3:WO_3 planar ceramic target with a substrate temperature of 50°C, ITiO from a 99:1 wt. % In_2O_3:TiO_2 planar ceramic target with a substrate temperature of 100°C and AZO from a 99:1 wt. % ZnO:Al_2O_3 planar ceramic target at room temperature. The comparison of various TCO properties and their integration in SHJ solar cells with nc-SiO_x:H(n) layer is presented in Sec. 6.3.1. Before the sputtering process, the chamber was evacuated to a base pressure below 10^{-3} µbar. Then the high-purity argon (Ar) and dioxygen (O_2) were introduced into the system as precursor gases under a given process pressure.

Screen printing The metallization process on front and back side of the wafer is one of the most crucial steps for producing SHJ solar cells. Currently it is commonly carried out by screen printing technology in the PV industry due to its relative simplicity, capability of extremely high throughput operation and cost efficiency. During the screen printing process a metal-containing conductive paste was forced through the openings of a screen to a wafer to form the circuits or contacts [88]. In this work a low-temperature silver paste was used and the screens with the certain patterned opening were designed for the SHJ solar cells fabricated on quartered or full-size M2 wafers. After screen printing an annealing treatment at 170°C for 40 mins was followed to get rid of the organic binders in the paste.

Electron-beam evaporation Electron Beam Evaporation is a form of physical vapor deposition (PVD). The target material is put on a charged tungsten filament in a high vacuum chamber, and bombarded with an electron beam to convert it to a gaseous state. Then these atoms or molecules in a vapor phase precipitate and form a thin film coating on the substrate. In this work, electron beam evaporation was used to deposit magnesium fluoride (MgF_2) layer upon the complete solar cells as anti-reflection coating (ARC).

Thermal evaporation Another PVD technique used in this work is thermal evaporation. The target material was placed on a tungsten boat in a vacuum chamber with a pressure below 3×10^{-3} Pa. A high electrical current was driven through the boat, heating it beyond the evaporation temperature of the target material, which was converted to a gaseous state for deposition evenly on the interior of the chamber including the substrate. In this thesis, two rectangular coplanar silver contacts of $5 \times 3.5\,\mathrm{mm}^2$ in a distance of 0.5 mm and with a thickness of 700 nm were thermal evaporated on the material samples. These coplannar silver contacts were prepared for the dark conductivity (σ) measurement.

3.2. Material characterization

The detailed information on different types of material samples prepared for material characterization is summarized in Tab. 3.1. The silicon layers at a thickness of $30 \sim 50\,\mathrm{nm}$ were deposited on corning glass (Corning Eagle 2000) for reflectance (R) and transmittance (T) measurement, spectroscopy ellipsometry (SE), Raman spectroscopy, dark conductivity measurement and photothermal deflection spectroscopy (PDS). Double side polished n-type float-zone (FZ) wafers with a

Table 3.1.: *The detailed information on the samples prepared for material characterization.*

material	thickness	substrate	characterization
Si thin-film	$30 \sim 50\,\text{nm}$	corning glass	UV-vis-NIR, Raman, conductivity, PDS, SE
Si thin-film	$30 \sim 50\,\text{nm}$	polish wafer	eCV, ToF-SIMS,SE
Si thin-film	$30 \sim 50\,\text{nm}$	high resistivity polish wafer	FTIR
Si thin-film	$5 \sim 15\,\text{nm}$	polish wafer	UPS
TCO thin-film	$80 \sim 110\,\text{nm}$	corning glass	UV-vis-NIR, four-point probe, Hall, SE

<111> crystal orientation and a resistivity of $1 \sim 5\,\Omega\text{cm}$ were utilized for SE, electrochemical capacitance voltage (eCV), time-of-flight secondary ion mass spectroscopy (ToF-SIMS) and ultraviolet photoelectron spectroscopy (UPS). For Fourier transform infrared spectroscopy (FTIR) the silicon layers were prepared on p-type polished wafers with resistivity of $10\,\Omega\text{cm}$. Hall effect, R and T, SE and four-point probe measurement were conducted for TCO layers deposited on corning glass.

3.2.1. Structural properties

Thickness The precise determination of the film thickness (d) is very essential to calculate deposition and material properties, e.g., deposition rate (r_{D}), absorption coefficient (α), oxygen content (c_{O}), hydrogen content (c_{H}) and σ. A step profiling system (Vecco DEKTAK 6M Stylus Profiler) was applied in this work to determine the d of the material samples. Several small pieces of wafer were placed on each glass and Si substrate as masks prior to deposition. After deposition a sharp step between the substrate and layer was obtained by removing the small wafers mechanically, which was scanned by a fine probing tip in the system. The corresponding height difference between the substrate and the film surface gives the value of d. Furthermore, spectroscopy ellipsometry (SE) was also used to determine the thickness of thin-films and will be introduced in Sec. 3.2.3. The r_D was acquired via dividing the measured thickness by the deposition time.

Raman spectroscopy Raman spectroscopy is a fast and non-destructive measurement. It was used to estimate the crystalline volume fraction (F_c) of the nc-SiO$_\mathrm{x}$:H films in this work. Raman spectroscopy is a vibrational spectroscopic technique based on the Raman effect that first reported by Raman in 1928 [89]. If the incident photon imparts energy to the lattice in the form of a phonon (phonon emission) it emerges as a lower-energy photon. This down-converted frequency shift is known as Stokes-shifted scattering. During Raman spectroscopy measurements the sample is illuminated by an intense monochromatic light source, such as laser. The weak scattered light or signal is passed through a double monochromator and the Raman-shifted wavelengths are detected by a photodetector. The Raman spectroscopy is sensitive to the crystal structure or the polarizability of the bond, which makes it

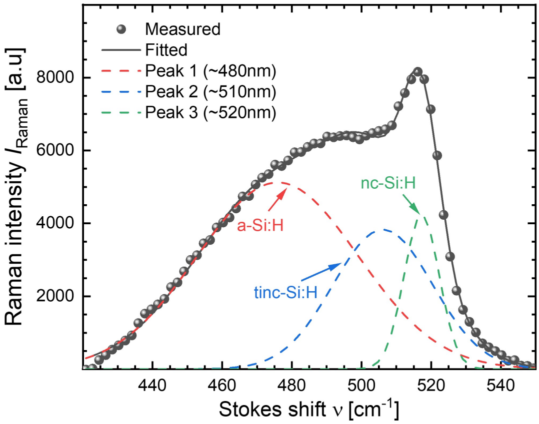

Figure 3.3.: *The Raman intensity (I_{Raman}) as a function of the Stokes shift (ν) for a nc-SiO$_x$:H layer. The spectrum is deconvoluted into an a-Si:H peak (480 cm^{-1}), a tinc-Si:H peak (506 cm^{-1}) and a nc-Si:H peak (520 cm^{-1}) to calculate the crystalline volume fraction (F_c).*

a complementary technique to FTIR for the investigation of bond states in compounds [90].

As shown in Fig. 3.3 the spectrum of nc-SiO$_x$:H layer was composed by three spectra, which is a Gaussian distribution near 480 cm^{-1} corresponding to the transverse optical (TO$_1$) modes of Si-Si bonds in a-Si:H, a Gaussian peak around 506 cm^{-1} resulting from the intermediate mode of tiny nanocrystalline or crystal-like phase at grain boundaries (tinc-Si:H), and a Lorentzian peak near 520 cm^{-1} originating in the asymmetric TO$_2$ vibrational mode of crystalline silicon (nc-Si) [91,92]. The relevant volume fraction of each component ($F_{\text{a-SiO}_\text{x}}$, $F_{\text{tinc-Si}}$ and $F_{\text{nc-Si}}$) was defined as the ratio of the integrated area of the corresponding deconvoluted spectrum to the total peak area. The F_c is the sum of $F_{\text{tinc-Si}}$ and $F_{\text{nc-Si}}$.

In this work, the nc-SiO$_x$:H films of 5 $\sim$ 50 nm thick were deposited on glass substrate. A Renishaw inVia Raman Microscope with a UV-laser source (325 nm) was used. The penetration depth of the UV photons for silicon layers is 10 $\sim$ 20 nm, much lower than the one from normal green laser, which can reduce the effects of the glass substrate on the measurement result, especially for the samples with thin layer thickness. The power intensity of the UV-laser was carefully calibrated to avoid additional crystallization of the silicon films.

Fourier transform infrared spectroscopy (FTIR) FTIR was used to investigate the detailed bond structure and the stoichiometry of the nc-SiO$_x$:H films in this thesis. In infrared (IR) spectroscopy, the sample was exposed to the IR radiations, some of which were absorbed by the samples owing to the interaction of the photons with electric dipoles in the material and some were just passed through. The resulting spectrum represents the molecular absorption and transmission related to the bonding and the dielectric constant of the material, giving information on the bonding structure and its close chemical environments. The samples were deposited on polished Si wafer and the FTIR spectra was recorded by a Nicolet 5700 Fourier transform infrared spectrometer under nitrogen purging at room temperature. A reference wafer, taken from the same wafer as the substrate, was used to calibrate the device prior to a measurement. The α was then calculated from the measured absorbance spectra [16]. A thickness correction factor was applied to α as described in Ref. [93].

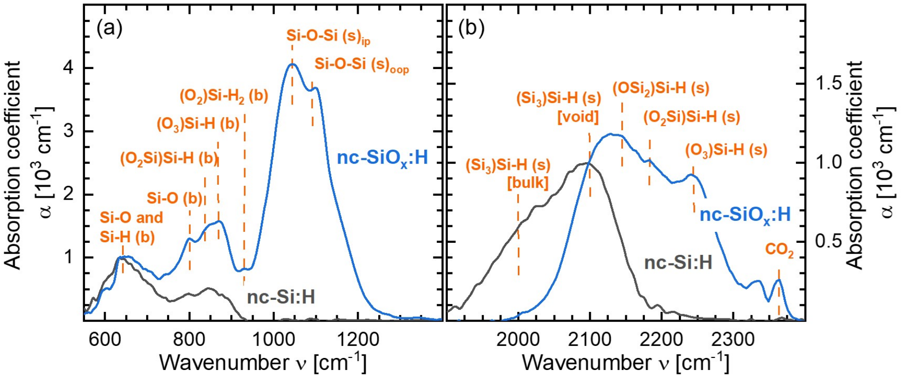

Figure 3.4.: *Typical Fourier transform infrared spectroscopy (FTIR) spectrum of a nc-Si:H and nc-SiO$_x$:H film in the spectral range of (a)* 550 ~ 1400 cm^{-1} *and (b)* 1900 ~ 2400 cm^{-1}. *The positions of the most prominent stretching (s) and bending (b) modes within the spectrum range are indicated, which were taken from Ref. [93, 94, 94–99].*

The typical bending ((b)) and stretching ((s)) modes present in hydrogenated nanocrystalline silicon (nc-Si:H) and nc-SiO$_x$:H films in the spectral range of 550 ~ 1400 cm^{-1} and 1900 ~ 2400 cm^{-1} are displayed in Fig. 3.4 (a) and (b), respectively. The absorption peaks at 630 cm^{-1} and 1800 ~ 2200 cm^{-1} could be ascribed to the wagging mode of Si-H vibration and the stretching mode of Si-H$_n$ vibration, respectively. Furthermore, the modes related to the Si-O-Si stretching vibration and the vibrations with O bonded to Si-H group are located in the spectral range of 1000 ~ 1200cm^{-1} and 2100 ~ 2300cm^{-1}, respectively [93–99]. More details on the vibrational modes at different wavenumbers can be found in Ref [100]. The bond content c_X was calculated based on the Eq. 3.5:

$$c_X = \frac{A_X}{N_{Si}} \int \frac{\alpha(\nu)}{\nu} d\nu, \tag{3.5}$$

where A_X is the proportionality constant for each vibration, $\alpha(\nu)$ is the absorption coefficient, ν is the wavenumber and $N_{Si} = 5 \times 10^{22}$ cm^{-3} is the atomic density of pure silicon. The c_O of nc-SiO$_x$:H films was yielded by numerical integration of the peak around 1000 to 1200 cm^{-1}, for which $A_{Si\text{-}O} = 2.8\times10^{19}$ cm^{-2} was used. The FTIR spectra of Si-H_n vibration at 1800 ∼ 2200 cm^{-1} could be fitted with two Gaussian-deconvoluted curves, which are the low stretching mode (LSM) at 2000 cm^{-1} and the high stretching mode (HSM) at 2090 cm^{-1}. Commonly the Si-H_n vibration in LSM is associated with isolated monohydride embedded in dense a-Si bulk and that in HSM is related to clustered H on the inner surfaces of voids [101, 102]. The bonded hydrogen content in LSM (c_H^{LSM}) and in HSM (c_H^{HSM}) were calculated via Eq. 3.5 using $A_{2000} = 9.1 \times 10^{19}\,cm^{-2}$ and $A_{2090} = 2.2 \times 10^{20}\,cm^{-2}$, respectively [93]. Then the microstructure factor (R^*) was defined to monitor the film qualities by Eq. 3.6 [103]:

$$R^* = \frac{c_H^{HSM}}{c_H^{HSM} + c_H^{LSM}}. \tag{3.6}$$

Time-of-flight secondary ion mass spectroscopy (ToF-SIMS) ToF-SIMS is a valuable technique to analyze the composition of solid materials with good depth resolution. The target material is sputtered with primary ions (O^+ and Cs^+). The charged secondary ions are ejected from the surface and accelerated in an electric field. Then the secondary ions are collected and identified in a mass spectrometer. In this study, the ToF-SIMS was used to determine the distribution profiles of P, O and H atoms in nc-SiO_x:H films or the stacks on the front side of devices. The area of Cs^+ beam with 1 keV kinetic energy is $400 \times 400\,\mu m^2$ and the analysis area is $41 \times 41\,\mu m^2$ to reduce the negative effect of the thin-film redeposition from the edges. The measurements were performed in the Central Institute for Engineering, Electronics and Analytics (ZEA-3), Forschungszentrum Jülich. More details can be found in Ref. [104].

Electrochemical capacitance voltage (eCV) The electrically active doping dopant concentration profile of the nc-SiO_x:H(n) films was obtained by eCV technique (WEP Wafer Profile CVP21). In eCV measurements, an electrolyte was used to form the Schottky-like barrier by contact to the surface of the semiconductor, where a depletion region was created. The carrier concentration then can be derived by measuring the capacitance of this area. A electrolytically etching process of the semiconductor was followed and then the capacitance measurements were repeated. The etching step can be set before and during the measurement manually. Both processes can be carried out in the same electrochemical cell. The repetitive etch/measure cycle was performed by the equipment system and a profile plot was generated after the measurement [105–107]. In this work a 0.1 molar ammonium hydrogen fluoride (NH_4HF_2) was used as the etching solution and the contact area of electrolyte is $1\,\mathrm{cm}^2$ defined by a plastic sealing ring. The nc-SiO_x:H thin-films were deposited on n-type polish wafers and the detailed operation of the measurement can be found in [108].

Ultraviolet photoelectron spectroscopy (UPS) UPS refers to the measurement of kinetic energy spectra of photoelectrons emitted by molecules which have absorbed ultraviolet (UV) photons. UPS is widely used for the valence band acquisition and electronic workfunction measurement [109, 110]. In this work, the UPS system is a MULTIPROBE MXPS system from Scienta Omicron with an ARGUS hemispherical electron spectrometer, which is part of the JOSEPH cluster system in the Research Center Jülich, IEK-5. The light source for UPS measurements is a HIS13 HeI gas discharge vacuum UV source from FOCUS (HeI radiation energy 21.22 eV). Spectra was collected with a path energy of 2 eV, a digital resolution of 0.01 eV and a sample bias of 6 V at a takeoff angle of 0°. We measured six position on the sample to determine the ionization energy E_i from the distance of the cutoff at low kinetic energies and the valence band edge at high kinetic energies by linear fits to the spectrum. Then the work function (Φ) was calculated by $\Phi = 21.22 - E_\mathrm{cutoff}$, where E_cutoff is the cutoff energy of UPS in high binding energy regime. The samples with $5 \sim 15\,\mathrm{nm}$ thick nc-SiO_x:H stacks were prepared on polished wafers and immediately transferred into the load chamber of the UPS system after the PECVD deposition.

3.2.2. Electrical properties

Conductivity To determine the lateral dark conductivity of the nc-SiO_x:H films two rectangular coplanar silver contacts of $5 \times 3.5\,\mathrm{mm}^2$ in a distance of 0.5 mm were deposited on material samples. A scan in steps of 10 V in a voltage range between -100 and $+100$ V was performed between the sample and measuring probes at room temperature and in dark ambient air. The upper limit of the source measurement unit is 1 mA. If the resulting current is more than the limitation, then the probe voltage will be adjusted. Finally, using the thickness of the sample and the geometry of the contacts, the dark conductivity of the sample was calculated according to Eq. 3.7:

$$\sigma = \frac{I}{V}\,\frac{w}{d\,l}. \tag{3.7}$$

In Eq. 3.7, w represents the distance between the silver contacts, l is the length of the contact and d is the thickness of the films.

Hall effect measurement Hall effect measurements are important to semiconductor material characterization because from both the Hall voltage and the resistivity, the conductivity type, carrier density and carrier mobility can be derived. The physical principle underlying the Hall effect is the Lorentz force, which is a combination of two separate forces: the electric force and the magnetic force. More details about Hall effect can be found in Ref. [111,112]. In order to determine the resistivity (ρ), the electron mobility (μ) and the carrier concentration (n_e) of the semiconductor, the van der Pauw technique was used. This technique is a combination of a resistivity measurement and a Hall measurement at room temperature [113]. The glass samples with the thin semiconductor films were cut into the size of $1.2 \times 1.2\,\mathrm{cm}^2$. Then the samples were contacted with sharp metal needles at their four edges. Detailed step by step information of the measurement can be found in [111,112,114].

Four-point probe The four-point probe method was used to determine the sheet resistance (R_sheet) of the TCO films. Four contact needles were arranged equidistant in a line and connected to a source/sensing unit in 4-wire configuration. A current was passed through two outer probes and a voltage was induced in the inner probes. Compared to the method of van der Pauw, this is a faster method and can be applied to large samples. Using the voltage and current reading from the probe, the R_sheet can be determined via Eq. 3.8:

$$R_\mathrm{sheet} = \frac{V}{I}\,\frac{\pi\,d}{\ln(2)}, \tag{3.8}$$

where the d is the thickness of the TCO films and $\pi/ln(2) \approx 4.532$.

3.2.3. Optical properties

Spectrophotometry The films were deposited on the glass substrates for the spectral transmittance and reflectance measurement using a calibrated Ultraviolet-Visible-Near Infrared Spectroscopy (UV-Vis-NIR), Perkin Elmer LAMBDA 950. The system is equipped with a deuterium/halogen dual light source and a 150 mm diameter integrating sphere with $0^\circ/8^\circ$ port configuration to include scattered light. The two detectors of the system, namely a photomultiplier tube and an InGaAs detector, allow a measurement range of λ from $250 \sim 2500$ nm. The total transmittance and reflectance of the material samples were characterized in a spectral range of $300 \sim 1500$ nm with a step width of 5 nm. The samples were always oriented with the film side towards the probing incident light. The sample was positioned before the optical entrance of the sphere for the transmittance measurement and on the opposite side of the optical entrance for the reflectance measurement. The total absorptance (A) is calculated via $A(\lambda) = 1 - T(\lambda) - R(\lambda)$. Using the thickness of films, the absorption coefficient was determined by applying the Hishikawa method [115]:

$$e^{\alpha d} \approx \frac{T(\lambda)}{1 - R(\lambda)}. \tag{3.9}$$

This relation eliminates the interference patterns observed in the T and R spectra for most of the samples and is allowed to determine E_{04} of the material.

Photothermal deflection spectroscopy (PDS) During the PDS measurement, samples were placed inside a cave filled with a liquid deflection medium (typically CCl_4), for which the temperature dependent change in the refractive index (n) is well known. Then the samples were heated up by a pump beam of monochromatic light and in consequence also the surrounding deflection medium. A probing laser beam (632 nm) was placed in parallel to the sample surface and then deflected by the refractive index gradient of the deflection medium due to its change in temperature, which will be detected by a photodetector. This deflection of the probing beam is related to the light absorbed in the sample and was used for the determination of α. The signal detected by the photodetector is directly proportional to the amount of absorbed light and therefore to the absorptance of the sample as well as the absorption coefficient if the thickness is known.

Spectroscopy ellipsometry (SE) Spectroscopy ellipsometry is a non-destructive and optical measurement technique that uses polarized light to characterize thin films, surfaces and material microstructures [116,117]. Fig. 3.5 (a) shows a schematic drawing of the SE measurement setup in our group. The unpolarized light first passes through a polarization filter, resulting in linearly polarized light, which passes a rotating compensator and reaches the substrate surface. After reflection from the substrate the light is elliptically polarized. It then passes a fixed polarization state analyzer and finally enters the detector. The polarization change is characteristic of the structure of sample. Therefore, analyzing this polarization change can yield various information about the material, such as the real (ε_1) and imaginary (ε_2) part of the complex permittivity, n, the extinction coefficient (k), the roughness and the layer thickness. Since the absolute intensity of the reflected light does not have to be measured, no special reference samples need to be maintained. Besides, no special measurement environment is required for it. The spectroscopy ellipsometry is commonly used to investigate the dielectric properties of thin films. In this thesis, we used a J.A. Woollam Co. M2000® UV ellipsometer mounted on a gonio stage allowing for the measurements under different angles. The retrieved data is analyzed with the CompleteEASE® software. A Bruggeman effective medium approach model with Tauc-Lorentz and Drude oscillator was used for the TCO and silicon

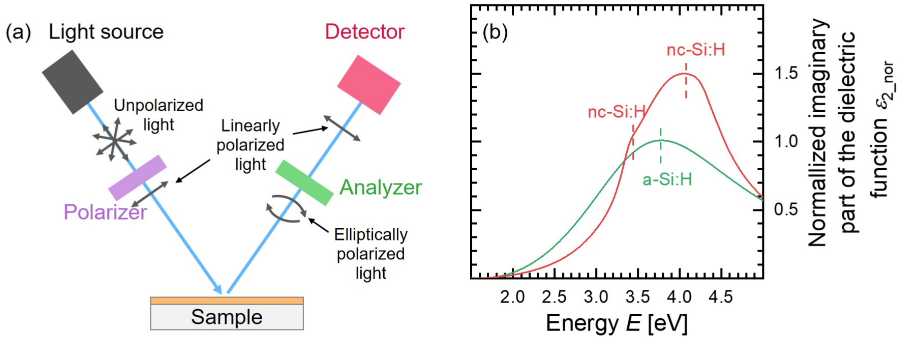

Figure 3.5.: *(a) Schematic overview of a spectroscopy ellipsometry (SE) measurement. (b) The imaginary part (ε_2) of the complex permittivity of silicon thin films as a function of the photon energy. The green and red ε_2 curve is a example for a-Si:H and nc-SiO$_x$:H thin film, respectively.*

films to determine the complex refractive index ($N = n - k\mathrm{i}$), and the complex dielectric constant ($\varepsilon = \varepsilon_1 - \varepsilon_2\mathrm{i}$), The ε is related to N by $\varepsilon_1 = n^2 - k^2$ and $\varepsilon_2 = 2nk$. The absorption coefficient is related to k as $\alpha = 4\pi k/\lambda$. Besides, the structure properties of the silicon films can also be characterized by analyzing their imaginary part of the dielectric constant, as shown in Fig. 3.5 (b). The ε_2 peak at 3.4 eV and 4.2 eV is correspond to direct band to band transitions in crystalline and nano/micro crystalline silicon thin films, respectively [118–122]. Besides, ε_2 having a broad hump with peak position near 3.5∼3.6 eV is a characteristic signature of a-Si:H films [118, 121, 123, 124].

3.3. Solar cell characterization

Photoconductance lifetime measurement The Sinton consulting WCT-120 setup with the transient analysis mode was used in this work to investigate the passivation quality of the device after PECVD and TCO depositions. The resistivity, dopant type, and thickness of the samples were used as input parameters. The effective minority carrier lifetime (τ_{eff}) in Si wafer was determined by the photoconductance method. During the measurement the sample on the stage with RF coil underneath was exposed to a pulse of light. The sheet conductance was detected simultaneously by the RF coil inductively coupled to the sample, from which a average excess carrier density (Δn_{e}) for each moment in time can be extracted. Meanwhile the intensity of the flash was recorded by the calibrated light sensor. Since the IR light was removed by an IR filter, the generation rate ($G(t)$) of the electron-hole pairs in the sample for each moment in time was converted from the flash intensity. Then the τ_{eff} was calculated from the continuity equation $d\Delta n(t)/dt = G(t) - \Delta n(t)/\tau_{\text{eff}}(t)$. In this study, the τ_{eff} was always taken at $\Delta n = 1 \times 10^{15}$ cm^{-3}. In most of the device, there may be several source of recombination, such as recombination through impurities in the wafer bulk, or recombination at the surfaces. The effective lifetime represents the combined impact of all of these competing recombination channels and can be described as the reciprocal sum of the lifetimes from the different recombination mechanisms:

$$\frac{1}{\tau_{\text{eff}}} = \frac{1}{\tau_{\text{intr}}} + \frac{1}{\tau_{\text{extr}}} = \frac{1}{\tau_{\text{Aug}}} + \frac{1}{\tau_{\text{rad}}} + \frac{1}{\tau_{\text{SRH}}} + \frac{1}{\tau_{\text{surface}}}. \tag{3.10}$$

In Eq. 3.10, τ_{intr} is the intrinsic lifetime including lifetime components due to Auger recombination (τ_{Aug}) and radiative recombination (τ_{rad}), and the τ_{extr} is the extrinsic lifetime containing the lifetime owing to Shockley-Read-Hall (SRH) recombination (τ_{SRH}) and surface recombination (τ_{sur}) [125]. The τ_{sur} is expressed by the following equation [126]:

$$\frac{1}{\tau_{\mathrm{surface}}} = \frac{S}{W} + J_0 \frac{N_D + \Delta n}{q n_i^2 W}, \tag{3.11}$$

where S is the surface recombination velocity of the front surface, W is the thickness of the Si substrate, n_{i} is the intrinsic carrier concentration and J_0 is the surface saturation current density of the rear surface. To extract the value of J_0 from the QSSPC data, a slope method at high injection levels was proposed by Kane and Swanson [127], which has been implemented in the Sinton WTC-120 software. The effective lifetime can be expressed by:

$$\frac{1}{\tau_{\mathrm{eff}}} = \frac{1}{\tau_{\mathrm{SRH}}} + J_0 \frac{N_D + \Delta n}{q n_i^2 W}. \tag{3.12}$$

Under the reasonable assumption that the bulk lifetime (τ_{bulk} is much larger than τ_{sur}, τ_{eff} is a direct measure for τ_{sur}, which is related to the c-Si surface passivation quality of the films on both sides of the Si wafer. Another representation of the passivation quality frequently used is the implied open circuit voltage (iV_{oc}), which is the upper limit for V_{oc} of the final device. It can be evaluated by the lifetime measurement via the Eq. 3.13:

$$iV_{oc} = \frac{k_{\mathrm{B}} T}{q} \ln\left(\frac{(\Delta n + N_{\mathrm{D}})\Delta n}{n_{\mathrm{i}}^2}\right), \tag{3.13}$$

where the k_{B} is the Boltzmann's constant, T is thermodynamic temperature and q is elemental charge, N_{D} is the donor doping concentration [128]. Ref. [129] is recommended for further readings.

Photoluminescence (PL) Photoluminescence provides a non-destructive and contactless technique for the determination of certain impurities in semiconductors and spatially resolved information about the passivation quality of cell precursors. It is applicable at all steps in the solar cell production processes. The sample was excited with an optical source, typically a laser with an energy larger than the band gap energy of the material. Then the electron-hole pairs were generated in the sample and radiatively recombined with a certain probability. The detected emission spectrum contains information about the energy levels of the recombination center, e.g., band-to-band recombination or defect recombination. Further details about dynamic PL can be found in literature [130–133]. For the measurements in this work the PL images were taken by an Xenics Cheetah 640-CL InGaAs camera which was cooled to 0 °C. The samples were illuminated by an LED array for 200 ms followed by a 1 s delay.

Current density-Voltage (JV) characteristics In this work, the current density versus voltage characteristics of solar cells at standard test conditions (AM1.5G, 100 mW/cm^2, 25 °C) was measured by the LOANA solar cell analysis system from PV-Tools GmbH with a Wavelabs Sinus 220 light sources. The datasheet of the light source can be found in Aarnink1990eWAVELABS2019. To describe the JV behaviour of a solar cell, a two-diode model is introduced and the equivalent circuit is shown in Fig. 3.6 [134–136]. It represents the superposition of the collected photo-current and the injected current due to the voltage at the p-n junction (V_J) as a constant current source in parallel to two ideal diodes. The first diode represents the "ideal" diode of the Shockley 's diode equation, describing the so-called diffusion current. This diode is characterized by a saturation current density J_{01}, related to the recombination in the base and the emitter as well as their surface [17, 135]. The second diode is the so-called recombination or second diode, characterized by a saturation current density J_{02} and an ideality factor n_2. This second current component stems from recombination within the depletion region, edges or the localized regions with a high defect density [134, 136–140]. A shunt resistance R_SH describes parasitic leakage currents that are proportional to the voltage. A series resistance R_s lumps together the contributions of joule heat losses. The current density of a solar cell is described by Eq. 3.14 [134]:

$$\begin{aligned} J(V) = J_{01}[\exp(\frac{q(V-J(V)R_\mathrm{S})}{n_1kT})-1] + J_{02}[\exp(\frac{q(V-J(V)R_\mathrm{S})}{n_2kT})-1] \\ +\frac{V-J(V)R_\mathrm{S}}{R_\mathrm{SH}} - J_\mathrm{ph}, \end{aligned} \tag{3.14}$$

Table 3.2.: *The main characteristic values of the solar cell measured by each JV measurement.*

JV-dark	Break through behaviour, R_{SH}
JV-light	Efficiency, I_{sc}, V_{oc}, FF, J_{mpp}, V_{mpp}
JV-$J_{\mathrm{sc}}V_{\mathrm{oc}}$	pFF, R_{s}, R_{SH}
JV-double light	R_{s}

where n is the ideality factor and J_0 is the recombination current density, both for diode 1 and 2, k is the Boltzmann constant, T is the temperature in Kelvin and J_{ph} is the photo-current density.

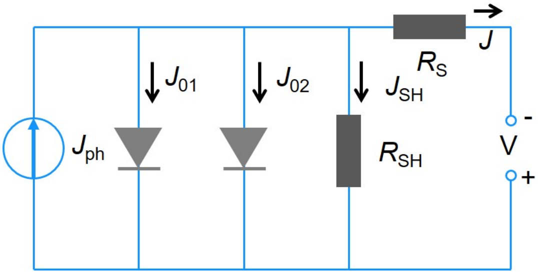

Figure 3.6.: *The equivalent circuit diagram of the double diode model including the parasitic series and the shunt resistances.*

There are four kinds of JV measurements, including JV-dark, JV-light, $JV-J_{\mathrm{sc}}V_{\mathrm{oc}}$ and JV-double light. The main characteristic values of the solar cell evaluated by these JV measurements are summarized in Tab. 3.2. The breakthrough behavior in reverse mode and the shunt resistance in dark condition can be determined by JV-dark measurement. The JV-light is a JV sweep under the illumination of 1 sun, from which we can obtain the open circuit voltages (V_{oc}) at V ($J = 0$ mA/cm^2), the short circuit current densities (J_{sc}) at J ($V = 0$ V), and the voltage at the maximum power point (V_{mpp}) as well as the current density (J_{mpp}) [141]. The power conversion efficiency of the solar cell is defined as

$$\eta = \frac{P_{\mathrm{max}}}{P_{\mathrm{sun}}} = \frac{J_{\mathrm{mpp}}V_{\mathrm{mpp}}}{P_{\mathrm{sun}}} = \frac{J_{\mathrm{sc}}V_{\mathrm{oc}}FF}{P_{\mathrm{sun}}}, \tag{3.15}$$

where the P_{max} is the power density at maximum power point, the P_{sun} is the input power density of the sun simulator (100 mW/cm^2) and the FF is the fill factor defined as

$$FF = \frac{J_{\mathrm{mpp}} V_{\mathrm{mpp}}}{J_{\mathrm{sc}} V_{\mathrm{oc}}}. \tag{3.16}$$

The JV-$J_{\mathrm{sc}}V_{\mathrm{oc}}$ curve was determined under the illumination of various light intensity and measured in two sweeps (in short circuit and open circuit conditions). The series resistance is neither effecting the V_{oc} nor the J_{sc} when the $R_{\mathrm{s}} < 10\,\Omega\,\mathrm{cm}^2$. Therefore, an almost R_{s} free JV-sweep can be obtained by combining the intensity data of both measurements, from which the pseudo fill factor (pFF) can be extracted. A detailed description of the principle and setup is given in Ref. [142].

Quantum efficiency and reflection measurement The spectrally resolved quantum efficiency provides a detailed insight into the optical absorption and the carrier extraction in solar cells as a function of the light wavelength. The external quantum efficiency (EQE) is defined as the fraction of charge carriers collected by the solar cell per incident photon (Φ_{in}):

$$EQE = \frac{J_{\mathrm{sc}}}{q\Phi_{\mathrm{in}}} \tag{3.17}$$

and is determined by measuring the short circuit current response to illumination with monochromatic light. Assuming a conformal response of the solar cell, the short-circuit current density evaluated from the EQE ($J_{\mathrm{sc,EQE}}$) is expressed by Eq. 3.18:

$$J_{\mathrm{sc,EQE}} = q \int EQE(\lambda)\Phi_{\mathrm{AM1.5g}}(\lambda)d\lambda, \tag{3.18}$$

where $\Phi_{\mathrm{AM1.5g}}(\lambda)$ is the photon flux of the AM1.5g spectrum. An integrating sphere with highly reflective and diffuse internal coating was used to measure the reflection (R) of the solar cell. The internal quantum efficiency (IQE) is the ratio between absorbed photons and collected electrons, $IQE = EQE/(1 - R)$, excluding optical loss arising from cell reflectance. The analysis of the IQE provides information about the emitter quality, the diffusion length and the independent observation of losses within the solar cell. In this work the LOANA system from PV-Tools GmbH was used for the EQE and R measurement in a wavelength range of $280 \sim 1200\,\mathrm{nm}$ in steps of 10 nm. The probing spot for both measurement is usually at the size of $12 \times 12\mathrm{mm}^2$.

Transfer length method (TLM) The transfer length method was used to determine the contact resistivity (ρ_c) of a layer stack on the front and the rear side of the rear-junction SHJ solar cells. The resistor geometry on the front side is displayed in Fig. 3.7 (a). The two contacts are located on the layer stack and connect with the external circuit for I-V measurement. The current flows through all thin-films vertically and then laterally through the wafer which has the lowest sheet resistance of the layers. The measured total resistance consists of several components:

$$R_\mathrm{T} = 2R_\mathrm{Ag} + 2R_\mathrm{Ag/TCO} + 2R_\mathrm{TCO} + 2R_\mathrm{TCO/n} + 2R_\mathrm{n} + 2R_\mathrm{i} + R_\mathrm{Si}. \tag{3.19}$$

In Eq. 3.19, R_Ag, R_TCO, R_n, R_i and R_Si are the resistance due to the silver contact, TCO layer, n-layer, intrinsic a-Si:H layer and silicon wafer, respectively. Besides, $R_\mathrm{Ag/TCO}$ and $R_\mathrm{TCO/n}$ are associated with the silver/TCO and TCO/n-layer interface, separately. In most situation, the resistivity of the silver contact and the vertical resistance of the thin-film are so low that R_Ag, R_TCO, R_n, R_i and $R_\mathrm{Ag/TCO}$ can be neglected. Thus, Eq. 3.19 can be simplified:

$$R_\mathrm{T} \approx 2R_\mathrm{TCO/n} + R_\mathrm{Si} \approx \frac{R_\mathrm{sheet}}{W}(L + 2L_\mathrm{T}), \tag{3.20}$$

$$L_\mathrm{T} = \sqrt{\frac{\rho_\mathrm{c}}{R_\mathrm{sheet}}}, \tag{3.21}$$

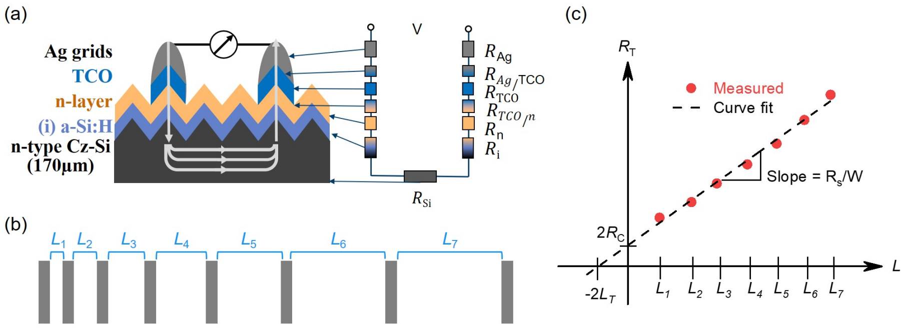

Figure 3.7.: *(a) Horizontal view of two contact pads of TLM device structure. (b) Top/-down view of TLM structure. (c) Plot to extract contact resistivity and transfer length from the TLM method.*

where the R_{sheet} is the sheet resistance of the films, L is the distance between two silver contacts, W is the width of the silver contact and L_{T} is the transfer length [143]. Eight silver contact pads with various spacing between the contacts were used in this work. Fig. 3.7 (b) shows the top-down view of the arrangement of the contact pads and the image of TLM patterns in fabricated devices can be found in Ref. [144]. The resistance between each adjacent contact obtained by the IV measurement is plotted as a function of the distance between two silver contacts, as shown in Fig. 3.7 (c). Based on the Eq. 3.20 and Eq. 3.21, the contact resistance, the specific contact resistivity and the transfer length were determined. More details on the TLM measurement can be found in [145].

3.4. Tools for simulation

OPAL 2 OPAL 2 is an optical simulator for the front surface of a photovoltaic solar cell. The main advantage of this software is a rapid simulation due to a statistical approach to simulate the interaction of light rays with a given surface texture. The user selects the structure of a solar cell and OPAL 2 calculates the reflection from its front surface, the absorption in its thin-film coatings, and the transmission into its substrate over a range of wavelengths. OPAL 2 also calculates the photocurrent that is generated within the cell for a given incident spectrum. Ref. [146–150] provide detailed explanation of the approximations and machinations of the OPAL 2 simulator. In this study, reflectance, absorptance, transmittance and the photocurrent losses of the devices with electron transport layer (ETL) at various structure and thickness were calculated by OPAL 2 and used as the input parameters for Quokka3 simulation. The surface morphology of the device is random upright pyramid with a characteristic angle of 54.7 °. The spectrum of the incident illumination was set at AM1.5g and the substrate width is 170 µm. The spectrally resolved n and k of a-Si:H, nc-SiO$_{\text{x}}$:H, nc-Si:H, MgF$_2$ and TCO layers as well as their thickness were used as the input parameters for the simulations. The values of n and k were acquired by the spectroscopy ellipsometry measurement.

Quokka3 Quokka3 is a commercial solar cell simulator specifically developed for the silicon solar cells and the enhancement of the popular free solar cell simulator Quokka2 [151]. It is an 3D/2D finite volume implementation in MATLAB, featuring conductive boundaries and the quasi-neutrality condition. Based on the model in Ref. [152], Quokka3 accounts for the non-ideal recombination currents at the boundaries and the recombination losses in the emitter, and is enhanced by the contact resistance effects. It supports different predefined cell designs and the setup with a range of device properties as well as solver options, such as IV-curve, open circuit, parameter sweep, luminescence image, etc [151, 153, 154]. To calculate the generation rate, a lumped parameter optical model, named Text-Z model, was used in Quokka3 simulator [155]. The input lumped parameter of the front layer stacks can be extracted from the OPAL 2 simulator based on the refractive index and extinction coefficient measured by spectroscopy ellipsometry. A Detailed description on the input parameters of the simulation of SHJ solar cells is given in Ref. [156]. In this work, Quokka3 was used to analyze the power losses of the bifacial SHJ solar cells with nc-SiO_x:H(n) in Chapter 5 and to simulate the electrical solar cell parameters of the devices with various cell geometry in Chapter 6.

AFORS-HET AFORS-HET (Automate FOR Simulation of HETerostructures) is a 1D free-on-demand simulation program for homojunctions as well as heterojunctions [157]. The software solves Poissons equation and the continuity equations, based on Maxwell-Boltzmann statistics, in the whole structure, which can be an arbitrary stack of different semiconductor layers. For more details, a complete user guide for AFORS-HET can be found in [158]. In this work, the band diagrams of the device with various nc-SiO_x:H(n) and ETL structures at thermal equilibrium were calculated by AFORS-HET.

4. Upscaling of n-type nc-SiO$_x$:H material growth

The nc-SiO$_x$:H is a mixture material, consisting of oxygen-rich amorphous silicon oxide and doped nanocrystalline silicon phases. By tuning the composition of the material phases in nc-SiO$_x$:H thin films, their opto-electronic properties, such as E_{04}, F_c, σ, c_O, n and ε etc., can be adjusted to fulfill certain requirements for the window layers in SHJ solar cells, including tunable n, high transparency with a sufficient σ. In this chapter, nc-SiO$_x$:H(n) layers have been developed in PM3 of the industrial multi substrate PECVD system (AK 1000 Inline) from Meyer Burger Technology AG, detailed description of which can be found in Sec. 3.1. The first section provides information on the influence of the deposition power density and the process pressure on the properties of nc-SiO$_x$:H(n) layers. In the second section the dependence of nc-SiO$_x$:H(n) layers' optical and electrical properties in the component of the PECVD process gases is presented and discussed. Lastly, an overview of the material properties of the nc-SiO$_x$:H films deposited in this work is summarized and compared with results collected from literature as well as previous works in our group.

4.1. Effect of power density and pressure

In this section, the experimental results regarding the influence of P and p on the properties of nc-Si:H and nc-SiO$_x$:H are presented. The H_2 gas flow was kept constant at 990 sccm and the maximum value of the H_2 mass flow controller is 1000 sccm. The f_{SiH_4} and f_{PH_3} were set at 1%. The layer thickness was between 30 and 50 nm. In the power density series, the deposition power density was varied in a range from 40 mW/cm^2 to 200 mW/cm^2 at the pressure of 2.5 mbar. In the pressure series, the deposition pressure was set at 2.5mbar, 3.5mbar and 4.5mbar with the power density of 40 mW/cm^2. The deposition rate of the films was determined by dividing the measured thickness to the deposition time. The silane utilization ($U_{\mathrm{SiH_4}}$) was defined via the Eq. 4.1:

$$U_{\mathrm{SiH4}} = \frac{[\mathrm{SiH_4}] \ \times t \times \rho_{\mathrm{SiH_4}}}{2A \times d \times \rho_{\mathrm{Si}}}, \tag{4.1}$$

where [SiH$_4$] is the input gas flow of silane, t is the deposition time, $\rho_{\mathrm{SiH_4}}$ is the density of silane, A is the area of the electrode, d is the thickness of the nc-SiO$_x$:H layer and ρ_{Si} is the density of Si.

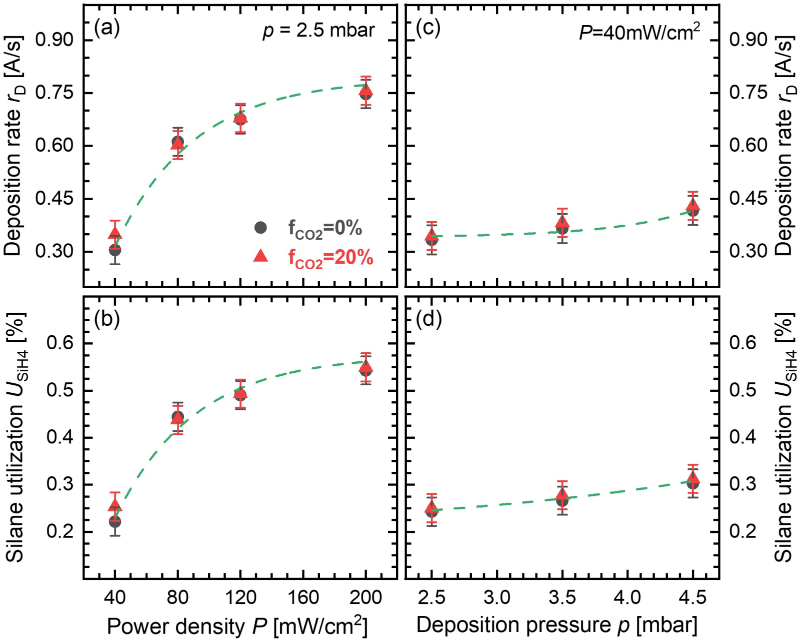

Figure 4.1.: *Effect of the deposition power density on (a) the deposition rate (r_D) and (b) the silane utilization (U_{SiH_4}) as well as the pressure on (c) the r_D and (d) the U_{SiH_4}. In the power density series, the deposition power density was varied in a range from 40 mW/cm^2 to 200 mW/cm^2 at the pressure of 2.5 mbar. In the pressure series, the deposition pressure was set at 2.5mbar, 3.5mbar and 4.5mbar with the power density of 40 mW/cm^2. The dash line serves as a guide to the eye.*

Fig. 4.1 shows the dependency of r_D and $U_{\mathrm{SiH_4}}$ on the deposition power density and the pressure at $f_{\mathrm{CO_2}}$ of 0% and 20%. The dash line serves as a guide to the eye. A similar trend of the deposition rate and the silane utilization of the nc-SiO$_\mathrm{x}$:H films is observed as the nc-Si:H (when $f_{\mathrm{CO_2}} = 0\%$) films when varying the power density or the process pressure. An increase of r_D from 0.3 to 0.75 Å/s is obtained by increasing the power density from 40 to 200 mW/cm^2. As shown in Fig. 4.1 (b), a higher silane usage is demonstrated at a higher power density, which could be due to the increase of the electron density in the plasma [159, 160]. More electrons would promote the dissociation of SiH$_4$ molecules, leading to more SiH$_3$ ions or radicals near the substrate. These ions or radicals would be captured by the dangling-bond sites forming Si-Si bond and increase the deposition rate as well as the silane utilization [72, 75]. In Fig. 4.1 (a) and (b) the slope of the dash lines decreases with increasing the power density, which could be attributed to the etching process related to the hydrogen atoms [161]. More hydrogen radicals or atoms are also generated at a higher power density, which would reach the film-growth surface and break Si-Si bonds, preferentially weak bonds involved in the amorphous network structure. As a result, the removal of Si atoms would happen [162]. When increasing the power density, the etching process could become more severe and predominant in the deposition process, balancing the improvement of the radical deposition on the film surface. As shown in Fig. 4.1 (c) and (d), raising the deposition pressure results in a slight increase of r_D and $U_{\mathrm{SiH_4}}$. This result could be assigned to the increased residence time (t_res) of the gas particles in the plasma space. During the PECVD process, the deposition pressure has an influence on t_res, which can be estimated by Eq. 4.2 [163]:

$$t_\mathrm{res} = \frac{A\ p_\mathrm{dep}}{f_\mathrm{total}\ p_0}. \tag{4.2}$$

In Eq. 4.2, A denotes the substrate area, p the deposition pressure, f_total the total gas flow and p_0 the standard pressure (1013 hPa). By increasing p, a longer duration of the gas particles in the chamber is obtained, leading to the increase of $U_{\mathrm{SiH_4}}$ and r_D in Fig. 4.1.

Fig. 4.2 shows the c_O, the F_c, the E_{04} and the σ of nc-SiO$_\mathrm{x}$:H(n) layers as a function of the power density at $f_{\mathrm{CO_2}}$ of 0% and 20%. For nc-Si:H layer, the crystalline volume fraction decreases from 55.5% to 34.3% with increasing the power

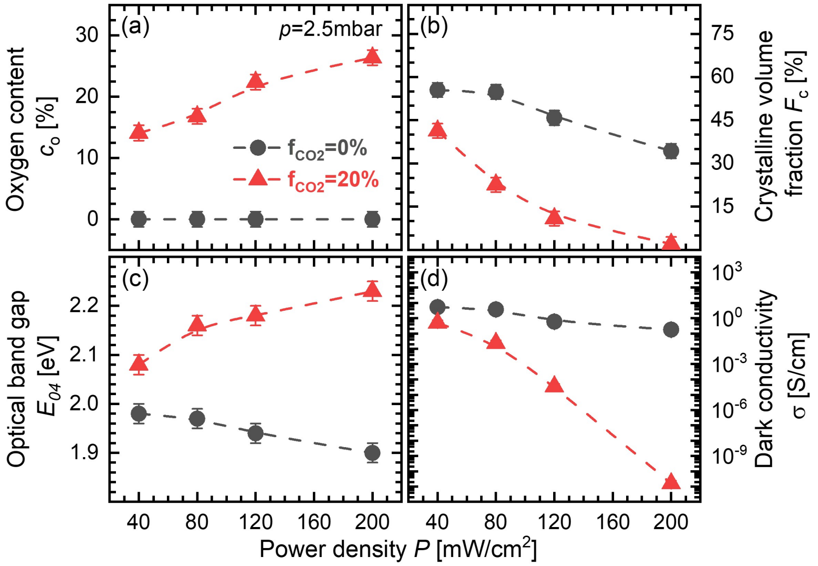

Figure 4.2.: *Effect of the deposition power density (P) on (a) the oxygen content (c_O), (b) crystalline volume fraction (F_c), (c) optical band gap (E_{04}) and dark conductivity (σ). The dash lines serve as a guide to the eye.*

density up to 200 mW/cm^2. The optical band gap of nc-Si:H layer declines from 1.99eV at 40 mW/cm^2 to 1.90eV at 200 mW/cm^2. A reduction of the dark conductivity from 5.2 to 0.18 S/cm is observed upon increasing the power density from 40 to 200 mW/cm^2. For nc-SiO$_x$:H layer, an increase of the oxygen content can be seen in Fig. 4.2 when increasing the power density. It indicates that more oxygen incorporated in the silicon matrix, consistent with the result observed by Sarker et al [164]. The crystalline volume fraction of nc-SiO$_x$:H is 40% at P of 40 mW/cm^2 and the material becomes totally amorphous (F_c=0%) at 200 mW/cm^2. The E_{04} increases from 2.09 to 2.24 eV and the dark conductivity of the nc-SiO$_x$:H decreases from 0.49 to 1.6×10^{-11} S/cm with increasing the power density, as shown in Fig. 4.2 (c) and (d), respectively. During the deposition of nc-Si:H, the ion bombardment effect on the growth surface always happened and became more severe at high RF power density. This effect could deteriorate the growth of crystallites and increase the structural disorder, causing more amorphous silicon phase in the films. Furthermore, high electric power leads to a rapid dissociation of SiH_4, giving rise to a reduced probability of the gas-phase reactions of SiH_2, SiH and Si species with the SiH_4 molecules. Thus, a deterioration of the film structure properties may take place [69]. As a direct semiconductor material, the absorption coefficient of a-Si:H is higher than nc-Si:H, which could be responsible for the decrease of E_{04} with increasing the power density. Besides, the quantum confinement effect and the short- and medium-range order of the layers play a role on the band gap of nc-Si:H films [165–167]. Therefore, the reduction of E_{04} could be attributed to the increased structural disorder and to the decreasing number of nc-Si:H grains as well as the associated grain boundaries [168]. Because of the lower doping efficiency in the a-Si phases compared with the nc-Si phases [169], the decreased dark conductivity of the nc-Si:H films can be explained by the decline of F_{c} with increasing P. The trend of electrical properties of nc-SiO_x:H with varying power density is similar as the nc-Si:H, whereas the optical properties trend of both layers are quiet different. This difference could be due to the oxygen incorporated in the silicon matrix of nc-SiO_x:H. During the deposition of nc-SiO_x:H layer, CO_2 was added into the process chamber as the oxygen source, which was dissociated into CO and O in the plasma. The oxygen incorporation in the amorphous silicon phase leads to the building of Si-O-Si complexes as FTIR measurements on hydrogenated amorphous silicon oxide layers [170]. A relatively higher dissociation of CO_2 molecules could be reached upon increasing the power density during the nc-SiO_x:H deposition, causing an increased incorporation of oxygen in the films [164, 171]. It was reported that the oxygen in the nc-SiO_x:H films would inhibit the growth of the crystalline phases and incorporate in the amorphous silicon phase, forming a oxygen-rich amorphous silicon matrix, which is more transparent than the a-Si:H phase [57,170,172]. Therefore, a possible explanation for the decreased F_{c} and the increased E_{04} in Fig. 4.2 with raising P is the increase of the a-SiO_x volume fraction. Compared with the nc-Si phase, the doping efficiency in the a-SiO_x phase is much lower, making the thin-films prepared at higher power density less conductive.

Fig. 4.3 shows the c_{O}, the F_{c}, the E_{04} and the σ of nc-SiO_x:H layers as a function of the process pressure at $f_{\mathrm{CO_2}}$ of 0% and 20%. A similar variation trend of the material properties can be found for the nc-Si:H and the nc-SiO_x:H films with varying the deposition pressure from 2.5 to 4.5mbar, whereas the influence

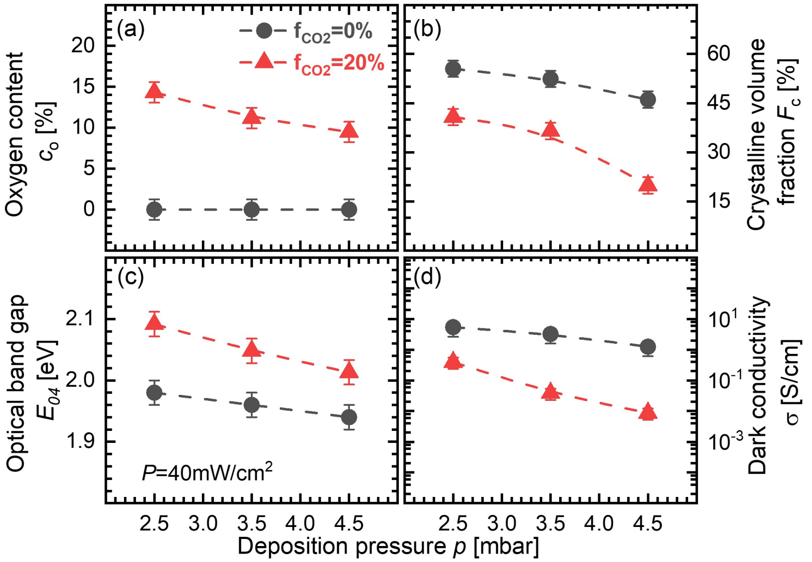

Figure 4.3.: *Effect of the deposition pressure (p) on (a) the oxygen content (c_O), (b) the crystalline volume fraction (F_c), (c) the optical band gap (E_{04}) and the dark conductivity (σ) at the power density of* 40 mW/cm^2. *The dash line serves as a guide to the eye.*

on the nc-SiO$_x$:H is slightly more severe than the nc-Si:H. The oxygen content, the crystalline volume fraction, the optical band gap and the dark conductivity all decrease when increasing the pressure. Because of the increased number of gas phase collisions at higher pressure, less oxygen precursors were provided for the growth of the films, leading to a continuous decrease in the oxygen incorporation in the nc-SiO$_x$:H films [173, 174]. During the growth of nc-Si:H or nc-SiO$_x$:H, the presence of the atomic hydrogen could enhance the etching of the amorphous silicon and provide an additional heating during the film-growing by hydrogen exchange reactions, which is very crucial for the formation of the crystalline silicon phase. With increasing the deposition pressure, the mean free path of the gases was reduced and the kinetic energy of H falls. Therefore, a relatively lower concentration of the atomic hydrogen near the substrate surface could be achieved, hampering the crystalline growth on the growth surface [173, 175–177]. The decrease in E_{04} and σ are observed in Fig. 4.3 (c) and (d), respectively, as a consequence of the decline of c_O

and F_c. The n and the ε_2 of the nc-SiO$_x$:H films in the power and the pressure series were derived from spectroscopy ellipsometry measurement as illustrated in Fig. 4.4. It can be seen that the refractive index decreases with increasing the power density, indicating a loose structure of the layers obtained at high power density. This result could be interpreted by the increased incorporation of O in the films, as shown in Fig. 4.2. It was reported that more oxygen in the nc-SiO$_x$:H film shifts the phase from a dense structure to a more disordered structure [178]. When increasing P from 40 to 200 mW/cm^2, the peak of the ε_2 at 4.2 eV shows a drastic drop accompanied with a blue-shift in energy, which could be associated with an additional hydrogenation and oxidation at a higher energy density [119, 179]. With increasing the power density, more electron density was provided in the plasma, causing an increased association

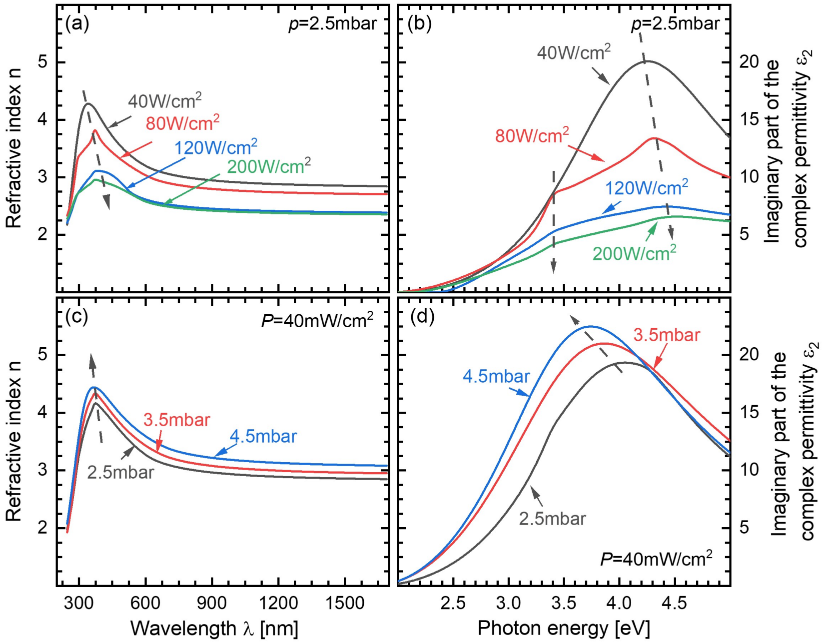

Figure 4.4.: *Wavelength dependence of the refractive index (n) of the nc-SiO$_x$:H layers prepared at (a) various power density and (c) process pressure. The imaginary part of the complex permittivity (ε_2) of the nc-SiO$_x$:H deposited at (b) various deposition power density (P) and (d) deposition pressure (p) as a function of the photon energy.*

rate of the hydrogen in the plasma. Thus, more hydrogen may be incorporated in the a-SiO$_x$:H matrix. The lowest peak height at 3.4 eV is obtained at 200 mW/cm^2 without any shift, indicating more voids in the films. This result is consistent with the refractive index result in Ref. [118, 119]. Another possible explanation is the smaller size of grains in the film with increasing P [121]. As mentioned in Sec. 3.2.3, the nc-Si:H dielectric function shows two well-defined features near 3.4 eV and 4.2 eV, corresponding to the crystal silicon phase [118–122]. The reduction of the amplitude at both energy could be the consequence of the amorphization of the crystalline silicon phase when increasing the deposition power. This observation is in a good agreement with the F_c result in Fig. 4.2. As shown in Fig. 4.4 (c), the refractive index curve as a function of the wavelength shifts up with increasing the deposition pressure, indicating a denser nc-SiO$_x$:H films. A higher amplitude of ε_2 is achieved at 4.5 mbar, accompanied with a peak shift to the lower photon energies, near 3.5$\sim$3.6 eV. The broad hump on this photon energy range is related to the amorphous silicon phase [118, 119, 121, 123, 124].

4.2. Effect of gas flow

In this section, the influence of the gas composition used in the PECVD process of nc-SiO$_x$:H layers was investigated. We kept the power density and pressure at 200 mW/cm^2 and 2.5 mbar, respectively. The thickness of the layers was on the range between 30 and 50nm. Three types of nc-SiO$_x$:H series were prepared and will be introduced in the following sections: total gas flow, PH$_3$ gas flow fraction and SiH$_4$ gas flow fraction series.

4.2.1. Total gas flow

Since the gas consumption is a significant cost factor in the industrial manufacture, a low gas flow during the deposition process is required. However, the deposition rate is limited by the silane supply. Besides, the material properties are affected by the gas compositions. Thus, a certain gas flow is necessary to achieve high deposition rate and suitable material properties. In this section it is examined how strongly the deposition rate and the material properties are related to the total gas flow. Fig. 4.5 shows the process gas flows and their gas flow fraction versus the total gas flow. The total gas flow was varied from 520 to 1560 sccm, while $f_{\mathrm{PH_3}}$, $f_{\mathrm{SiH_4}}$, $f_{\mathrm{CO_2}}$ and $f_{\mathrm{H_2}}$ were kept constant at 1%, 1%, 20% and 98.74%, separately.

Fig. 4.6 depicts the deposition rate and the silane utilization as a function of the total gas flow. The r_{D} goes up from 0.6 to 0.82 Å/s with raising the total gas flow from 520 to 1560 sccm while the $U_{\mathrm{SiH_4}}$ decreases from 0.6% to 0.3%. More SiH_4 and H_2 were supplied for the deposition of nc-SiO_x:H at high total gas flow, contributed

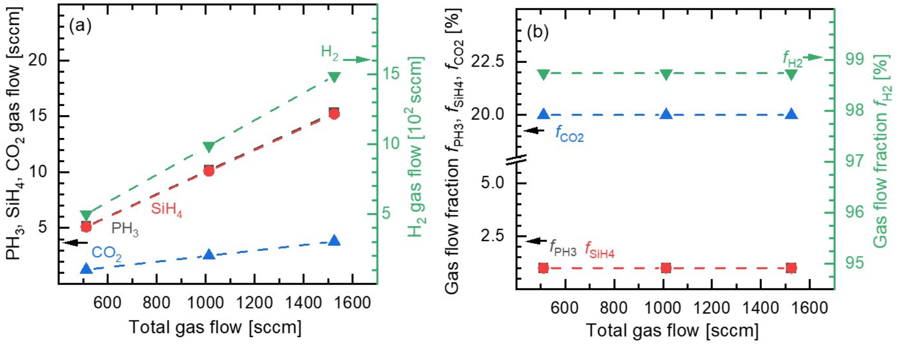

Figure 4.5.: *(a) The process gas flow and (b) the gas flow fraction versus the total gas flow (f_{total}). The dash lines are guides to the eyes.*

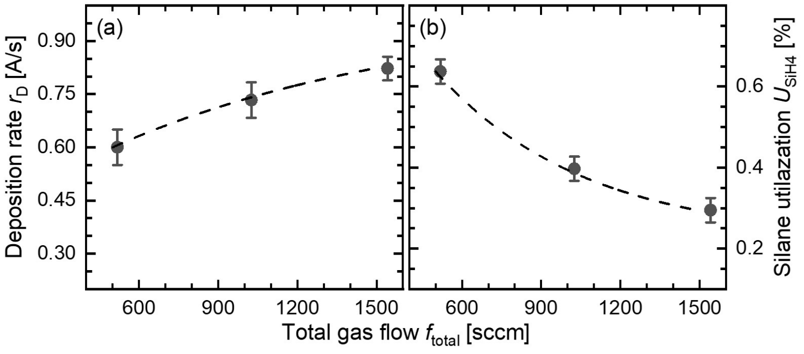

Figure 4.6.: *The influence of total gas flow (f_{total}) on (a) the deposition rate (r_{dep}) and (b) the silane utilization (U_{SiH_4}). The dash lines are the exponential fit-curves.*

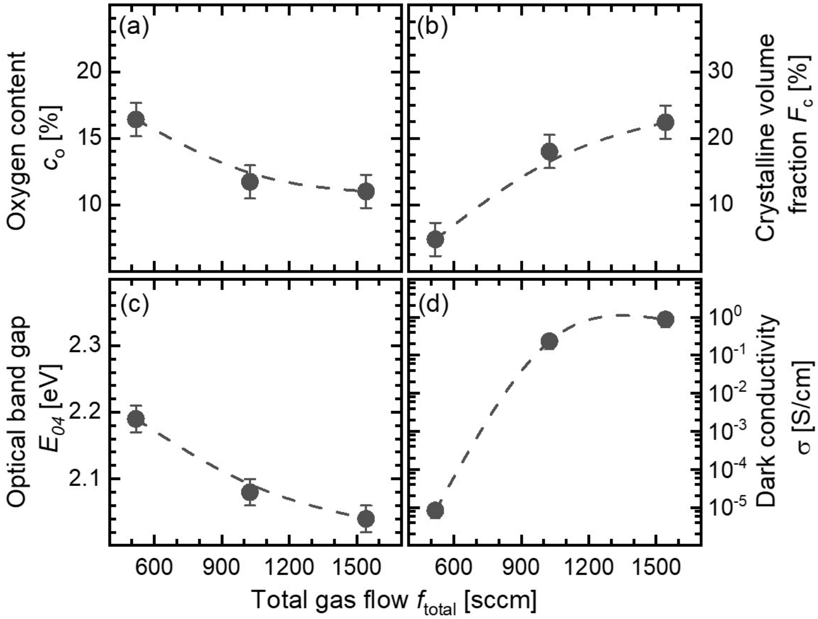

Figure 4.7.: *The influence of total gas flow (f_{total}) on (a) the oxygen content (c_O), (b) the crystalline volume fraction (F_c), (c) the optical band gap (E_{04}) and (d) the dark conductivity (σ). The dash lines are the exponential fit-curves.*

to more SiH_3 and H radicals on the substrate surface. This could enhance the growth of the silicon films and increase deposition rates. Eq. 4.2 reveals that a reduced gas residence time is obtained as increasing the total gas flow, which could be the reason for the reduction of the silane utilization in Fig. 4.5.

Fig. 4.7 shows the effects of the total gas flow variation on the material properties of the nc-SiO_x:H layers. For a nc-SiO_x:H layer deposited at an increased total gas flow, the oxygen content is reduced from 16% to 11%, accompanied with an increase of F_c from 5% to 22%. This result indicates that the microstructure of nc-SiO_x:H(n) is strongly affected by the total gas flow. The optical band gap decreases from 2.19 eV at 520 sccm to 2.04 eV at 1560 sccm. The dark conductivity increases by more than four orders of magnitudes with raising the total gas flow from 520 sccm to 1040 sccm. Further increasing the total gas flow leads to a saturation of the conductivity. Brain et al. demonstrated that a long gas residence time can lead to gas phase polymerization, contributed to a more porous structure of the material [163]. As increasing the total gas flow, less residence time of the gas particles can be achieved, promoting the growth of the dense structure, such as the crystal silicon phase in the films. What's more, the collisions of electrons with the process gas molecules in the plasma gas phase lead to the ionization and the dissociation of the precursor gases, resulting in the formation of positive ions and radicals. The ionization energies are 11.6, 14.5 and 15.4 eV, and the thresholds for the dissociation reactions are 8.3, 11.5 and about 10 eV for SiH_4, CO_2 and H_2, respectively [71, 171, 180, 181]. Therefore, a higher electron energy is required to produce oxygen ions and radicals compared to SiH_x radicals and SiH_x^+ ions. When increasing the total gas flow, the power per molecule in the process chamber could be reduced and even lower than the threshold energy for the CO_2 dissociation reaction or ionization since the power density of the generator was kept constant. Therefore, the density of oxygen ions or radicals in the plasma would be reduced, leading to the drop of the oxygen content in the nc-SiO_x:H films. As a consequence of less oxygen incorporated in the films, more crystal silicon phase grows and the volume fraction of oxygen-rich amorphous silicon phase decreases, which is demonstrated by the FTIR spectra of nc-SiO_x:H layers in Fig. 4.8.

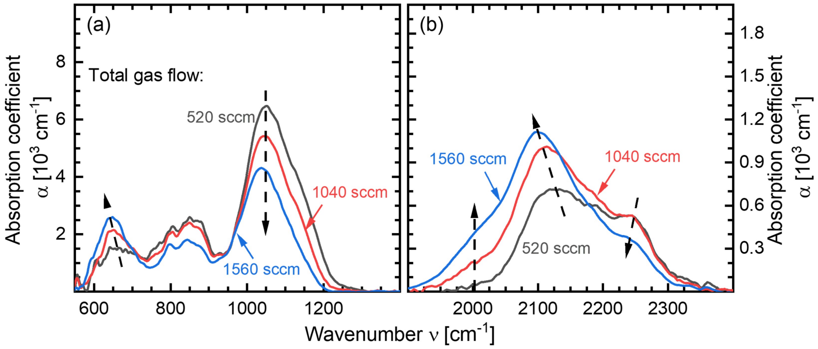

Figure 4.8.: *The FTIR spectra of the nc-SiO_x:H films prepared at various total gas flow on the wavenumber range of (a) 550~1400* cm^{-1} *and (b) 1900~2400* cm^{-1}.

The FTIR spectra of the nc-SiO_x:H films prepared at various total gas flow in the wavenumber range of 550∼1400 cm^{-1} and 1900∼2400 cm^{-1} are plotted in Fig. 4.8. The wagging and stretching modes of Si-H bonds are present at 640 cm^{-1} and 2000 cm^{-1}, respectively, where the total hydrogen content and the microstructure factor can be estimated as described in Sec. 3.2.1. It is notable that there is an increased amplitude of the absorption coefficient curve at the wavenumber peak near 640 cm^{-1} and 2000 cm^{-1}, indicating the increase of hydrogen content and less voids in the films. More hydrogen were pumped into the chamber as increasing the total gas flow, providing more hydrogen ions or radicals near the substrate surface. The extra hydrogen ions or radicals could facilitate the breakage of the weak SiH$_2$ bonds and the formation of the strong Si-H bonds, producing a more ordered and relaxed network with low void fraction [93,182]. Besides, the presence of oxygen has an influence on the Si-H vibrations in the phases, especially in the oxygen rich a-

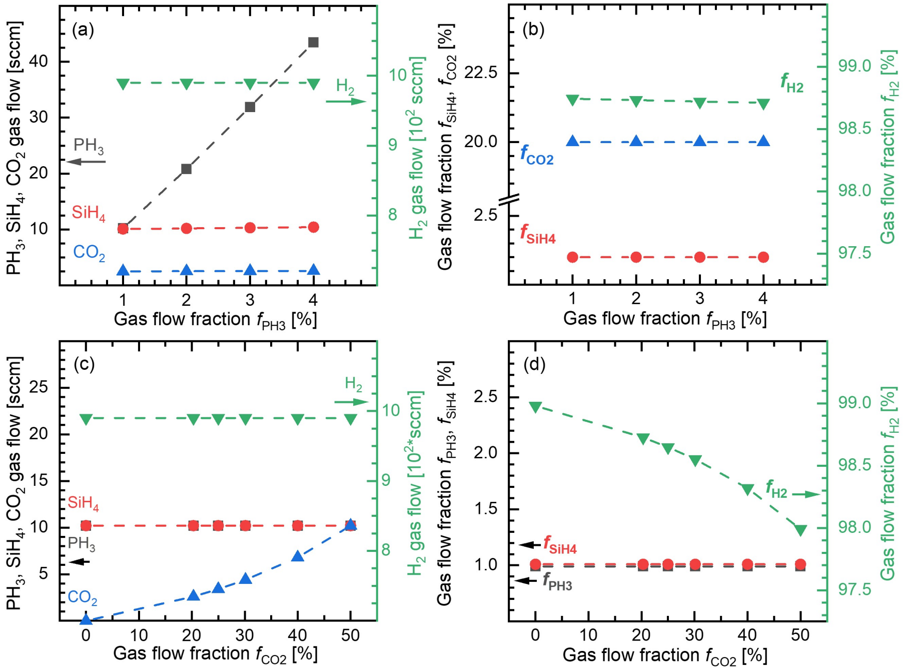

Figure 4.9.: *(a) The process gas flow and (b) the gas flow fraction versus the PH$_3$ gas flow fraction (f_{PH_3}). (c) The process gas flow and (d) the gas flow fraction versus the CO$_2$ gas flow fraction (f_{CO_2}). The dash lines are guide for eyes.*

SiO_x phase, and contributes to the (OSi_2) Si-H, (O_2Si) Si-H and (O_3) Si-H stretching modes near 2150, 2188 and 2250 cm^{-1} [93, 94, 96]. In Fig. 4.8 (b), a decreased peak intensity near 2250 cm^{-1} and an increased value near 2150 cm^{-1} can be observed, revealing a decrease of the oxygen-rich a-SiO_x phase in the nc-SiO_x:H layers. As a result, the thin-films become less transparent and more conductive when increasing the total gas flow.

4.2.2. Phosphine gas flow fraction

Fig. 4.9 (a) and (b) shows, as one example, the process gas flow and the gas flow fraction versus f_{PH_3} at the f_{CO_2} of 20%. The H_2 gas flow was kept constant at 990 sccm in this series. The PH_3 flow was varied from 10 (f_{PH_3}=1%) to 45 sccm (f_{PH_3}=4%). The gas flow of CO_2 and SiH_4 were slightly adjusted to maintain the f_{CO_2} and the f_{SiH_4} at 20% and 1%, respectively. For the PH_3 series, the CO_2 gas fraction was varied by varying the CO_2 flow, an example of which with f_{PH_3} at 1% is displayed in Fig. 4.9 (c) and (d). The CO_2 flow was tuned from 0 to 10 sccm and the flow of other gases was kept constant, leading to a f_{CO_2} variation in the range of 0%∼50%. Since the hydrogen gas flow was fixed at 990 sccm, the f_{H_2} decreases from 99.0% at f_{CO_2} of 0% to 98% at f_{CO_2} of 50%.

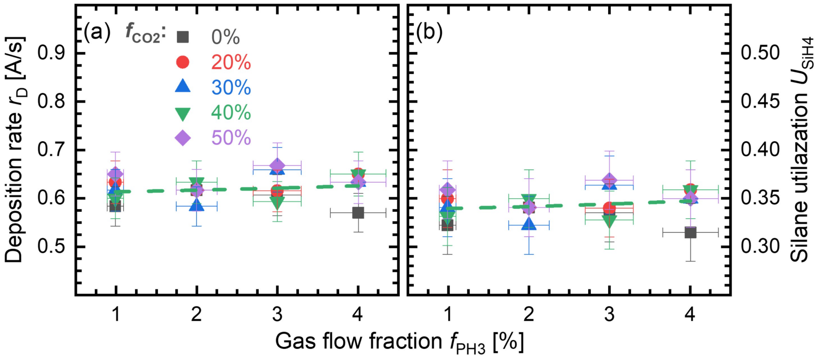

Figure 4.10.: *(a) The deposition rate (r_D) and (b) the silane utilization (U_{SiH_4}) versus the PH_3 gas flow (f_{PH_3}). The carbon dioxide gas flow fraction (f_{CO_2}) used for each series is indicated. The dash lines are guides for eyes.*

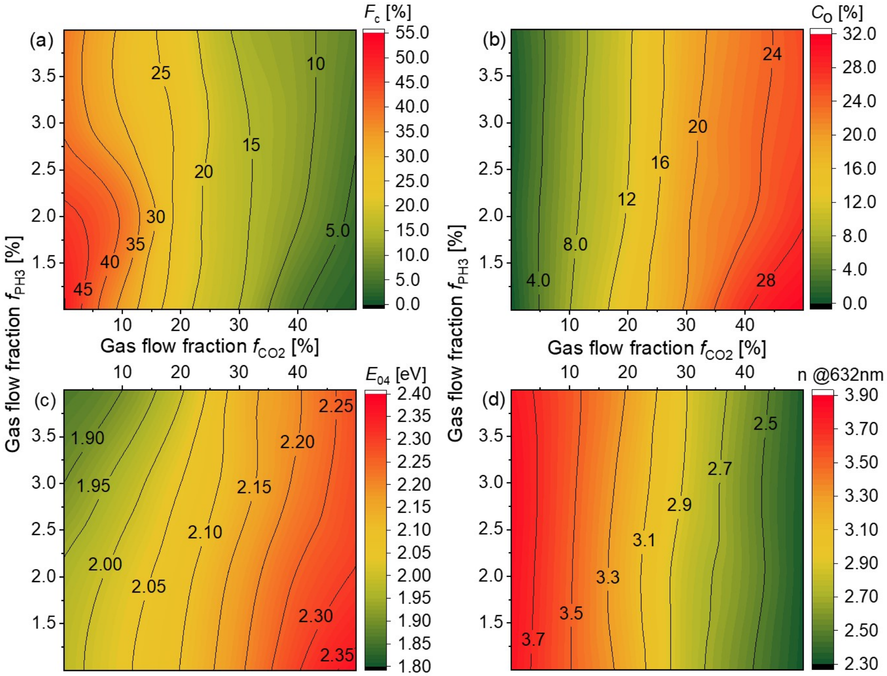

Figure 4.11.: *The contour map of (a) the crystalline volume fraction (F_c), (b) the oxygen content (c_O), (c) the optical band gap (E_{04}) and (d) the refractive index (n)) at 632 nm plotted versus the gas flow fraction of carbon dioxide (f_{CO_2}) and phosphine (f_{PH_3}).*

Fig. 4.10 shows the deposition rate and the silane utilization as a function of $f_{\mathrm{PH_3}}$ with various $f_{\mathrm{CO_2}}$. The r_{D} and $U_{\mathrm{SiH_4}}$ of the deposition process of nc-SiO$_\mathrm{x}$:H(n) films are independent of the $f_{\mathrm{PH_3}}$ in the range between 1% and 4%. Increasing the $f_{\mathrm{CO_2}}$ from 0% to 50% has no obvious influence on the r_{D} and the $U_{\mathrm{SiH_4}}$. Fig. 4.11 displays the contour map of the crystalline volume fraction, the oxygen content, the optical band gap and the refractive index at 632 nm plotted versus $f_{\mathrm{CO_2}}$ and $f_{\mathrm{PH_3}}$. A decreased F_{c} and an increased c_{O} can be observed as increasing the $f_{\mathrm{CO_2}}$ from 0% to 50%, which is consistent with the results in [57, 172, 183, 184]. More oxygen incorporated in the silicon matrix at a higher $f_{\mathrm{CO_2}}$ promotes the amorphization process of silicon phase in the nc-SiO$_\mathrm{x}$:H films and is beneficial to the replacement of a-Si:H by the a-SiO$_\mathrm{x}$:H matrix. This change of the microstructure in nc-SiO$_\mathrm{x}$:H films contributes to the increase of E_{04} and the reduction of n. For the films prepared without CO_2 in the process gases, the crystalline volume fraction decreases from 50% to 39% and the optical band gap from 2.03 eV to 1.84 eV with increasing the f_{PH_3} from 1% to 4%. No obvious influence of the f_{PH_3} on the refractive index can be found for the nc-Si:H(n) layers. When adding CO_2 into the process chamber, a different trend of the material properties with the variation of f_{PH_3} can be observed. The F_c increases firstly but then decreases or tends to be saturated once the f_{PH_3} reaching to an optimized moderate value (opti-f_{PH_3}). The opti-f_{PH_3} becomes higher at larger f_{CO_2}. For the nc-SiO_x:H films, increasing f_{PH_3} results in a decreased oxygen content, which is more obvious at higher f_{CO_2}. This result illustrates that the utilization of PH_3 could weaken the oxygen incorporation into the material moderately, in a good agreement with the results reported by Jia et al [185]. A decline of the optical band gap can be observed at higher f_{PH_3}. This could be the consequence of the transition of a-SiO_x to a-Si or nc-Si phases in the nc-SiO_x:H films, especially for the one prepared at larger f_{CO_2}. Fig. 4.11 demonstrates a slight increase of the refractive index as raising the PH_3 gas flow fraction. This observation suggests a nc-SiO_x:H films with denser structure at a higher f_{PH_3}.

Fig. 4.12 (a) illustrates the dark conductivity versus the f_{PH_3} of the nc-SiO_x:H(n) prepared at various f_{CO_2}. Increasing f_{CO_2} leads to a degradation of σ. This could be attributed to the decline of the crystalline volume fraction. The dark conductivity is determined by the effective carrier mobility (μ) and carrier density of the films. The μ is mainly dependent on the microstructure of the films, especially the fraction of highly conductive crystalline silicon phases, which act as the percolation paths for the transport of charge carriers in the nc-SiO_x:H layers [11, 16, 186, 187]. More incorporated oxygen at higher f_{CO_2} inhibits the growth of Si crystallites and cut down such percolation paths within the films. Consequently, the dark conductivity of the nc-SiO_x:H layers prepared at higher f_{CO_2} drops. The PDS result in Fig. 4.12 (b) demonstrates a decrease of the absorption coefficient at low energy range with increasing the f_{CO_2}. This result suggests a lower free carrier absorption and a reduction of the active doping concentration in the nc-SiO_x:H films when raising the f_{CO_2}, which is consistent with the decreased dark conductivity in Fig. 4.12.

For the nc-Si:H(n) layers, a slight increase of σ is achieved when varying the

f_{PH_3} up to 4%. This result may be associated with the increase of the active dopants in the films, which compensates the negative effect of the decreased crystalline phase on the dark conductivity. For nc-SiO$_x$:H layers, the σ increases firstly, but then decreases and tends to be saturated with increasing the f_{PH_3} from 1% to 4%. This result coincides with the result of F_c in Fig. 4.11. The value of opti-f_{PH_3} increases when varying the f_{CO_2} from 0% to 50%, as indicated by the arrow. Meanwhile, the σ of the nc-SiO$_x$:H films prepared at higher f_{CO_2} is more sensitive to the PH$_3$ gas flow fraction. This could be due to the achievement of the effective doping in the amorphous phase by increasing the amount of the doping source [185]. Therefore, it can be clearly deduced that there is a synergistic effect of CO$_2$ and PH$_3$ on the material properties of nc-SiO$_x$:H(n) films. An increase of the absorption coefficient at the low energy range can be found in Fig. 4.12 (c) when increasing the f_{PH_3}, revealing more active dopants in the doped films. To systematically investigate the influence of f_{PH_3} on the growth of nc-SiO$_x$:H(n) thin film as well as the opto-electronic properties, another PH$_3$ series over a wide range of f_{PH_3} (0%~10%) was

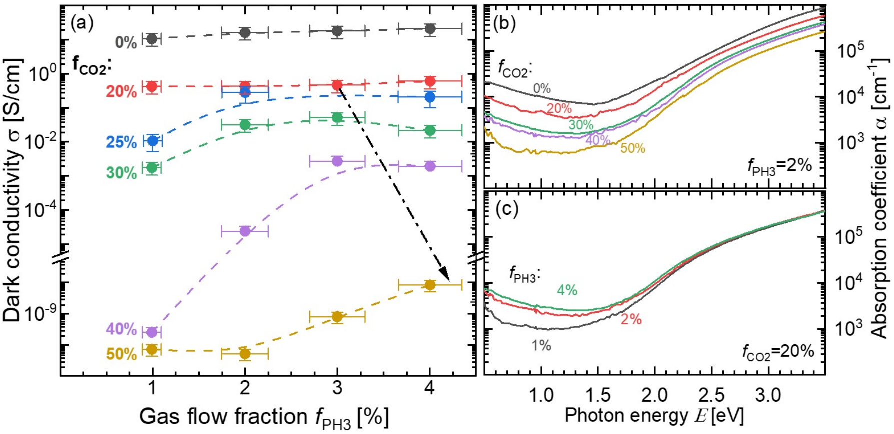

Figure 4.12.: *(a) The dark conductivity (σ) of the nc-SiO$_x$:H(n) versus the PH$_3$ gas flow fraction (f_{PH_3}) at various carbon dioxide gas flow fraction (f_{CO_2}). The absorption coefficient (α) of the nc-SiO$_x$:H for (b) CO$_2$ series and (c) PH$_3$ series measured by photo-thermal deflection spectroscopy (PDS) versus the photon energy (E). The material for both series was prepared at a f_{PH_3} and f_{CO_2} as indicated on the graphs.*

Table 4.1.: *The oxygen content (c_O), crystalline volume fraction (F_c), optical band gap (E_{04}), refractive index (n) at 632 nm and dark conductivity (σ) of the nc-SiO$_x$:H films prepared at different f_{PH_3}.*

Material properties	$f_{\mathrm{PH_3}}$ 0%	1%	2%	4%	7%	10%
c_{O} [%]	22.0	21.1	21.0	20.7	20.3	20.0
F_{c} [%]	31.0	33.5	39.4	30.2	22.6	10.9
E_{04} [eV]	2.29	2.26	2.24	2.22	2.19	2.16
σ [S/cm]	1.55×10^{-6}	0.0043	0.112	0.082	0.0086	1.96×10^{-6}
n @632nm	2.9	2.94	3.01	3.06	3.08	3.23

designed and carried out. The $f_{\mathrm{CO_2}}$ and the $f_{\mathrm{SiH_4}}$ were kept constant at 25% and 0.75%, respectively. The power was set at 200 W and 2.5 mbar of pressure was used in this series. The material properties, such as c_{O}, F_{c}, E_{04}, n and σ of the nc-SiO$_{\mathrm{x}}$:H prepared at different $f_{\mathrm{PH_3}}$ are summarized in Tab. 4.1.

A similar trend as the results shown in Fig. 4.11 and Fig. 4.12 can be found when increasing the $f_{\mathrm{PH_3}}$ from 0% to 4%. Further raising the PH$_3$ gas flow fraction from 2% to 10% leads to a drop of F_{c} from 39.4% to 10.9% and σ from 0.112 to 1.96×10^{-6} S/cm. The transition from the crystalline phase to the amorphous phase can be attributed to the excessive phosphorus (P) atoms in the films. These considerable amounts of dopants in the lattice may disrupt the periodicity of the crystal lattice and retard the growth of the nc-Si phase, causing a dramatic drop of the σ [11,16,186, 187]. Fig. 4.13 displays the profiles of the P intensity (I_{P}) and the electrically active dopant concentration (n_{act}) of the nc-SiO$_{\mathrm{x}}$:H thin films, extracted from the SIMS and the eCV measurement, respectively. The P concentration increases when increasing the $f_{\mathrm{PH_3}}$ from 0 to 10%, demonstrating more phosphorus atoms incorporated in the thin films. However, the active doping concentration increases firstly when increasing the $f_{\mathrm{PH_3}}$ from 1 to 2%, and decreases as further increasing it to 10%, which is consistent with the aforementioned σ results in Tab. 4.1. The active P atoms are supposed to be incorporated in the silicon lattice to provide extra electrons and improve the electronic conductivity. When $f_{\mathrm{PH_3}}$ is low (< 2%), the dopants are insufficient in the silicon lattice and the extra P atoms due to the increased $f_{\mathrm{PH_3}}$

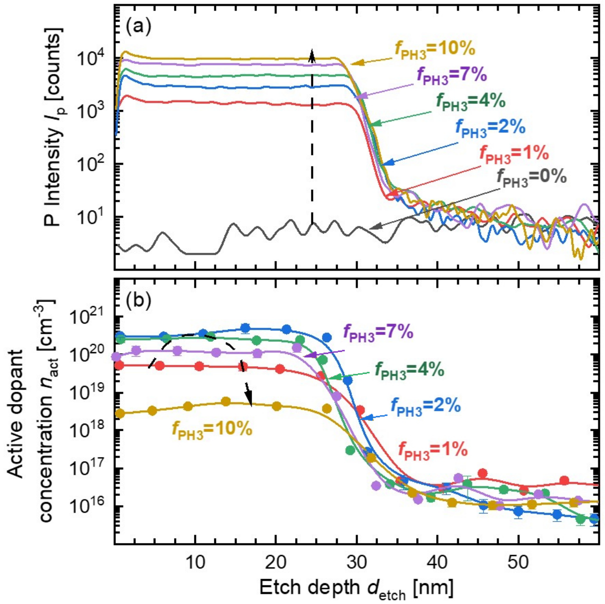

Figure 4.13.: *(a) SIMS phosphorous profiles and (b) ECV effective doping concentration profiles of the nc-SiO$_x$:H(n) films prepared under different PH$_3$ gas flow fraction (f_{PH_3}).*

would play a big role on the active dopant concentration. Meanwhile, more crystaline phases which are easier to be doped than the amorphous phases [11] can be achieved in the nc-SiO$_x$:H films upon increasing the $f_{\mathrm{PH_3}}$ from 1 to 2%, enhancing the active doping level of the nc-SiO$_x$:H films. When $f_{\mathrm{PH_3}}$ is more than 2% the increased P dopants in the film is not in a doping active state and the formerly active P dopants are no longer active for films prepared at higher $f_{\mathrm{PH_3}}$. This reveals that the doping efficiency of phosphorus in the nc-SiO$_x$:H layers is deteriorated.

Fig. 4.14 illustrates the effects of the $f_{\mathrm{CO_2}}$ and the $f_{\mathrm{PH_3}}$ on the complex permittivity of the nanocrystalline silicon oxide films. We can see that the increase of the CO$_2$ gas flow fraction leads to a decrease of the amplitude of ε_1 near 3.3 eV without any shift and increase near 4.5 eV, which is consistent with the result reported in Ref. [188]. Hübner et al. demonstrated that there are chemical transition regions at the Si-SiO$_2$ interfaces [188]. Additionally, the total electronic properties of SiO$_x$ vary quantitatively and qualitatively with the average chemical composition

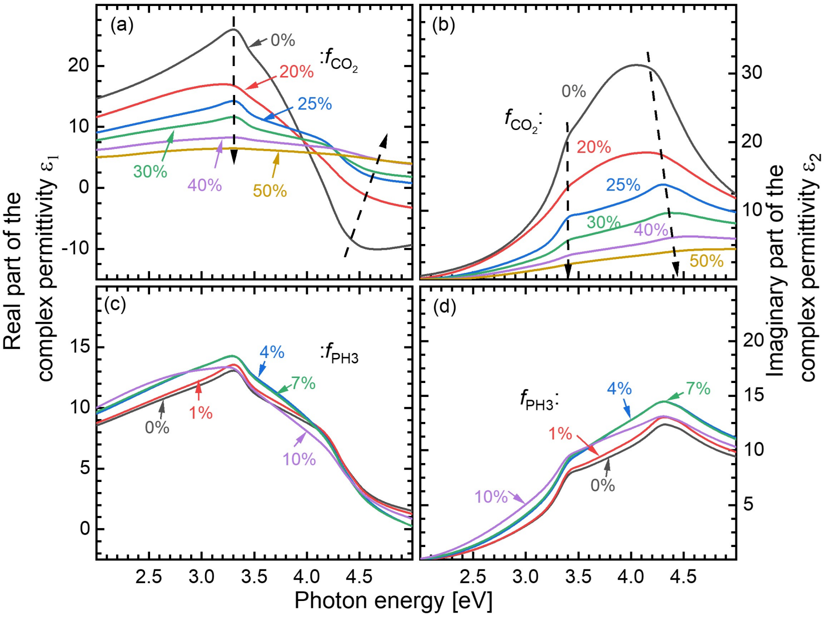

Figure 4.14.: *Effect of (a), (b) the CO_2 gas flow fraction (f_{CO_2}) and (c), (d) PH_3 gas flow fraction (f_{PH_3}) on the complex permittivity of nc-SiO$_x$:H films.*

x between the corresponding Si and SiO$_2$ properties [188]. The imaginary part of the complex permittivity decreases as increasing the $f_{\mathrm{CO_2}}$ from 0% to 50%. Besides, an slight shift of the ε_2 maximum to higher photon energy range can be observed, indicating the amorphization of the crystalline silicon phase in the nc-SiO$_{\mathrm{x}}$:H films prepared at a higher $f_{\mathrm{CO_2}}$. A change of the curve shapes can be found in Fig. 4.14 (a) and (b) when increasing $f_{\mathrm{CO_2}}$ beyond 40%. This variation could be due to the transform of the binding configurations in the silicon films. Mui et al. proposed a tetrahedron model for the optical dielectric function of the a-Si:H films [189]. They demonstrated that replacing Si-Si bonds by stronger Si-H bonds slightly lowers the values of the maximum of the real and the imaginary part of the dielectric functions [189]. Besides, Adele et al. extended the model to the hydrogen-rich silicon oxynitride materials and revealed that the binding configurations of Si-O affects the dielectric functions as well [179]. A set of distribution probabilities for the five random-bonding tetrahedra Si-Si$_y$-O$_{4-y}$, where $y = 0$ to 4, as a function of the oxygen content was reported in Ref. [58, 188, 190]. For the oxygen content lower than 20% the concentration of Si-Si$_3$-O is much higher than that of Si-Si$_2$-O$_2$ and Si-Si-O$_3$, and only Si-Si$_3$-O has an effect on the optical properties. More oxygen will be incorporated in the silicon films if increasing the CO$_2$ gas flow fraction. When the $f_{\mathrm{CO_2}}$ is more than 40%, the concentration of Si-Si$_2$-O$_2$ becomes comparable with that of Si-Si$_3$-O, making the change of the curve shape happen. As shown in Fig. 4.14 (c) and (d), the maximum of ε_1 and ε_2 increases slightly as raising the $f_{\mathrm{PH_3}}$ from 0% to 7% and decreases as further increasing it to 10% without any shift of the peak position.

The random mixture model (RMM) was demonstrated to be a most likely better method to describe the microstructure of the nc-SiO$_x$:H films prepared with CO$_2$ as the oxygen source gas than the random bond model (RBM) [58]. Therefore, the nc-SiO$_x$:H films in this work were evaluated with the RMM. In this model, the nc-SiO$_x$:H material is considered with three fractions: nc-Si:H, a-Si:H and a-SiO$_2$ in an almost stoichiometric configuration [58, 188, 191]. The volume fraction of the nc-Si:H phase is determined by UV-Raman measurement and the a-SiO$_2$ volume fraction ($F_{\text{a-SiO}_2}$) was calculated via the following equation:

$$F_{\text{a-SiO}_2} = \frac{\frac{x}{2N_{\mathrm{SiO_2}}}}{\frac{x}{2N_{\mathrm{SiO_2}}} + \frac{2-x}{2N_{\mathrm{Si}}}}. \tag{4.3}$$

In Eq. 4.3, the x, $N_{\mathrm{SiO_2}}$ and N_{Si} are the stoichiometry factor, atomic density of

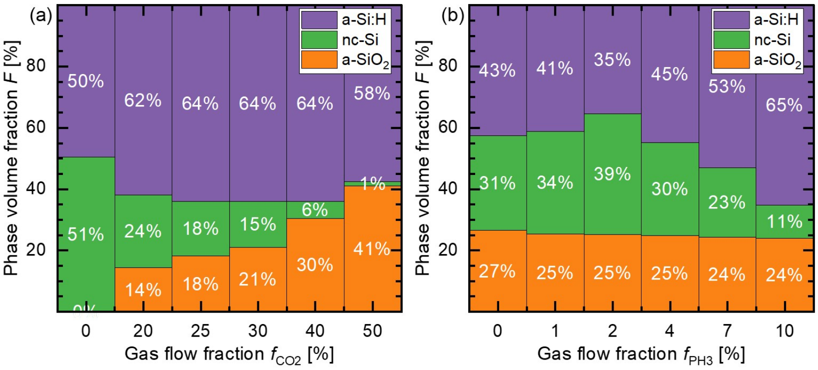

Figure 4.15.: *The effect of (a) f_{CO_2} and (b) f_{PH_3} on the volume fraction of nc-Si, a-Si and a-SiO$_2$ phase in nc-SiO$_x$:H(n) films.*

2.27×10^{22} cm^{-3} for pure a-SiO$_2$ and atomic density of 5×10^{22} cm^{-3} for pure silicon, respectively [58, 192]. The x is calculated by Eq. 4.4:

$$c_O = \frac{x}{x+1}. \tag{4.4}$$

The a-Si:H volume fraction ($F_{\text{a-Si:H}}$) was calculated as $F_{\text{a-Si:H}} = 1 - F_c - F_{\text{a-SiO}_2}$. Fig. 4.15 displays the volume fraction of a-Si, nc-Si and a-SiO$_2$ phases in the nc-SiO$_x$:H(n) film prepared at various f_{CO_2} and f_{PH_3}. Adding a small amount of CO$_2$ ($f_{CO_2} < 20\%$) into the process chamber leads to the amorphization of the crystalline phase. A substitution of the nc-Si phases by the a-SiO$_2$ phases can be achieved by further increasing the f_{CO_2} towards 50%. This result reveals the enhancement of the oxygen on the transformation of the crystalline phases to the amorphous silicon oxide phases. The ratio of the a-Si:H and the nc-Si phase in the nc-SiO$_x$:H films can be affected by the doping concentration, yet no obvious influence on the a-SiO$_2$ volume fraction.

4.2.3. Silane gas flow fraction

Fig. 4.16 shows the process gas flow and the gas flow fraction of the precursor gases versus the f_{SiH_4}. The H$_2$ gas flow was kept constant at 990 sccm and the SiH$_4$ gas flow was tuned from 5 to 20.5 sccm to achieve a f_{SiH_4} range between 0.5% and 2%. The gas flow of CO$_2$ and PH$_3$ were slightly adjusted to preserve the f_{CO_2} of 20%

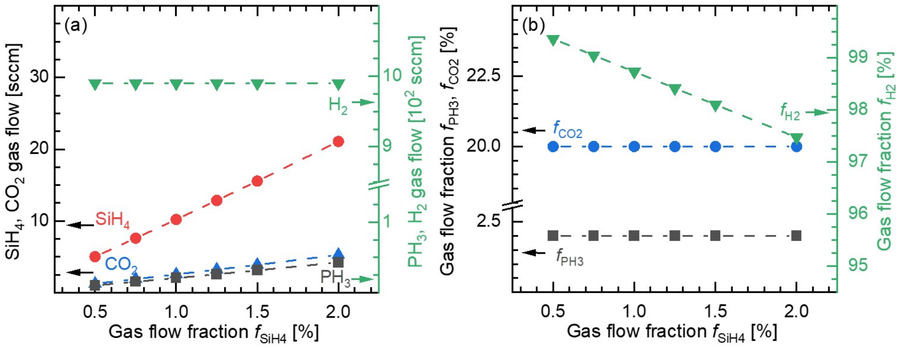

Figure 4.16.: *(a) The process gas flow and (b) the gas flow fraction versus the silane gas flow fraction (f_{SiH_4}). The dash lines are guide for eyes.*

and the $f_{\mathrm{PH_3}}$ of 2%, respectively. As a consequence of the increased $f_{\mathrm{SiH_4}}$, the $f_{\mathrm{H_2}}$ decreases from 99.5% to 97.5%.

Fig. 4.17 shows the deposition rate and the silane utilization as a function of the SiH$_4$ gas flow fraction with different $f_{\mathrm{CO_2}}$. The r_{D} increases linearly as raising $f_{\mathrm{SiH_4}}$ over the investigation range, whereas only a slight increase of $U_{\mathrm{SiH_4}}$ can be observed in Fig. 4.17 (b). This result is different with the trend observed in Fig. 4.1 with variation of the power density. More SiH$_4$ added into the process chamber at the higher $f_{\mathrm{SiH_4}}$ could lead to a escalation of the SiH$_3$ ions or radicals near the surface of substrate, boosting the growth of the nc-SiO$_x$:H films. Besides, the r_{D} and the $U_{\mathrm{SiH_4}}$ is independent of the $f_{\mathrm{CO_2}}$. Fig. 4.18 displays the contour map of the crystalline volume fraction, the oxygen content, the optical band gap and the refractive index at 632 nm plotted versus the $f_{\mathrm{CO_2}}$ and the $f_{\mathrm{SiH_4}}$. For the nc-Si:H(n) films a decreased F_{c} and E_{04} is obtained when increasing the $f_{\mathrm{SiH_4}}$ from 0.5% to 2% as well as an increased refractive index. When the $f_{\mathrm{CO_2}}$ is more than 0%, the F_{c} increases firstly and then decreases as increasing the $f_{\mathrm{SiH_4}}$. For the nc-SiO$_x$:H layers prepared at a lower $f_{\mathrm{SiH_4}}$ more oxygen is incorporated in the films, yielding an increased optical band gap and a decreased refractive index. The c_{O} and E_{04} of the nc-SiO$_x$:H films produced at a larger $f_{\mathrm{CO_2}}$ is more sensitive to the variation of the silane gas flow fraction.

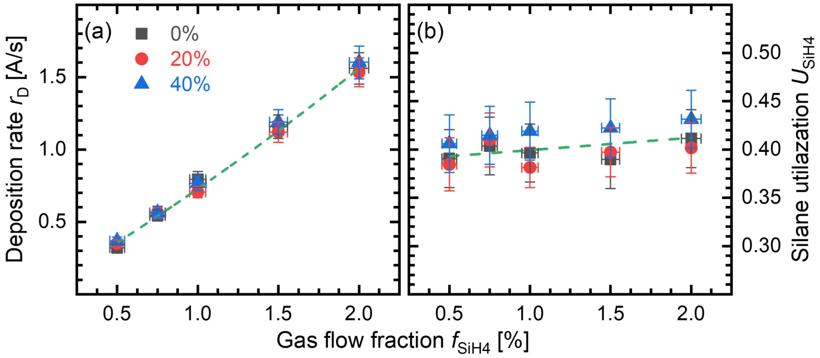

Figure 4.17.: *(a) The deposition rate (r_D) and (b) silane utilization versus the silane gas flow (f_{SiH_4}). The carbon dioxide gas flow fraction (f_{CO_2}) used for each series are indicated. The dash lines are guide for eyes.*

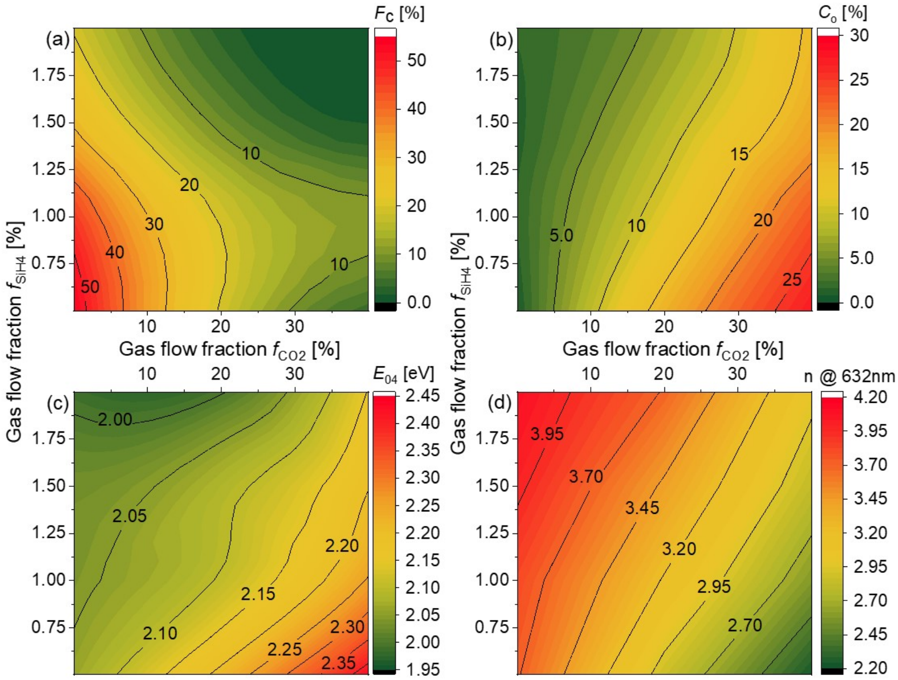

Figure 4.18.: *The contour map of (a) the crystalline volume fraction (F_c), (b) oxygen content (c_O), (c) optical band gap (E_{04}) and (d) refractive index (n) at 632 nm plotted versus the gas flow fraction of CO_2 (f_{CO_2}) and SiH_4 (f_{SiH_4}).*

Fig. 4.19 (a) displays the dark conductivity plotted versus the SiH_4 gas flow fraction at the f_{CO_2} of 0%, 20% and 40%. For the $f_{CO_2} = 0\%$ series, the σ decreases from 14.0 to 8.2 S/cm as increasing the f_{SiH_4} from 0.5% to 1%. But then an significant decline by two orders of magnitudes is observed when further rising the f_{SiH_4} up to 2%. For the series at f_{CO_2} of 20% or 40% , the dark conductivity increases first as raising the silane gas flow fraction and then decreases when the f_{SiH_4} is more than 1%. The nc-SiO_x:H films deposited at higher f_{CO_2} is susceptible to the change of f_{SiH_4}. The PDS results of the SiH_4 series with 20% of f_{CO_2} are plotted versus the photon energy in Fig. 4.19 (b). The absorption coefficient in the sub-band gap range (photon energies below 1.1 eV) goes up with increasing the f_{SiH_4} from 0.5% to 1%. This result indicates more free carrier absorption in the films, which could be

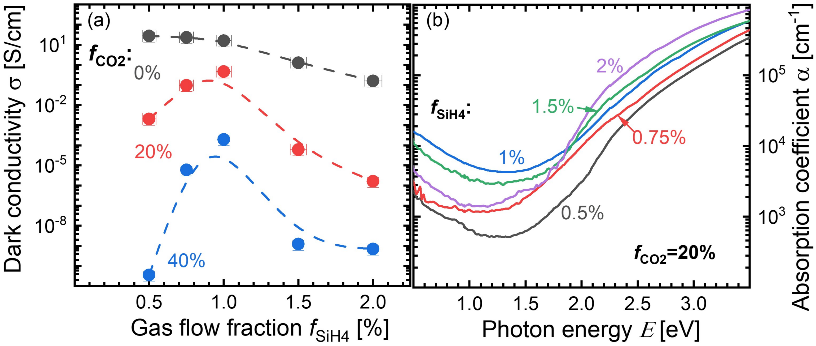

Figure 4.19.: *(a) The dark conductivity of the nc-SiO$_x$:H(n) versus the silane gas flow fraction (f_{SiH_4}) at various carbon dioxide gas flow fraction (f_{CO_2}). (b) The absorption coefficient (α) of the nc-SiO$_x$:H films versus the photon energy (E) for the SiH$_4$ series with 20% of f_{CO_2}. The absorption coefficient was measured by photo-thermal deflection spectroscopy (PDS).*

attributed to the increase of the active doping concentration. When further rising the $f_{\mathrm{SiH_4}}$ up to 2%, a reduction of the absorption coefficient is observed, which is in a good agreement with the trend of the dark conductivity.

The FTIR spectra of the nc-SiO$_x$:H films prepared at various $f_{\mathrm{SiH_4}}$ in the wavenumber range of 1900~2400 cm^{-1} is plotted in Fig. 4.20 (a). The $f_{\mathrm{CO_2}}$ was set at 20%. The lowest a-Si:H related peak at 2000 cm^{-1} and highest (O$_3$)Si-H (s) peak near 2250 cm^{-1} is found for the nc-SiO$_x$:H layer prepared at $f_{\mathrm{SiH_4}}$ of 0.5%. This result suggests a high amount of the O-rich a-SiO$_x$ phases in the nc-SiO$_x$:H(n) films produced at low $f_{\mathrm{SiH_4}}$. When increasing the $f_{\mathrm{SiH_4}}$ from 0.5% to 2%, a reduction of the maximum value near 2250 cm^{-1} and an increase of that near 2000 cm^{-1} is observed, which demonstrates the deterioration of the a-SiO$_x$ phase. A dramatic increase of the amplitude of the absorption coefficient curve near 2000 cm^{-1} can be found as increasing the $f_{\mathrm{SiH_4}}$ from 1% to 1.5%. This observation could be a consequence of the degeneration of the nc-Si phase in the nc-SiO$_x$:H films. Fig. 4.20 (b) shows the ε_2 of the nc-SiO$_x$:H films prepared at various $f_{\mathrm{SiH_4}}$ as a function of the photon energy. Two peaks of the ε_2 dielectric function at 3.4 eV and 4.2 eV can be found when $f_{\mathrm{SiH_4}}$ < 1%, which are correspond to the nc-Si phases mentioned in Sec. 3.2.3. Raising the silane gas flow fraction from 0.5% to 1% leads to an increased peak at 4.2 eV.

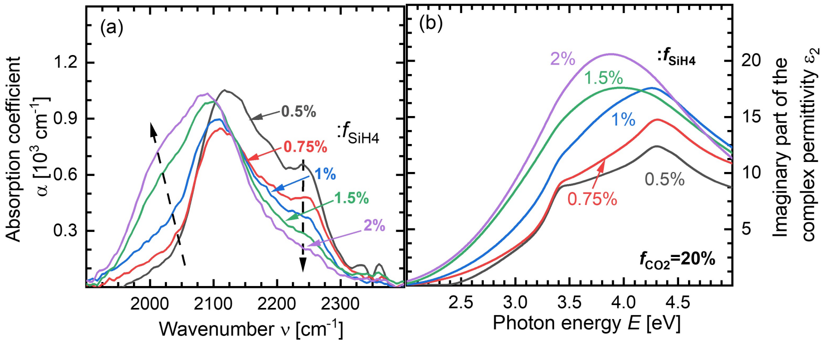

Figure 4.20.: *(a) The FTIR spectra and (b) the imaginary part of the dielectric function (ε_2) of the nc-SiO$_x$:H films prepared at various silane gas flow fraction (f_{SiH_4}). The carbon dioxide gas flow fraction (f_{CO_2}) for this series was fixed at 20%.*

This indicates the more nc-Si phases in the films produced at higher $f_{\mathrm{SiH_4}}$, which is consistent with the Raman results shown in Fig. 4.18 (a). The broad hump with the peak position near 3.5∼3.6 eV was reported to be a characteristic signature of a-Si:H films [118, 121, 123, 124]. When $f_{\mathrm{SiH_4}} > 1\%$, a red-shift of the peak can be observed in Fig. 4.20 (b), revealing the deterioration of the nc-Si phases.

Fig. 4.21 displays the volume fraction of a-Si:H, nc-Si:H and a-SiO$_2$ phases in the nc-Si:H(n) and nc-SiO$_\mathrm{x}$:H(n) films prepared at various $f_{\mathrm{SiH_4}}$. The evolution of the phases in the nc-SiO$_\mathrm{x}$:H(n) films as varying $f_{\mathrm{SiH_4}}$ is different from that in the nc-Si:H(n) films. A substitution of the nc-Si phases by the a-Si phases is observed for the nc-Si:H layers when increasing the $f_{\mathrm{SiH_4}}$. For the nc-SiO$_\mathrm{x}$:H(n) films, we can see a transformation of the a-SiO$_2$ phases to the nc-Si phases as tuning the $f_{\mathrm{SiH_4}}$ from 0.5% to 1%. Further increasing the $f_{\mathrm{SiH_4}}$ above 1.5% leads to a significant amorphization of the crystalline phases in the nc-SiO$_\mathrm{x}$:H(n) films.

In general, the effect of the $f_{\mathrm{SiH_4}}$ on the growth of nc-SiO$_\mathrm{x}$:H is interpreted in terms of several growth models, including the hydrogen etching model, the surface mobility model, and the chemical annealing model [75]. Due to the reduction of the $f_{\mathrm{SiH_4}}$, a decreased deposition rate and an improved crystalline fraction is achieved for the nc-Si:H(n) films. This result reveals that hydrogen etching plays a big role in the growth of the nc-Si:H(n) layers. On the surface of the growth region, the

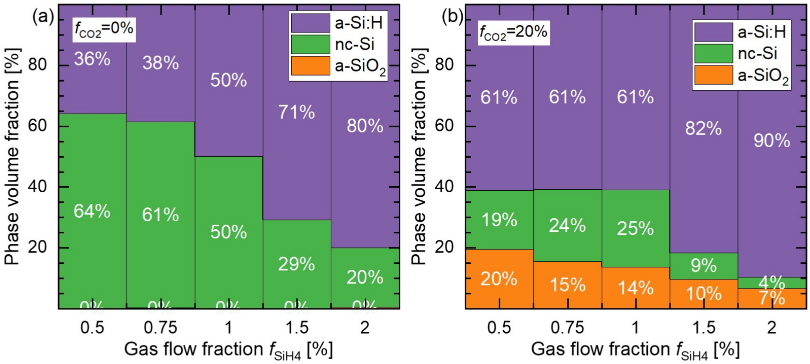

Figure 4.21.: *The effect of the silane gas flow fraction (f_{SiH_4}) on the volume fraction of nc-Si, a-Si and a-SiO$_2$ phase in the nc-Si:H(n) and the nc-SiO$_x$:H(n) films.*

hydrogen atoms can break the weak Si-Si bonds and capture the H in Si-H bonds during deposition. Those processes are very helpful and crucial for the formation of the firmer covalent bonds and the ordered structure. As a result, an improved crystallization in the amorphous silicon matrix can be acquired. As mentioned in Fig. 4.16, the hydrogen gas flow fraction decreases as increasing the f_{SiH_4} from 0.5% to 2%. Therefore, the scission of the weak Si-Si bond by the insertion of the H atoms would be undermined, resulting in a drop of the crystalline volume fraction and the dark conductivity. When adding CO_2 into the process chamber, the influence of the silane concentration on the chemical reactivity in the plasma could be different. It is notable that an increased number of the reactions in the plasma have to be considered in the case of the nc-SiO$_x$:H deposition, because of the additional oxygen containing molecules, ions and radicals. The threshold energies of the electrons needed to perform the dissociation reactions are 8.3, 11.5 and about 10 eV for SiH_4, CO_2 and H_2, respectively. As increasing the f_{SiH_4}, more SiH_4 gas is provided for the growth of the nc-SiO$_x$:H films. The increased SiH_4 molecules could weaken the dissociation processes of the CO_2 molecules since the power density was fixed. Therefore, less oxygen ions and radicals would be created in the plasma when increasing the silane gas flow fraction, causing the reduction of the incorporated oxygen in the films. Consequently, the transformation of the a-SiO$_x$ phases to the nc-Si or a-Si phases would be promoted as raising f_{SiH_4} from 0.5% to 1%, leading to the strong increase of the dark conductivity and decrease of the optical band gap as shown in Fig. 4.18. Additionally, the substitution of the a-SiO$_x$ phase by the nc-Si phase is demonstrated by the FTIR spectra and the ε_2 dielectric function in Fig. 4.20. The decrease of (O$_3$)Si-H (s) peak near 2250 cm^{-1} indicates a deterioration of the a-SiO$_x$ phases and the increased peak of ε_2 demonstrates an improved growth of the nc-Si phases in the nc-SiO$_x$:H(n) films. When further increasing the f_{SiH_4} beyond 1.5%, the dissociation of H$_2$ would be affected, leading to a insufficient atomic H density for the growth of the nc-Si phases, which is similar as the nc-SiO$_x$:H films in Region I, "fully amorphous region" proposed by Alexei [13]. Although the reduction of the oxygen content has benefits to the growth of the nc-Si phases, the decreased H density could overcompensate this influence of the oxygen and be the dominant factor to the nc-Si phase growth, leading to the replacement of the a-SiO$_x$ or nc-Si phase by the a-Si phase. As a consequence, the E_{04} and the σ decreased as raising the f_{SiH_4} from 1% to 2%.

4.3. Overview of optical and electrical properties

Various n-type nc-SiO$_x$:H layers at the thickness range between 20 and 50 nm were deposited in the industrial PECVD system during the material development for the

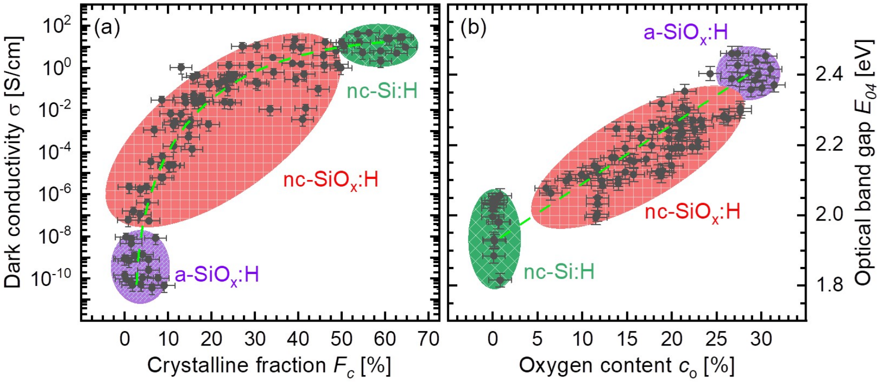

Figure 4.22.: *(a) The dark conductivity (σ) versus the crystalline volume fraction (F_c) and (b) the optical band gap (E_{04}) as a function of the oxygen content (c_O).*

SHJ solar cells. An overview of their opto-electronic properties are presented in Fig. 4.22. The σ is associated with F_c and E_{04} is linked to c_O, which is consistent with the results reported in Ref. [58, 100]. Based on the value of the F_c and the c_O, these data points can be divided into three groups: a-SiO$_x$:H, nc-SiO$_x$:H and nc-Si:H. In the nc-Si:H group, no oxygen is incorporated in the films and the F_c is more than 50%. This suggests that the dominant component of the nc-Si:H films in this group is the nc-Si phase, which is highly conductive and less transparent than the a-SiO$_x$ phase. As a consequence, the average σ in this group is much higher than the others, but the E_{04} is lower. The CO_2 was introduced into the working gases in the nc-SiO$_x$:H region and the oxygen is incorporated in the amorphous matrix, which would hinder the growth of the crystalline silicon phase and promote the formation of the amorphous phases. More and more oxygen combined in the films leads to the deterioration of the percolation paths built up by the nc-Si phase, through which the charge carriers could be transported. A significant drop of the σ can be found in Fig. 4.22 when F_c is less than 20%. By adjusting the deposition parameters, the dark conductivity of the films with 20~50nm thickness in the nc-SiO$_x$:H region can be tuned from 1×10^{-7} to 1×10^{1} S/cm, and the E_{04} from 2.0 to 2.35 eV. When the $c_O > 25\%$, the dominant component in the nc-SiO$_x$:H films is the a-SiO$_x$ phase, which is highly transparent and almost insulated, leading to the $\sigma < 1 \times 10^{-8}$ S/cm and the $E_{04} > 2.3$ eV.

The dark conductivity of the nc-SiO$_x$:H films is plotted versus the optical band gap in Fig. 4.23. The films with a high E_{04} and σ is appropriate to be used as a window layer in the SHJ solar cells. A trade-off between the optical and electrical properties of the nc-SiO$_x$:H films is observed in Fig. 4.23. Richter et al. reported a dramatically decreased FF for the SHJ solar cells when reducing the σ of the nc-SiO$_x$:H(n) layer below 1×10^{-3}S/cm [100]. In this work, nc-SiO$_x$:H films with σ of 1×10^{-3} S/cm and E_{04} of 2.3eV can be acquired at thickness of 30~50nm. When the E_{04} is more than 2.3eV, the σ decreases significantly and reaches 1×10^{-9}S/cm at 2.4eV E_{04}. Fig. 4.23 also displays the comparison between the opto-electronic properties of nc-SiO$_x$:H films in this work and that of films from literature, which were all prepared by PECVD with radio frequency [16, 58, 59, 100]. The films in this work were deposited at low-power-low-pressure conditions, below 100 mW/cm^2 and 4.5mbar, in a industrial chamber with a 50×50 cm^2 substrate area. The films reported in literature were prepared in a small chamber, with 10 × 10 cm^2 of carrier area. The power density for these films is in the range of 133∼350 mW/cm^2 and the pressure is between 0.5 and 6 mbar. The thickness of films in Ref. [16, 58, 59, 100] is in the range of 200nm to 2µm, which is quiet thicker than the films (30∼50nm) prepared in this work, and the final films (5∼30nm) used in the SHJ solar cells. Nearly identical location of the data points from this work as those reported in Ref. [16, 58, 59, 100] is observed in Fig. 4.23, indicating the success of the material development in upscaling. The optoelectronic properties of the nc-SiO$_x$:H films by

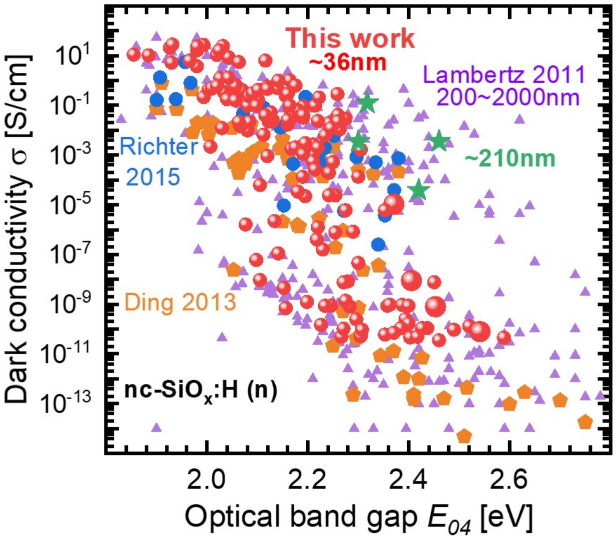

Figure 4.23.: *The dark conductivity (σ) versus the optical band gap (E_{04}) of the films prepared in this work and reported in literature [16, 58, 59, 100]. All films were prepared by RF-PECVD system. The films in this work are with 30∼50nm of thickness and were deposited at low-power-low-pressure conditions, below 100 mW/cm^2 and 4.5mbar, in a industrial chamber with a* 50 × 50 *cm^2 electrode area. The red stars represent the thick films (210nm) prepared under the same deposition conditions as the thin films (36nm), marked with larger red balls. The films from literature are in the thickness range of 200*nm *to 2*µm. *They were prepared in a much smaller chamber, with* 10 × 10 *cm^2 of carrier area, and at the power density in the range of 133∼350 mW/cm^2 and 0.5∼6 mbar of pressure.*

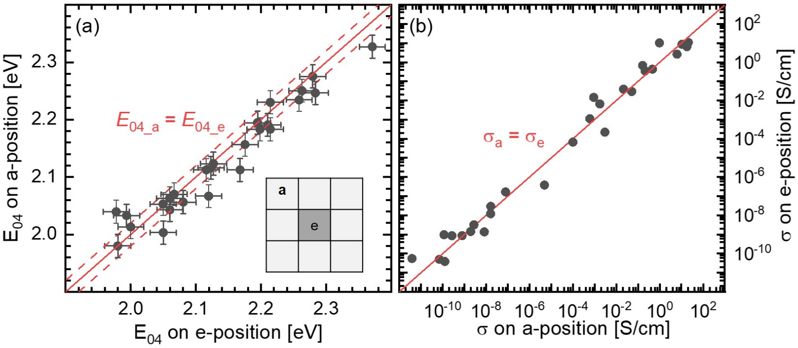

Figure 4.24.: *(a) The optical band gap (E_{04}) and (b) the dark conductivity (σ) on the a-position versus that on the e-position. The layout of the positions on the substrate holder is displayed in Figure (a). The red solid lines are where the material properties on two positions are the same.*

Lambertz et al. are in a more extensive range than this work, which could be due to the difference of the thickness [58, 59]. Additionally, decreased σ and F_c were reported by Ding et al. when reducing the thickness of nc-SiO$_x$:H from 400nm to 20nm [16]. Thus, we selected several recipes for the preparation of thick nc-SiO$_x$:H layers (~210nm), the properties of which are presented by the red stars in Fig. 4.23. The red balls with a larger size are the thinner films prepared at same deposition parameters as the red stars. An improvement of the conductivity and a reduction of the E_{04} is obtained, reaching the extension region reported by Lambertz et al [58,59].

As mentioned in Sec. 3.1, it is capable to put 9 M2-sized wafers or glass substrates of an equivalent area into the PECVD system in one processing run. To monitor the homogeneity of the nc-SiO$_x$:H properties, two substrates were placed on the different position of the holder, named a-position and e-position. The material properties of the films prepared on the a-position versus that on the e-position are shown in Fig. 4.24. The data points are located on the region near the red solid lines, where the material properties on two positions are the same, indicating a good homogeneity of the films prepared in the large-area system.

5. Application of n-type nc-SiO$_x$:H in SHJ solar cells

For high-efficient c-Si solar cells, high-quality surface passivation is of extreme importance. It has been proved that the utilization of the intrinsic and the doped a-Si:H double layer in SHJ solar cells is a promising strategy to achieve excellent surface passivation [193]. The power conversion efficiency of such SHJ designs has been above 25% for the both-side contacted devices and 26% for the cells with the IBC structure [12,37]. Although the doped a-Si:H window layer is only a few nanometers thick (5∼10 nm), it still absorbs a significant amount of the incoming light, leading to the reduction of J_{sc} (∼1.6 mA/cm^2) for SHJ solar cells. This parasitic absorption in the doped a-Si:H layer limits the η of the SHJ devices [10, 11]. The doped nc-SiO$_x$:H material has been demonstrated to be a highly promising alternative to the commonly used a-Si:H in the SHJ solar cells [13, 60, 194]. In this chapter, the n-type nc-SiO$_x$:H is integrated in the rear-junction SHJ solar cells. Based on the material development results in Sec. 4, several deposition recipes were selected for the nc-SiO$_x$:H(n) films, which are used as window layers in the SHJ solar cells to reduce the parasitic absorption in the short wavelength region and improve the cell performance. The preliminary development of the SHJ solar cells with nc-SiO$_x$:H(n) on quartered M2 wafers is presented in this section before the systematic optimization of the devices, which will be described in Sec. 6. The first part introduces the fabrication processes of the SHJ solar cells in this thesis. Secondly, the effect of the intrinsic and doped silicon layer stack on the passivation quality is introduced. Afterwards, the influence of the $f_{\mathrm{CO_2}}$ and the $f_{\mathrm{PH_3}}$ on the c-Si surface passivation and the performance of the rear-junction SHJ solar cells are investigated. Finally, the power losses of the best performed solar cell in this section were analyzed by

Quokka3 simulator, and then a road map to reach 24% of power conversion efficiency is presented.

5.1. Fabrication of SHJ solar cells

All solar cells were produced on random-pyramid textured n-type doped Czochralski (CZ) silicon wafers, the thickness and resistivity of which are 170 µm and 1-5 Ω cm, respectively. An overview of the fabrication steps of the rear-junction SHJ solar cells is shown in Fig. 5.1.

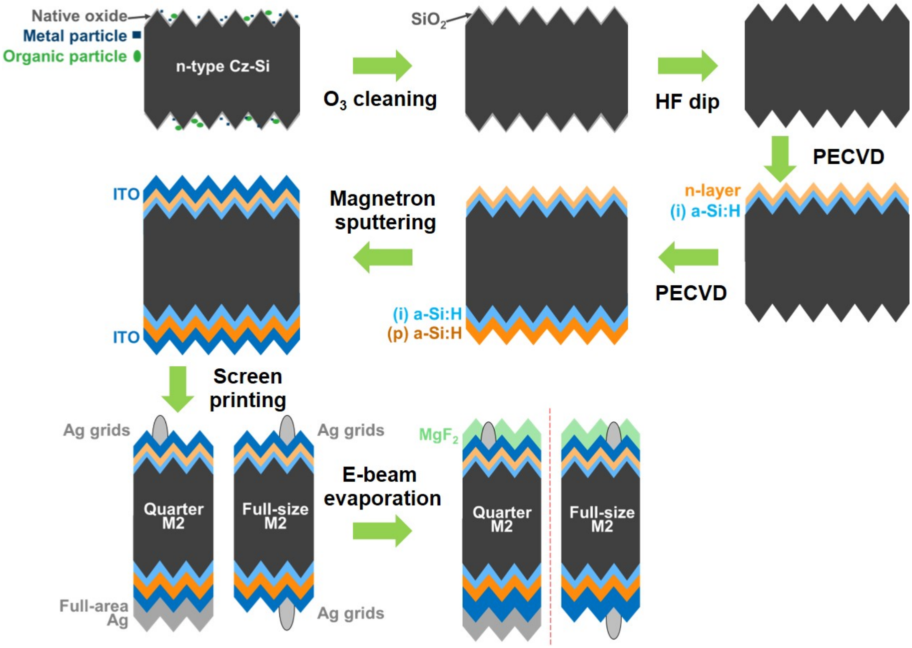

Figure 5.1.: *Fabrication processes of the rear-junction SHJ solar cells: 1) surface cleaning of the textured wafer substrate; 2) dipping in the HF to remove the surface silicon dioxide layer; 3) PECVD deposition of the a-Si:H(i) and n-type layer on the front side; 4) PECVD deposition of the a-Si:H(i) and p-type layer on the rear side; 5) magnetron sputtering of the ITO on the front and rear side; 6) screen printing the Ag electrodes on both sides; 7) deposition of MgF$_2$ on the front side by E-beam evaporation.*

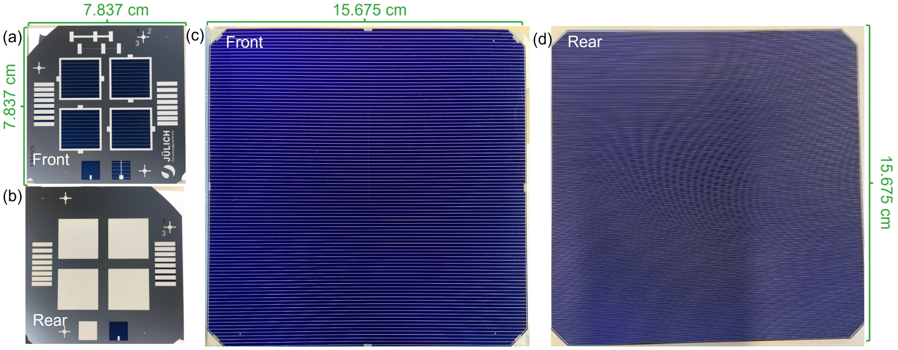

Figure 5.2.: *(a) (b) Layout of 3.61 cm^2 cells on a quartered M2 wafer and (c) (d) busbarless cell on a full-size M2 wafer (244.3 cm^2).*

Before the PECVD depositions, the wafers were cleaned by an Ozone cleaning procedure [195]. The textured wafers were immersed in an acidic solution containing hydrochloric acid (HCl), ozone (O_3) and hydrofluoric acid (HF). There, metallic impurities were removed by HCl and the wafers then were oxidized by O_3, creating an oxide layer on the surface of the wafers that also trapped the other impurities, which were removed by HF. Afterwards, rinsing in the deionized (DI) was followed. The wafers then were put into another bath with HCl and O_3 to further remove the impurities and build up uniform oxide layers that protect the wafers. Then the wafers after rinsing in the DI were dipped in the 1% HF for 10 mins. After rinsing and drying, the wafers were immediately transferred to the holder in the load chamber of the PECVD system to prevent re-oxidation. The wafers were pre-heated up for 2 mins with the heater temperature of 200 °C in LM2 of the PECVD system and then transported to PM3 (see in Fig. 3.1). Another 5 mins preheating in a H_2 atmosphere was followed and then the a-Si:H(i) as front passivation layer and the n-type layer as electron transport layer (ETL) were deposited on the front side of the wafers in the S-Cube of PM3. Subsequently, the wafers were rotated in the hot state and ambient air, then put on the carrier in LM1 manually. The preheating steps in LM1 and PM2, and the deposition of the a-Si:H(i) layer as the back passivation layer in PM2 were followed. Next, the wafers were transported to LM1 and then to PM1 without breaking the vacuum, where the deposition of the a-Si:H(p) layer was carrier out. Afterwards, the ITO layers were deposited through a shadow mask on each side at a substrate temperature of 200 °C by direct current (DC) sputtering. The Ag electrode on the both sides was screen printed, afterwards the samples were annealed at 170 °C for 40 mins in the ambient air to facilitate contact formation. In this work, quartered or full-size M2 wafers were used. Depending on the wafer size, different shadow mask for the ITO sputtering deposition and various screen pattern for metallization process was used. Fig. 5.2 shows the pictures of the fabricated solar cells on a quartered or a full-size M2 wafer. Four solar cells with the active area of 19×19 mm^2 are embedded in a quartered M2 wafer and surrounded by the busbar. The TLM electrode patterns are on the left and the right side of the wafer. The metal patterns on the top of the wafer were prepared for the determination of the grid finger and the busbar line resistance. The solar cell on the M2 sized wafer is bifacial and with busbar-less grid, as shown in Fig. 5.2 (c) and (d). In this work, the number of fingers on the front and rear side is 96 and 250, respectively. For some samples 110 nm MgF$_2$ thin-film was evaporated as the ARC layer on the front side [196].

5.2. Integration of nc-SiO$_x$:H(n) in SHJ solar cell

In this section, the n-type nc-SiO$_x$:H(n) layer was integrated in the rear-junction SHJ solar cells to replace the commonly used a-Si:H(n).

5.2.1. Impact on the passivation

The passivation quality of the intrinsic amorphous layer is sensitive to the deposition of nc-SiO$_x$:H and TCO layers. Therefore, preserving a high passivation level from the underlying a-Si:H(i) layer after the deposition of nc-SiO$_x$:H(n) and TCO layers is a stringent requirement for the high-efficiency SHJ solar cells. In order to evaluate the passivation capability of the baseline process, four kinds of lifetime samples with symmetric structures, named S1, S2, S3 and S4, were fabricated. Their cross-section structures are displayed in Fig. 5.3. The a-Si:H(i) layers at the thickness of 13nm were deposited on the textured n-type wafer as the interfacial passivation layers for S1. Thinner a-Si:H(i) layers (6 nm) were utilized in S2, S3 and S4, wherein about

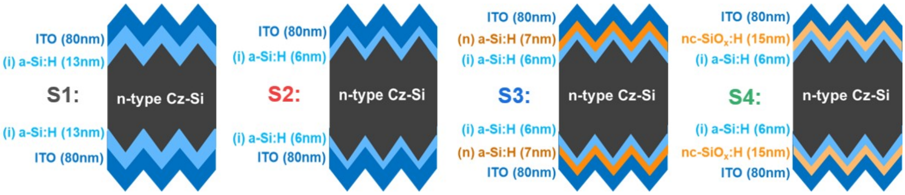

Figure 5.3.: *Sketch of four kinds of the lifetime samples, named S1, S2, S3 and S4. The structure is not drawn to scale.*

7nm a-Si:H(n) layers and 15nm nc-SiO$_x$:H(n) layers at 20% f_{CO_2} were deposited upon the a-Si:H(i) as the ETL in S3 and S4, respectively. No doped layers were applied in S1 and S2. After PECVD processes, 80nm ITO layers were deposited on the both sides to investigate the influence of sputtering processes on the passivation quality of the underlying silicon films. The standard baseline DC magnetron sputtering process was applied at the sputtering power of 5000 W, the process pressure of 3 μbar, the substrate temperature of 200 °C and the argon and oxygen flows of 90 and 5 sccm, respectively. Afterwards, the samples were put into a oven for the annealing treatment in the air ambient at the temperature of 170 °C for 40 min. This annealing treatment is same as the curing process after the screen printing metallization mentioned in Sec. 5.1. The QSSPC measurement was followed immediately after each step.

Fig. 5.4 (a), (b) and (c) shows the minority carrier lifetime as a function of the minority carrier density after the PECVD process, the ITO sputtering deposition and the annealing treatment, respectively. The minority carrier lifetime of 4 ms (at an excess carrier density of 10^{15}cm^{-3}) is obtained in Fig. 5.4 (a) for the S1 with intrinsic films as thin as 13 nm, indicating an excellent passivation quality of a-Si:H(i). When the a-Si:H thickness decreases from 13nm to 6nm, a reduction of the lifetime is observed. Compared to the S2, the subsequent depositions of the extra 7 nm a-Si:H(n) or 15 nm

As mentioned in Sec. 3.3, the value of τ_{eff} is strongly dependent on tjhe surface recombination for SHJ devices. Normally, there are considerable localized dangling bonds (DB) on the wafer surface, whose electronic state levels lie within the band gap, leading to a severe surface recombination. By depositing the hydrogenated

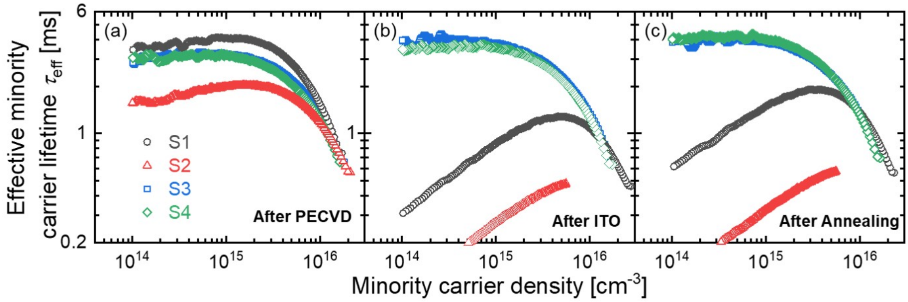

Figure 5.4.: *Minority carrier lifetime measurements performed on lifetime samples after (a) PECVD process, (b) ITO sputtering deposition and (c) annealing treatment. The cross-section structure of four kinds of lifetime samples, S1, S2, S3 and S4 can be found in Fig. 5.3. The annealing treatment is same as the curing process after screen printing mentioned in 5.1, at* 170 °C *for* 40 min *in air atmosphere.*

intrinsic amorphous silicon layer on the surface, the DBs can be passivated with H, resulting in a reduction of the interface defect density [19,197,198]. Therefore, τ_{sur} is dependent on the properties of the intrinsic a-Si:H bulk, the external a-Si:H surface and the a-Si:H/c-Si interface. Kondo et al. found an inhomogeneous of the thin intrinsic a-Si:H layer along the growth direction [197,199]. During the initial island growth, the a-Si:H is SiH$_2$-rich layer with unsaturated bonds of the c-Si surface. With the further growth of the film, a more stable SiH-rich layer is formed and these dangling bond defects are saturated by the hydrogen forming SiH bonds, causing a reduction of the defect density in the thick a-Si:H layer [16,197,199–202]. This is consistent with the a-Si:H thickness dependent lifetime observed in Fig. 5.4 (a). Besides, the charge carriers generated in the substrate could transfer through the intrinsic thin-film and recombine at the external a-Si:H surface or the next defect-rich interface [200,203]. The microstructure change of the a-Si:H layer with increasing the thickness could also lead to the variation of the optoelectronic properties. The change of the properties may lift the band offset of the a-Si:H/c-Si heterojunction and reduce the tunnel probability of carriers to reach the a-Si:H region or the external surface [200,202,204,205]. The doped films could principally induce a field effect near the a-Si:H(i)/c-Si interface. This electrical field could drive the minority carriers in the c-Si back and reduce the defects on the external a-Si:H(i) surface, leading to a high minority carrier lifetime [202,206,207]. Nevertheless, it was demonstrated that the increased doping leads to an increased defect densities in the n-type layers with few nanometers. These defects would hinder the displacement of the Fermi level (E_f) toward the conduction band minimum, where such increased defect densities have been linked to the enhanced recombination at the a-Si:H(i)/c-Si interface [208]. Therefore, a slightly worse passivation quality is observed in Fig. 5.4 for the S3 and S4 compared to the S1.

Fig. 5.4 (b) shows a dramatical decrease of the lifetime for the S1 and S2 after directly depositing ITO on the a-Si:H(i) layer. The lifetime of the S2 decreased from 2 ms to 0.3 ms and that of the S1 with the thicker a-Si:H(i) from 4 ms to 1 ms. For the samples with the doped overlayer no obvious influence of the ITO process on the lifetime can be found. This reveals that the lifetime degradation can be avoided by capping a doped layers upon the intrinsic layers. During the sputtering processes the substrates are exposed to the plasma radiation and the high-energy particles, such as the sputtered atoms, the reflected neutrals, ions and electrons with kinetic energies, etc. , which modify the nanometer thin layers and interfaces below and could lead to a strong increase in the recombination [209]. The ITO layer was deposited directly upon the intrinsic a-Si:H for the S1 and S2. Therefore, the sputtering process could cause a penetration of the sputtering ions or rupture of the weak Si-Si bonds in the a-Si:H(i) bulk. As a result, defects may be induced in the a-Si:H(i) bulk or the wafer surface, leading to a decrease of the lifetime in the low injection level related to SRH recombination. For the S1, less energy or particles are expected to transferred to the area near a-Si:H(i)/c-Si interface since a thicker a-Si:H(i) layer was used in the S1 compared to the S2. Therefore, less degradation of the effective lifetime after the ITO deposition is observed for the S1 in Fig. 5.4 (b). By capping a doped layers upon the intrinsic layers in the S3 and S4, the sputter damage can be eliminated. This could be attributed to the protective effect of the doped layers against the ion bombardment to the underlying a-Si:H(i) layers. Meanwhile, the capping layer could prevent the escape of H from the a-Si:H(i) layers to a vacuum as well, inhibiting the generation of the dangling bond defects due to Si-H bond breakage. A slight recover of passivation from 1 ms to 1.5 ms is achieved for the S1 by the annealing treatment, which is inefficacious for the S2. Besides, we also observes a small improvement of the passivation for the S3 and the S4 in Fig. 5.4 (c) after the annealing treatment.

It was reported that a re-distribution of the hydrogen or a conversion of two DBs into a strained Si-Si bond could happen in the a-Si:H(i) upon a annealing process, yielding a lower density of DBs at the a-Si:H(i)/c-Si interface [210, 211]. This could be the reason for the increased lifetime of the S3 and the S4 after the annealing treatment. For the S1 and the S2, the annealing treatment doesn't work. This is probably related to the loss of the hydrogen in the a-Si:H(i) layer or the epitaxial growth at the a-Si:H(i)/c-Si interface induced by the ITO sputtering process [212].

5.2.2. Impact on the cell performance

The rear-junction SHJ solar cells with various nc-SiO_x:H(n) single layers were fabricated on the quartered M2 wafers. The influence of the nc-SiO_x:H(n) opti-electronic properties on the cell performance was investigated by tuning f_{CO_2} from 0% to 40% and f_{PH_3} from 0% to 7%. The thickness of nc-SiO_x:H layers was fixed at 15 nm. The detailed deposition parameters and material properties of the nc-SiO_x:H(n) layers used in these two series are summarized in Tab. 5.1 and Tab. 5.2, separately.

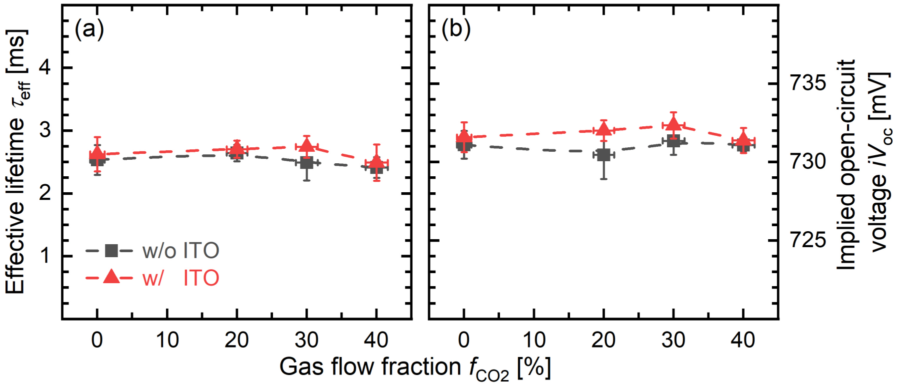

Figure 5.5.: *(a) The effective lifetime at the minority density (τ_{eff}) of 10^{15} cm^{-3} and (b) the implied open-circuit voltage (iV_{oc}) of the cell precursors before and after ITO depositions versus the CO_2 gas flow fraction (f_{CO_2}).*

Table 5.1.: *Deposition parameters and material properties of the nc-SiO$_x$:H(n) layers used in the rear junction SHJ solar cells for the CO$_2$ series.*

	f_{CO_2} [%]	f_{SiH_4} [%]	f_{PH_3} [%]	p [mbar]	P [mW/cm^2]	σ [S/cm^2]	F_c [%]	E_{04} [eV]	c_O [%]
RF	0	8.3	2	2.5	48	5.0×10^{-4}	0	1.8	0
C1	0	0.75	2	2.5	80	1.3	49	1.98	0
C2	20	0.75	2	2.5	80	9.6×10^{-2}	23.7	2.16	13.3
C3	30	0.75	2	2.5	80	3.5×10^{-3}	16.1	2.26	18.8
C4	40	0.75	2	2.5	80	6.0×10^{-6}	8.4	2.35	22.5

CO$_2$ gas flow fraction

The effective carrier lifetime at the carrier density of 10^{15} cm^{-3} and the implied open-circuit voltage at the light intensity corresponding to the AM1.5 solar spectrum were extracted from the QSSPC results and are plotted as a function of f_{CO_2} in Fig. 5.5. The τ_{eff} and iV_{oc} are almost constant as varying f_{CO_2}, reaching 2.5ms and 731mV, respectively. A slightly increase is observed after annealing treatment, which is consistent with the results shown in Fig. 5.4. The I-V parameters of the corresponding final devices are plotted in Fig. 5.6. The box plots summarize the statistic of more than 4 samples per group and the line is the median position. The devices with 7nm a-Si:H(n) layers are the reference (RF) in this series. A similar open-circuit voltage as the reference is obtained for the solar cells with the nc-SiO$_x$:H(n) layer, in good agreement with the results in Fig. 5.4. As varying the f_{CO_2} from 0% to 40%, we can see an increase of the J_{sc} from 35.8 to 37.3% mA/cm^2 and a decrease of the FF from 76% to 65%, giving rise to the best efficiency of 19.9% at the f_{CO_2} of 20% in this series. An increased difference between the pFF and the FF is obtained as varying the f_{CO_2} from 0% to 40%, indicating an increased series resistance. Compared with the reference, about 1.5%$_{abs}$ improvement of the FF is found at f_{CO_2} of 0% in the cost of 0.25 mA/cm^2 reduction of J_{sc}. For the devices with the nc-SiO$_x$:H(n) prepared at 20%, around 1mA/cm^2 gain of the J_{sc} is achieved without compromise to the FF, leading to 0.25%$_{abs}$ higher efficiency than the reference.

The correlation between the electrical performance of SHJ devices and the material properties of nc-SiO$_x$:H layers is displayed in Fig. 5.7. The series resistance increases from 1.0 to 2.9 Ω cm^2 as increasing the f_{CO_2} from 0% to 40%. Meanwhile, the contact resistivity of the ITO/n-layer (ρ_c) increases from 0.18 to 1.28 Ω cm^2. These results reveals that the variation of the R_s is mainly ascribed to the ρ_c. A reduction of the ρ_c can be observed as increasing the conductivity, crystalline volume fraction or reducing the optical band gap of the nc-SiO$_x$:H(n) layers. It could be explained by the variation of the charge carriers transport in the nc-SiO$_x$:H films and the band alignment near ITO/n-layer interface. On one hand, the nc-Si phases

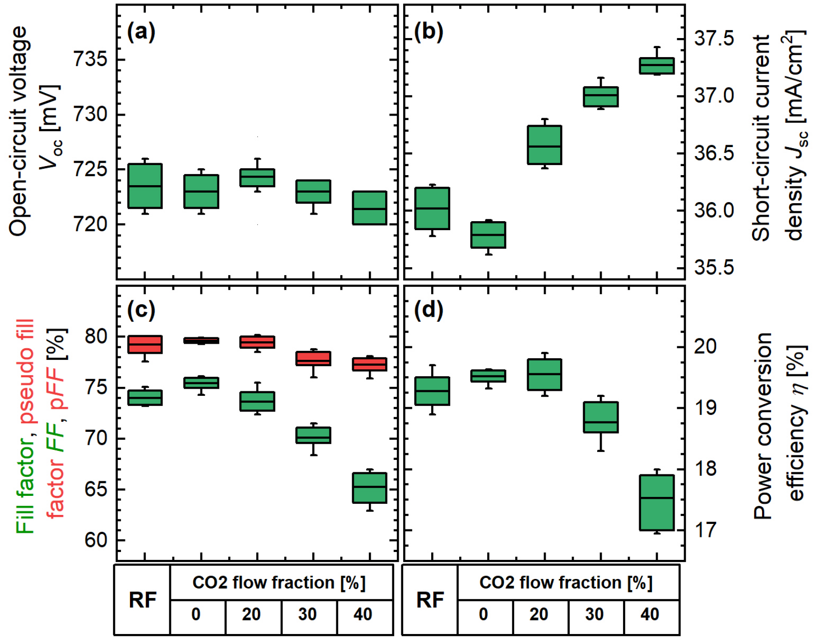

Figure 5.6.: *(a) Open circuit voltage (V_{oc}), (b) short circuit current density (J_{sc}), (c) fill factor (FF), pseudo fill factor (pFF), and (d) power conversion efficiency (η) of the solar cells with the hydrogenated nanocrystalline silicon oxide (nc-SiO$_x$:H) prepared at various CO$_2$ gas flow fraction (f_{CO_2}). The box plots summarize the statistic of more than 4 samples per group and the line is the median position. The solar cells with 7nm a-Si:H(n) layers were fabricated as the reference (RF).*

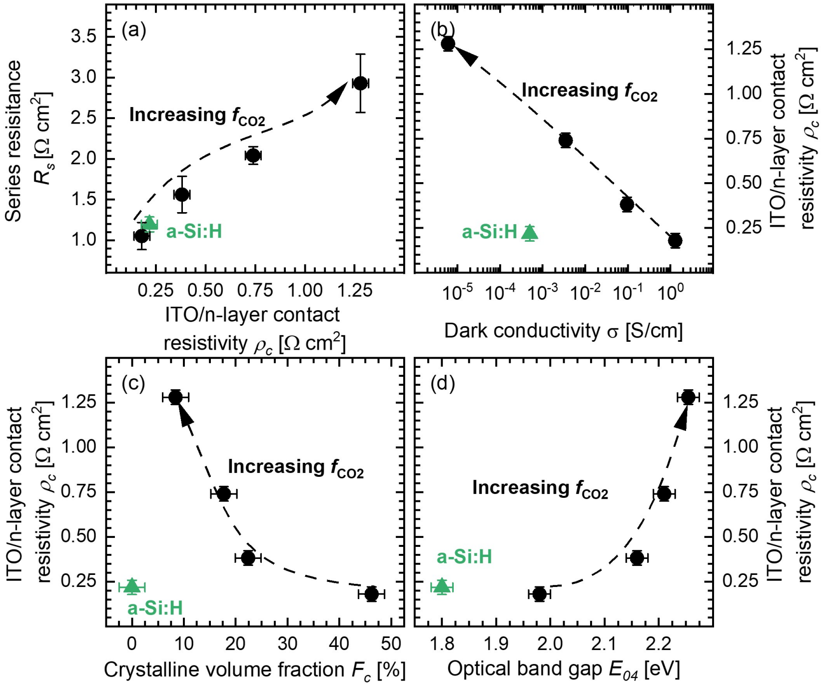

Figure 5.7.: *(a) The effect of the contact resistivity (ρ_c) of ITO/n-layer on series resistance (R_s) of the SHJ solar cells with different n-layer. The contact resistivity as a function of (b) the dark conductivity (σ), (c) the crystalline volume fraction (F_c) and (d) the optical band gap (E_{04}).*

in the nc-SiO$_x$:H films are assumed as the percolation paths for the transport of the charge carriers. More nc-Si phases would contribute to a higher doping concentration in the films, yielding to more conductive nc-SiO$_x$:H(n) layers and lifting the fermi level up to the conduction band edge. Fig. 5.8 shows the band bending diagram of the ITO/nc-SiO$_x$:H(n)/a-Si:H(i)/c-Si(n) structure in the thermal equilibrium, evaluated by the AFORS-HET simulator. The doping concentration and the band gap are named by N_d and E_g, separately. There are band offsets at the ITO/nc-SiO$_x$:H(n) and nc-SiO$_x$:H(n)/a-Si:H(i) interfaces, which could be barriers for the carrier transport. Lower conduction band offset at the nc-SiO$_x$:H(n)/a-Si:H(i) interface and narrower barrier to the electrons are acquired in Fig. 5.8 when in-

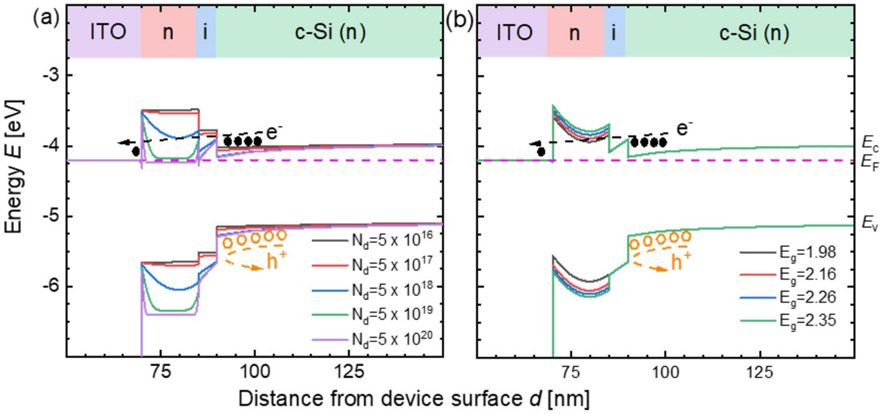

Figure 5.8.: *Energy band diagrams of the ITO/nc-SiO$_x$:H(n)/a-Si:H(i)/c-Si(n) structure in the thermal equilibrium for the nc-SiO$_x$:H(n) at different (a) doping concentration (N_d) and (b) band gap (E_g).*

creasing the doping concentration of nc-SiO$_x$:H. This could promote the tunnelling process of the electron through the silicon films and improve the contact properties. Besides, a higher barrier at the valence band is observed at higher doping concentration, which is beneficial for repelling the holes away from the n-layer. This effect would enhance the selectivity of the electron transport and lead to the reduction of the front contact resistivity. On the other hand, an increased electron affinity and a decreased activation energy of the nc-SiO$_x$:H(n) layers with less oxygen content were reported by Biron et al [213]. The incorporated oxygen in the lattice would shift the conduction band edge up and lower the valence band edge, yielding a wider band gap of the nc-SiO$_x$:H layer. Consequently, a higher conduction band offset on the ITO/n-layer interface is induced, as shown in Fig. 5.8 (b). Therefore, by using nc-SiO$_x$:H(n) layer at lower band gap, a improved contact property is achieved as illustrated in Fig. 5.7 (d).

The external quantum efficiency (EQE), absorptance ($A = 1 - R$) and internal quantum efficiency (IQE) spectra of the devices with various n-layers are displayed in Fig. 5.9. The increased EQE and IQE spectra are found in the wavelength range from 280 to 600nm as varying the $f_{\mathrm{CO_2}}$ from 0% to 40%. The short-circuit current density extracted from the EQE spectra ($J_{\mathrm{sc,EQE}}$) increases upon increasing the E_{04}, as shown in Fig. 5.9 (c)). The $J_{\text{sc,EQE}}$ was calculated via the equation $J_{\text{sc,EQE}} = \int_{280}^{1200} qEQE(\lambda)\Phi_{\text{AM 1.5g}} d\lambda$, where q is the electron charge and $\Phi_{\text{AM 1.5g}}(\lambda)$ is the incident photon flux of the AM1.5g spectrum. There is about 1.6 mA/cm^2 gain of the $J_{\text{sc,EQE}}$ as varying the E_{04} from 2.05eV to 2.25eV by increasing the f_{CO_2} from 0% to 40%. This result is consistent with the trend of the J_{sc} shown in Fig. 5.6 and demonstrates that the increased J_{sc} is due to the wider optical band gap of the nc-SiO$_x$:H films prepared at higher f_{CO_2}. Although the E_{04} of the nc-Si:H layer is higher than the a-Si:H layer, a lower EQE in the wavelength range between 280 and 500nm is observed for devices with nc-Si:H(n) compared to the reference.

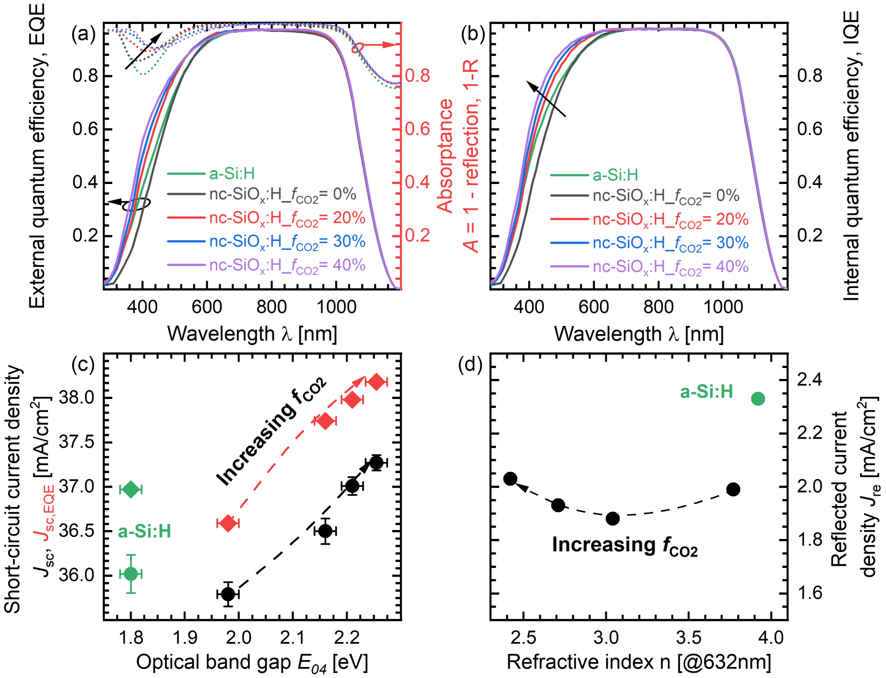

Figure 5.9.: *(a) The external quantum efficiency (EQE), the absorptance ($A = 1 - R$) and (b) the internal quantum efficiency (IQE) spectra of the devices with various n-layers. (c) The short-circuit current density (J_{sc}) and the integrated J_{sc} from the EQE spectra ($J_{sc,EQE}$) versus the optical band gap of the n-layer. (d) The reflected current density (J_{re}) as a function of the n-layer refractive index (n) at the wavelength of 632nm.*

Table 5.2.: *Deposition parameters and material properties of the nc-SiO$_x$:H(n) layers used in the rear junction SHJ solar cells for the PH$_3$ series.*

	f_{CO_2} [%]	f_{SiH_4} [%]	f_{PH_3} [%]	p [mbar]	P [mW/cm^2]	σ [S/cm^2]	F_c [%]	E_{04} [eV]	c_O [%]
P1	20	0.75	0	2.5	80	1.3×10^{-6}	30.2	2.28	22.0
P2	20	0.75	1	2.5	80	1.1×10^{-2}	33.5	2.26	21.0
P3	20	0.75	2	2.5	80	2.8×10^{-1}	39.4	2.25	20.9
P4	20	0.75	4	2.5	80	2.0×10^{-1}	30.2	2.22	20.7
P5	20	0.75	7	2.5	80	2.1×10^{-2}	22.6	2.19	20.2

Consequently, a drop of the $J_{\mathrm{sc,EQE}}$ from 37.0 to 36.6 mA/cm^2 is found. The reason for this contrary is the thickness difference of these cells. A thicker nc-Si:H layer (15nm) is used in devices compared with the reference, where a 7nm a-Si:H layer is integrated. The peak of the absorptance shifts to a higher wavelength when increasing the f_{CO_2}, accompanying with a decreased amplitude. This observation can be interpreted by the change of the nc-SiO$_x$:H refractive index. Fig. 5.9 (d) shows the reflected current density (J_{re}) as a function of the n at the wavelength of 632nm. The J_{re} was calculated via the equation $J_{\mathrm{re}} = \int_{280}^{1200} qR(\lambda)\Phi_{\mathrm{AM\ 1.5g}}(\lambda)d\lambda$, where $R(\lambda)$ is the reflection at certain wavelength. A slight decrease of J_{re} from 2.0 to 1.88 mA/cm^2 is achieved when reducing the n from 3.8 to 3.0. This can be explained by the improved anti-reflection effect caused by the better n matching of the front stack, which progressively increases from air to the c-Si substrate. Further decreasing the n to 2.4 leads to an increase of the J_{re}. This is because the lower refractive index is close to that of the ITO layer. A much higher reflected current density is found for the reference, which could be attributed to the refractive index and the thickness mismatch of the front layers in the reference.

PH$_3$ gas flow fraction

The devices with 15nm nc-SiO$_x$:H(n) prepared at various PH$_3$ gas flow fraction were fabricated on the quartered M2 wafer. Tab. 5.2 summarizes the detailed deposition parameters and the corresponding material properties of the nc-SiO$_x$:H(n) layers used in this series. The CO$_2$ gas flow fraction was kept constant at 20% and the $f_{\mathrm{PH_3}}$ was varied from 0% to 7%. The cell performance is shown in Fig. 5.10.

There is no obvious change of iV_{oc} when varying $f_{\mathrm{PH_3}}$. Therefore, one conclusion can be drawn that the passivation quality of the a-Si:H(i)/nc-SiO$_x$:H(n) stacks is independent on the $f_{\mathrm{PH_3}}$ in this series. For the solar cells with the non-doped nc-SiO$_x$:H(n), the value of the V_{oc}, J_{sc}, pFF and FF are the lowest, as well as the η. The bad cell performance could be due to the large loss of the Schottky barrier at the non-doped nc-SiO$_x$:H/ITO interface, which is demonstrated by the following TLM result (see Fig. 5.11). When increasing the $f_{\mathrm{PH_3}}$ from 1% to 7%, the V_{oc} is unaffected but the J_{sc} decreases by 0.2 mA/cm^2, which could be ascribed to the

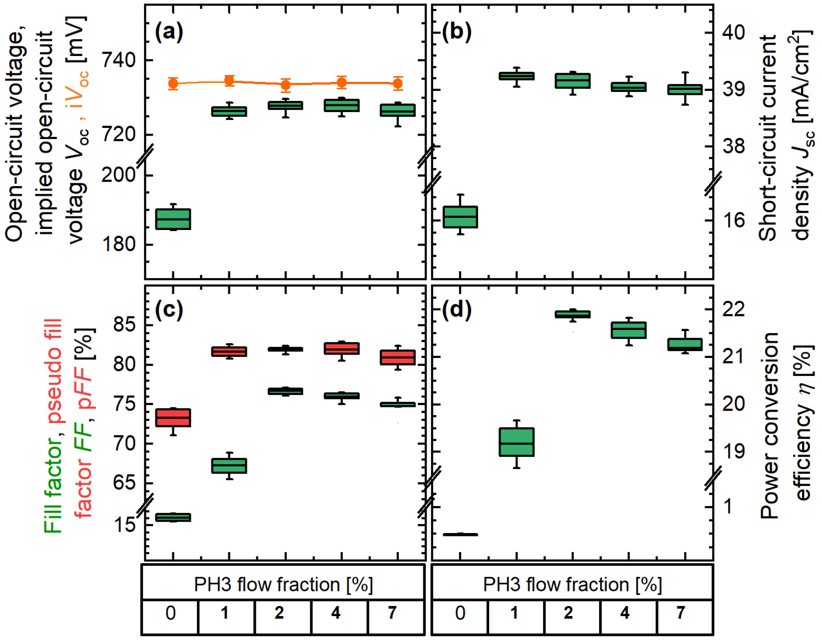

Figure 5.10.: *(a) Open-circuit voltage (V_{oc}), implied open-circuit voltage, (b) short-circuit current density (J_{sc}), (c) fill factor (FF), pseudo fill factor (pFF), and (d) power conversion efficiency (η) of the solar cells with the nc-SiO$_x$:H(n) layer prepared at various PH$_3$ gas flow fraction. The box plots summarize the statistic of more than 4 samples per group and the line is the median position.*

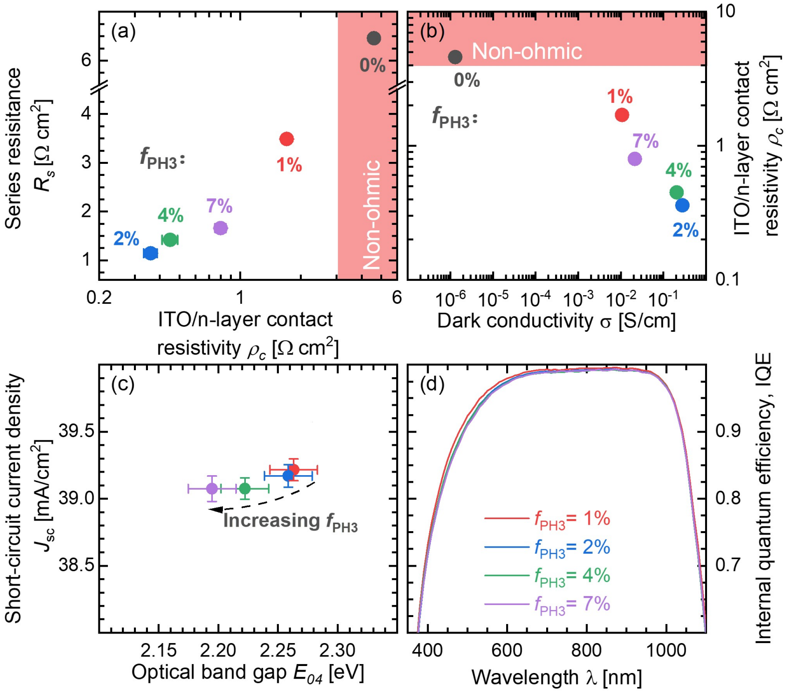

Figure 5.11.: *(a) The relationship between the series resistance (R_s) and the contact resistivity (ρ_c) of the ITO/n-layer. (b) The ρ_c as a function of the dark conductivity (σ) of the nc-SiO$_x$:H layers. (c) The short-circuit current density (J_{sc}) versus the optical band gap of the n-layer. (d) The internal quantum efficiency (IQE) spectra of the devices with the nc-SiO$_x$:H(n) prepared at various phosphine gas fraction (f_{PH_3}).*

reduction of the E_{04} or the increased losses related to the free-carrier absorption in the nc-SiO$_x$:H layer. As rising the PH$_3$ gas fraction from 0% to 2%, an increase of the FF from 15.8% to 76.9% is illustrated in Fig. 5.10 (c). However, around 1.8%$_{\text{abs}}$ reduction of the FF is observed when further increasing the f_{PH_3} from 2% to 7%. As a result, the best cell performance in this series is achieved at 2% of f_{PH_3}, exhibiting V_{oc} of 728 mV, FF of 76.7%, J_{sc} of 39.1 mA/cm^2 and η of 21.83%. We can see a dramatic improvement of the cell performance in the PH$_3$ series, especially the J_{sc} and FF, compared with that of CO$_2$ series. This improvement is due to the optimization of the cleaning process and the metallization of electrodes.

The correlation between the opto-electronic properties of the nc-SiO$_x$:H(n) and the relevant cell performance is displayed in Fig. 5.11. Higher series resistance is found for the cells with a higher ITO/nc-SiO$_x$:H(n) contact resistivity. This observation reveals that the change of the FF in Fig. 5.10(c) is mainly attributed to the variation of the ITO/nc-SiO$_x$:H(n) contact resistivity. An extremely high value of ρ_c is observed for the devices with the non-doped nc-SiO$_x$:H as the window layer, revealing a non-ohmic contact on the front side of the devices. A reduction of ρ_c from 4.6 to 0.36 Ω cm^2 is found when increasing f_{PH_3} from 0% to 2%. This indicates that the contact transfers from non-ohmic to ohmic when adding few P dopants ($f_{PH_3} < 2\%$) into the nc-SiO$_x$:H(n) layers. Further increasing f_{PH_3} from 2% to 7% results in an increase of ρ_c, which is in good agreement with the dark conductivity of nc-SiO$_x$:H(n). Fig. 5.11 (b) illustrates a reduced ρ_c with the increased σ. This result could be assigned to the increase of the active doping concentration in the nc-SiO$_x$:H(n), which could lift the fermi level up to the conduction band edge and help to reduce the barriers on the conduction band. Thus, a improved tunnelling probability of the electrons from c-Si to ITO may be acquired. The relationship between the J_{sc} of the solar cells and the optical band gap of the nc-SiO$_x$:H(n) layer used in this series is shown in Fig. 5.11 (c). A lower J_{sc} is found for the cells with a decreased optical band gap of nc-SiO$_x$:H(n) layer. This is explained by the increased parasitic absorption in the nc-SiO$_x$:H(n) films as illustrated in Fig. 5.11 (d). No noticeable change of the IQE in the long wavelength is observed when varying the f_{PH_3} from 1% to 7%. Therefore, the drop of the J_{sc} observed in Fig. 5.10 is not the consequence of the optical losses related to the free carrier absorption in nc-SiO$_x$:H(n) layer [16].

5.3. Power loss analysis

In this section, a detailed power loss analysis for the best performed SHJ solar cell in Sec. 5.2.2 has been conducted by the Quokka3 simulation tool. The detailed IV parameters of this cell are listed in Tab. 5.3. The front and rear view of a symmetry element of the whole solar cell for the Quokka3 simulation are shown in Fig. 5.12. The symmetry element of the whole solar cell is a quarter of the cell.

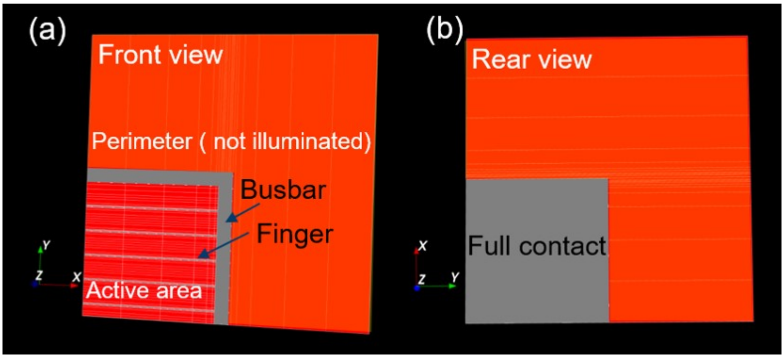

Figure 5.12.: *(a) The front and (b) rear view of a symmetry element of the whole solar cell fabricated on a quartered M2-sized wafer, including the busbar (located outside the active area) and the dark perimeter, as simulated in 3D with Quokka3.*

Table 5.3.: *Comparison of the experimental and the simulated IV parameters of the champion cell mentioned in Sec. 5.2.2.*

	V_{oc} [mV]	J_{sc} [mA/cm^2]	FF [%]	η [%]
Experiment	726.9	39.12	77.09	21.92
Simulation	727	39.16	77.01	21.92

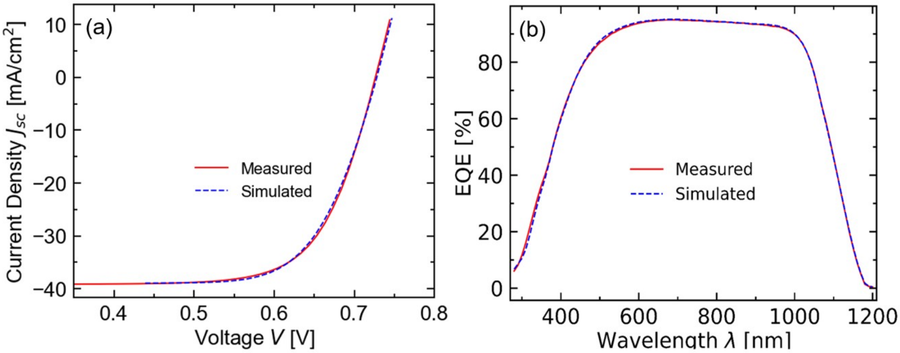

Figure 5.13.: *(a) The IV curve and (b) the external quantum efficiency (EQE) comparison between the results obtained by the measurement and the Quokka3 simulation.*

The busbar is located outside the active cell area and the perimeter with the a-Si:H(i)/nc-SiO$_x$:H(n) stack is not illuminated. The main input parameters for the simulation are derived from the dedicated test structure and summarized in Tab. 5.4. The specific contact resistivity of Ag/ITO, ITO/nc-SiO$_x$:H and ITO/a-Si:H were determined by TLM, the details of which can be found in Sec. 3.3. The grid finger and busbar line resistance were determined at the dedicated metal structure, as shown in Fig. 5.2. To calculate the generation rate, a lumped parameter optical model, named Text-Z model, was used in Quokka3 simulator [155]. The input lumped parameters of the front layer stacks, such as the surface transmission T, reflectance R and absorptance A, were extracted from the OPAL 2 simulator based on the refractive index and the extinction coefficient of ITO, nc-SiO$_x$:H(n) and a-Si:H(i) layer. The pathlength enhancement Z was parameterized based on the experimental EQE and R data. The fitting parameters of the Text-Z model are also listed in Tab. 5.4. The sheet resistance of the ITO layer was measured by the four point probe measurement. In order to determine the surface passivation quality, the lifetime samples with the symmetrical structures (i/n or i/p) were prepared. The S_{eff} values were extracted from injection-dependent effective lifetime τ_{eff} data, details of which can be found in Sec. 3.3.

Table 5.4.: *Main input parameters for the Quokka3 device simulation.*

Bulk properties:		Optical model:	
Wafer thickness W	170 µm	T$_{\text{ext}}$-Z model	Z$_0$=17
Base resistivity ρ	1.2 Ωcm	parameters	Z$_{\text{inf}}$=1.6
Bulk lifetime τ_{bulk}	5000 µs		Z$_{\text{p}}$=1.3
Front skin:		**Rear skin:**	
Sheet resistance R_{SH}	260 Ω	Sheet resistance R_{SH}	260 Ω
Recombination velocity S_{eff}	1.5 cm/s	Recombination velocity S_{eff}	3.0 cm/s
Resistivity $\rho_{\text{c,front}}$	0.36 Ω cm^2	Resistivity $\rho_{\text{c,rear}}$	0.5 Ω cm^2
Front metal grid:		**Rear metal contact:**	
Finger pitch	1730 µm	Contact geometry	Rectangle
Finger width	65 µm	Contact size	Full area
Contact resistivity	0.003 Ω cm^2	Contact resistivity	0.003 Ω cm^2

As shown in Fig. 5.13 and Tab. 5.3, our simulations simultaneously match the IV parameters and the external quantum efficiency of the fabricated cell, demonstrating that a highly predictive model is achieved. The power losses of the investigated cell were quantify by the free energy loss analysis (FELA) approach. This method is extended with approximate optical power losses by multiplying the respective current density loss with the maximum power point voltage and implemented in Quokka3 [214]. The resulting power loss breakdown is plotted in Fig. 5.14. The optical losses related to the shading, front transmission and imperfect light trapping are responsible for 61% of the total losses, which has the dominating potential for the improvement of the cell performance. As shown in Fig. 5.14 (b), shading

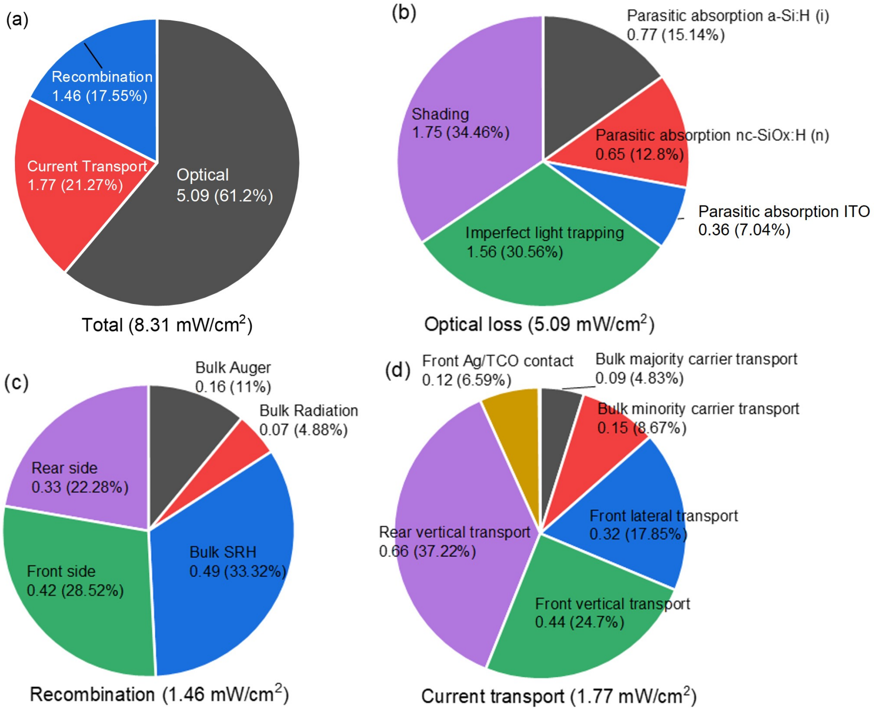

Figure 5.14.: *(a) Total, (b) optical, (c) recombination and (d) current transport related power loss breakdown of the fabricated solar cell with the nc-SiO$_x$:H(n) layer prepared at 20% of f_{CO_2} and 2% of f_{PH_3}.*

is the leading optical loss, followed by the escape of the light at the front due to imperfect light trapping. The losses associated with the parasitic absorption in a-Si:H(i), nc-SiO$_x$:H(n) and ITO layers are 0.77 mW/cm^2, 0.65 mW/cm^2 and 0.36 mW/cm^2, respectively. On the electrical side, the losses can be categorized into the current transport and the recombination. The largest contributor to the recombination losses is the SRH recombination in the wafer bulk, which could be assigned to the active impurities within the wafer. This loss could be reduced by using wafers with better quality. The recombination at the passivated region of the front surface (0.48 mW/cm^2) is more than that of the rear surface (0.33 mW/cm^2). This result indicates that improving the passivation quality of the front a-Si:H(i)/nc-SiO$_x$:H(n) stack is on a higher priority than that of the a-Si:H(i)/a-Si:H(p) at the rear side for the optimization of our devices. It is notable that a larger loss related to the front recombination is observed in Fig. 5.14, although a higher S_{eff} was assumed (see Tab. 5.4). This result is due to the higher total number of the carriers that suffer from the recombination, as a consequence of the higher excess carrier density at the front. Fig. 5.14 (d) reveals that the main current transport loss originates from the rear and front vertical transport. Besides, The front lateral transport and the front Ag/TCO contact account for 0.32 mW/cm^2 and 0.12 mW/cm^2 in power,

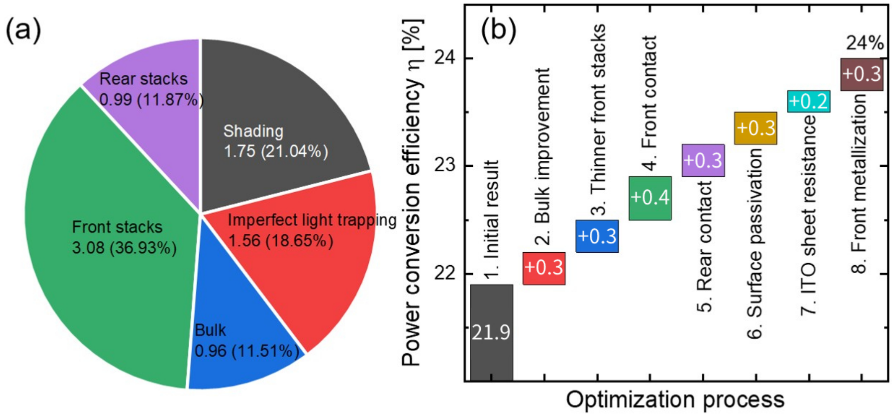

Figure 5.15.: *(a) Power loss breakdown of the fabricated solar cell with nc-SiO$_x$:H(n) prepared at 20% of f_{CO_2} and 2% of f_{PH_3}. (b) Roadmap for SHJ solar cells to 24%.*

Table 5.5.: *Comparison of the main input parameters for the Quokka3 device simulation of the solar cell before (Initial) and after optimized (Opti).*

	τ_{bulk} [ms]	$d_{\text{nc-SiOx:H}}$ [nm]	$d_{\text{a-Si:H,front}}$ [nm]	$\rho_{\text{c,front}}$ [Ω cm^2]	$\rho_{\text{c,rear}}$ [Ω cm^2]	S_{eff} [cm/s]	R_{SH} [Ω]	Finger width [µm]
Initial	6	15	6	0.36	0.5	1.5	260	65
Opti	20	10	4	0.1	0.2	0.8	160	45

respectively.

It appears that the bottleneck limiting the cell performance of our current SHJ solar cells is the property of the front stacks, as illustrated in Fig. 5.15 (a). By means of the Quokka3 simulation, the cell performance improvement have been estimated and a road-map for our SHJ solar cells is plotted in Fig. 5.15 (b). It is expected that the cell efficiency can reach 24% after optimizations. The comparison of the electro-optical input parameters for the initial and optimized SHJ solar cells are listed in Tab. 5.5. The losses related to the SRH recombination in the wafer bulk can be reduced by using wafers with better quality. About 0.3%$_{\text{abs}}$ improvement of η is estimated by Quokka3 simulator if we integrate 10nm nc-SiO$_x$:H(n) and 4nm a-Si:H(i) in the cells instead of 15nm nc-SiO$_x$:H(n) and 6nm a-Si:H(i). Decreasing the thickness of nc-SiO$_x$:H(n) and a-Si:H(i) layer is a simple way to reduce the optical losses related to the parasitic absorption, which will be introduced in Sec. 6.1.1 and Sec. 6.2. The losses due to the vertical current transport is attributed to the contact properties of the layer stacks and electrodes on both sides. To reduce these losses lower contact resistivity of the TCO layer and the doped layer or electrode should be achieved. The Quokka3 simulation results demonstrate that the increase of η is about 0.7%$_{\text{abs}}$ if we can decrease $\rho_{\text{c,front}}$ from 0.36 to 0.1 Ω cm^2 and $\rho_{\text{c,rear}}$ from 0.5 to 0.2 Ω cm^2. Using multi-layer, such as nc-Si:H(n)/nc-SiO$_x$:H(n) or a-Si:H(n)/nc-SiO$_x$:H double layer, as ETL is one way to optimize the contact properties of TCO/n-layer, which will be shown in Sec. 6.1.2. Additionally, the application of the innovative TCO material could be another option to improve the contact properties on both side as well as to reduce the losses related to the lateral current transport. About 0.3%$_{\text{abs}}$ improvement of η is found in Fig. 5.15 (b) when reducing S_{eff} from 1.5 to 0.8 cm/s. One strategy to enhance the surface passivation provided by a-Si:H(i) is the usage of the hydrogen plasma treatment during the deposition of a-Si:H(i) layer and another method is to increase the doping concentration of the nc-SiO$_x$:H(n) layer, which will be presented in Sec. 6.2. Besides, the optical losses due to the shading of electrode on the front can be reduced by adjusting the finger width and finger pitch. It is worth noting that the optimization is always a trade-off between the optical and electrical losses, while for simplification we only take one of them into account when calculating the potential of the performance improvement.

6. Optimization of SHJ solar cells with nc-SiO_x:H(n) layer

In the Sec. 5.3, it has been demonstrated that the dominant power loss for the best solar cell with the nc-SiO_x:H(n) layers in our preliminary study is related to the properties of the front stacks. By varying the value of the input parameters in Quokka3 simulator, such as the front contact resistivity, the transmission of the ITO/nc-SiO_x:H(n)/a-Si:H(i) stacks, the sheet resistance of the ITO and the surface recombination velocity etc., a potential to 24% of the power conversion efficiency is expected. In this section, we focus on the optimization of the front stacks of the SHJ solar cells. Besides, several strategies were used to improve the cell performance. The SHJ solar cells with the nc-SiO_x:H(n) single layer, the a-Si:H(n)/nc-SiO_x:H(n) or nc-SiO_x:H(n)/nc-Si:H(n) multi-layer at different thickness were fabricated. The influence of those structures on the cell performance is presented in the first part of this chapter. The second part describes the optimization of the a-Si:H(i) layer by introducing H_2 plasma treatment during the a-Si:H(i) depositions as well as adjusting the layer thickness. In the third part, different kinds of TCO layers were integrated in the devices with the nc-SiO_x:H single layers. The fourth part presents a detailed Quokka3 simulation on the perimeter recombination in the quarter-M2-sized solar cells. Lastly, the SHJ solar cells with the optimized intrinsic a-Si:H, ITO, a-Si:H(p) and ETL structure were fabricated on the full-size M2 wafers. An optimization for the full-size solar cells with 5 nm nc-Si:H(n) is carried out by increasing the F_c of the nc-Si:H(n) layer. Meanwhile, the effect of the sputtering process on the passivation quality and the device performance are investigated.

6.1. Optimization of nc-SiO$_x$:H(n) layer

This section deals with the optimization of the nc-SiO$_x$:H(n) layers in the SHJ solar cells. A straightforward way to improve cell performance is decreasing the thickness of nc-SiO$_x$:H(n) layer as a consequence of the reduced parasitic absorption in nc-SiO$_x$:H(n). However, the crystalline growth of nc-SiO$_x$:H(n) layer is substrate selective and thickness dependent. The crystalline process often starts after a certain amorphous incubation layer. [51, 215–217]. Depositing nc-SiO$_x$:H upon a nc-Si:H seed layer has been suggested to induce a fast nucleation of crystallites, thereby resulting in a ultra-thin nc-SiO$_x$:H layer with a higher crystalline volume fraction [218–221]. Besides, S. Kirner et al. found that the contact property of TCO layer and p-type nc-SiO$_x$:H layer can be improved by inserting a p-type nc-Si:H contact layer between TCO and nc-SiO$_x$:H layers [50]. L. Mazzarella et al. applied a nc-Si:H(n) contact or seed layer in the solar cells with the nc-SiO$_x$:H(n) layer at

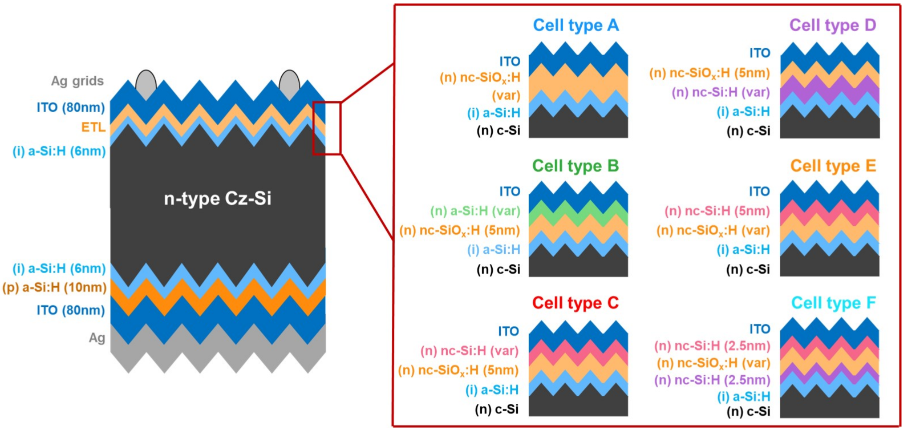

Figure 6.1.: *Schematic cross-section of the rear-junction SHJ solar cells with six different electron transport layer (ETL) stacks: the nc-SiO$_x$:H(n) single layer (cell type A); the a-Si:H(n) contact layer and 5 nm nc-SiO$_x$:H(n) (cell type B); the nc-Si:H(n) contact layer and 5 nm nc-SiO$_x$:H(n) (cell type C); the nc-Si:H(n) seed layer and 5 nm nc-SiO$_x$:H(n) (cell type D); the 5 nm nc-Si:H(n) contact layer and nc-SiO$_x$:H(n) (cell type E); and the 2.5 nm nc-Si:H(n) contact layer, nc-SiO$_x$:H(n) and 2.5 nm nc-Si:H(n) seed layer (cell type F).*

different thickness. They compared the performance of different cells and found that applying nc-Si:H(n) seed layer below nc-SiO$_x$:H(n) is beneficial for the improvement of cell performance [221]. In this work, the solar cells with six kinds of ETL structure were prepared and compared to have a knowledge on the carrier transport mechanism in SHJ devices and to optimize the front contact properties. The schematic illustrations of these devices are shown in Fig. 6.1, where the variation of the ETL thickness is indicated. Cell type A has the ETL consisting of the nc-SiO$_x$:H(n) single layer, the thickness of which is varied from 5 to 20 nm. Cell type B, C, D and E has the ETL stack consisting of the a-Si:H(n)/nc-SiO$_x$:H(n) or nc-SiO$_x$:H(n)/nc-Si:H(n) double layer. In Cell type B, the ETL stack includes 5 nm nc-SiO$_x$:H film and the a-Si:H(n) at various thickness, tuned from 0 to 4 nm. The thickness of nc-SiO$_x$:H(n) film is fixed at 5 nm in Cell type C and D, while that of nc-Si:H(n) is varied from 0 to 10 nm. In Cell type E, the thickness of nc-Si:H(n) is fixed at 5nm and that of nc-SiO$_x$:H(n) is changed from 0 to 10 nm. Cell type F has the ETL stack consisting of nc-Si:H(n)/nc-SiO$_x$:H(n)/nc-Si:H(n) triple layer, where the thickness of both nc-Si:H layers is kept constant at 2.5 nm but that of nc-SiO$_x$:H(n) film is varied from 0 to 7 nm. The deposition parameters and the material properties of the silicon films at thickness of 30∼40 nm are summarized in Tab. 6.1. The deposition condition of the nc-SiO$_x$:H(n) layer used in this section is same as the one used in the best performed solar cell in the preliminary study (see Sec. 5.3).

Table 6.1.: *Deposition parameters and material properties of the n-type silicon layers for the SHJ solar cells. The thickness of the layers used for the material property characterization is 30∼40 nm.*

n-layer type	$f_{\mathrm{CO_2}}$ [%]	$f_{\mathrm{SiH_4}}$ [%]	$f_{\mathrm{PH_3}}$ [%]	p [mbar]	P [W]	σ [S/cm^2]	F_c [%]	E_{04} [eV]	n @ 632 nm
a-Si:H	0	8.3	2	2.5	80	3.4×10^{-4}	0	1.81	4.08
nc-Si:H	0	0.75	2	2.5	200	1.3	49	1.98	3.78
nc-SiO$_x$:H	25	0.75	2	2.5	200	0.28	39.4	2.16	3.12

6.1.1. nc-SiO$_x$:H single layer

To quantify the optical loss due to the parasitic absorption in nc-SiO$_x$:H layer, we calculated the current density loss (J_{abs}) via Eq. 6.1:

$$J_{\mathrm{abs}} = \int_{300}^{1200} qA(\lambda)\Phi_{\mathrm{AM1.5g}}(\lambda)d\lambda, \tag{6.1}$$

where q, $\Phi_{\mathrm{AM1.5g}}(\lambda)$, λ and $A(\lambda)$ are the elementary charge, the incident photon flux of AM1.5g spectrum, the wavelength and the spectral absorptance in the nc-SiO$_x$:H(n) layer, respectively. Based on Beer-Lambert absorption law, the $A(\lambda)$ can be calculated by the equation: $A(\lambda) = 1 - e^{-\alpha(\lambda)d_{\text{nc-SiOx:H}}}$, where $d_{\text{nc-SiOx:H}}$ is the thickness of nc-SiO$_x$:H(n) layer and $\alpha(\lambda)$ is the absorption coefficient. The $\alpha(\lambda)$ can be evaluated from the k measured by the spectroscopy ellipsometry: $\alpha(\lambda) = \frac{4\pi k(\lambda)}{\lambda}$. The spectral absorptance in 7 nm a-Si:H(n) layer or in the nc-SiO$_x$:H(n) layer at various thickness (5∼20 nm) is displayed in Fig. 6.2 (a), where the corresponding current density loss can also be found. Compared with the a-Si:H(n), the absorption of nc-SiO$_x$:H(n) is much lower in the range between 500 and 600 nm. As a result, there is more than 1.0 mA/cm^2 reduction of the J_{abs} when replacing 7 nm a-Si:H with 7 nm nc-SiO$_x$:H layer. About 0.7 mA/cm^2 decline of the J_{abs} can be acquired by decreasing the thickness of nc-SiO$_x$:H(n) layer from 15 to 5 nm. The SHJ solar cells with nc-SiO$_x$:H(n) layer at various thickness (cell type A) were fabricated.

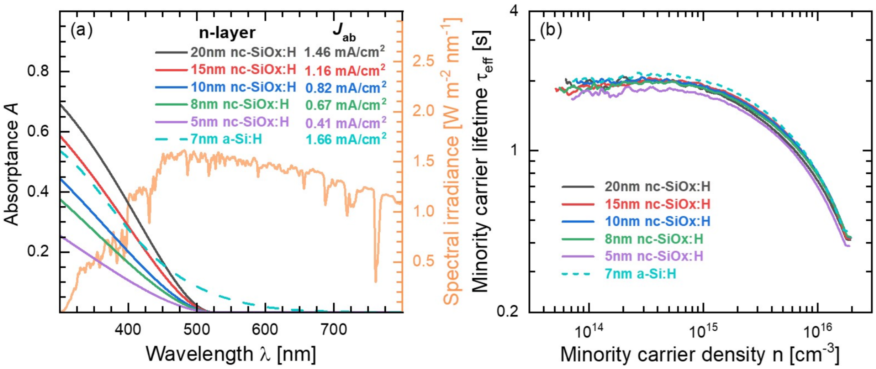

Figure 6.2.: *(a) Absorptance of the a-Si:H(n) and nc-SiO$_x$:H(n) layers at different thickness. (b) Minority carrier lifetime (τ_{eff}) curve of the solar cells with different n-layers, measured after the PECVD depositions.*

Fig. 6.2 (b) shows the quasi steady-state photo conductance (QSSPC) results measured after the PECVD depositions. The lifetime curves of all samples are similar, except the one with 5 nm nc-SiO$_x$:H(n), which is slightly lower. This could be due to the worse field-effect passivation induced by the thinner doped layer.

The IV parameters of the solar cells with the nc-SiO$_x$:H single layer at different thickness ($d_{\text{nc-SiOx:H}}$) are shown in Fig. 6.3. The box plot summarizes the statistic of 8 ∼ 10 cells per group. The cells with 7 nm a-Si:H(n) are used as the reference for this series. When decreasing the $d_{\text{nc-SiOx:H}}$ from 20 to 10 nm the V_{oc} is unaffected, but decreases when $d_{\text{nc-SiOx:H}}$ is below 10 nm. The iV_{oc} of the cell type A are on the same level as the reference. Fig. 6.3(b) shows that the J_{sc} increases with decreasing the $d_{\text{nc-SiOx:H}}$ by 0.058 mA cm^{-2}/nm and the gain of the J_{sc} is 0.4 ∼ 1.4 mA/cm^2 compared with the reference. Fig. 6.3(c) shows that the FF decreases when reducing

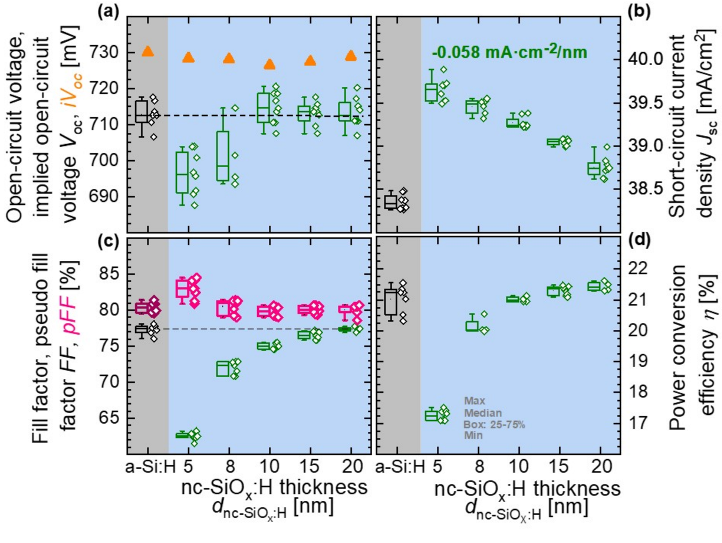

Figure 6.3.: *(a) Open circuit voltage (V_{oc}) and implied open circuit voltage (iV_{oc}), (b) short circuit current density (J_{sc}), (c) fill factor (FF), pseudo fill factor (pFF), and (d) power conversion efficiency (η) of the solar cells with the nc-SiO$_x$:H(n) at different thickness ($d_{nc\text{-}SiOx:H}$). The box plots summarize the statistic of more than four samples per group and the line is the median position. The solar cells with 7 nm a-Si:H(n) layer were fabricated as the reference.*

$d_{\text{nc-SiOx:H}}$. Besides, the FF is more sensitive to the variation of $d_{\text{nc-SiOx:H}}$ when it is below 10 nm. Furthermore, there is an increase of the difference between pFF and FF, which reveals an increase of the R_s when reducing the $d_{\text{nc-SiOx:H}}$. Although the η of the solar cell with 5 nm nc-SiO$_x$:H layer is lower than the others (see Fig. 6.3(d)), a high J_{sc} of 39.9 mA/cm^2 and similar iV_{oc} as the reference are obtained, which indicates a potential to reach a high efficiency if a low series resistance could be kept.

Fig. 6.4 (a) shows the current density as a function of the voltage (J-V curve) of the solar cells with 7 nm a-Si:H(n) or the nc-SiO$_x$:H(n) layers at different thick-

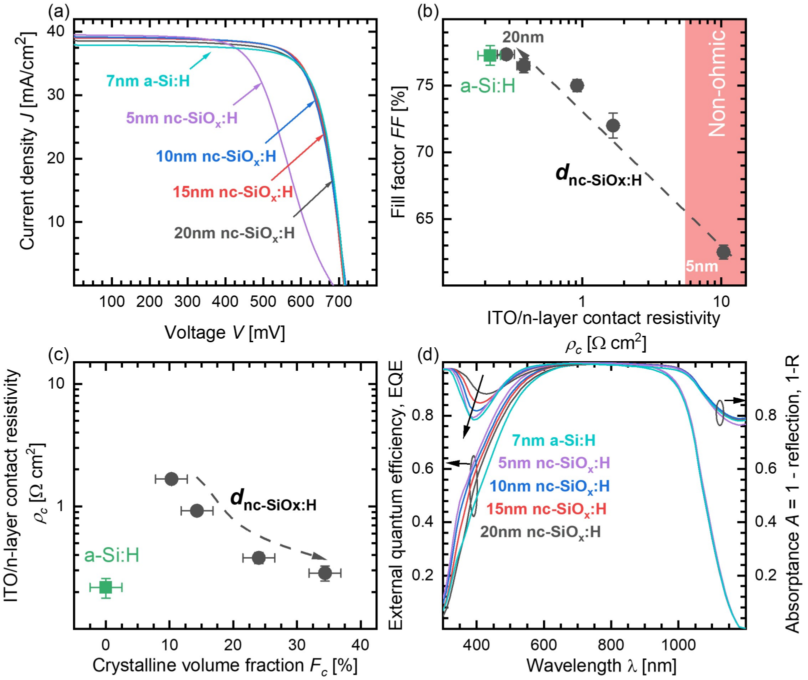

Figure 6.4.: *(a) The current density as a function of the voltage (J-V curve), (b) the effect of the contact resistivity (ρ_c) of the ITO/n-layer on the fill factor (FF)), (c) the crystalline volume fraction (F_c) versus the ρ_c, (d) the external quantum efficiency (EQE) and the absorptance ($A = 1 - R$) spectra of the devices with the ncSiO(n) at different thickness. The solar cells with 7 nm a-Si:H(n) layer were fabricated as the reference.*

ness. The solar cell with 5 nm nc-SiO$_x$:H(n) has an s-shaped J-V curve resulting in a low FF and a low V_{oc}, which cannot be observed for the solar cells with thicker nc-SiO$_x$:H(n) layers. The s-shaped J-V curve for the solar cell with 5 nm nc-SiO$_x$:H(n) layer might be related to the electrical transport barrier on the front side, which is demonstrated by the TLM results shown in Fig. 6.4 (b) and (c). A significant increase of the ITO/n-layer contact resistivity (ρ_c) is observed when reducing the thickness of nc-SiO$_x$:H(n) layer from 20 to 5 nm, resulting in a reduction of FF from 77% to 63%. During the deposition process of nc-SiO$_x$:H, a certain amorphous phase appears firstly as the nucleation of the crystalline phase, then the epitaxial growth is followed [51, 215–217]. Decreasing the thickness of nc-SiO$_x$:H layer leads to a layer with lower crystalline volume fraction, as shown in Fig. 6.4(c), giving rise to a shift of the Fermi level to the valence band edge and an increase of E_a, as reported in ref. [222]. Therefore, for the cells with thinner nc-SiO$_x$:H(n) layer the conduction band offset at ITO /nc-SiO$_x$:H(n) interface might be higher than the solar cells with thicker nc-SiO$_x$:H(n) layer, which may act as a Schottky barrier for the electrons and lead to the lower FF and the higher contact resistivity. Fig. 6.4(d) shows the external quantum efficiency and absorptance as a function of the wavelength for solar cells with 7 nm a-Si:H(n) or the nc-SiO$_x$:H(n) at different thickness. The solar cells with nc-SiO$_x$:H(n) show a higher EQE in the wavelength range from 300 to 600 nm compared with the cells with a-Si:H(n). The EQE for the solar cells with thinner nc-SiO$_x$:H layer increases as expected thanks to a reduced parasitic absorption. Additionally, the absorptance decreases for the cells with thinner nc-SiO$_x$:H layer, which is the consequence of the increased reflection. This provides an additional chance to further increase theJ_{sc} by tuning the anti-reflection coating thickness in further investigations.

6.1.2. nc-SiO$_x$:H multi-layer

The experimental optical data of the a-Si:H(i), nc-SiO$_x$:H(n), a-Si:H(n), nc-Si:H(n) and ITO layers used in this work was input into OPAL2 simulator for the computational analysis, details of which can be found in Sec. 3.4. The simulations were performed on a pyramidal surface morphology. The comparison of the simulated photocurrent density loss due to the light absorbed and reflected (J_{re}) in different

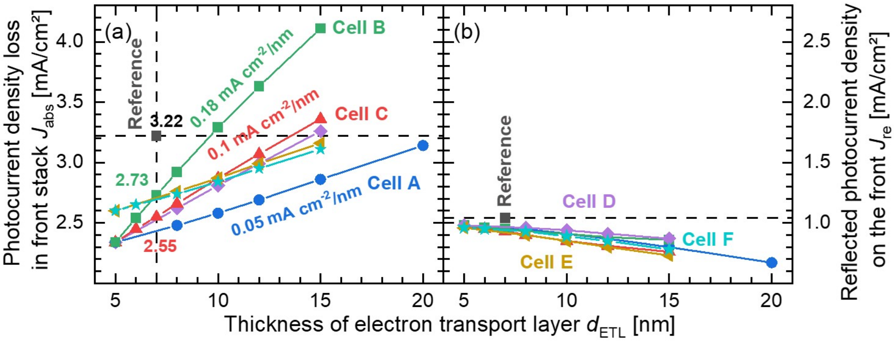

Figure 6.5.: *Photocurrent density loss due to the light (a) absorbed (J_{abs}) and (b) reflected (J_{re}) in the front multi-layer stack of different solar cells versus the thickness of electron transport layer (d_{ETL}). Solar cells with six kinds of ETL structure were fabricated, the cross sectional sketch of which can be found in Fig. 6.1. The Cell A has an ETL consisting of nc-SiO$_x$:H(n) single layer. The Cell B is with the a-Si:H(n) contact layer and 5 nm nc-SiO$_x$:H(n) layer on the front. The Cell C is with the nc-Si:H(n) contact layer and 5 nm nc-SiO$_x$:H(n) layer. The Cell D is with 5 nm nc-SiO$_x$:H(n) and the nc-Si:H(n) seed layer. The Cell F is with 2.5 nm nc-Si:H(n) contact and seed layer, and the nc-SiO$_x$:H(n) layer. The reference are cells with 7 nm a-Si:H(n) layer.*

multi-layer stacks on the front is shown in Fig. 6.5. Solar cells with 7nm a-Si:H(n) were fabricated as the reference.

The value of the current density parasitically absorbed by the front stack increases almost linearly for the six kinds of solar cells when increasing the ETL thickness. The J_{abs} increases by 0.05 mA cm^{-2}/nm for the Cell A, 0.18 mA cm^{-2}/nm for the Cell B and 0.1 mA cm^{-2}/nm for the Cell C. The Cell B is much more sensitive to the variation of d_{ETL}, while the curve of the Cell A is the most moderate among these six kinds of cells. The reason for the difference is the different material used in the cells. The film at various thickness is nc-SiO$_x$:H(n) for the Cell A, a-Si:H(n) for the Cell B and nc-Si:H(n) for the Cell C. As listed in Tab. 6.1, the E_{04} of the a-Si:H is 1.81 eV, which is much lower than that of the nc-Si:H (1.98 eV) and the nc-SiO$_x$:H (2.16 eV). The horizontal black dash line is where the J_{abs} equals to the reference. The d_{ETL} needed to achieve a similar J_{abs} as the reference is about 21 nm for the Cell A, whereas it is about 9 nm for the Cell B, 14 nm for the Cell C, 15 nm for the Cell D and 16 nm for the Cell E and Cell F. The vertical black dash line is where the d_{ETL} is same as the reference. By replacing 7 nm a-Si:H(n) with 5 nm nc-SiO$_x$:H(n)/ 2 nm a-Si:H(n) double layer, around 0.5 mA/cm^2 reduction of the parasitic absorption loss can be acquired, which is 0.7 mA/cm^2 for the cells with 5 nm nc-SiO$_x$:H(n)/ 2 nm nc-Si:H(n) double layer. At the same d_{ETL}, the parasitic

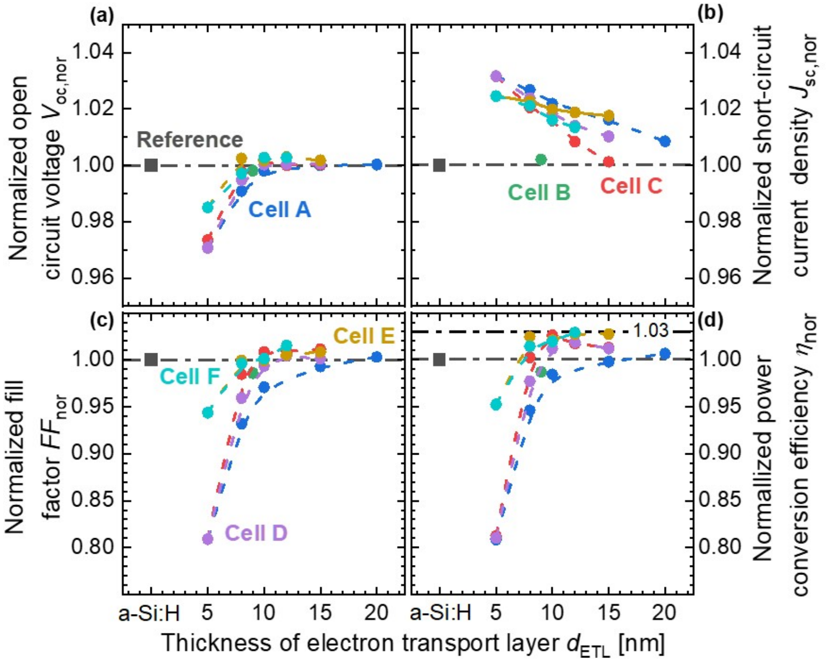

Figure 6.6.: *(a) Normalized open-circuit voltage ($V_{oc,nor}$), (b) short-circuit current density ($J_{sc,nor}$), (c) fill factor (FF_{nor}), and (d) power conversion efficiency (η_{nor}) of the solar cells with various electron transport layer (ETL) at different thickness (d_{ETL}). Solar cells with six kinds of ETL structure were fabricated, the cross sectional sketch of which can be found in Fig. 6.1. The Cell A has an ETL consisting of nc-SiO$_x$:H(n) single layer. The Cell B is with the a-Si:H(n) contact layer and 5 nm nc-SiO$_x$:H(n) layer on the front. The Cell C is with the nc-Si:H(n) contact layer and 5 nm nc-SiO$_x$:H(n) layer. The Cell D is with 5 nm nc-SiO$_x$:H(n) and the nc-Si:H(n) seed layer. The Cell F is with 2.5 nm nc-Si:H(n) contact and seed layer, and the nc-SiO$_x$:H(n) layer. The reference are the solar cells with 7 nm a-Si:H(n) layer.*

absorption loss for the Cell C is slightly higher than that for the Cell D, suggesting that a higher J_{sc} could be achieved when using nc-Si:H(n) as seed layer in stead of contact layer. The J_{abs} of the Cell E or Cell F with 5 nm d_{ETL} is higher than the others. This is due to that the ETL for Cell E or Cell F is nc-Si:H(n) layer when d_{ETL} is 5 nm, while it is nc-SiO$_x$:H(n) layer for the other cells. The value of J_{re} is much lower than J_{abs}, as shown in Fig. 6.5(b). A reduction of J_{re} by 0.2 mA/cm^2 is observed as raising d_{ETL} from 5 to 15 nm. The light reflected on the front of the Cell D is slightly higher than the other cells, which could be attributed to the refractive index mismatch of the front layer stack.

The IV parameters of the solar cells with different ETL were normalized to the reference and are displayed in Fig. 6.6. We can see that the lowest normalized V_{oc} and FF in each series are found for the cell with 5 nm ETL. This is probably owing to the incomplete crystallization of ETL as indicated in Fig. 6.7 (a), causing

Table 6.2.: *Input parameters of the layers for AFORS-HET simulator.*

Parameter	ITO	nc-SiO$_x$:H (n)	nc-Si:H (n)	a-Si:H (n)	a-Si:H (i)	c-Si (n)
Thickness [nm]	70	10	5	5	6	170000
Electron affinity χ [eV]	4.2	3.41	3.41-3.6	3.41	3.8	3.9
Band gap E_g [eV]	3.2	2.1-2.24	1.98	1.72	1.72	1.12
Activation energy E_a [eV]	0	0.08-0.18	0.03	0.13	-	-
Electron (hole) mobility [cm^2/Vs]	40 (20)	20 (5)	40 (10)	20 (5)	20 (5)	1335 (463)
Effective conduction (valence) band density	1×10^{20} (1×10^{20})	1×10^{20} (1×10^{20})	1×10^{20} (1×10^{20})	1×10^{20} (1×10^{20})	1×10^{20} (1×10^{20})	2.85×10^{19} (2.85×10^{19})
Layer density	2.328	2.328	2.328	2.328	2.328	2.328

a non-ohmic contact on the front. As increasing the ETL thickness, the V_{oc} and FF increases with a sacrifice of the J_{sc}. This result is ascribed to the thickness dependent material properties and the stronger capability of more conductive ETL to achieve low ITO/n-layer contact resistivity, which is demonstrated by the TLM result in Fig. 6.7. Specifically, the Cell B with 4 nm a-Si:H(n) contact layer on top of 5 nm nc-SiO$_x$:H(n) exhibits a higher FF and V_{oc} than the Cell A at the same d_{ETL}, yielding an improvement of the power conversion. However, a considerable drop of the J_{sc} is found for Cell B, which cannot be compensated by the gain of FF, leading to a lower η than the reference. The Cell C and Cell D shows a similar trend of the cell performance as tuning the thickness of ETL. The J_{sc} decreases almost linearly when increasing d_{ETL} but more rapidly for the Cell C than the Cell D, consistent with the simulated result in Fig. 6.5. By using nc-SiO$_x$:H multi-layer as ETL, the value of the normalized FF can be above 1. This indicates that a better electrical performance than the reference is obtained. As a consequent, 3% relative gain of efficiency is achieved for the cells with the nc-SiO$_x$:H multi-layer. It is notable that the FF and η of the Cell C are higher than the Cell B and the Cell D. This result suggests that adding the nc-Si:H contact layer between ITO and 5 nm nc-SiO$_x$:H(n) is a more efficient method to improve the cell performance than the a-Si:H contact layer and the nc-Si:H seed layer. Besides, the cell performance of the solar cell with double layer (Cell E) is better than that with triple layer (Cell F) when d_{ETL} is less than 12 nm. This reveals that the ETL with double layer is more suitable for the SHJ solar cell with ultra-thin nc-SiO$_x$:H(n) layer to reach high-efficiency compared to the triple layer structure.

Fig. 6.7 (a) shows the crystalline volume fraction of ETL, consisting of different layer stack, as a function of d_{ETL}. An increase of the F_c is observed for all samples as increasing the thickness of electron transport layer. More crystalline ETL is obtained for the ETL with nc-Si:H(n) contact or seed layer compared to that with nc-SiO$_x$:H(n) single layer at the same thickness. The F_c of the ETL for the Cell D and Cell F is slightly higher than that for the Cell C. This reveals that the nc-Si:H seed layer plays a significant role in prompting the rapid growth of the crystalline phase in the nc-SiO$_x$:H(n) layers. Those ETL structures are integrated in SHJ solar cells and the ITO/n-layer contact resistivity is reported in Fig. 6.7 (b). The ρ_c of 5 nm ETL and ITO is too high to be extracted accurately by TLM, indicating a

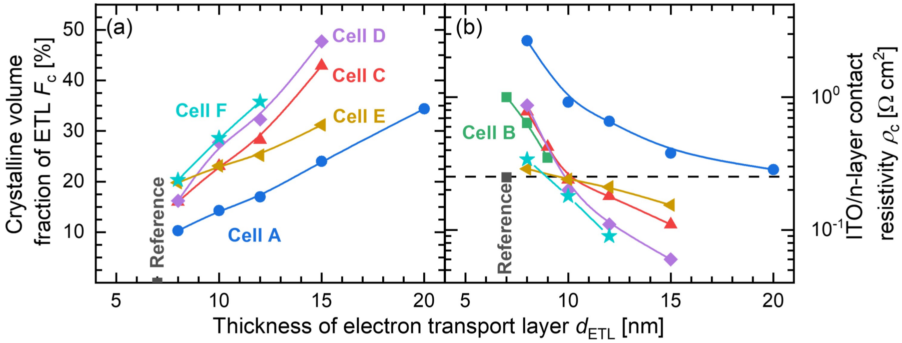

Figure 6.7.: *(a) The crystalline volume fraction (F_c) of electron transport layer (ETL) and (b) the contact resistivity (ρ_c) of ITO/n-layer as a function of the thickness of ETL (d_{ETL}). Solar cells with six kinds of ETL structure were fabricated, the cross sectional sketch of which can be found in Fig. 6.1. The Cell A has an ETL consisting of nc-SiO$_x$:H(n) single layer. The Cell B is with the a-Si:H(n) contact layer and 5 nm nc-SiO$_x$:H(n) layer on the front. The Cell C is with the nc-Si:H(n) contact layer and 5 nm nc-SiO$_x$:H(n) layer. The Cell D is with 5 nm nc-SiO$_x$:H(n) and the nc-Si:H(n) seed layer. The Cell F is with 2.5 nm nc-Si:H(n) contact and seed layer, and the nc-SiO$_x$:H(n) layer. The reference are the cells with 7 nm a-Si:H(n) layer.*

non-ohmic contact on the front. This could be the reason for the low normalized V_{oc} and FF of the devices in Fig. 6.6. By increasing the d_{ETL} above a certain value, the contact transforms from non-ohmic to ohmic, resulting in an increase of FF in Fig. 6.6. The ρ_{c} of Cell C, Cell D, Cell E and Cell F is lower than the reference when the d_{ETL} is above 10 nm. However, for the Cell A with 20 nm ETL, the contact resistivity is still slightly higher than the reference. At the same d_{ETL}, the contact resistivity of the Cell A is much higher than the other types of solar cells, demonstrating the beneficial of the highly crystalline nc-Si:H(n) contact or seed layer or the a-Si:H(n) contact layer for improving the contact properties of ITO/ETL.

To investigate the principle of the optimization by using the contact or seed layer, the energy band diagrams of the solar cells were simulated by the device simulator, AFORS-HET [157, 158, 223]. The input parameters of the layers are listed in Tab. 6.2. The values of the electron (hole) mobility, the effective conduction (valence) band density and the layer density are collected from the literature [50,

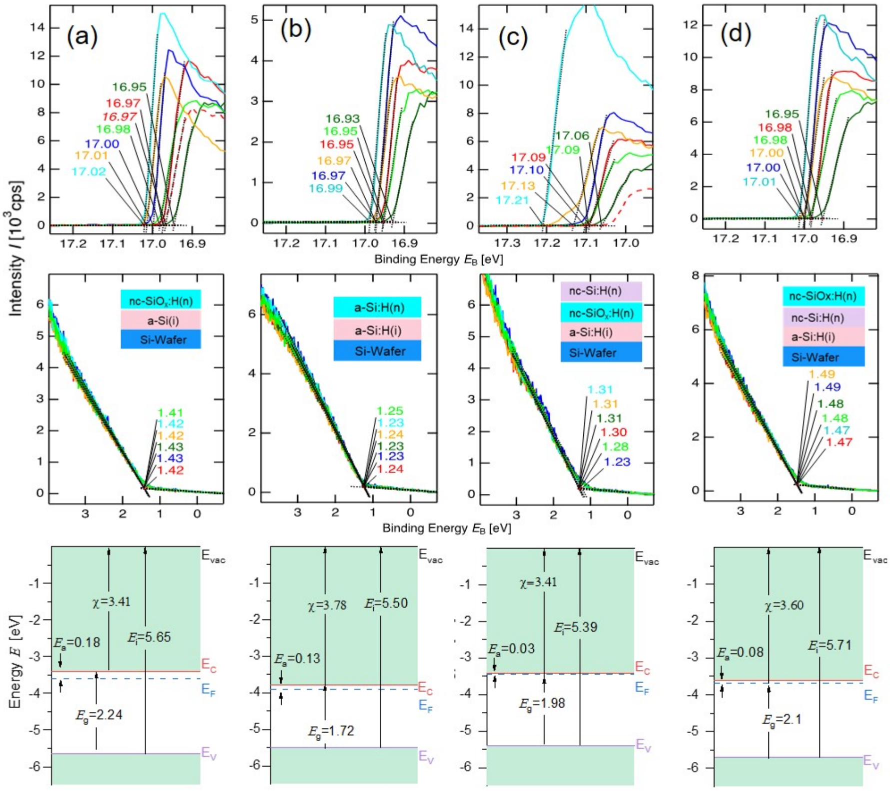

Figure 6.8.: *The UPS results and band diagrams of (a) the nc-SiO$_x$:H(n), (b) the a-Si:H(n), (c) the nc-Si:H(n) layer with nc-SiO$_x$:H underneath and (d) the nc-SiO$_x$:H(n) layer with nc-Si:H underneath.* E_{vac}, E_c, E_v, E_f, E_i, E_a, E_g *and* χ *is the vacuum energy level, conductive band energy, valence band energy, Fermi level, ionization energy, activation energy, band gap and electron affinity, respectively.*

213, 224]. The electron affinity (χ) of a-Si:H(n), nc-SiO$_x$:H(n) and nc-Si:H(n) layers was determined by UPS. Four samples were prepared on polish wafer for UPS measurement, more details on which can be found in Sec. 3.2.1. We measured six positions for each sample and determined the ionization energy E_i from the distance of the cutoff at low kinetic energies and the valence band edge at high kinetic energies by linear fits to the spectrum, as shown in Fig. 6.8. The band diagram of the nc-SiO$_x$:H(n), the a-Si:H(n), the nc-Si:H(n) layer with nc-SiO$_x$:H underneath and the nc-SiO$_x$:H(n) layer with nc-Si:H underneath were constructed from the result of the E_g from the absorption coefficient measurement, the E_i from the UPS measurement and the E_a from the temperature dependent dark conductivity measurement.

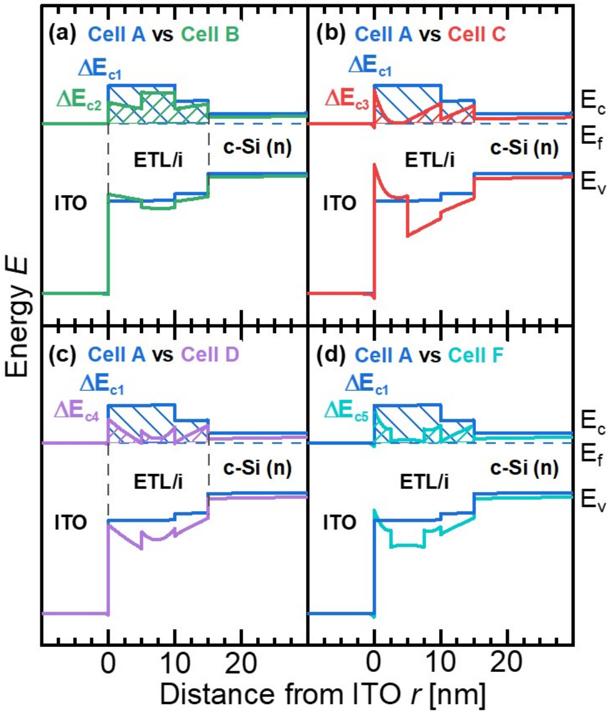

Figure 6.9.: *Band diagram at equilibrium of 10 nm electron transport layer (ETL) of different SHJ solar cells, (a) Cell A vs Cell B, (b) Cell A vs Cell C, (c) Cell A vs Cell D and (d) Cell A vs Cell F, calculated by simulator AFORS-HET. Cell A has an ETL consisting of 10 nm nc-SiO$_x$:H(n) single layer. Cell B is with 5 nm a-Si:H(n) contact and 5 nm nc-SiO$_x$:H(n) layer. Cell C is with 5 nm nc-Si:H(n) contact and 5 nm nc-SiO$_x$:H(n) layer. Cell D is with 5 nm nc-SiO$_x$:H(n) and 5 nm nc-Si:H(n) seed layer. Cell F is with 2.5 nm nc-Si:H(n) contact layer, 5 nm nc-SiO$_x$:H(n) layer and 2.5 nm nc-Si:H(n) seed layer. The E_c (E_v) and E_f is the conduction (valence) band energy level and Quasi-Fermi level, respectively. The cell structures are depicted in Fig. 6.1.*

Fig. 6.9 shows the band diagrams of five different kinds of SHJ solar cells (Cell

A, B, C, D and F) with 10 nm ETL at thermal equilibrium, simulated by AFORS-HET simulator. Band offsets can be found on the ITO/ETL and ETL/a-Si:H(i) interfaces. The patterned areas in the conduction band denote the energy barriers for electrons. They are defined by the band offset at the hetero-interface and the inner band bending in the doped layers. By using the mutil-layer instead of the nc-SiO$_x$:H(n) single layer, a reduction of the patterned area is observed, promoting the electron transport on the front. Meanwhile, the barrier to holes is enhanced. As a result, holes could be repelled away from the ETL/a-Si:H(i)/c-Si(n) interface, leading to a reduction of the surface recombination velocity. Fig. 6.9(a) and (c) illustrates that the band offset on the interface of ITO and ETL in the Cell A is higher than that in the Cell B and the Cell D. These differences of the conduction band bending could be responsible for the lower FF and higher contact resistivity of the Cell A, compared with the Cell B and Cell D (see Fig. 6.6 and Fig. 6.7). The nc-SiO$_x$:H(n) is a two-phase material with the nanocrystalline silicon phase that has higher doping efficiency than a-Si:H(n), embedded in a highly transparent amorphous silicon oxide matrix [225,226]. During the deposition process of nc-SiO$_x$:H(n) layer, a certain amorphous phase appears firstly as the nucleation of crystalline phase, then the epitaxial growth is followed [51, 215–217]. Decreasing the thickness of nc-SiO$_x$:H(n) layer leads to a layer with lower crystalline volume fraction, as shown in Fig. 6.7(a), and higher percentage of amorphous silicon oxide phase. When more oxygen incorporation in silicon films, a higher average Si-Si bond energy in lattice can be achieved [224]. The energy level of the valence band edge may move down and the conduction band edge come up in energy, giving rise to a lower electron affinities of the thinner nc-SiO$_x$:H(n) [224,227]. Therefore, for cells with 5 nm nc-SiO$_x$:H(n) layer the conduction band offset (ΔE_c) at the ITO / nc-SiO$_x$:H(n) interface might be higher than the solar cells with thicker nc-SiO$_x$:H(n) layer, acting as a Schottky barrier for the electrons and resulting in a lower FF and higher contact resistivity. By using the highly crystalline nc-Si:H(n) as seed layer, a nc-SiO$_x$:H layer with higher crystalline volume fraction at the same d_{ETL} is obtained, as shown in Fig. 6.7(a) and Ref [219]. This could contribute to the lower band offset at ITO / ETL interface as well as the energy barriers to the electron in the Cell D. Due to the high doping concentration in the nc-Si:H(n) contact layer, a sharp barrier is induced on the ETL/ITO and ETL/i-layer interface of the Cell C, which is also observed in

Table 6.3.: *Detailed information on the a-Si:H(i) and nc-SiO$_x$:H(n) layers used in SHJ solar cells. The $d_{a\text{-}Si:H,front}$ and $d_{a\text{-}Si:H,rear}$ are the thickness of a-Si:H(i) used on front and rear side, respectively.*

	a-Si:H(i)			n-layer
	Type	$d_{\text{a-Si:H,front}}$	$d_{\text{a-Si:H,rear}}$	f_{PH_3}
A	I	6 nm	6 nm	2%
B	II	6 nm	6 nm	2%
C	III	4 nm	6 nm	2%
D	IV	4 nm	6 nm	4%

the Cell F. This sharp barrier could provide a transport channel for electrons with a high tunneling probability and improve the front contact properties in the Cell C and Cell F, consistent with the TLM results in Fig. 6.7(b).

6.2. Optimization of a-Si:H(i) passivating layer

A low surface recombination velocity provided by the ultra-thin a-Si:H(i) layer is very critical for SHJ solar cells to reach high open-circuit voltage and short-circuit current density. As mentioned in Sec. 5.3, the main recombination losses in our devices are related to the passivation quality of the a-Si:H(i) layer. The optimization of nc-SiO$_x$:H(n) can't dramatically improve the c-Si surface passivation a lot according to the previous results. Besides, a severe parasitic absorption in a-Si:H(i) is also observed for the devices prepared in the preliminary study (see Fig. 5.14). Thus, varying the deposition conditions of a-Si:H (i) layer is an option for the further improvement of cell performance. In this section, the optimization of the a-Si:H(i)/nc-SiO$_x$:H(n) stack is presented. Four samples with different a-Si:H(i)/nc-SiO$_x$:H(n) stacks are investigated in terms of the passivation quality and cell performance, marked as A, B, C and D. The details of the samples are listed in Tab. 6.3. The n-layer used here is 5 nm nc-SiO$_x$:H(n) layer with 5 nm nc-Si:H(n) contact layer. Two types of a-Si:H(i) layer, named Type I (standard) and Type II (optimized), were integrated in the SHJ solar cells.

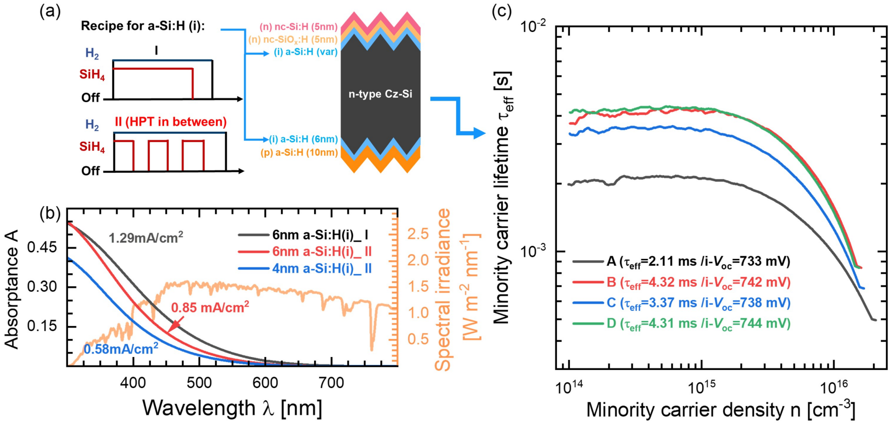

Figure 6.10.: *(a) The schematic representation of the deposition sequences of two kinds of a-Si:H(i) layer, Type I and Type II. (b) Absorptance of 6 nm a-Si:H(i) Type I, 6 nm a-Si:H(i) Type II and 4 nm a-Si:H(i) Type II. (c) Minority carrier lifetime (τ_{eff}) curve of four kinds of solar cell with different a-Si:H(i)/nc-SiO$_x$:H(n)/nc-Si:H(n) stack, measured after the PECVD depositions. The current density loss (J_{abs}) due to parasitic absorption in a-Si:H(i) layer was calculated via Eq. 6.1 and is displayed in figure (b). The details of the samples are listed in Tab. 6.3.*

Fig. 6.10(a) shows the schematic representation of the deposition sequences of these two layers. The Type I a-Si:H(i) is the initial layer and the Type II is optimized by H_2 plasma treatment (HPT) during the deposition process. A lower absorptance of the Type II is found in Fig. 6.10 compared with the Type I. The current density loss due to parasitic absorption in a-Si:H(i) layer was calculated via Eq. 6.1 and is displayed in Fig. 6.10(b). There is a reduction of J_{abs} about 0.4 mA/cm^2 due to the parasitic absorption in the Type II compared with the Type I. This observation could be attributed to the hydrogen induced bandgap widening of the a-Si:H layer [205]. Furthermore, a thinner a-Si:H(i) layer and an n-layer with higher doping concentration were deposited on the front side to further reduce the parasitic absorption and maintain the passivation quality. The effective minority carrier lifetime of four samples is plotted as a function of the minority carrier density (n) in Fig. 6.10(c). The lifetime values at n of 10^{15} cm^{-3} are roughly doubled for the sample with the HPT treated a-Si:H layer on both side, consistent with Ref. [228].

The interface defect density is determined by the local network structure at the a-Si:H(i)/c-Si interface and the bulk properties of the a-Si:H(i) film [211]. More hydrogen content and voids were reported in the treated a-Si:H(i) layer, approaching the crystallization transition, which could lead to a better hydrogenate wafer/film interface [228]. Besides, an increase in the valence band offset (ΔE_v) at the interface of the treated a-Si:H layer and c-Si was demonstrated [205]. The increased ΔE_v may act as a barrier and repel the hole away the interface, resulting in a decreased surface recombination rate. The lifetime curve shifts down slightly when reducing the thickness of the front a-Si:H(i) from 6 nm to 4 nm. This is in good agreement with the thickness dependent lifetime result observed by Kondo et al [199]. When reducing the thickness of a-Si:H(i), the Si-H bonding in the a-Si:H(i) layer becomes less and less stable, causing an increase of defect density in layer [197,199,201,202].

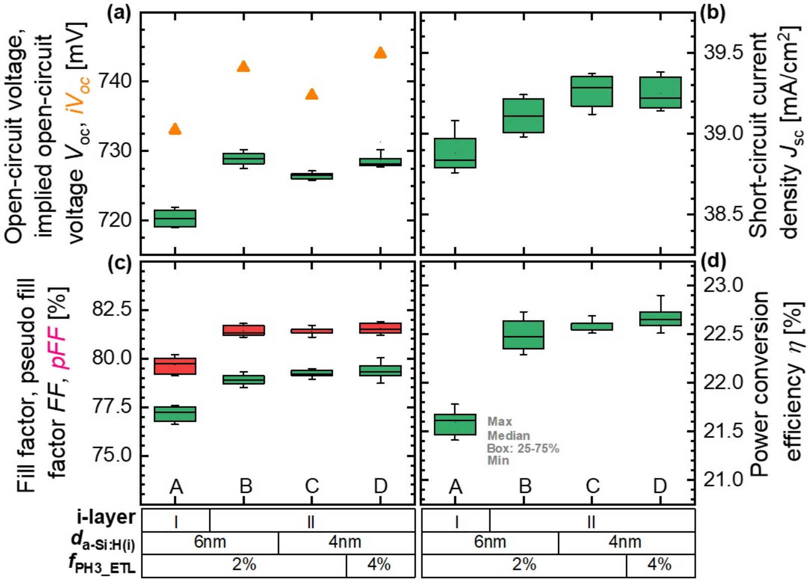

Figure 6.11.: *(a) Open-circuit voltage (V_{oc}), (b) short-circuit current density (J_{sc}), (c) fill factor (FF), and (d) power conversion efficiency (η) of solar cells with various i/n stacks. The details of the samples are listed in Tab. 6.3. The cross sectional sketch of solar cells without metallization can be found in Fig. 6.10 (a).*

Moreover, for a thinner layer the tunnel probability to the carriers increases. As a result, the charge carriers generated in the substrate could transfer through the intrinsic thin-film and recombine at the external a-Si:H surfaces or the next defect-rich interface [200,203]. The worse passivation quality can be recovered by increasing the doping concentration of the nc-SiO$_x$:H/nc-Si:H(n) double layer. The doped films could principally induce a field effect near the a-Si:H(i)/c-Si interface, driving the minority carriers in the c-Si back and reducing the defects on the external a-Si:H(i) surface [202,206,207]. When increasing the f_{PH_3} of n-layer, a more powerful internal electric field could be created, resulting in a improvement of the surface passivation.

Fig. 6.11 shows the cell performance of the solar cells with different i/n stacks. We can see that an increase of V_{oc} by 10 mV, J_{sc} by 0.3 mA/cm^2, FF by 1.2%$_{abs}$ is reached by using the a-Si:H(i) layer with HPT, giving rise to around 1%$_{abs}$ gain of η. The increase of pFF for samples B is consistent with the QSSPC results in Fig. 6.10. This indicates that the improvement of FF could originate from the better surface passivation on both sides. Reducing the thickness of a-Si:H(i) from 6 to 4 nm contributes to about 0.15 mA/cm^2 gain of J_{sc} and 0.4%$_{abs}$ of FF, accompanying with a drop of the V_{oc} and iV_{oc}. By increasing the f_{PH_3} of nc-Si:H/nc-SiO$_x$:H(n) double layer from 2% to 4%, a slight increase of V_{oc} and FF can be observed without

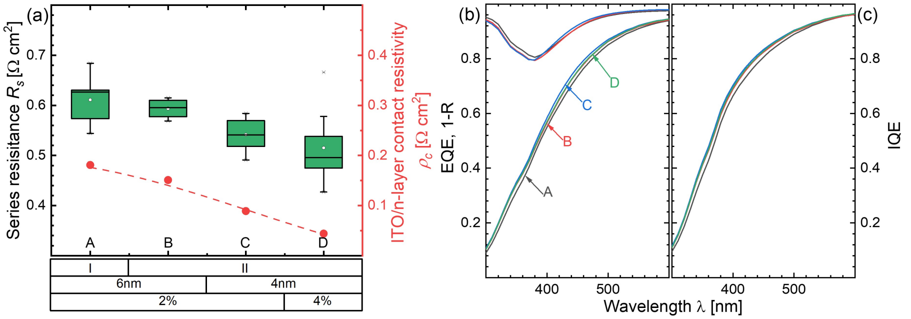

Figure 6.12.: *(a) Series resistance (R_s) and ITO/n-layer contact resistivity (ρ_c), (b) external quantum efficiency (EQE) and absorptance (1-R), and (c) internal quantum efficiency (IQE) spectra of solar cells with various a-Si:H(i)/nc-SiO$_x$:H(n)/nc-Si:H(n) stacks. The details of the samples are listed in Tab. 6.3. The cross sectional sketch of the solar cells without metallization can be found in Fig. 6.10 (a).*

compromising to the J_{sc}. As a consequence, about 0.1%$_{\mathrm{abs}}$ gain of η is acquired for the sample D. The best cell of the sample D exhibits a η of 22.9%, V_{oc} of 728.4 mV, FF of 80.02% and J_{sc} of 39.28 mA/cm^2. The series resistance and the ITO/n-layer contact resistivity is reported in Fig. 6.12 (a). Compared with the sample A, there is only a slight decrease of R_{s} and ρ_{c} for the sample B with treated a-Si:H(i) layer. This reveals that the main contribution to the gain of FF in Fig. 6.11(c) is not the improvement of front contact properties but the optimized surface passivation. A lower R_{s} and ρ_{c} is obtained by using the thinner optimized a-Si:H(i) layer and the nc-SiO$_x$:H/nc-Si:H(n) layer prepared at higher $f_{\mathrm{PH_3}}$. This could be due to the increased probability to the tunneling process of electrons on the front side. The EQE, 1-R and IQE spectra of cells with various i/n stack in the wavelength range between 300 and 600 nm is plotted in Fig. 6.12. The solar cell with 6 nm optimized a-Si:H(i) layer shows a higher EQE and IQE than that with the standard a-Si:H(i), corresponding well to the optical properties of the i-layer mentioned in Fig. 6.10.

The fill factor is strongly influenced by the carrier recombination and the ohmic resistance. To investigate the reasons for the FF difference of solar cells with various i/n stack in this series, a method based on the two-diode model was used, detailed information on which can be found in Ref. [229]. The distribution of the FF losses is presented in Fig. 6.13. $FF_{\mathrm{J_{01}}}$ is the saturation current density (J_{01}) limited fill factor, determined by assuming the absence of R_{s}, R_{SH} and saturation current density (J_{02}). More information on the two-diode model, J_{01} and J_{02} can be found in Sec. 3.3. $\Delta FF_{\mathrm{J_{02}}}$, $\Delta FF_{\mathrm{R_{SH}}}$ and $\Delta FF_{\mathrm{R_s}}$ are defined as the FF loss from the J_{02} related recombination, the R_{SH} and the R_{s}, respectively. From the FF loss analysis, it is obvious that the dominant loss is due to the recombination in the space charge region, followed by the loss related to the series resistance. The shunt resistance does not contribute a notable loss to FF. By using the optimized a-Si:H(i) as passivation layer on both sides, an increase of $FF_{\mathrm{J_{01}}}$ from 84.78% to 85.03%, a reduction of $\Delta FF_{\mathrm{J_{02}}}$ from 4.12% to 3.24% and a decrease of $\Delta FF_{\mathrm{R_s}}$ from 3.23% to 2.98% are acquired. These results demonstrate that the improvement of the passivation in the sample B is the main contributor to the gain of FF in Fig. 6.11 compared with the sample A. Around 0.5%$_{\mathrm{abs}}$ reduction of FF loss related to R_{s} is obtained when decreasing the thickness of a-Si:H(i) from 6 nm to 4 nm. This decreased $\Delta FF_{\mathrm{R_s}}$ compensates the increase of $\Delta FF_{\mathrm{J_{02}}}$ (0.1%$_{\mathrm{abs}}$), yielding 0.4%$_{\mathrm{abs}}$ gain of FF (see

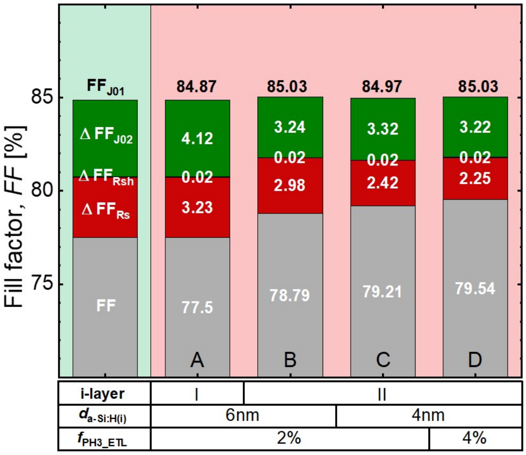

Figure 6.13.: *Fill factor (FF) loss analysis of the solar cells with various a-Si:H(i)/nc-SiO$_x$:H(n)/nc-Si:H(n) stacks.* $FF_{J_{01}}$ *is the saturation current density* (J_{01}) *limited fill factor, determined by assuming the absence of* R_s, R_{SH} *and saturation current density* (J_{02}). $\Delta FF_{J_{02}}$, $\Delta FF_{R_{SH}}$ *and* ΔFF_{R_s} *are defined as the* FF *loss from* J_{02} *related recombination,* R_{SH} *and* R_s*, respectively. The details of the samples are listed in Tab. 6.3. The cross sectional sketch of solar cells without metallization can be found in Fig. 6.10 (a).*

Fig. 6.11). The usage of the n-layer prepared at higher doping gas fraction gives rise to 0.1%$_{\mathrm{abs}}$ and 0.2%$_{\mathrm{abs}}$ reduction of $\Delta FF_{\mathrm{J_{02}}}$ and $\Delta FF_{\mathrm{R_s}}$, respectively, which is in good agreement with the IV parameters and the TLM results mentioned previously.

6.3. Optimization of anti-refraction coating

6.3.1. Comparison of various TCO layers

Transparent conductive oxide layers are used on top of the silicon films in SHJ solar cells, not only as an anti-reflection coating layer but also to ensure efficient lateral carrier transport towards the metal contacts. TCO is directly grown on the nc-SiO$_{\mathrm{x}}$:H(n) layer here, the contact resistance between this two layers matters a lot for the efficiency of the SHJ solar cells. The development of TCO materials with high-mobility and low parasitic absorption is very important for high-efficiency SHJ solar cells. ITO is most commonly adapted in SHJ solar cells due to its mature sputtering process and we rank it as the standard TCO material for the SHJ baseline in our group. However, due to the moderate carrier mobility of ITO, a limitation for this material to achieve low parasitic absorption with high conductivity was reported [230, 231].

To overcome this obstacle, high mobility TCO materials, such as IO:H, IWO and ITiO, were developed and utilized in SHJ solar cells [231–234]. Besides, there is an economical problem for the industrial fabrication of SHJ solar cells with ITO due to the high price and the supply risk of indium [235]. Thanks to the abundance of zinc in the earth's crust, zinc-based TCO layers, such as AZO, were investigated and supposed to be an attractive low-cost substitute for ITO [236]. In this section, we present a detailed comparison of the material properties of different TCO films. Additionally, these TCO films were deposited on the front of the SHJ solar cells and their cell performance are compared. The investigated TCO films are ITO, IWO, ITiO and AZO, the detailed deposition parameters of which can be found in Sec. 3.1. Fig. 6.14 shows the absorptance and electrical properties of 80 nm TCO

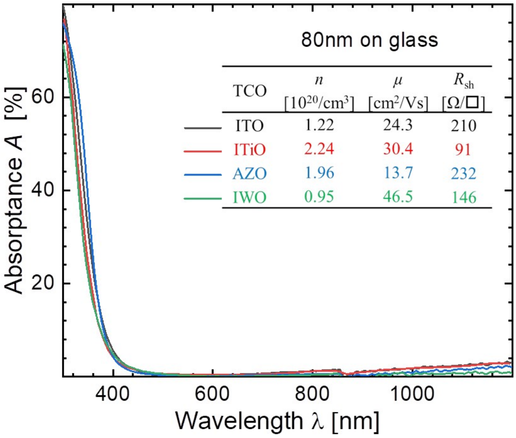

TCO	n [10^{20}/cm^3]	μ [cm^2/Vs]	R_{sh} [Ω/□]
ITO	1.22	24.3	210
ITiO	2.24	30.4	91
AZO	1.96	13.7	232
IWO	0.95	46.5	146

Figure 6.14.: *Optical absorptance of various TCO films at thickness of 80 nm deposited on 1.1mm thick corning glass (Corning Eagle 2000). The inserted table summarizes the corresponding electrical properties of TCO films.*

Table 6.4.: *Cell performance of the solar cells with nc-SiO$_x$:H(n) layer and different TCO layers.*

	J_{sc} [mA/cm^2]	V_{oc} [mV]	FF [%]	η [%]	R_{s} [Ωcm^2]	ρ ITO/n [Ωcm^2]	ρ ITO/Ag [Ωcm^2]
ITO	39.55	734.1	79.28	23.02	0.9	0.69	0.041
ITiO	39.68	733.5	79.39	23.11	0.82	0.51	0.012
AZO	39.76	732.2	78.58	22.88	1.03	0.46	0.09
IWO	39.80	732.9	78.4	22.87	1.07	0.41	0.10

films deposited on 1.1mm thick corning glass (Corning Eagle 2000).

A lower absorptance than the ITO at short wavelength (λ<400 nm) is detected for the ITiO and IWO, but higher for the AZO. This may be related to the difference of the carrier mobility and can be explained by the Burstein-Moss effect [237]. At long wavelength (λ>800 nm), less light is absorbed in the IWO compared with the other TCO films, indicating a reduction of the free carrier absorption. For the ITiO film, the carrier density and mobility both are larger than the ITO, yielding a much lower sheet resistance (R_{sheet}), 91$\Omega/\square$. The carrier mobility of the IWO is the highest among these four kinds of TCOs, while its carrier density is the lowest, giving rise to a moderate value of the R_{sheet}. Solar cells with different TCO on the front side and the ITO on the rear side were fabricated, the performance of which is

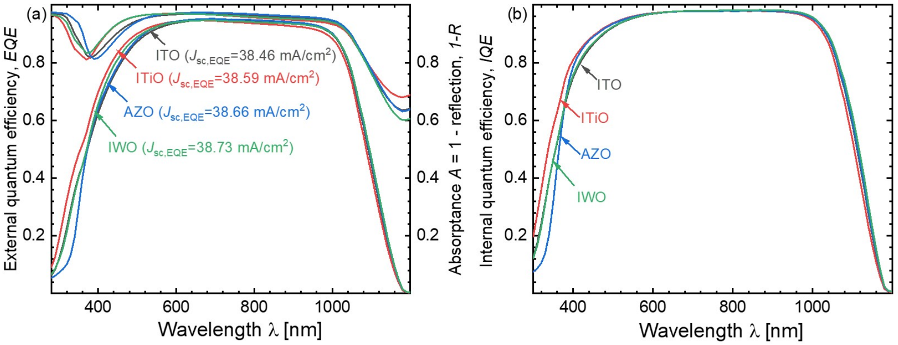

Figure 6.15.: *(a) External quantum efficiency (EQE) and absorptance $(1 - R)$, and (b) internal quantum efficiency (IQE) spectra of solar cells with various TCO layers.*

displayed in Tab. 6.4. Compared with the standard ITO layer, there is a expected increase of J_{sc} and FF for the cells with ITiO, leading to around 0.1%$_{\mathrm{abs}}$ gain of η. This observation is in good agreement with the material properties in Fig. 6.14. For the cells with AZO and IWO, there is about 0.6∼0.8%$_{\mathrm{abs}}$ reduction of FF. This drop of FF can not be compensated by the gain of J_{sc}, yielding a 0.2%$_{\mathrm{abs}}$ decrease of the efficiency. Besides, we can see a significant increase of the contact resistivity of Ag/AZO or Ag/IWO, consistent with the FF results. The EQE, 1-R and IQE spectra of the solar cells with various TCOs are plotted in Fig. 6.15. The difference among various spectra is mainly observed in the wavelength range between 300 and 600 nm. Compared to the standard ITO layer, the cells with the ITiO layer exhibits a $J_{\mathrm{sc,EQE}}$ gain of 0.1 mA/cm^2, while the improvement of $J_{\mathrm{sc,EQE}}$ for the AZO or the IWO layer is about 0.2 mA/cm^2. Those observations correspond well to the reported optical properties of the TCOs given in Fig. 6.14 and the cell performance listed in Tab. 6.4. A lower EQE in the long wavelength range is found for the cell with ITiO compared to the one with ITO, which could be attributed to the increased free-carrier absorption in the ITiO layer.

6.3.2. ITO/MgF$_2$ anti-reflection coating layer

As mentioned in Sec. 5.3, there is about 33% of the optical loss is due to the imperfect light trapping on the front. In order to further improve the device efficiency, a magnesium fluoride (MgF$_2$)/ITO double-layer was integrated in SHJ solar cells as anti-reflection coating, as shown in Fig. 6.16(a). The refractive index of MgF$_2$, ITO, nc-SiO$_x$:H(n), a-Si:H(i) and c-Si at wavelength of 632 nm is 1.38, 2.05, 3.17, 3.77 and 3.87, respectively, making a progressive increase of n from air to wafer. This layer stack could reduce the light reflection at each interface and let more light go into the absorber. Optical simulations by OPAL 2 were carried out to quantify the current density loss due to the reflected light (J_{re}) on the illuminated side and the parasitic absorption in the front stack ($J_{\mathrm{abs,front}}$). The thickness of ITO (d_{ITO}) is varied from 40 to 100 nm, accompanying with the thickness variation of MgF$_2$ capping layer ($d_{\mathrm{MgF_2}}$) from 0 to 150 nm. The contour map of the simulated J_{re}, $J_{\mathrm{abs,front}}$ and current density absorbed in silicon $J_{\mathrm{abs,Si}}$ is presented in Fig. 6.16. The device with 80 nm ITO and 0 nm MgF$_2$ acts as reference, marked with black balls.

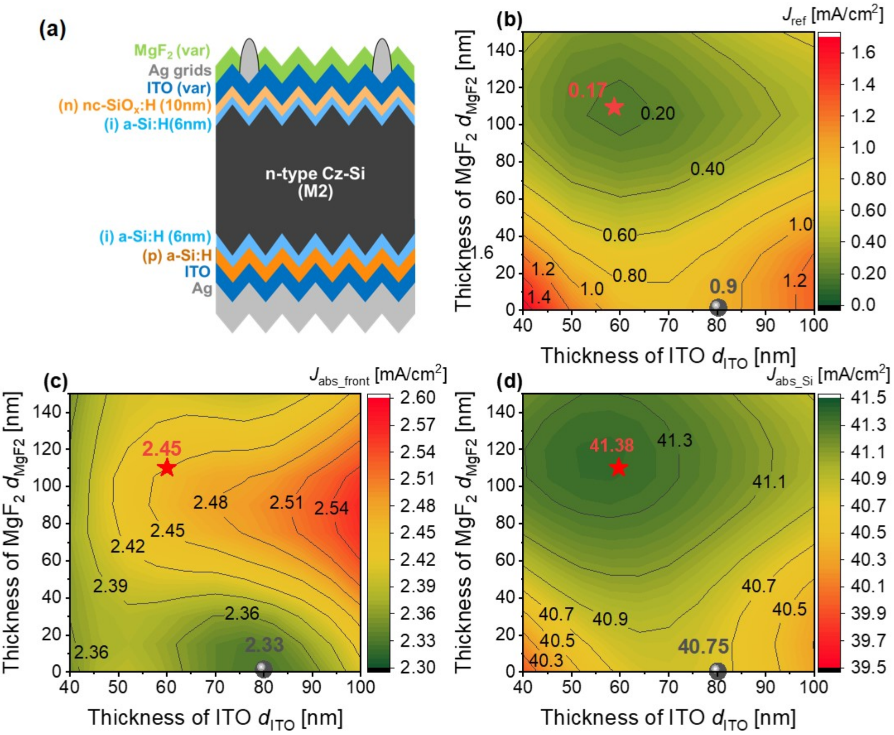

Figure 6.16.: *(a) The schematic sectional structure of the solar cells with MgF_2/ITO double layer. The contour map of the simulated current density loss due to (b) the reflected light (J_{re}) and (c) the parasitic absorption in the front stack ($J_{abs,front}$), and (d) the current density absorbed in silicon ($J_{abs,Si}$).*

The optimum of the double-layer ARC is positioned at d_{ITO} of 60 nm and d_{MgF_2} of 110 nm, marked with red stars. Compared with the reference, 0.73 mA/cm^2 decline of J_{re} and 0.12 mA/cm^2 increase of $J_{\text{abs,front}}$ are found at the optimum points, giving rise to a 0.63 mA/cm^2 gain of $J_{\text{abs,Si}}$. Further reducing d_{ITO} from the optimum will present a trade-off between the decreased parasitic absorption in ITO and the increased reflection losses on the front. For the solar cells without MgF_2, the highest $J_{\text{abs,Si}}$ is obtained at d_{ITO} of 70 nm. A decreased d_{ITO} will lead to a higher R_{sheet} and cause an increase of the device's series resistance. Therefore, we prepared the solar cells with the ITO layers at different thickness. Then 110 nm MgF_2 layer was

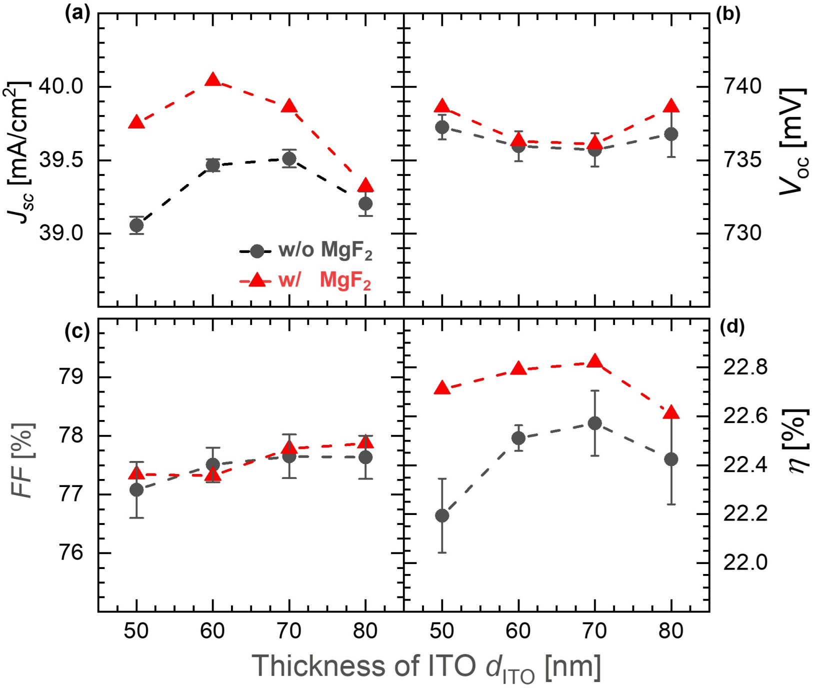

Figure 6.17.: *(a) Short-circuit current density (J_{sc}), (b) open-circuit voltage (V_{oc}), (c) fill factor (FF), and (d) power conversion efficiency (η) of solar cells with the ITO layer at various thickness. For each group at least four cells were fabricated. One cell from each group was selected to deposit 110 nm MgF$_2$ layer on top of ITO, marked by red color.*

deposited on top of the selected cells by e-beam evaporation. The cell performance is shown in Fig. 6.17.

For the solar cells without MgF$_2$, the J_{sc} increases first and then decreases as increasing the d_{ITO} from 50 to 80 nm. A slightly higher FF is obtained for the solar cells with thicker ITO layer. It could be explained by the better lateral carrier collection in the thicker ITO layer due to its lower sheet resistance. Hence, the best cells in this series are found at d_{ITO} of 70 nm. By applying 110 nm MgF$_2$ layer on top of the front ITO, about 0.6 mA/cm^2 gain of J_{sc} is achieved for the cells with 50 or 60 nm ITO, without compromising to the FF and V_{oc}, leading to 0.3%$_{abs}$ improvement of η. Due to the thickness mismatch of the anti-reflection coating, the

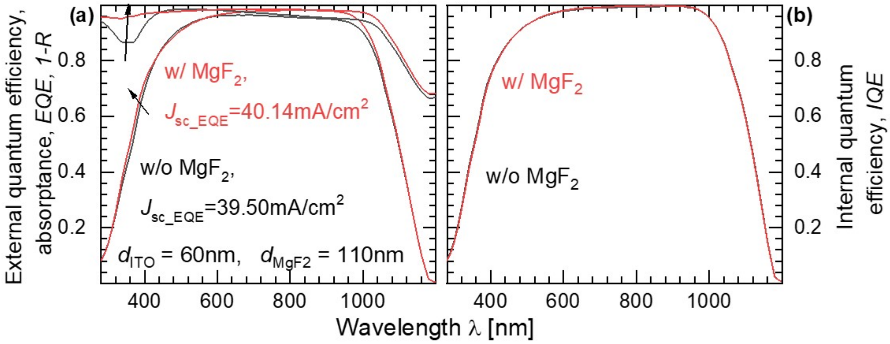

Figure 6.18.: *(a) EQE, 1-R and (b) IQE spectra of the solar cell with 60 nm ITO, measured before and after the MgF_2 depositions.*

difference between the J_{sc} of the cells without and with MgF_2 is getting smaller as increasing d_{ITO}. A comparison of the EQE, 1-R and IQE spectra measured before and after MgF_2 depositions is presented in Fig. 6.18. The thickness of the ITO layer used in this cell is 60 nm. We can see a dramatic increase of the absorptance in the wavelength range from 300 to 400 nm and 600 to 1200 nm. Accordingly, an increase of EQE is observed in the same range. The cell with ITO/MgF_2 double-layer exhibits a $J_{sc,EQE}$ gain of 0.6 mA/cm^2 compared to that without MgF_2. There is no notable change of the IQE spectra before and after the MgF_2 depositions.

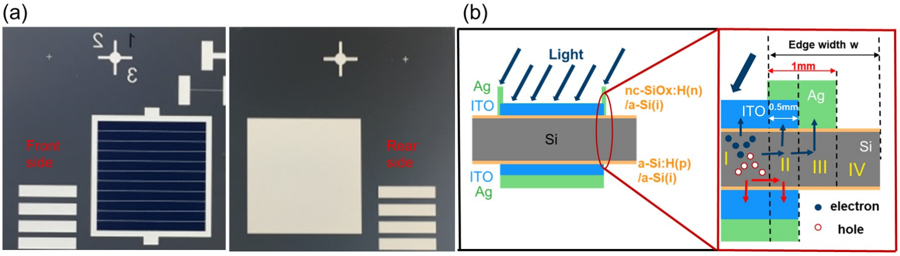

Figure 6.19.: *(a) Image and (b) sectional illustration of a small size solar cell embedded in one wafer. The wafer bulk of the illuminated cell can be divided into four regions: I) the illuminated region, II) the dark region with ITO, III) the dark region with busbar and IV) the dark region without busbar.*

6.4. Perimeter recombination

Four small size solar cells (1.9×1.9 cm^2) are embedded in the quarter-M2-sized wafer (7.8×7.8 cm^2) according to the current small size cell design in Sec. 5.1. The image of a small size solar cell is shown in Fig. 6.19 (a). A surrounding busbar can be found on the front side, defining the illumination area during I-V measurement. The dark region is out of the surrounding busbar, in which no excess charge carrier is generated. Hence, a gradient in the carrier concentration from the illuminated region to the dark region is created. The concentration difference forces the carriers diffuse into the shaded perimeter region and recombine, which is called perimeter recombination. This is an important loss mechanism in Si solar cell, especially for the small area cells with a large circumference to area ratio [238–241]. The perimeter recombination had been demonstrated to cause an increase in the nonideal dark saturation current and a decrease in FF and V_{oc} [238–244]. Haase et al. reported a difference in the V_{oc} of 10 mV and the efficiency of 0.4%$_{\text{abs}}$ between the aperture area measurement and the full area measurement for a typical 4 cm^2 SHJ solar cell [245]. A simplified cross-section structure of the solar cell is presented in Fig. 6.19(b). Half busbar is located on the ITO layer, while the other part contacts to the nc-SiO$_x$:H(n) layer directly. The distance from the illumination edge to the wafer edge is named edge width (w), which is about 17mm for the small cell prepared in this work. During the JV curve measurement through a mask, the illuminated cell can be divided into four regions: I) the illuminated region, II) the dark region with ITO, III) the dark region with busbar and IV) the dark region without busbar, as shown in Fig. 6.19(b). The carriers in the region II can be easily collected due to the ohmic contact of ITO and silver, while the carrier collection is difficult in the region III and region IV since the contact between nc-SiO$_x$:H(n) and Ag is non-ohmic. In this section, the influence of the perimeter recombination on cell performance is investigated by Quokka3 simulator. We built a model for the small size solar cell and varied the edge width from 0 to 4.5mm.

The simulated I-V parameters versus the edge width are plotted in Fig. 6.20. A reduction of V_{oc} by 3 mV and 1.3%$_{\text{abs}}$ gain of FF is obtained as increasing the w from 0 to 0.5mm, giving rise to 0.33%$_{\text{abs}}$ increase in the efficiency. Raising the w up to 1mm leads to a similar trend in V_{oc} but a slight decrease of FF. When further

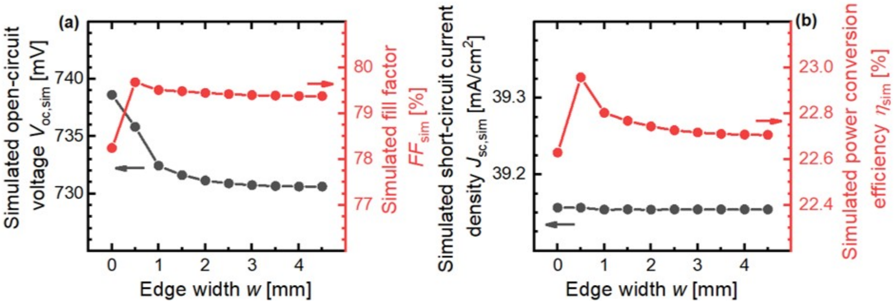

Figure 6.20.: *(a) Simulated open-circuit voltage ($V_{oc,sim}$), (b) short-circuit current density ($J_{sc,sim}$), (c) fill factor (FF_{sim}), and (d) power conversion efficiency (η_{sim}) as a function of the edge width (w), which is defined by the distance between the illumination edge and wafer edge. The sectional structure of the solar cell can be found in Fig. 6.19.*

increasing w, the V_{oc} becomes less dependent on w and tends to be saturated, while the FF is almost constant. It is notable that $0.3\%_{\mathrm{abs}}$ increase of η is reached if the edge width of the solar cell is 0.5mm instead of 4.5mm. Fig. 6.21 shows the cross-section images of the simulated excess electron density (Δn_{e}) and the electron current density (J_{e}) distribution in the c-Si bulk of the SHJ solar cell at the maximum power point under 1 sun illumination.

The distribution of Δn_{e} in the lateral direction is very uniform and no lateral current density in c-Si bulk is observed when w is 0mm. When the edge width is more than 0mm, a lower Δn_{e} than the illuminated c-Si bulk is found in the perimeter region, the value of which is more than 0 cm^{-3}. A lateral current flowing from the illuminated region to the perimeter region can be observed. This reveals that the wafer bulk conduction does contribute to the lateral carrier collection. The value of J_{e} is getting larger when approaching the edge of the illuminated region and decreases rapidly on the edge of ITO layer. When w = 0mm, the cell becomes full-sized and there is no region II, III and IV in the cell as well as the busbar. Hence, the lateral carrier collection in the full-sized cell is dependent on the ITO layer. When increasing the w up to 0.5mm, the dark region with ITO (region II) appears, causing the perimeter recombination and the drop of V_{oc} in Fig. 6.20. When further increasing the volume of the perimeter section, this recombination could become more severe. Moreover, the illuminated section is surrounded by the busbar, which

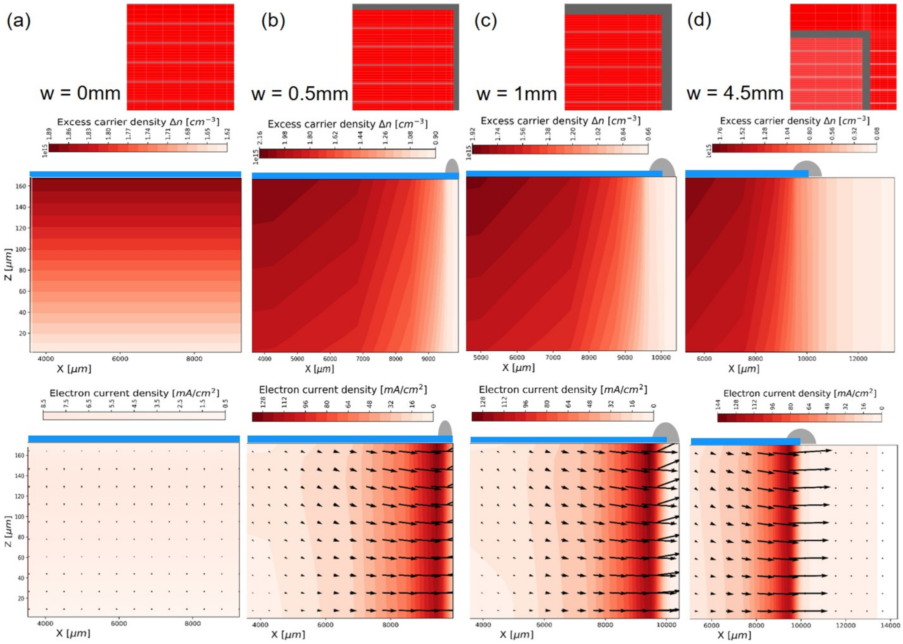

Figure 6.21.: *The cross-section images of the simulated excess electron density (Δn_e) and the electron current density (J_e) distribution in the c-Si bulk of the SHJ solar cell at a edge width (w) of (a) 0mm, (b) 0.5mm, (c) 1mm and (d) 4.5mm.*

is more conductive than the fingers. This is beneficial for the carrier collection and could be responsible for the increase of FF in Fig. 6.20. The carriers in the region close to the busbar are easy to be extracted to the external circuit, leaving a large gradient of the Δn_e and J_e near busbar. Further increasing the w from 0.5 to 1mm makes the area of the wafer be more than that of the ITO. Hence, a direct contact of the silver and the nc-SiO$_x$:H(n) layer is found. Since the Ag/nc-SiO$_x$:H(n) contact is non-ohmic, this is helpless to the carrier collection and causes the decrease of FF. When further raising w, the effect of w on the cell performance is less pronounced. This result could be due to the longer distance between the cell boundary and the region IV compared with the region II and region III.

To reduce the effect from the perimeter region, three kinds of cell design were pointed out, named D1, D2 and D3, and the initial cell design acts as reference (RF).

Fig. 6.22 shows the models of these four cell designs built in Quokka3 simulator. In the D1, the busbars near the bottom and top boundaries are omitted to reduce the volume of region II and III. In the D2, the area of the illuminated wafer bulk is same as that of ITO layer and the busbars were printed upon the nc-SiO$_x$:H(n) layer to eliminate the region II completely. In the D3, there is no busbar surrounding the cell boundaries to get rid of the perimeter recombination. The simulated cell performance is displayed in Fig. 6.23. The highest simulated efficiency is obtained by the cell at the D2 design. There is about 2 mV V_{oc} and 0.5%$_{\mathrm{abs}}$ FF increase for

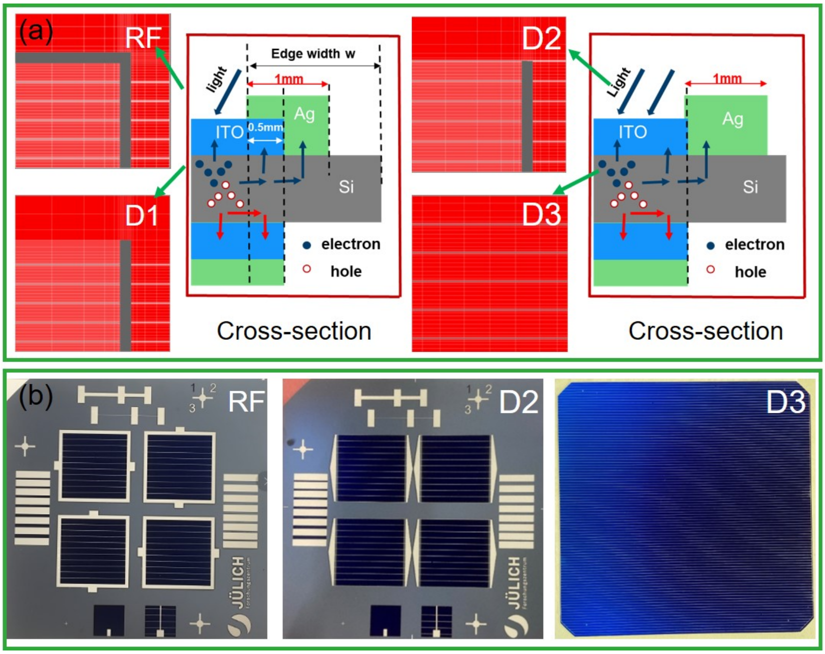

Figure 6.22.: *(a) Schematic illuminations of four kinds of cell design, named RF, D1, D2 and D3. In the D1, the busbars near the bottom and top boundaries are omitted compared with the RF. In the D2, the area of the illuminated wafer bulk is same as the ITO layer and the busbars were printed upon the nc-SiO$_x$:H(n) layer. In the D3, there is no busbar surrounding the cell boundaries. (b) Images of the fabricated solar cells at RF, D2 and D3 cell design. The RF and D2 cells are embedded in the quartered M2-sized wafers and the rear contact is full-area contact. The D3 cells are bifacial and were prepared on full-size M2 wafers.*

the D2 compared with the RF. The highest simulated V_{oc} is found at the D3 design accompanying with a lowest FF among these four kinds of cells. This result is due to the absence of perimeter recombination and busbars in D3, as mentioned previously. Afterwards, RF, D2 and D3 cell design were selected for the cell fabrication. The images of the final cells are shown in the bottom row of Fig. 6.22. The RF and D2 cells are embedded in the quartered M2-sized cells and the rear contact is full-area contact. The D3 cells are bifacial and were prepared on the full-size M2 wafers. The iV_{oc} of three kinds of solar cells is on a similar level, while the gap between the V_{oc} and iV_{oc} is getting smaller as changing the cell design from RF to D3. Compared with the RF, about 3 mV gain of V_{oc} is achieved for the D2 cells as well as 0.2

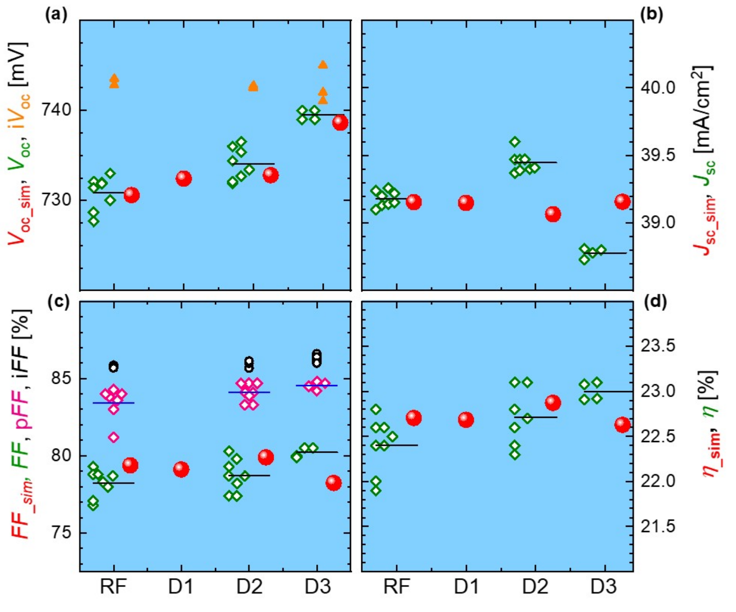

Figure 6.23.: *(a) Simulated open-circuit voltage ($V_{oc,sim}$), open circuit voltage (V_{oc}), implied open circuit voltage (iV_{oc}), (b) simulated short-circuit current density ($J_{sc,sim}$), short-circuit current density (J_{sc}), (c) simulated fill factor (FF_{sim}), fill factor (FF), (d) simulated power conversion efficiency (η_{sim}) and power conversion efficiency (η) of solar cells prepared with different cell designs. The schematic illuminations of different cell designs can be found in Fig. 6.22.*

mA/cm^2 increase of J_{sc}. This observation could be attributed to the thinner fingers used in the D2 cells. Finally, the new cell design on the quarter-M2-sized wafer brings around 0.2%$_{\mathrm{abs}}$ improvement of the efficiency. For the full-size solar cells, 6 mV higher V_{oc} and a similar FF as the D2 cells are observed in Fig. 6.23. Due to the worse reflection of grids than full-area silver contact on the rear side, the J_{sc} of the full-size cells is lower than the small size solar cells, which can be optimized by using back-reflector, such as the full area silver, the a-Si:H, the MgF$_2$, the SiO$_2$ etc [196, 246].

6.5. Optimization of full-size SHJ solar cells

In this section, SHJ solar cells with the optimized a-Si:H(i), ITO, a-Si:H(p) and ETL structure were fabricated on full-size M2 wafers. Firstly, we compare the performance of the solar cells with various ETL structure. Then one conclusion is drawn that the properties of the nc-Si:H(n) seed layer need to be optimized in order to further improve the power conversion efficiency. Secondly, the solar cells with 5 nm nc-Si:H(n) were fabricated at different deposition parameters. Afterwards, the effect of the ITO sputtering process on cell performance is investigated. Thirdly, the optimized nc-Si:H(n) layer is developed and utilized as seed layer in the solar cells with nc-Si:H/nc-SiO$_{\mathrm{x}}$:H(n) double layer.

6.5.1. Integration of nc-SiO$_{\mathrm{x}}$:H(n) in full-size SHJ solar cell

Fig. 6.24 (a) presents the sectional structure of bifacial SHJ solar cells on full-sized M2 wafers. For comparison, 10 nm nc-SiO$_{\mathrm{x}}$:H(n) single layer (Cell A), 5 nm nc-SiO$_{\mathrm{x}}$:H(n) with 5 nm nc-Si:H(n) contact layer (Cell C) and 5 nm nc-SiO$_{\mathrm{x}}$:H(n) with 5 nm nc-Si:H(n) seed layer (Cell D) are utilized as ETL in this section. According to the results in Sec. 6.2, 4 nm a-Si:H(i) was deposited as passivating layer on the front. Although a better cell performance is obtained for solar cells with the ITiO layer in Sec. 6.3.1, we used 70 nm ITO for the full-size device due to the size limitation of the substrate in the sputtering tool for ITiO. Tab. 6.5 summarizes the performance of the solar cells with three kinds of ETL. For the full-size solar

Table 6.5.: *I-V parameters of the full-size rear-junction SHJ solar cells with different electron transport layer (ETL): i) Cell A is with 10 nm nc-SiO$_x$:H(n) single layer, ii) Cell C is with double layer (5 nm nc-SiO$_x$:H(n) and 5 nm nc-Si:H(n) contact layer), and iii) Cell D is with double layer (5 nm nc-SiO$_x$:H(n) and 5 nm nc-Si:H(n) seed layer). The ETL structure is depicted in Fig. 6.1.*

	V_{oc} [mV]	J_{sc} [mA/cm^2]	FF [%]	η [%]	R_s [Ω cm^2]
Cell A	740.1 ±0.71	39.15 ±0.02	79.57 ±0.16	23.06 ±0.06	1.12 ±0.03
Cell C	739.6 ±0.52	38.95 ±0.19	81.15 ±0.5	23.38 ±0.09	0.70 ±0.08
Cell D	740.1 ±0.37	38.91 ±0.06	81.43 ±0.18	23.45 ±0.05	0.68 ±0.02

cells with double layer, more than 1.4%$_{abs}$ increase in the FF and 0.3%$_{abs}$ in the η are demonstrated, compared to the cells with nc-SiO$_x$:H(n) single layer. The FF of the solar cells with the nc-Si:H seed layer is 0.3%$_{abs}$ higher than that with the contact layer. Hence, about 0.07%$_{abs}$ increase of η is observed for the cells with the seed layer. The best full-size cell in this series is with 5 nm seed layer and 5 nm nc-SiO$_x$:H(n), showing V_{oc} of 740.1 mV, FF of 81.43%, J_{sc} of 38.91 mA/cm^2 and η of 23.45%.

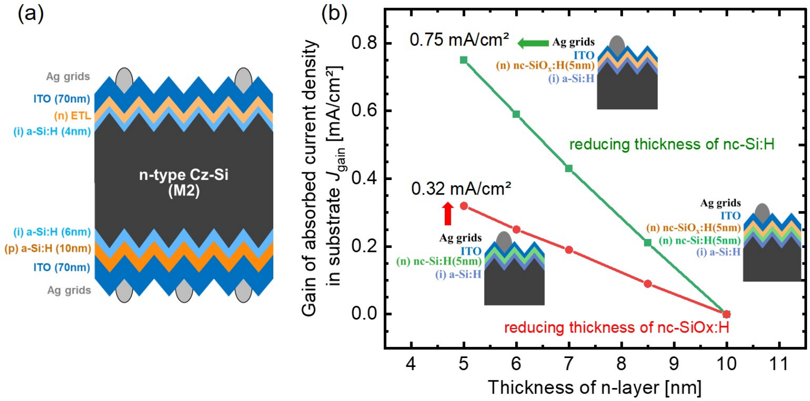

Figure 6.24.: *(a) Sectional structure of the full-size bifacial silicon heterojunction (SHJ) solar cells. (b) Simulated gain of the absorbed current density in the substrate (J_{gain}) as varying the electron transport layer thickness (d_{ETL}).*

Fig. 6.24(b) shows the gain of the absorbed current density in the substrate (J_{gain}) for Cell D as a function of the n-layer thickness, simulated by the OPAL 2 simulator. There is about 0.32 or 0.75 mA/cm^2 gain of current density for Cell D when decreasing the thickness of nc-SiO$_\mathrm{x}$:H(n) or nc-Si:H(n) from 5 to 0 nm, respectively. However, it is notable that varying the thickness of n-layer is a trade-off between J_{sc} and FF of the solar cells as mentioned in Sec. 6.1.2. Therefore, the full-size SHJ solar cells with nc-Si:H(n) seed layer were fabricated. The thickness of seed layer is varied from 5 to 0 nm, while thickness of nc-SiO$_\mathrm{x}$:H ($d_{\text{nc-SiOx:H}}$) is kept constant at 5 nm. The cells with 5 nm nc-Si:H(n) single layer as ETL are used as

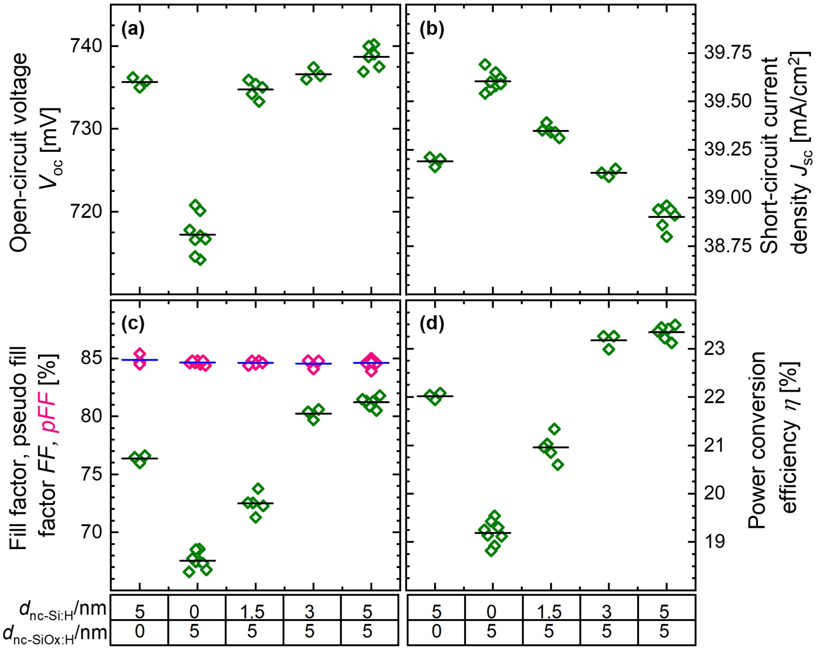

Figure 6.25.: *(a) Open-circuit voltage (V_{oc}), (b) short-circuit current density (J_{sc}), (c) fill factor (FF) and pseudo fill factor (pFF) and (d) power conversion efficiency (η) of the solar cells with nc-SiO$_x$:H/nc-Si:H double layer. The nc-Si:H(n) layer is below the nc-SiO$_x$:H(n) layer as a seed, thickness of which ($d_{\text{nc-Si:H}}$) is reduced from 5 nm to 0 nm. The thickness of nc-SiO$_x$:H ($d_{\text{nc-SiOx:H}}$) is kept constant at 5 nm.*

reference. Fig. 6.25 shows a deterioration of the V_{oc} and FF as varying $d_{\text{nc-Si:H}}$ from 5 to 0 nm, which can not be overcompensated by the increase of J_{sc}. Hence, the efficiency decreases from 23.45% to 23.2% when reducing $d_{\text{nc-Si:H}}$ from 5 to 3 nm. Further decreasing $d_{\text{nc-Si:H}}$ to 0 nm leads to a significant reduction of η to 19.2%. This result reveals that the performance of the cells with nc-SiO$_x$:H/nc-Si:H double layer is very sensitive to the thickness of nc-Si:H seed layer. The cell performance of reference is better than that with 5 nm nc-SiO$_x$:H single layer but worse than that with double layer (5 nm nc-SiO$_x$:H and 5 nm nc-Si:H seed layer). It indicates that the properties of nc-Si:H(n) seed layer need to be optimized to provide a faster crystallization growth and thinner incubation layer, otherwise it would be a obstacle to the further improvement of cell performance if using thinner n-layer.

6.5.2. Optimization of nc-Si:H(n) seed layer

Cell performance

The optical and electrical properties of nc-Si:H(n) layers can be adjusted by tuning the deposition parameters, such as the f_{SiH_4}, f_{PH_3} and P, as mentioned in Sec. 4. In this work, two kinds of nc-Si:H(n) films, named F1 and F2, were produced, the deposition parameters and opto-electronic properties of which are listed in Tab. 6.6. By reducing f_{SiH_4} from 0.75% to 0.5%, decreasing P from 200 to 100 W and increasing f_{PH_3} from 2% to 4%, a more conductive and crystalline nc-Si:H(n) film is obtained with slightly higher transparency and less density. Afterwards, we applied these two kinds of films at 5nm thickness in SHJ solar cells as ETL, named D1 and

Table 6.6.: *Deposition parameters and opto-electronical properties of two kinds of nc-Si:H(n) layers, named F1 and F2, at thickness of 35 nm and with 6 nm a-Si:H(i) underneath.*

	f_{SiH_4} [%]	f_{PH_3} [%]	p [mbar]	P [W]	σ [S/cm^2]	F_c [%]	E_{04} [eV]	n @ 632nm
F1	0.75	2	2.5	200	0.9	49	2.01	3.98
F2	0.5	4	2.5	100	27	63.5	2.03	3.83

D2, respectively.

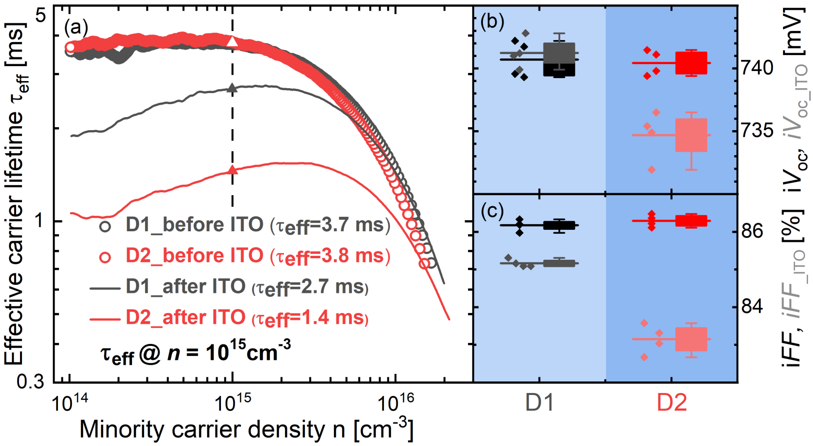

Figure 6.26.: *(a) The effective carrier lifetime (τ_{eff}) versus the minority carrier density (n), (b) the implied open-circuit voltage (iV_{oc}) and (c) the implied fill factor (iFF) of the D1 and D2 before and after the ITO sputtering process. The value of τ_{eff} indicated in the graph is determined at the minority carrier density of 10^{15} cm^{-3}. The nc-Si:H(n) films, named F1 and F2, are used in the D1 and D2, respectively, the detailed parameters of which are listed in Tab. 6.6. The box plots summarize the statistic of more than 4 samples per group and the line is the median position.*

The effective carrier lifetime (τ_{eff}) of the D1 and the D2 before and after the ITO sputtering process is illustrated in Fig. 6.26 (a). There is no noticeable difference between the lifetime curve of two samples before the ITO deposition. The τ_{eff} reaches 3.8ms at the minority carrier density of 10^{15} cm^{-3}. After the ITO deposition, a drop of lifetime curve can be observed in Fig. 6.26 (a), especially for the D2 from 3.8 to 1.4ms, which is much more severe than the D1. The difference of the passivation degradation between the D1 and D2 reveals that the sputter damage could be affected by the properties of nc-Si:H(n) layers. The iV_{oc} and iFF of the samples before and after ITO depositions are plotted in Fig. 6.26 (b) and (c), respectively. The iV_{oc} and iFF of both samples are similar before the ITO deposition, achieving 740 mV and 86.1%, respectively. After the ITO deposition, about 5 mV reduction of iV_{oc} can be noted for the D2, while the iV_{oc} of the D1 is almost the same as before.

Nevertheless, the iFF degradation of the D1 (1%$_{\mathrm{abs}}$) is much less than that of the D2 (3%$_{\mathrm{abs}}$).

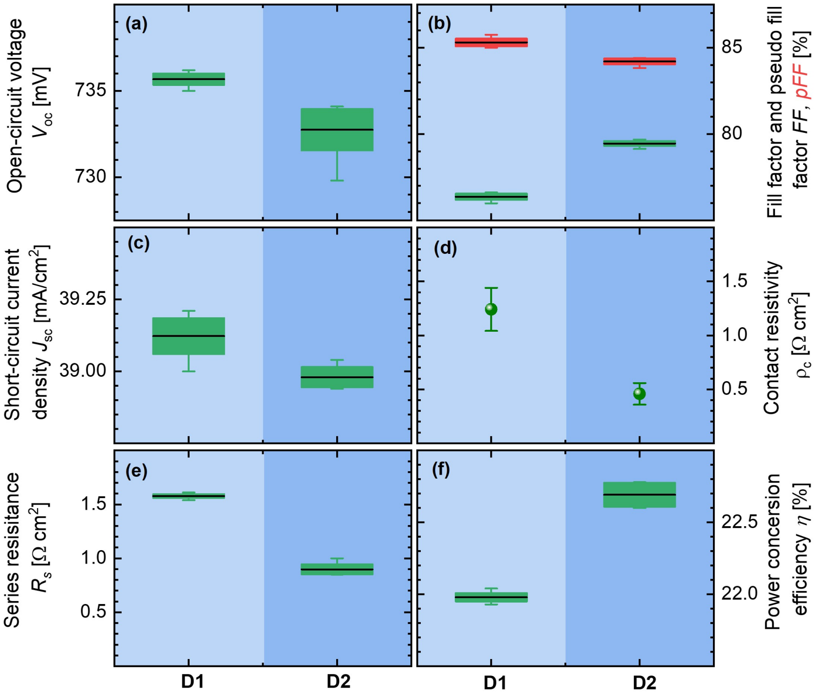

Figure 6.27.: *(a) Open-circuit voltage (V_{oc}), (b) fill factor (FF) and pseudo fill factor (pFF), (c) short-circuit current density (J_{sc}), (d) front total contact resistivity (ρ_c), (e) series resistance (R_s) and (f) power conversion efficiency (η) of the solar cells, named D1 and D2. The nc-Si:H(n) films, named F1 and F2, are used in the D1 and D2, respectively, the detailed parameters of which are listed in Tab. 6.6. The box plots summarize the statistic of more than 4 samples per group and the line is the median position.*

Fig. 6.27 shows the cell performance of the solar cells with different nc-Si:H(n) as electron transport layer. Compared to the D1, lower V_{oc} and pFF are obtained for the D2, consistent with the trend of iV_{oc} and iFF mentioned in Fig. 3. These results illustrate that the deterioration of the passivation during the sputtering process cannot be fully recovered by the annealing treatment after screen printing. Compared to the D1, a decreased gap between the pFF and FF and an increase of FF

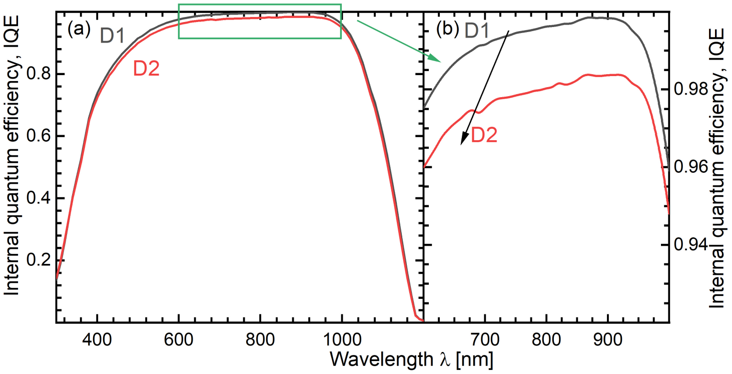

Figure 6.28.: *(a) Internal quantum efficiency (IQE) of the D1 and D2 as a function of the wavelength. (b) Zoom-in of the region highlighted in the graph (a).*

from 76% to 79% are observed for the D2. Around 0.1 mA/cm^2 reduction of J_{sc} is obtained in the D2 compared to the D1. This is due to the lower internal quantum efficiency in the wavelength range between 400 and 1000 nm as shown in Fig. 6.28, which could be interpreted by the worse carrier collection related to the passivation issue in D2 [247]. Furthermore, replacing F1 with F2 in the SHJ solar cells leads to a decline of the total contact resistivity from 1.3 to 0.5 Ω cm^2, which is contributed to the reduction of series resistance from 1.6 to 0.9 Ω cm^2. This result is in good agreement with the significant increase of FF mentioned previously. As a consequence, more than 0.6%$_{\text{abs}}$ gain of η is achieved by applying more conductive and crystalline nc-Si:H(n) as electron transport layer, reaching 22.8%. Although the FF of the D2 is 3%$_{\text{abs}}$ higher than that of the D1, the pFF of the D2 is about 1%$_{\text{abs}}$ lower. This is attributed to the serious passivation degradation after ITO deposition, which could be the limitation of η for the D2. Therefore, reducing the sputtering damage is very critical for the further improvement of the cell performance above 23%.

Analysis of the sputter damage

According to the previous discussion, a change of the sputter damage behavior is found when modifying the deposition parameters of nc-Si:H(n) layers. To reveal the correlation between the microstructure of nc-Si:H(n) and the sputter damage, here

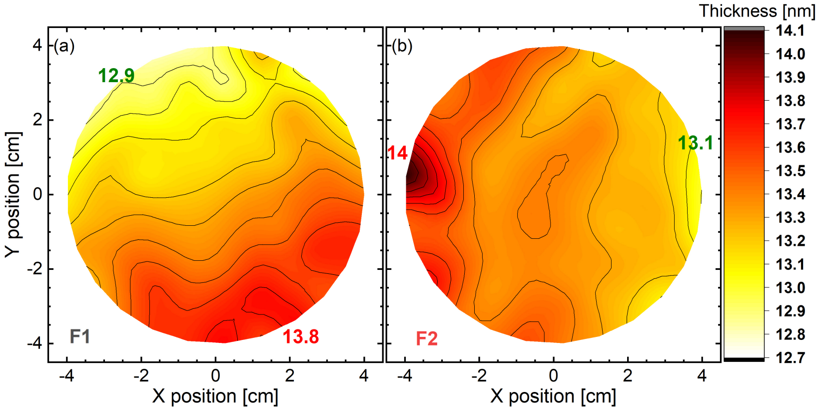

Figure 6.29.: *Total thickness distribution of the a-Si:H(i)/nc-Si:H(n) bi-layers at device-relevant thickness, (a) F1 and (b) F2, on polished wafer.*

two kinds of a-Si:H(i) / nc-Si:H(n) bi-layer, named F1 and F2 corresponding to the recipe used for nc-Si:H(n) layer, were deposited on the polished wafer and corning glass at device-relevant thickness. The total thickness distributions of the F1 and the F2 on the polished wafers are presented in Fig. 6.29, which are extracted from the spectroscopy ellipsometry via Tauc-Lorentz and Bruggeman effective medium approximation models [118]. Both films are with a thickness fluctuation below 1 nm. The average total thickness of both films is at the similar value, around 13.5 nm.

Fig. 6.30 shows the optical and structural properties of the nc-Si:H(n) films prepared at different deposition parameters. It is notable that the F2 is more transparent and with lower absorption coefficient than the F1, which is consistent with the optical band gap listed in Tab. 6.6. Therefore, one possibility for the worse passivation obtained in the D2 could be the increased transparency of the silicon layers. More vacuum ultraviolet (VUV) or ultraviolet (UV) photons reach the passivation layer or the wafer surface in the D2, yielding breakage of Si-H bonds and more dangling bonds in a-Si:H(i) bulk or a-Si:H(i)/c-Si(n) interface [210, 248–251]. The IR spectra of the F1 and the F2 in the wavenumber range of 1800~2200cm^{-1} is displayed in Fig. 6.30 (c) and Fig. 6.30 (d), respectively. The spectra can be fitted with two Gaussian-deconvoluted curves, which are the Si-H low stretching mode

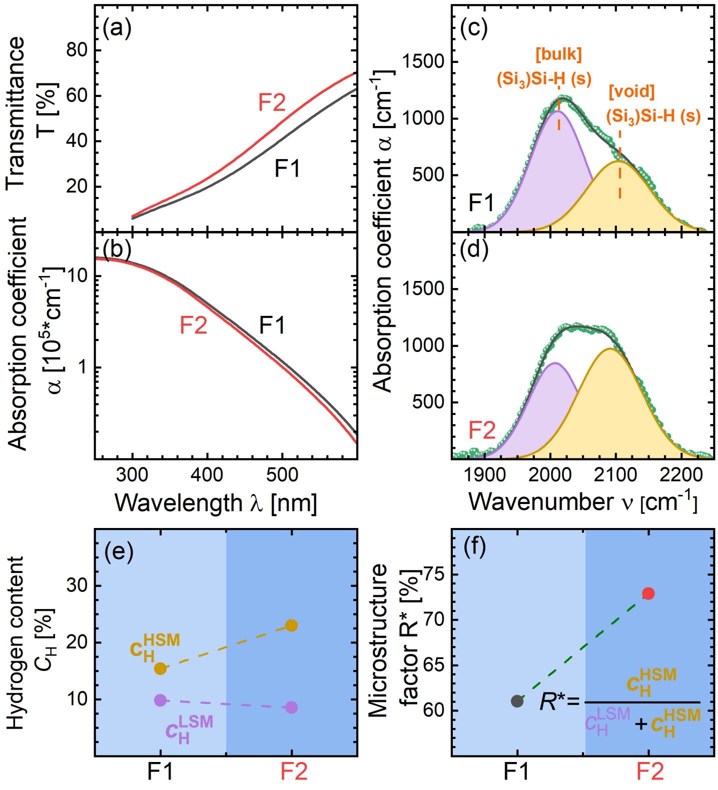

Figure 6.30.: *(a) Transmittance (T) and (b) absorption coefficient (α) of the a-Si:H(i)/nc-Si:H(n) stacks as a function of the wavelength. (c-d) Deconvolution of the IR absorption spectrum for the a-Si:H(i)/nc-Si:H(n) stacks into Si-H low stretching mode (LSM) and high stretching mode (HSM). The vertical dash lines define the position of the LSM and HSM. (e) The hydrogen content* c_H^{LSM}, c_H^{HSM} *and (f) the microstructure factor* R^* *estimated from the equation indicated in the graph. Two kinds of a-Si:H(i)/nc-Si:H(n) stacks at device-relevant thickness were prepared in this work, named F1 and F2, corresponding to the recipes used for nc-Si:H(n) layer in D1 ans D2.*

(LSM) at 2000cm^{-1} and high stretching mode (HSM) at 2090cm^{-1} [101, 102], marked with different color. Commonly the Si-H vibration in LSM is associated with the isolated monohydride embedded in the dense a-Si bulk and that in HSM is related to the clustered H on the inner surfaces of voids [101, 102]. The bonded hydrogen

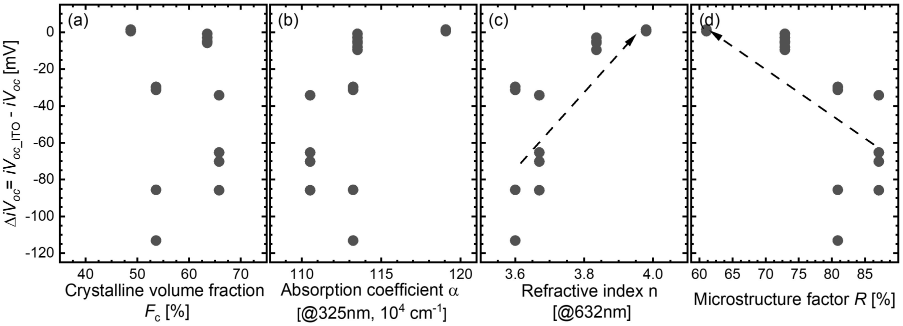

Figure 6.31.: *The difference of implied open-circuit voltage ($\triangle iV_{oc}$) before and after ITO deposition for the devices with different nc-Si:H(n) layers versus (a) their crystalline volume fraction (F_c), (b) absorption coefficient (α) at the wavelength of 325 nm, (c) refractive index (n) at wavelength of 632 nm and (d) microstructure factor (R^*). The dash line works as a guide for eyes.*

content in the LSM (c_H^{LSM}) and HSM (c_H^{HSM}) can be extracted from the IR spectrum via Eq. 3.5 [93, 252], more information of which can be found in Sec. 3.2.1. It is notable that higher c_H^{HSM} and slightly lower c_H^{LSM} are obtained in the F2 compared with the F1. This result reveals more voids and less dense structure are generated in the amorphous network of the F2. Hence, an increase of the microstructure factor (R^*), defined by equation: $R^* = (c_H^{LSM})(c_H^{LSM}+c_H^{HSM})$, from 61% to 73% is found in Fig. 6.30(f), demonstrating a more porous film [103,253–255]. The difference of iV_{oc} ($\triangle iV_{oc}$) before and after ITO deposition for the devices with different nc-Si:H(n) layers in Ref [256] is plotted versus the material properties in Fig. 6.31. No noticeable relationship between the F_c and the $\triangle iV_{oc}$ can be observed in Fig. 6.31 (a), while lower absolute value of the $\triangle iV_{oc}$ is obtained at lower R^*, higher α or higher n. This reveals that the microstructure of the nc-Si:H layers could play a dominant role on the generation of the sputter damage.

Evidence from literatures demonstrates that the sputter damage could be assigned to not only the VUV or UV radiations related to the oxygen or Argon plasma but also to the ion bombardment during the sputter-deposition of ITO layers [257–262]. The substrate is exposed to thermal and high energy electrons and the atoms/ions of the target material or the process gases [263]. An excess of charge

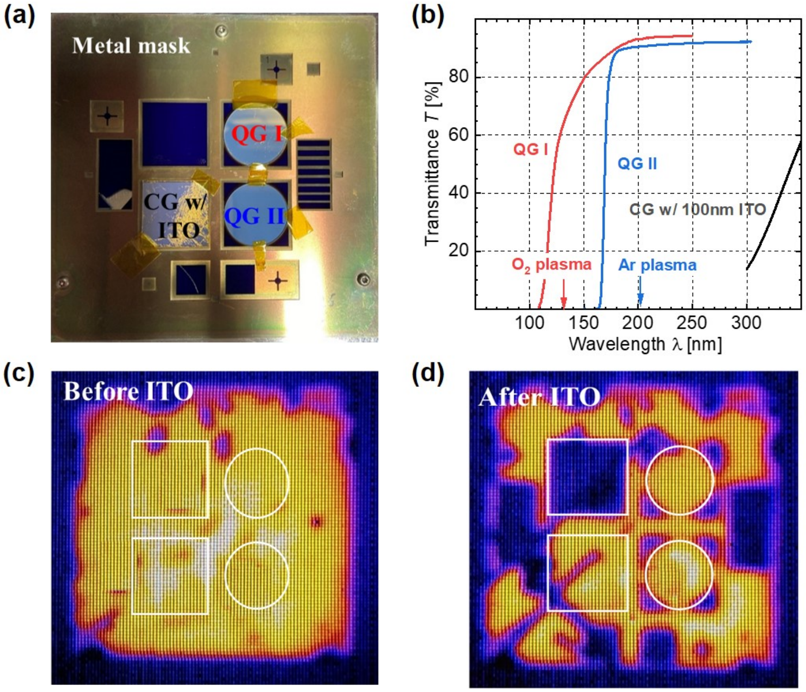

Figure 6.32.: *(a) Layout of the lifetime sample with a metal mask and three kinds of filters: MgF_2, quartz glass (QG) and corning glass (CG), on corresponding positions. (b) The transmittance of the filters as a function of the wavelength. The arrow marks are located in the emission peak of the O_2 plasma or Ar plasma. The photo-luminescence images of the lifetime sample (c) before and (d) after the ITO sputter process. The positions of the filters are marked with white circles or rectangles.*

carriers or electron-hole pairs in the silicon film could be excited by the secondary electron emission or the ionization energy provided by the ion neutralization process. These carriers would facilitate the emission of H and the breakage of the Si-H bonds in the a-Si:H(i) layer or on the c-Si surface, causing the deterioration of the surface passivation [258, 264–266].

In order to clarify where the sputter damage comes from in this work, lifetime sample with different filters on top was fabricated, the detailed layout of which is displayed in Fig. 6.32 (a). The wafer was put into a metal mask before the sputtering process, by which four small squares with area of 20 × 20 mm^2 can be defined. During the ITO deposition, three of them were shielded by filters (corning glass (CG), MgF$_2$ and quartz glass (QG)) to distinguish the degradation of the passivation related to the optical radiation from the ion bombardment. The filter excludes the ion bombardment and other potential direct reactions of the plasma with the silicon layers. Fig. 6.32 (b) shows the transmittance curves of different filters used in this work. The MgF$_2$ filter blocks the photons with wavelengths below 110 nm (>11.3 eV), whereas it has a 60% transmittance at the emission peak of 130.5 nm (9.5 eV) related to the oxygen plasma. The cutoff wavelength of the QG filter is 160 nm (>7.75 eV) while it has 90% of transmittance at the emission peak of 210 nm (5.9 eV) associated with Ar plasma [262,267]. The photons with wavelength <250 nm are all absorbed by the CG to get rid of the potential degradation induced by the VUV and UV radiation. Fig. 6.32 (c) and (d) shows the photo-luminescence (PL) image of the lifetime sample before and after the ITO depositions. A strong

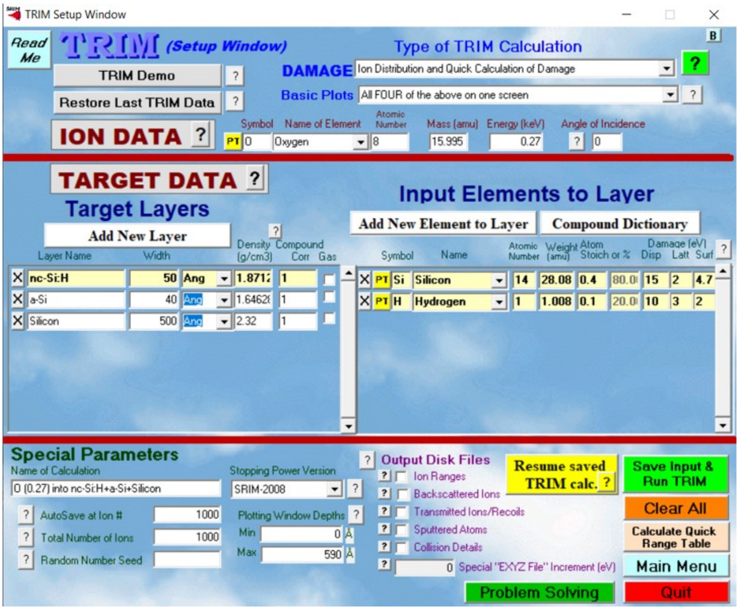

DAMAGE: Ion Distribution and Quick Calculation of Damage

Basic Plots: All FOUR of the above on one screen

	Symbol	Name of Element	Atomic Number	Mass (amu)	Energy (keV)	Angle of Incidence
PT	0	Oxygen	8	15.995	0.27	0

	Layer Name	Width		Density (g/cm3)	Compound Corr	Gas
☒	nc-Si:H	50	Ang	1.871	1	☐
☒	a-Si	40	Ang	1.6462	1	☐
☒	Silicon	500	Ang	2.32	1	☐

		Symbol	Name	Atomic Number	Weight (amu)	Atom Stoich	or %	Damage (eV) Disp	Latt	Surf
☒	PT	Si	Silicon	14	28.08	0.4	80.0	15	2	4.7
☒	PT	H	Hydrogen	1	1.008	0.1	20.0	10	3	2

Name of Calculation: 0 (0.27) into nc-Si:H+a-Si+Silicon

Stopping Power Version: SRIM-2008

AutoSave at Ion #: 1000

Total Number of Ions: 1000

Random Number Seed:

Plotting Window Depths: Min 0 Å, Max 590 Å

☐ Ion Ranges
☐ Backscattered Ions
☐ Transmitted Ions/Recoils
☐ Sputtered Atoms
☐ Collision Details
0 Special "EXYZ File" Increment (eV)

Figure 6.33.: *Setup window of the Stopping and Range of Ions in Matter (SRIM) software based on Monte Carlo simulation method.*

sputter damage is observed as expected for the small square without the filter, while no noticeable deterioration of the passivation can be found for the squares with the filter. This result demonstrates that the ion bombardment is the dominant reason for the sputter damage in the present situation. A notable drop of the absorptance in HSM after the ITO sputtering process was reported by Stefan de Wolf et al., demonstrating the sputter damage may mainly arise from the bonding changes of the a-Si:H subsurface region [261]. Compared to the F1, more hydrogen bonded on the inner surface of voids is detected for the F2, which could suffer from a stronger rupture of the Si-H bonds and promote the deterioration of passivation. Furthermore, the ions with kinetic energies impinging on the nc-Si:H(n) film could displace the surface or bulk Si atoms of the nc-Si:H layer or even penetrate into the a-Si:H(i) underneath by ion-Si atoms collisions. These activities would cause the generation of metastable defects in the Si network along the ion incursion path in the films [258, 268, 269]. The voids in the network are much easier to be passed through by ions. Hence, a larger injured area in the D2 may be induced compared to the D1, giving rise to more severe degradation of the passivation quality.

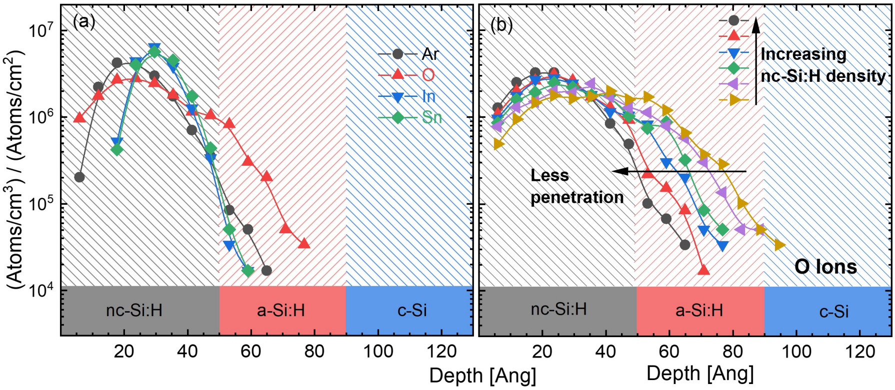

Figure 6.34.: *Distribution of (a) different ions involved in the sputtering plasma and (b) the oxygen ions with an initial kinetic energy of 270 eV in the a-Si:H(i)/nc-Si:H(n) stacks simulated by SRIM. The properties of the nc-Si:H(n) layer in the graph (a) was set constant while the density of the layer in the graph (b) was tuned by changing the Si/H ratio.*

Fig. 6.34 (a) shows the penetration depth of different atoms with an initial kinetic energy of 270 eV in a-Si:H(i)/nc-Si:H(n) stacks, evaluated via the Stopping and Range of Ions in Matter (SRIM) software based on the Monte Carlo simulation method [270, 271]. The detailed setup of the SRIM in this work can be found in Fig. 6.33. A silicon wafer is used as the substrate and the double layer (40 angstrom a-Si:H and 50 angstrom nc-Si:H) is put upon the wafer. The binding energies (displacement energy, surface binding energy, and lattice binding energy) of the target atoms are left as defaults. The density of the nc-Si:H films can be

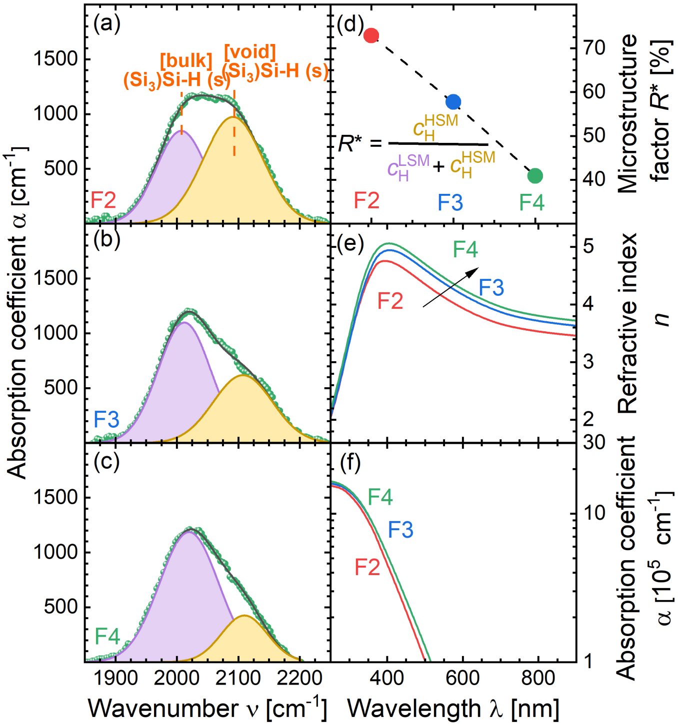

Figure 6.35.: *Deconvolution of the IR absorption spectrum for the a-Si:H(i)/nc-Si:H(n) stacks with (a) F2, (b) F3 and (c) F4 into Si-H low stretching mode (LSM) and high stretching mode (HSM). (d) The microstructure factor, (e) refractive index curves and (f) absorption coefficient curves of the F2, F3 and F4. The deposition parameters of F2, F3 and F4 can be found in Tab. 6.7.*

adjusted by tuning the stoichiometry of silicon and hydrogen element. The initial energy of the ions, such as O, Ar, In and Sn, was set at 270 eV since the voltage between the substrate and target is about 270 V during the sputtering process. The angle of incidence is defined with respect to the target surface, which is set at 0° since the ion is usually perpendicular to the target surface. As shown in Fig.6.34, all ions penetrate into the nc-Si:H(n) film and reach the bulk of the passivation layer. The incursion depth of Ar, In and Sn is smaller than O, which is expected to be the majority element of the negative charge incident on the substrate during the sputtering process [263]. A depth of 80 angstrom within the nc-Si:H(n)/a-Si:H(i) stack for the energetic oxygen atoms is demonstrated, which is very close to the a-/c-Si interface. This observation is in good agreement with that reported by Tusch et al [260]. There may be a high probability that some stray ions reach the a-Si:H(i)/c-Si(n) interface and cause the deterioration of the surface passivation. Fig. 6.34 (b) shows the oxygen ion distribution in the nc-Si:H(n)/a-Si:H(i) stack when varying the density of nc-Si:H(n). By depositing denser capping layer upon a-Si:H(i), a reduced spreading depth of the O ions in silicon films can be achieved, which could be a sufficient way to relieve the sputter damage in the D2.

Strategy to reduce sputter damage

Researches demonstrated that increasing the process pressure during the nc-Si:H deposition gives rise to a reduction of the microstructure factor as well as the intensity in HSM [272, 273]. Therefore, a variation of the pressure from 2.5mbar to 4.5mbar, was carried out in order to improve the layer quality. The detailed deposition param-

Table 6.7.: *Deposition parameters and layer properties of the nc-Si:H(n) layers, named F2, F3 and F4, at thickness of 35 nm and with 6 nm a-Si:H(i) underneath.*

	$f_{\mathrm{SiH_4}}$ [%]	$f_{\mathrm{PH_3}}$ [%]	p [mbar]	P [W]	σ [S/cm^2]	F_c [%]	E_{04} [eV]	n @632nm	R^* [%]
F2	0.5	4	2.5	100	27	63.5	2.03	3.83	73
F3	0.5	4	3.5	100	16.1	60.4	1.99	4.0	58
F4	0.5	4	4.5	100	6.8	56.1	1.96	4.1	41

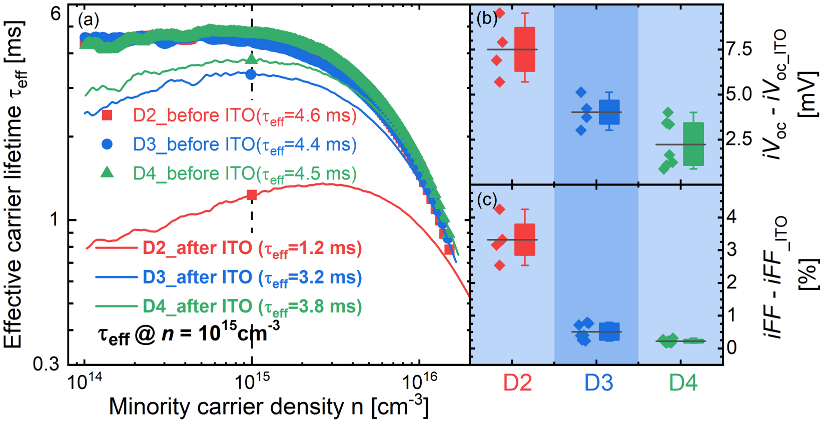

Figure 6.36.: *(a) Effective carrier lifetime (τ_{eff}) versus the minority carrier density (n) and the difference of (b) the implied open-circuit voltage (iV_{oc}) and (c) the implied fill factor (iFF) of the precursor devices, D2, D3 and D4, before and after the ITO sputtering process. The value of τ_{eff} indicated in the graph is determined at the minority carrier density of 10^{15} cm^{-3}. The nc-Si:H(n) layers, named F2, F3 and F4, are used in the D2, the D3 and the D4, respectively, the detailed deposition parameters of which are listed in Tab. 6.7. The box plots summarize the statistic of more than 4 samples per group and the line is the median position.*

eters and the opto-electronic properties of corresponding nc-Si:H films, named F2, F3 and F4, are listed in Tab. 6.7. The deconvolution of the IR absorption spectrum, the refection index curve and the absorption coefficient curve of these films are plotted in Fig. 6.35. Although a slight decrease of the optical band gap and crystalline volume fraction is detected at higher deposition pressure, an expected reduction of the microstructure factor of the nc-Si:H(n) films is acquired, accompanying with an increase of the refractive index. This result evidences a denser nc-Si:H(n) film achieved at higher pressure.

Afterwards, we applied the optimized nc-Si:H(n) films as electron-selective layer in rear-junction SHJ solar cells, named D2, D3 and D4. The QSSPC results of the precursor devices before and after ITO deposition are plotted in Fig. 6.36. All the lifetime results before ITO deposition are quite similar. No noticeable detriment on the passivation quality is found when varying the pressure during the deposition

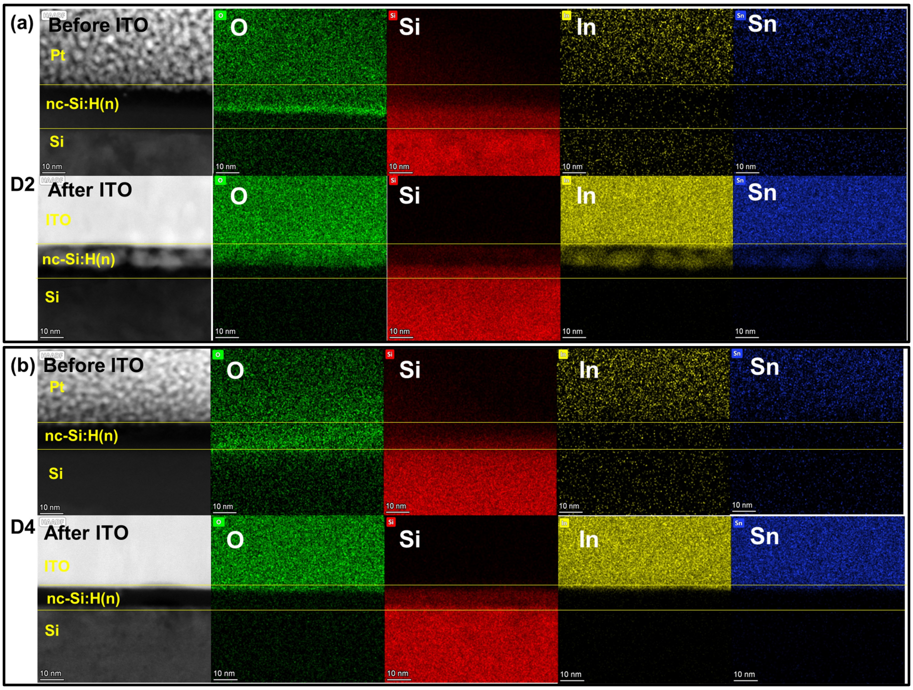

Figure 6.37.: *The scanning transmission electron microscopy (STEM) high-angle annular dark-field (HAADF) images combined with chemical compositional mapping measured by energy-dispersive X-ray (EDX) of (a) the D2 and (b) the D4 before and after ITO depositions. The yellow solid lines are guides to the eyes for distinguishing c-Si/a-Si:H(i) and nc-Si:H/ITO interfaces.*

of n-layer. The drop of the lifetime curve originated from the sputtering processes is reduced by increasing the deposition pressure of nc-Si:H(n) films. As shown in Fig. 6.36 (b) and (c), the difference of the iV_{oc} and the iFF measured before and after ITO deposition decreases from 7.5 to 2.5 mV and from 3.5%$_{\mathrm{abs}}$ to 0.3%$_{\mathrm{abs}}$, respectively. This observation demonstrates the success of the strategy to release the sputter damage by using a denser capping layer. The scanning transmission electron microscopy (STEM) high-angle annular dark-field (HAADF) images combined with energy-dispersive X-ray (EDX) mapping results of the D2 and the D4 before and after ITO sputtering process is shown in Fig. 6.37. There are O, In and Sn in the nc-Si:H for the D2 after ITO deposition, which cannot be found before ITO deposition, except O. This illustrates that an invasion of O, In and Sn into the nc-Si:H film for the D2 does happen during the ITO sputtering process. For the D4 that is with the denser nc-Si:H than the D2, no penetration of O, In and Sn is observed, proving that the denser nc-Si:H shows more resilience to the ion bombardment during the ITO sputtering process. This observation is consistent with the previous explanation on the sputter damage in the D2 and the simulation results shown in Fig. 6.34. The presence of O on the nc-Si:H films before ITO deposition is associated with the oxidation during the test sample preparation.

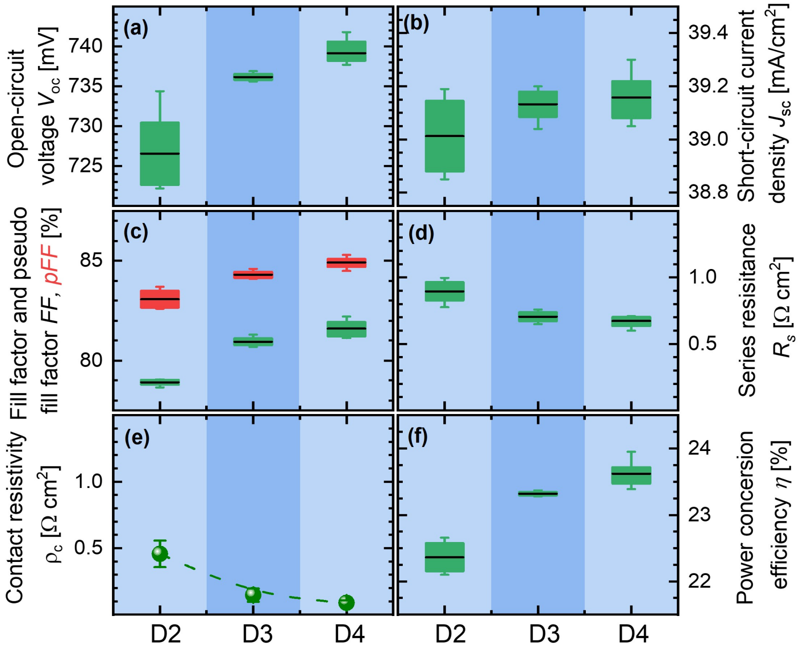

Figure 6.38.: *(a) Open-circuit voltage (V_{oc}), (b) short-circuit current density (J_{sc}), (c) fill factor (FF), pseudo fill factor (pFF), (d) series resistance (Rs), (e) front total contact resistivity (c) and (f) power conversion efficiency (η) of the solar cells, named D2, D3 and D4. The nc-Si:H(n) layers, named F2, F3 and F4, are used in the D2, the D3 and the D4, respectively, the detailed parameters of which are listed in Tab. 6.7. The box plots summarize the statistic of more than 4 samples per group and the line is the median position.*

Table 6.8.: *The I-V parameters of the full-size rear-junction SHJ solar cells with the nc-Si:H(n) layers at different thickness and without anti-reflectance coating on top.*

$d_{\text{nc-Si:H}}$ [nm]	iV_{oc} [mV]	$iV_{\text{oc,ITO}}$ [mV]	J_{sc} [mA/cm^2]	V_{oc} [mV]	FF [%]	η [%]	R_{s} [Ω cm^2]	ρ_{c} [Ω cm^2]
1.5	742.9 ±1.6	675.2 ±17	34.15 ±0.13	640.5 ±5.9 ±5.9	77.55 ±0.60	16.96 ±0.09	0.83 ±0.05	0.142
3	744.7 ±2.3	740.5 ±1.3	39.54 ±0.04	738.5 ±1.5	81.65 ±0.05	23.83 ±0.03	0.65 ±0.02	0.098
5	744.3 ±2.4	742.3 ±2.1	39.27 ±0.09	740.6 ±0.9	82.02 ±0.22	23.85 ±0.11	0.63 ±0.05	0.088

The final cell performance of the devices with different nc-Si:H(n) layers is displayed in Fig. 6.38. The average V_{oc} of the D4 increases by 12 mV compared with the D2. This improvement originates from the aforementioned decrease of the sputter damage. A slight gain of J_{sc} is achieved when using the denser nc-Si:H(n) layers, which is opposite to the optical properties shown in Tab. 6.7. This contrary could be explained by the improvement of the carrier transport and the collection in the silicon bulk due to the reduction of the front surface recombination. More apparently, a dramatic increase of FF from 79% to 81.5% and pFF from 83% to

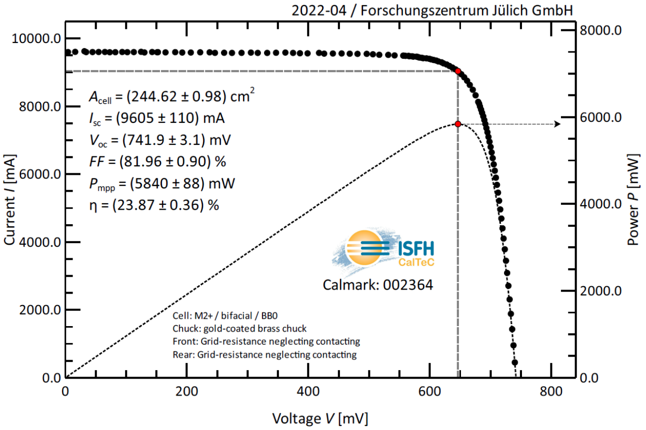

Figure 6.39.: *The IV characteristics and parameters of a 23.87% efficiency solar cell with 5nm nc-Si:H(n) as contact layer on a total area of 244.62 cm^2, certificated by ISFH.*

85% can be found in Fig. 6.38 (c) as varying the nc-Si:H(n) layer from F2 to F4, as a consequence of the reduced sputter damage. Furthermore, a lower R_s is also obtained in the D4, suggesting a reduced resistive loss and enhanced charge carrier transport. A reduced contact resistivity between ITO and nc-Si:H(n) from 0.48 to 0.1 Ω cm^2 is demonstrated in Fig. 6.38 (e) when increasing the deposition pressure of the nc-Si:H(n) layer from 2.5 to 4.5 mbar. Finally, an enhancement of the average power conversion efficiency from 22.4% to 23.6% is acquired. The best solar cell in this work exhibits a V_{oc} of 741.8 mV, FF of 82.2%, J_{sc} of 39.27 mA/cm^2 and η of 23.95% on the full-sized M2 wafer. Additionally, this cell was selected to be certificated at ISFH CalTec (Hamelin, Germany) and the measured IV parameters are represented in Fig. 6.39, showing a total area efficiency of 23.87 ±0.36%.

Before applying the optimized nc-Si:H(n) layer in the solar cells as seed layer, we prepared devices with thinner nc-Si:H(n) single layer ($d_{\text{nc-Si:H}} < 5$ nm) on full-size wafers. The I-V parameters are listed in Tab. 6.8. We can see that no obvious effect on the iV_{oc} after PECVD depositions when reducing $d_{\text{nc-Si:H}}$ from 5 to 1.5 nm. After the ITO deposition, the iV_{oc} of the cells with 3 nm nc-Si:H(n) is similar as that with 5 nm nc-Si:H(n). This reveals that 3 nm nc-Si:H is thick enough for the solar cell to overcome the ion bombardment issue during the sputtering process. Reducing $d_{\text{nc-Si:H}}$ from 5 to 3 nm leads to a expected increase of J_{sc} and decrease of FF. This is owing to the decline of the front parasitic absorption and the decreased crystalline volume fraction of the nc-Si:H layer. A dramatic reduction is found for the cells with 1.5 nm nc-Si:H(n) layer after ITO process. This could be explained by that the nc-Si:H capping layer is too thin to prevent the a-Si:H(i) or a-Si:H(i)/wafer interface underneath from the harmful ion bombardment. As a result, the performance of the cells with 1.5 nm nc-Si:H(n) layer is much worse than the others. Afterwards, we applied 2 nm nc-Si:H(n) as seed layer in SHJ solar cells, above which 3 nm nc-SiO$_x$:H(n) layer was deposited. The deposition parameters of the nc-SiO$_x$:H(n) layer are same as the nc-Si:H(n) layer, except CO$_2$ gas flow fraction (f_{CO_2}), which is varied from 0% to 50%. The solar cells with 5 nm nc-Si:H(n) single layer (f_{CO_2} = 0%) act as reference.

Fig. 6.40 presents the I-V parameters. A gain of J_{sc} is achieved as increasing the f_{CO_2} from 0 to 20% at the cost of FF reduction, yielding a similar η as the

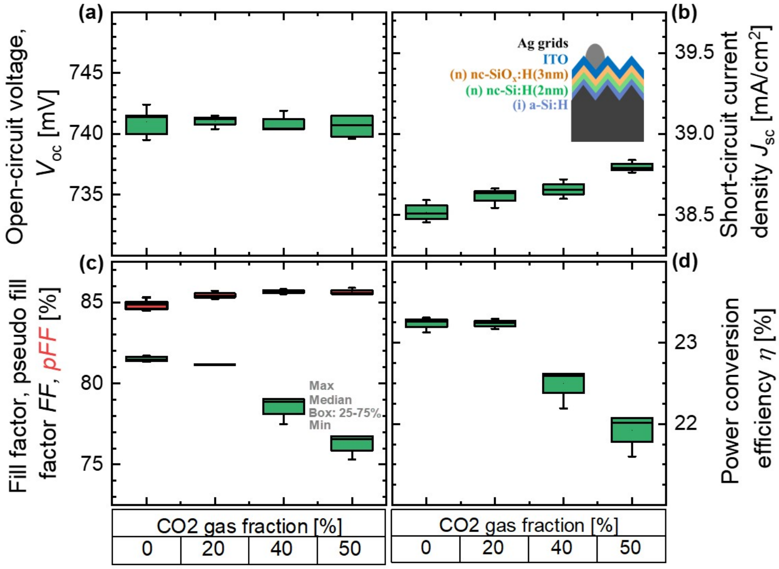

Figure 6.40.: *(a) Open-circuit voltage (V_{oc}), (b) short-circuit current density (J_{sc}), (c) fill factor (FF) and pseudo fill factor (pFF), and (d) power conversion efficiency (η) of the solar cells with a nc-SiO$_x$:H/nc-Si:H double layer. The cross-sectional structure of the layer stack on the front is indicted. About 2 nm nc-Si:H(n) was applied in the devices as seed layer, above which a 3 nm nc-SiO$_x$:H(n) layer was deposited. The deposition parameters of nc-SiO$_x$:H(n) are same as nc-Si:H(n), except f_{CO_2}, which was varied from 0 to 50%. The solar cells with 5 nm nc-Si:H(n) single layer (f_{CO_2} = 0%) act as reference.*

reference. Introducing more CO$_2$ ($f_{\mathrm{CO_2}} > 20\%$) into the deposition chamber results in a significant decrease in FF.This can not be compensated by the increase of J_{sc}, causing the reduction of the η. Due to the fluctuation of wafer quality and preparation process, the solar cells from this batch show a worse performance than these listed in Tab. 6.8, which can be seen from the reference cell.

7. Summary and Outlook

In this chapter, a summary of the main results in this work is presented. Besides, an outlook on the topic related to the application of nc-SiO$_x$:H layer in SHJ solar cells is presented.

7.1. Summary

7.1.1. Material development

The nc-SiO$_x$:H film consists of oxygen-rich amorphous silicon oxide and nanocrystalline silicon phases. The opto-electronic properties, such as E_{04}, F_c, σ, c_O, n and ε etc., can be adjusted by tuning the composition of the material phases in nc-SiO$_x$:H thin films. In this part of the thesis, the silicon films were deposited at low-power-low-pressure conditions, below 100 mW/cm^2 and 4.5mbar, in an industrial PECVD system with a 50×50 cm^2 substrate area. The properties of nc-SiO$_x$:H and nc-Si:H layers at the thickness range of 30∼50nm were compared and investigated systematically by varying the deposition parameters, such as P, p, f_{total}, $f_{\mathrm{CO_2}}$, $f_{\mathrm{PH_3}}$ and $f_{\mathrm{SiH_4}}$.

Power density It was found that the r_D, $U_{\mathrm{SiH_4}}$ and material properties are strongly dependent on the power density. The r_D and $U_{\mathrm{SiH_4}}$ increased first and then tended to be saturated as raising the power density. For nc-Si:H layer, a reduction of F_c from 55.5% to 34.3%, E_{04} from 1.99 to 1.90eV and σ from 5.2 to 0.18 S/cm were obtained when varying the power density from 40 to 200 mW/cm^2. It was demonstrated that the electrical properties of nc-SiO$_x$:H(n) are more sensitive to the variation of P than nc-Si:H(n) and the optical properties trend of both films are quiet different. Due to the incorporation of oxygen in the nc-SiO$_x$:H film, a-SiO$_x$:H matrix was created, which cannot be found in the nc-Si:H film. More oxygen content and voids were found for the nc-SiO$_x$:H films prepared at higher P. Hence, an increased volume fraction of a-SiO$_x$:H phase was observed, giving rise to a more transparent and less conductive nc-SiO$_x$:H film.

Process pressure It was found that the r_D increases from 0.35 to 0.45 angstrom/s and the U_{SiH_4} from 0.25% to 0.3% when varying the p from 2.5 to 4.5 mbar at the power density of 40 mW/cm^2. This was explained by the increased residence time of gas particles at higher p. For nc-Si:H and nc-SiO$_x$:H films, the c_O, F_c, E_{04} and σ all decreased as increasing p, whereas its influence on the nc-SiO$_x$:H film was slightly more severe than the nc-Si:H film. It was demonstrated that the refractive index and ε_2 curve moves up as increasing the p, accompanying with a peak shift of ε_2 to the photon energy related to the amorphous silicon phase. Besides, increasing the p also decreased the incorporated oxygen and the crystalline phase in the films. This was interpreted by more collision of the gas phases in the plasma when increasing p, which results in a lower mean free path and a decreased kinetic energy of the oxygen precursors or atomic hydrogen.

Total gas flow Increasing f_{total} from 520 to 1560 sccm gave rise to a faster deposition process of the nc-SiO$_x$:H layer and a lower silane utilization. It was found that the microstructure and opto-electronic properties of nc-SiO$_x$:H layer is strongly associated with f_{total}. At higher f_{total} lower c_O and E_{04} were observed, accompanying with a increase of F_c and σ. More hydrogen content and less voids were found for the films deposited at higher f_{total}. When increasing f_{total}, more SiH_4 and H_2 were introduced into the deposition chamber. Hence, more SiH_3, H radicals or ions were created on the substrate surface, which could enhance the growth of the silicon films and facilitate the breakage of weak SiH_2 bonds as well as the formation of strong Si-H bonds. Therefore, more ordered and relaxed network at low void fraction was achieved for nc-SiO$_x$:H(n) films deposited at higher f_{total}. Moreover, the power per molecules in the process chamber could be reduced when increasing f_{total}, and even lower than the threshold energy of the CO_2 dissociation reaction or ionization. Thus, the density of oxygen ions or radicals in the plasma would be reduced, leading to the drop of the oxygen content in the nc-SiO$_x$:H films as well as the optical band gap.

Gas composition There was no notable effect on the $U_{\mathrm{SiH_4}}$ and r_{D} when varying $f_{\mathrm{CO_2}}$ and $f_{\mathrm{PH_3}}$. A linear increase of r_{D} was observed as increasing $f_{\mathrm{SiH_4}}$, whereas $U_{\mathrm{SiH_4}}$ was almost constant. Introducing CO$_2$ into the deposition chamber hindered the growth of the crystalline silicon phase in nc-SiO$_x$:H film and promoted that of the a-SiO$_x$:H phases. A synergistic effect of CO$_2$ and PH$_3$ on the material properties of nc-SiO$_x$:H (n) films was demonstrated. When increasing $f_{\mathrm{PH_3}}$, the F_{c} and E_{04} decreased and σ increased slightly for the nc-Si:H(n) layer. However, for the nc-SiO$_x$:H(n) layer the F_{c} and σ increased firstly and then decreased once $f_{\mathrm{PH_3}}$ reaching to an optimized moderate value (opti-$f_{\mathrm{PH_3}}$). It was observed that the value of opti-$f_{\mathrm{PH_3}}$ becomes larger for the nc-SiO$_x$:H(n) layer at higher $f_{\mathrm{CO_2}}$. A reduction of c_{O} and E_{04} was found when raising $f_{\mathrm{PH_3}}$. It was illustrated that the utilization of PH$_3$ may weaken the oxygen incorporation into the material moderately and promote the transition of a-SiO$_x$ to a-Si or nc-Si phases in the nc-SiO$_x$:H films, especially at larger $f_{\mathrm{CO_2}}$. More P atoms incorporated in nc-SiO$_x$:H(n) films when increasing PH$_3$ flow, which could be active dopants, providing extra electrons and improving the electronic properties, or inactive. It was observed that the dopants are insufficient in the silicon lattice when $f_{\mathrm{PH_3}}$ is low and the active doping level of nc-SiO$_x$:H films is enhanced by the extra P atoms if increasing $f_{\mathrm{PH_3}}$. When $f_{\mathrm{PH_3}}$ is more than opti-$f_{\mathrm{PH_3}}$ the increased P in the film was not in a doping active state and the formerly active P dopants were no longer active. These considerable amounts of dopants in the lattice may disrupt the periodicity of the crystal lattice and retard the growth of nc-Si phase, causing the drop of F_{c} and σ. Increasing $f_{\mathrm{SiH_4}}$ resulted in a substitution of nc-Si by a-Si phases for nc-Si:H layers, giving rise to a reduction of σ, E_{04}. For nc-SiO$_x$:H(n) layers, a transformation of a-SiO$_x$:H to nc-Si:H phases ($f_{\mathrm{SiH_4}}$<1%) or nc-Si:H to a-Si:H phases ($f_{\mathrm{SiH_4}}$>1%) was found as raising $f_{\mathrm{SiH_4}}$, contributed to a similar trend in σ as nc-Si:H. For nc-SiO$_x$:H layers prepared at lower $f_{\mathrm{SiH_4}}$ more oxygen were incorporated in the films, yielding an increased optical band gap and lower refractive index. Besides, more sensitive material properties to the variation of $f_{\mathrm{SiH_4}}$ were observed for the nc-SiO$_x$:H(n) films produced at larger $f_{\mathrm{CO_2}}$.

Overview of opto-electronic properties It was demonstrated that the opto-electronic properties of the silicon films are strongly dependent on the phase composition. The nc-Si:H phase provides the conductive transport path for carriers and the highly transparent oxygen-rich a-SiO$_x$:H phase is responsible for the wide optical band gap. Based on the microstructure and oxygen content, the silicon films prepared in this work can be divided into three groups: a-SiO$_x$:H, nc-SiO$_x$:H and nc-Si:H. For the films in nc-Si:H group, more than 50% of F_c, σ in the range of 1.0$\sim$100 S/cm, and 1.8$\sim$2.05 eV of E_{04} were achieved. It was found that the σ of the films in nc-SiO$_x$:H group can be varied in the range between 10^{-8} and 1.0 S/cm, and the E_{04} is between 2.0 and 2.35 eV. More transparent ($2.35<E_{04}<2.5$) but less conductive ($\sigma < 10^{-8}$ S/cm) films were obtained for the a-SiO$_x$:H group than the others. To acquire nc-SiO$_x$:H with high transparency and sufficient conductivity, high volume fraction of a-SiO$_x$:H and nc-Si:H phase but low a-Si:H volume fraction was suggested. The material properties of the nc-SiO$_x$:H(n) films prepared in this work were nearly identical to that of the films in literature, which are thicker (200$\sim$2000nm) and prepared in a much smaller chamber. Furthermore, a very good homogeneity of the nc-SiO$_x$:H(n) layer prepared in this large-area system was proved.

7.1.2. Integration in SHJ Solar cell

For the application in SHJ solar cells as window layer, the nc-SiO$_x$:H(n) films have to fulfill certain requirements: i) high transparency for low parasitic absorption, ii) suitable refractive index for low light reflection on the front, iii) sufficient conductivity and crystalline volume fraction for efficient carrier transport, iv) no negative effect to the passivation quality of a-Si:H(i) underneath and v) firm to prevent a-Si:H(i)/nc-SiO$_x$:H(n) from potential passivation damage related to TCO deposition process. To fulfill these requirements, the relationship between cell performance and opto-electronic properties of nc-SiO$_x$:H(n) was investigated. Then a detailed power loss analysis was carried out by Quokka3 simulation and strategies to reach 24% of η were pointed out. Afterwards, the comprehensive optimization was performed to further improve the cell performance and to lower fabrication cost, including adjusting the structure of ETL, utilizing hydrogen plasma treatment during the a-Si:H(i) deposition, using innovated TCO and highly conductive nc-Si:H(n) layers.

Impact on the passivation It was found that the passivation quality of a-Si:H(i) is thickness dependent and can be improved by introducing hydrogen plasma treatment into a-Si:H(i) deposition. Putting a n-type layer upon a-Si:H(i) improved the passivation level, especially in the low injection range. A slightly lower τ_{eff} was observed for the cell with a-Si:H(i)/n-layer stack than that with a-Si:H(i) single layer at the same thickness. This was explained by the increased defect density in the n-layer compared to the intrinsic layer. It was proved that the passivation quality of a-Si:H(i)/n-layer stack is almost the same when replacing 7nm a-Si:H(n) with 15nm nc-SiO$_{\mathrm{x}}$:H(n) layer. Besides, there was ignorable influence on the τ_{eff} and iV_{oc} for the devices with nc-SiO$_{\mathrm{x}}$:H(n) when varying $f_{\mathrm{CO_2}}$, $f_{\mathrm{PH_3}}$ or $d_{\text{nc-SiOx:H}}$. This result reveals that the field-effect passivation induced by nc-SiO$_{\mathrm{x}}$:H(n) is not the dominant passivation mechanism for our devices. Additionally, it was demonstrated that using 7nm a-Si:H(n) or 15nm nc-SiO$_{\mathrm{x}}$:H(n) capping layer can prevent the a-Si:H(i) underneath from the passivation quality degradation after the ITO sputtering process.

Solar cell parameters The nc-SiO$_{\mathrm{x}}$:H(n) layers prepared at different $f_{\mathrm{CO_2}}$ and $f_{\mathrm{PH_3}}$ were utilized in SHJ solar cells as electron transport layer. No effect was observed on iV_{oc} and V_{oc} when varying the material properties of nc-SiO$_{\mathrm{x}}$:H(n) layers. The FF decreased by $2\%_{\mathrm{abs}}$ and the R_{s} increased from 1.0 to 1.5 Ω cm^2 when reducing the σ of the nc-SiO$_{\mathrm{x}}$:H(n) layer from 1.3 to 0.096 S/cm. A decreased ITO/n-layer ρ_{c} was found as increasing the conductivity, crystalline volume fraction or reducing the optical band gap of the nc-SiO$_{\mathrm{x}}$:H(n) layers. The band offsets can be noted at the ITO/nc-SiO$_{\mathrm{x}}$:H(n) and nc-SiO$_{\mathrm{x}}$:H(n)/a-Si:H(i) interface, acting as barriers to the carrier transport. On one hand, a lower activation energy can be found for the nc-SiO$_{\mathrm{x}}$:H(n) layer at higher σ and F_{c}, which could induce a lower and narrower barrier on the conductive band. This variation of the barrier can promote the tunneling process of the electron through the silicon films, improving the contact properties. On the other hand, the lower band gap of nc-SiO$_{\mathrm{x}}$:H(n) layer is the consequence of the increased electron affinity, which is beneficial for the achievement of a lower transport barrier to electrons. Adjusting the E_{04} from 2.05 to 2.25 eV gave rise to about 1.6 mA/cm^2 gain of J_{sc}. As a result, the best cell performance in the preliminary development, exhibiting V_{oc} of 728 mV, FF of 76.7%, J_{sc} of 39.1 mA/cm^2 and η of 21.83%, was achieved. A highly predictive model was built in Quokka3 simulator and the loss analysis of this champion cell was carried out. It was demonstrated that no single loss channel is obvious to have the dominating potential for the cell performance improvement and the bottleneck is the property of the layer stacks on the front. A road map to 24% of η was put forward based on the Quokka3 simulation results, which includes improving the bulk quality of the wafer, reducing the thickness of nc-SiO$_x$:H(n) and a-Si:H(i), decreasing the contact resistivity of ITO/doped-layer, utilizing more conductive TCO layer, optimizing the passivation layer, ameliorating the pattern of the front electrodes and the metallization process, etc.

Optimization of the cell performance A trade-off between the electrical and optical performance of the SHJ solar cells was observed as varying the thickness of nc-SiO$_x$:H(n) layer, indicating that nc-SiO$_x$:H(n) single layer can not completely fulfill the requirements of ETL for high-efficiency SHJ solar cells. Thus, the SHJ solar cells with the a-Si:H(n)/nc-SiO$_x$:H(n) and nc-SiO$_x$:H(n)/nc-Si:H(n) multi-layer at different thickness were fabricated on quarter-M2-size wafer. We found that the J_{sc} increases by 0.05 mA cm^{-2}/nm, 0.18 mA cm^{-2}/nm and 0.1 mA cm^{-2}/nm when reducing the thickness of nc-SiO$_x$:H(n), a-Si:H(n) and nc-Si:H(n), respectively. A reduced contact resistivity of ITO/ETL and an increased FF were achieved when depositing a-Si:H(n) upon nc-SiO$_x$:H(n) as contact layer. This result was explained by the lower conduction band offset on the ITO/ETL interface than that with nc-SiO$_x$:H(n) single layer. However, using a-Si:H(n)/nc-SiO$_x$:H(n) double layer caused a worse cell performance compared to the nc-SiO$_x$:H(n) single layer, as a consequence of the reduced J_{sc}, which can not be compensated by the improvement of electrical performance for the cells with a-Si:H(n) contact layer. A higher crystalline volume fraction was obtained for the ETL with nc-SiO$_x$:H/nc-Si:H(n) seed layer than that with nc-SiO$_x$:H(n) single layer or nc-SiO$_x$:H/nc-Si:H(n) contact layer at the same thickness. By using nc-SiO$_x$:H/nc-Si:H mutil-layer as ETL, 3% relatively higher efficiency was obtained than the reference, suggesting that using nc-Si:H(n) contact or seed layer is a more efficient method to improve the cell performance than a-Si:H contact layer.

An improved surface passivation on both side and a decreased parasitic absorption on the front was found for the cells with hydrogen plasma treated a-Si:H(i), yielding about 1$\%_{\mathrm{abs}}$ increase of η. By reducing the front a-Si:H(i) thickness from 6 to 4 nm, lower parasitic absorption and contact resistivity on the front were achieved, accompanying with a worse surface passivation, which can be compensated by increasing the doping concentration of the ETL fortunately. The FF loss related to the recombination in the space charge region and emitter was reduced for the cells with the hydrogen plasma treated a-Si:H(i). The FF loss related to the series resistance decreased when reducing the a-Si:H(i) thickness or improving the doping level of ETL. Besides, the solar cells with various TCO were prepared. It was demonstrated that the contact properties of ITiO/nc-SiO_x:H(n), AZO/nc-SiO_x:H(n) or IWO/nc-SiO_x:H(n) is better than that of ITO/nc-SiO_x:H(n), while the contact resistivity of Ag/IWO or Ag/AZO is much higher than that of Ag/ITO and Ag/ITiO. By depositing 110 nm MgF_2 upon 60 nm ITO as ARC, more than 0.6 mA/cm^2 gain of J_{sc} and 0.3$\%_{\mathrm{abs}}$ improvement of η were observed without compromising to FF and V_{oc}, Hence, 40.06 mA/cm^2 of J_{sc} and 22.8% of η were achieved. It was proved that the small size cells embedded in a quarter-M2 sized wafer suffer from 9 mV reduction of V_{oc} compared with the full size cells. This was attributed to the perimeter recombination and limits the improvement of cell performance. To reduce the influence of the perimeter recombination, several new designs of the front electrodes were put forwards, achieving 3 mV increase of V_{oc}. To totally omit the perimeter recombination and prove the industrial applicability of nc-SiO_x:H material in SHJ solar cells, we transferred the optimized ETL, ITO, a-Si:H(i) and a-Si:H(p) from quartered M2 wafer to full-size M2 wafer. About 23.06% of efficiency for cells with nc-SiO_x:H(n) single layer and 23.45% for cells with nc-SiO_x:H(n)/nc-Si:H(n) double layer were obtained. To further improve the device performance, ultra-thin (5nm) nc-Si:H(n) films were utilized in SHJ solar cells and optimized by varying its deposition parameters. A sputter damage was observed for cells with more porous nc-Si:H(n). It was demonstrated that the sputter damage is related to the ion bombardment by photo-luminescence images. The simulations by SRIM were performed, which reveals that the ions with an initial kinetic energy of 270 eV are able to penetrate the 5 nm nc-Si:H(n) protective layer and affect the microstructure of a-Si:H(i) films. Consequently, metastable defects would be created along the ion incursion path in the films, causing the degradation of the passivation. By using a denser nc-Si:H(n), a decreased sputter damage and an enhancement of η from 22.4% to 23.6% were demonstrated. The best performed solar cell exhibits a V_{oc} of 741.8 mV, FF of 82.2%, J_{sc} of 39.27 mA/cm^2 and η of 23.95% on an M2-sized wafer (244.3 cm^2).

7.2. Outlook

Recommendations for further investigation on the industrial processes of the SHJ solar cells with nc-$\mathrm{SiO_x}$:H layer are followed.

Cell performance In accordance with literature, several approaches are suggested to further improve the power conversion efficiency of the solar cells with nc-$\mathrm{SiO_x}$:H layer: i) applying the $\mathrm{CO_2}$ plasma treatment before the nc-Si:H(n) seed layer deposition or the phosphorous treatment to accelerate the nucleation of nanocrystals in nc-$\mathrm{SiO_x}$:H film [81, 82, 274]; ii) utilization of p-type nc-$\mathrm{SiO_x}$:H and nc-Si:H stack on the rear side of the solar cell to induce a stronger band bending on the valence band and to achieve a reduced energy barrier to holes compared with a-Si:H(p) [275]; iii) using back-reflector, such as $\mathrm{MgF_2}$, $\mathrm{SiO_2}$ etc., to increase J_{sc} of bifacial solar cells [196, 246]; iv) applying light-soaking treatment to improve amorphous/crystalline silicon interface passivation [276–279], v) usage of TCO multi-layer to optimize the contact properties of TCO/ETL and TCO/Ag while maintaining low parasitic absorption, vi) soft deposition of TCO in reactive plasma deposition (RPD) or atomic layer deposition (ALD) system to minimize the passivation degradation during the TCO process [280–284].

Throughput and cost The deposition rate of the nc-$\mathrm{SiO_x}$:H layer used in the champion cell in this work is around 0.035 nm/s, which is much lower than that of a-Si:H ($\sim$ 0.37 nm/s). The low deposition rate would be a obstacle for the application of nc-$\mathrm{SiO_x}$:H(n) in the industrial mass production. To deal with this issue, one strategy is the usage of the power generator at very high frequency (VHF). It was reported that the ionic energy distribution for VHF plasma shifts to lower energy and the ionic flux is much higher compared with RF. Thus, a high deposition rate and high-quality nc-Si:H film can be acquired by VHF-PECVD [285–288]. Additionally, it was demonstrated that the deposition of nc-Si:H film can be even faster without compromising to the film quality by using high working pressure and high discharge power in the VHF-PECVD system [175, 176, 289]. The biggest obstacle to the large-volume fabrication of SHJ solar cells is the higher levelized cost of electricity (LCOE) compared with PERC. This disadvantage is assigned to the high cost of tools for cell production, low-temperature silver paste for metallization and indium-based TCO layer. Therefore, the activities on the reduction of silver usage, the development of Cu-plating technology to replace silver and the strategies for indium reduction or indium-free in SHJ solar cells will become very important and meaningful.

Perovskite/SHJ tandem Recently, a certified efficiency of 29.8% was reported for perovskite/SHJ tandem solar cells, surpassing the Shockley-Queisser limit of single-junction silicon solar cells (>29.4%) [290]. Silicon-based tandem solar cells are suggested to be the mainstream PV production in the future. As a mixed-phase material, the refractive index and microstructure of nc-SiO_x:H films can be tuned in a wide range, making it a good candidate to be the interlayer in between the silicon and perovskite subcells to achieve current matching. Besides, the nc-SiO_x:H layers are with high longitudinal but low lateral conductivity, which is beneficial for a lower top-cell shunting compared with commonly used TCO-based tunnel junctions.

A. Symbols and abbreviations

Variables and physical constants

α	absorption coefficient
A	absorptance
$A_{\mathbf{X}}$	proportionality constant for each vibration
(b)	bending
χ	electron affinity
$c_{\mathbf{H}}$	hydrogen content
$\mathbf{c}_{\mathbf{H}}^{\mathbf{HSM}}$	bonded hydrogen content in HSM
$\mathbf{c}_{\mathbf{H}}^{\mathbf{LSM}}$	bonded hydrogen content in LSM
$c_{\mathbf{O}}$	oxygen content
$c_{\mathbf{X}}$	bond content
d	thickness
$d_{\textbf{a-Si:H,front}}$	front passivation layer thickness
$d_{\textbf{a-Si:H,rear}}$	rear passivation layer thickness
$d_{\textbf{contact}}$	contact layer thickness
$d_{\textbf{ETL}}$	electron transport layer thickness
$d_{\textbf{ITO}}$	indium tin oxide layer thickness
$d_{\mathbf{MgF_2}}$	magnesium fluoride layer thickness
$d_{\textbf{nc-Si:H}}$	nanocrystalline silicon layer thickness
$d_{\textbf{nc-SiOx:H}}$	nanocrystalline silicon oxide layer thickness
$d_{\textbf{seed}}$	seed layer thickness
$\Delta E_{\mathbf{c}}$	conduction band offset
$\Delta E_{\mathbf{v}}$	valence band offset
Δn	excess carrier density
η	power conversion efficiency

$\eta_{\mathbf{nor}}$	normalized power conversion efficiency
$\eta_{\mathbf{sim}}$	simulated power conversion efficiency
ε	complex dielectric constant
ε_1	real part of the complex permittivity
ε_2	imaginary part of the complex permittivity
E_{04}	optical band gap
$E_{\mathbf{a}}$	activation energy
$E_{\mathbf{c}}$	conduction band edge
$E_{\mathbf{f}}$	Fermi level
$E_{\mathbf{g}}$	band gap energy
$E_{\mathbf{i}}$	ionization energy
EQE	external quantum efficiency
$E_{\mathbf{v}}$	valence band edge
$E_{\mathbf{vac}}$	vacuum energy level
$F_{\mathbf{a\text{-}Si:H}}$	volume fraction of a-Si:H
$F_{\mathbf{a\text{-}SiO}_2}$	volume fraction of a-SiO_2
$F_{\mathbf{a\text{-}SiO}_\mathbf{x}}$	volume fraction of a-SiO_x:H
$F_{\mathbf{c}}$	crystalline volume fraction
$F_{\mathbf{nc\text{-}Si}}$	volume fraction of nc-Si
$F_{\mathbf{tinc\text{-}Si}}$	volume fraction of tinc-Si:H
FF	fill factor
$FF_{\mathbf{J}_{01}}$	fill factor without considering R_s, R_SH and J_{02}
$\Delta FF_{\mathbf{J}_{02}}$	fill factor loss from J_{02} related recombination
$\Delta FF_{\mathbf{R_s}}$	fill factor loss from R_s
$\Delta FF_{\mathbf{R_{SH}}}$	fill factor loss from R_SH
$FF_{\mathbf{nor}}$	normalized fill factor
$FF_{\mathbf{sim}}$	simulated fill factor
$f_{\mathbf{total}}$	total gas flow
$f_{\mathbf{H}_2}$	H_2 gas flow fraction
$f_{\mathbf{PH}_3}$	PH_3 gas flow fraction
$f_{\mathbf{TMB}}$	TMB gas flow fraction
$f_{\mathbf{CO}_2}$	CO_2 gas flow fraction
$f_{\mathbf{B}_2\mathbf{H}_6}$	$B_2\ H_6$ gas flow fraction

$f_{\mathbf{SiH_4}}$	SiH_4 gas flow fraction
$G(t)$	generation rate
I	electrical current
$I_{\mathbf{Raman}}$	Raman intensity
$I_{\mathbf{P}}$	phosphorus intensity
iFF	implied fill factor
IQE	internal quantum efficiency
$iV_{\mathbf{oc}}$	implied open circuit voltage
$iV_{\mathbf{oc,ITO}}$	implied open circuit voltage measured after ITO deposition
J	current density
$J_{\mathbf{0}}$	dark saturation current density
$J_{\mathbf{01}}$	saturation current density of the first diode
$J_{\mathbf{02}}$	saturation current density of the second diode
$J_{\mathbf{abs}}$	photo-current density loss due to parasitic absorption
$J_{\mathbf{abs,front}}$	photo-current density loss due to parasitic absorption in the front stack
$J_{\mathbf{abs,Si}}$	current density absorbed in silicon
$J_{\mathbf{e}}$	electron current density
$J_{\mathbf{gain}}$	gain of the absorbed current density in the substrate
$J_{\mathbf{mpp}}$	current density at the maximum power point
$J_{\mathbf{ph}}$	photo-current density
$J_{\mathbf{R}}$	current density loss due to reflection
$J_{\mathbf{sc}}$	short circuit current density
$J_{\mathbf{sc,nor}}$	normalized short circuit current density
$J_{\mathbf{sc,sim}}$	simulated short circuit current density
$J_{\mathbf{sc,EQE}}$	integrated short circuit current density from the EQE spectrum
$J_{\mathbf{re}}$	reflected current density on the front side
k	extinction coefficient
$k_{\mathbf{B}}$	Boltzmann's constant
λ	wavelength
L	distance between two silver contacts
$L_{\mathbf{T}}$	transfer length
μ	charge carrier mobility

$\mu_{\mathbf{e}}$	Hall electron mobility
mpp	maximum power point
n	refractive index
n	minority carrier density
$n_{\mathbf{act}}$	active dopant concentration
$N_{\mathbf{d}}$	doping concentration
$n_{\mathbf{e}}$	electron density
$\Delta n_{\mathbf{e}}$	excess electron density
$n_{\mathbf{h}}$	hole density
$n_{\mathbf{i}}$	intrinsic carrier concentration
$N_{\mathbf{Si}}$	atomic density of pure silicon
$N_{\mathbf{SiO_2}}$	atomic density of pure a-SiO_2
Φ	work function
$\Phi_{\mathbf{in}}$	photon flux of the incident light
$\Phi_{\mathbf{AM1.5g}}(\lambda)$	photon flux of the AM1.5g spectrum
p	deposition pressure
p_0	standard pressure
P	deposition power density
pFF	pseudo fill factor
$P_{\mathbf{max}}$	power density at maximum power point
$P_{\mathbf{sun}}$	input power density of the sun simulator
q	electron charge
$r_{\mathbf{D}}$	deposition rate
ρ	resistivity
$\rho_{\mathbf{c}}$	contact resistivity
$\rho_{\mathbf{c,front}}$	front contact resistivity
$\rho_{\mathbf{c,rear}}$	rear contact resistivity
$\rho_{\mathbf{Si}}$	density of silicon
R	reflectance
R^*	microstructure factor
$R_{\mathbf{Ag}}$	resistance due to the silver contact
$R_{\mathbf{Ag/TCO}}$	resistance due to TCO and silver contact
$R_{\mathbf{i}}$	resistance due to passivation layer

$R_{\mathbf{n}}$	resistance due to n-layer
$R_{\mathbf{s}}$	series resistance
$R_{\mathbf{SH}}$	shunt resistance
$R_{\mathbf{sheet}}$	sheet resistance
$R_{\mathbf{Si}}$	resistance due to silicon wafer
$R_{\mathbf{TCO}}$	resistance due to TCO
$R_{\mathbf{TCO/n}}$	resistance due to TCO and n-layer contact
S	surface recombination velocity
$S_{\mathbf{eff}}$	effective recombination velocity
σ	dark conductivity
(s)	stretching
sccm	standard cubic centimeters
S	surface recombination velocity
$\tau_{\mathbf{Aug}}$	Auger recombination related lifetime
$\tau_{\mathbf{bulk}}$	bulk lifetime
$\tau_{\mathbf{extr}}$	extrinsic recombination related lifetime
$\tau_{\mathbf{intr}}$	intrinsic recombination related lifetime
$\tau_{\mathbf{eff}}$	effective minority carrier lifetime
$\tau_{\mathbf{sur}}$	surface recombination related lifetime
$\tau_{\mathbf{rad}}$	radiative recombination related lifetime
$\tau_{\mathbf{SRH}}$	SRH recombination related lifetime
T	transmittance
$t_{\mathbf{dep}}$	deposition time
$t_{\mathbf{res}}$	residence time
$T_{\mathbf{sub}}$	substrate temperature
$U_{\mathbf{SiH_4}}$	silane utilization
V	voltage
$V_{\mathbf{j}}$	voltage at p-n junction
$V_{\mathbf{mpp}}$	voltage at the maximum power point
$V_{\mathbf{oc}}$	open circuit voltage
$V_{\mathbf{oc,nor}}$	normalized open circuit voltage
$V_{\mathbf{oc,sim}}$	simulated open circuit voltage
w	edge width

ν	wavenumber
W	thickness of the substrate
x	stoichiometry factor

Material and elements

:H	hydrogenated
a-	amorphous
Ar	argon
Ag	silver
a-Si:H	hydrogenated amorphous silicon
a-SiO_x:H	hydrogenated amorphous silicon oxide
AZO	Al-doped zinc oxide
B	boron
B_2H_6	diborane
C	carbon
c-	crystalline
CCl_4	carbon tetrachloride
CO_2	carbon dioxide
CO	carbon oxide
Cs^+	Caesium ion
c-Si	crystalline silicon
H	hydrogen
H_2	hydrogen
H_2O	water
HF	hydrofluoric acid
HCl	hydrochloric acid
(i)	intrinsic
In	indium
IO:H	hydrogen doped indium tin oxide
ITO	indium tin oxide
ITiO	titanium doped indium oxide
IWO	tungsten doped indium oxide
MgF_2	magnesium fluoride

N	nitrogen
N_2	nitrogen
NH_4HF_2	ammonium hydrogen fluoride
(n)	n-type doped
nc-	nanocrystalline
nc-Si	crystalline silicon
nc-Si:H	hydrogenated nanocrystalline silicon
nc-SiO_x:H	hydrogenated nanocrystalline silicon oxide
O	oxygen
O_2	dioxygen
O_3	ozone
(p)	p-type doped
P	phosphorus
PH_3	phosphine
Si	silicon
SiH	mono-hydride
SiH_2	silylene
SiH_3	silanide
SiH_4	silane
SiO_2	silicon dioxide
SiO_x	sub-stoichiometric silicon oxide
TCO	transparent conductive oxide
tinc-Si:H	tiny nanocrystalline or crystal-like phase at grain boundaries
$B(CH_3)_3$	trimethylborane
μc-	microcrystalline
μc-Si:H	hydrogenated microcrystalline silicon
μc-SiO_x:H	hydrogenated microcrystalline silicon oxide

Abbreviations

AFORS-HET	Automate FOR Simulation of HETerostructures
ALD	atomic layer deposition
AM	Air-Mass
Al-BSF	aluminum back surface field

ARC	anti-reflection coating
BSF	back surface field
CVD	chemical vapor deposition
CZ	Czochralski
DB	dangling bond
DC	direct current
DI	deionized
eCV	electrochemical capacitance voltage
EDX	energy-dispersive X-ray
ETL	electron transport layer
FELA	free energy loss analysis
FSF	front surface field
FTIR	Fourier transform infrared spectroscopy
FZ	float-zone
FZJ	Forschungszentrum Jülich GmbH
HAADF	high-angle annular dark-field
HPT	hydrogen plasma treatment
HIT®	heterojunction with intrinsic thin layer
HSM	high stretching mode
IBC	interdigitated back contact
IR	infrared
ITRPV	International Technology Roadmap for Photovoltaic
LCOE	levelized cost of electricity
LSM	low stretching mode
OPAL 2	freeware program for the optical analysis of the front surface of a solar cell
PDS	photothermal deflection spectroscopy
PECVD	plasma enhanced chemical vapor deposition
PERC	Passivated Emitter and Rear Cell
PL	Photoluminescence
PV	photovoltaic
PVD	physical vapor deposition
QSSPC	quasi steady-state photo conductance

RBM	random bond model
RF	radio frequency
RMM	random mixture model
RPD	reactive plasma deposition
SE	spectroscopy ellipsometry
SHJ	silicon heterojunction
ToF-SIMS	time-of-flight secondary ion mass spectroscopy
STEM	scanning transmission electron microscopy
SRH	Shockley-Read-Hall
SRIM	Stopping and Range of Ions in Matter
SWE	Staebler-Wronski effect
TLM	transfer length method
TMB	trimethylborane
TOPCon	tunnel oxide passivated contact
UV	ultraviolet
UV-Vis-NIR	Ultraviolet-Visible-Near Infrared Spectroscopy
UPS	ultraviolet photoelectron spectroscopy
VHF	very high frequency
VUV	vacuum ultraviolet
W	tungsten
ZEA-3	Central Institute for Engineering, Electronics and Analytics

B. List of Publications

1. **D. Qiu**, W. Duan, A. Lambertz, K. Bittkau, P. Steuter, Y. Liu, A. Gad, M. Pomaska, U. Rau, and K. Ding, *Front contact optimization for rear-junction SHJ solar cells with ultra-thin n-type nanocrystalline silicon oxide*, **Solar Energy Materials and Solar Cells**, 209 (2020): 110471
2. **D. Qiu**, W. Duan, A. Lambertz, Z. Wu, K. Bittkau, K. Qiu, Z. Yao, U. Rau, and K. Ding, *Function analysis of the Phosphine Gas Flow for n-type Nanocrystalline Silicon Oxide Layer in Silicon Heterojunction Solar Cells*, **ACS Applied Energy Materials** 4, 8 (2021): 7544-755
3. **D. Qiu**, W. Duan, A. Lambertz, K. Bittkau, and K. Ding, *Utilization of ultra-thin n-type Hydrogenated Nanocrystalline Silicon for Silicon Heterojunction Solar Cells*, 2021 IEEE 48th Photovoltaic Specialists Conference (PVSC), pp. 0806-0808. IEEE, 2021
4. **D. Qiu**, W. Duan, A. Lambertz, K. Bittkau, K. Qiu, U. Rau, and K. Ding, *Effect of oxygen and hydrogen flow ratio on indium tin oxide films in rear-junction silicon heterojunction solar cells*, **Solar Energy** 231 (2022): 578-585
5. **D. Qiu**, W. Duan, A. Lambertz, A. Eberst, K. Bittkau, U. Rau, and K. Ding, *Transparent Conductive Oxide Sputtering Damage on Contact Passivation in Silicon Heterojunction Solar Cells with Hydrogenated Nanocrystalline Silicon*, **Solar RRL** 2200651 (2022): 19
6. Y. Liu, M. Pomaska, W. Duan, **D. Qiu**, S. Li, A. Lambertz, A. Gad, U. Breuer, F. Finger, U. Rau, and K. Ding, *Phosphorus Catalytic Doping on Intrinsic Silicon Thin Films for the Application in Silicon Heterojunction Solar Cells*, **ACS Applied Materials Interfaces** 12, 50 (2020): 56615-56621
7. Z. Wu, W. Duan, A. Lambertz, **D. Qiu**, M. Pomaska, Z. Yao, U. Rau, L.

Zhang, Z. Liu, and K. Ding, *Low-resistivity p-type a-Si: H/AZO hole contact in high-efficiency silicon heterojunction solar cells*, **Applied Surface Science** 542 (2021): 148749

8. Z. Yao, W. Duan, P. Steuter, J. Hüpkes, A. Lambertz, K. Bittkau, M. Pomaska, **D. Qiu**, K. Qiu, Z. Wu, H. Shen, U. Rau, and K. Ding, *Influence of Oxygen on Sputtered TitaniumDoped Indium Oxide Thin Films and Their Application in Silicon Heterojunction Solar Cells*, **Solar RRL** 5, 1 (2021): 2000501
9. W. Duan, K. Bittkau, A. Lambertz, K. Qiu, Z. Yao, P. Steuter, **D. Qiu**, U. Rau, and K. Ding, *Improved Infrared Light Management with Transparent Conductive Oxide/Amorphous Silicon Back Reflector in HighEfficiency Silicon Heterojunction Solar Cells*, **Solar RRL** 5, 3 (2021): 2000576
10. S. Li, M. Pomaska, A. Lambertz, W. Duan, K. Bittkau, **D. Qiu**, Z. Yao, M. Luysberg, P. Steuter, M. Köhler, K. Qiu, R. Hong, H. Shen, F. Finger, T. Kirchartz, U. Rau, and K. Ding, *Transparent-conductive-oxide-free front contacts for high-efficiency silicon heterojunction solar cells*, **Joule** 5, 6 (2021): 1535-1547
11. J. Yu, PS. Leonard, **D. Qiu**, Y. Zhao, A. Lambertz, C. Zahren, L. Volker, W. Duan, J. Yu, and K. Ding, *Light-induced performance of SHJ solar modules under 2000 h illumination*, **Solar Energy Materials and Solar Cells** 235 (2022): 111459
12. W. Duan, A. Lambertz, K. Bittkau, **D. Qiu**, K. Qiu, U. Rau, and K. Ding, *A route towards highefficiency silicon heterojunction solar cells*, **Progress in Photovoltaics Research Applications**, (2021): 1-9
13. Q. Tang, W. Duan, A. Lambertz, K. Bittkau, M. Ainul, Y. Zhao, K. Zhang, Q. Yang, **D. Qiu**, F. Gunkel, M. Weber, U. Rau, and K. Ding, *> 85 % Indium Reduction for High-Efficiency Silicon Heterojunction Solar Cells with Aluminum-Doped Zinc Oxide Contacts*, **Solar Energy Materials and Solar Cells**, (2023): 112120

C. Curriculum Vitae

Personal details

Name	Depeng Qiu
Date of birth	April 23th, 1993
Place of birth	Jiangxi, China
Citizenship	Chinese

Education

1999-2003	Tiandun Central Primary School, Shangrao, China
2003-2005	Shangrao Second Primary School, Shangrao, China
2005-2008	Shangrao Second Middle School, Shangrao, China
2008-2011	Shangrao Middle School, Shangrao, China
2011-2015	Huazhong University of Science and Technology, Wuhan, China School of Material Science and Technology Bachelor in Material Processing Engineering
2015-2017	Sun Yat-Sen University, Guangzhou, China School of Material Science and Technology Master in Material Engineering
2017-now	PhD student at the Forschungszentrum Jülich GmbH, IEK-5, Photovoltaik

References

[1] International Energy Agency, Snapshot of Global PV Markets 2021, Technical report, 2021.

[2] G. M. Wilson, M. Al-Jassim, W. K. Metzger, S. W. Glunz, P. Verlinden, G. Xiong, L. M. Mansfield, B. J. Stanbery, K. Zhu, Y. Yan, J. J. Berry, A. J. Ptak, F. Dimroth, B. M. Kayes, A. C. Tamboli, R. Peibst, K. Catchpole, M. O. Reese, C. S. Klinga, P. Denholm, M. Morjaria, M. G. Deceglie, J. M. Freeman, M. A. Mikofski, D. C. Jordan, G. Tamizhmani, and D. B. Sulas-Kern, Journal of Physics D: Applied Physics **53** (2020).

[3] Y. Chen, P. P. Altermatt, D. Chen, X. Zhang, G. Xu, Y. Yang, Y. Wang, Z. Feng, H. Shen, and P. J. Verlinden, IEEE Journal of Photovoltaics **8**, 1531 (2018).

[4] M. Hermle, F. Feldmann, M. Bivour, J. C. Goldschmidt, and S. W. Glunz, Applied Physics Reviews **7** (2020).

[5] M. Taguchi, K. Kawamoto, S. Tsuge, T. Baba, and H. Sakata, Progress in Photovoltaics: Research and Applications **8**, 503 (2000).

[6] ITRPV, Itrpv **11th Editi**, 76 (2020).

[7] A. Louwen, W. Van Sark, R. Schropp, and A. Faaij, Solar Energy Materials and Solar Cells **147**, 295 (2016).

[8] M. Taguchi, A. Yano, S. Tohoda, K. Matsuyama, Y. Nakamura, T. Nishiwaki, K. Fujita, and E. Maruyama, IEEE Journal of Photovoltaics **4**, 96 (2014).

[9] D. Adachi, J. L. Hernández, and K. Yamamoto, Applied Physics Letters **107**, 23 (2015).

[10] Z. C. Holman, A. Descoeudres, L. Barraud, F. Z. Fernandez, J. P. Seif, S. De Wolf, and C. Ballif, IEEE Journal of Photovoltaics **2**, 7 (2012).

[11] L. Mazzarella, S. Kirner, B. Stannowski, L. Korte, B. Rech, and R. Schlatmann, Applied Physics Letters **106** (2015).

[12] K. Yoshikawa, H. Kawasaki, W. Yoshida, T. Irie, K. Konishi, K. Nakano, T. Uto, D. Adachi, M. Kanematsu, H. Uzu, and K. Yamamoto, Nature Energy **2** (2017).

[13] A. Richter, V. Smirnov, A. Lambertz, K. Nomoto, K. Welter, and K. Ding, Solar Energy Materials and Solar Cells **174**, 196 (2018).

[14] A. Richter, L. Zhao, F. Finger, and K. Ding, 2015 IEEE 42nd Photovoltaic Specialist Conference, PVSC 2015 , 2 (2015).

[15] A. Lambertz, T. Grundler, and F. Finger, Journal of Applied Physics **109** (2011).

[16] K. Ding, *Nanostructured Si-alloys for silicon solar cells*, PhD thesis, RWTH Aachen, 2014.

[17] W. Shockley, The Bell System Technical Journal **28**, 435 (1949).

[18] W. Fuhs, K. Niemann, and J. Stuke, AIP Conf Proc **345**, 345 (1974).

[19] J. I. Pankove and M. L. Tarng, Applied Physics Letters **34**, 156 (1979).

[20] Y. Hamakawa, K. Fujimoto, K. Okuda, Y. Kashima, S. Nonomura, and H. Okamoto, Applied Physics Letters **43**, 644 (1983).

[21] K. Okuda, H. Okamoto, and Y. Hamakawa, Japanese Journal of Applied Physics, Part 2: Letters **22**, 605 (1983).

[22] H. Matsuura, A. Matsuda, H. Okushi, T. Okuno, and K. Tanaka, Applied Physics Letters **45**, 433 (1984).

[23] H. Matsuura, T. Okuno, H. Okushi, and K. Tanaka, Journal of Applied Physics **55**, 1012 (1984).

[24] C. M. Matsuyama, Takao; Baba, Toshiaki; Tanaka, Makoto; Isomura, Masao; Tsuda, Shinya; Nakano, Shoichi; Kuwano, Yukinori; Lampert, Improvement of the conversion efficiency of poly-crystalline silicon thin film solar cell, in *Tech. Digest 5th International Photovoltaic Science and Engineering Conference, Kyoto, Japan*, pages 689–692, 1990.

[25] M. Tanaka, M. Taguchi, T. Matsuyama, T. Sawada, T. Shina, S. Nakano,

H. Hanafusa, and Y. Kuwano, Jpn.J.Appl.Phys **31**, 3518 (1992).

[26] K. Sano, United States Patent, 1993.

[27] M. Tanaka, S. Okamoto, S. Tsuge, and S. Kiyama, Development of hit solar cells with more than 21efficiency and commercialization of highest performance hit modules, in *3rd World Conference onPhotovoltaic Energy Conversion, 2003. Proceedings of*, volume 1, pages 955–958 Vol.1, 2003.

[28] H. Kanno, H. Sakata, M. Taguchi, and E. Maruyama, 26th European Photovoltaic Solar Energy Conference and Exhibition , 871 (2011).

[29] H. Fujiwara and M. Kondo, Applied Physics Letters **90** (2007).

[30] M. Tucci and G. De Cesare, Journal of Non-Crystalline Solids **338-340**, 663 (2004).

[31] U. De, N. Faculte, and D. Sciences, (2009).

[32] L. Korte, E. Conrad, H. Angermann, R. Stangl, and M. Schmidt, Solar Energy Materials and Solar Cells **93**, 905 (2009).

[33] Q. Wang, M. R. Page, E. Iwaniczko, Y. Q. Xu, L. Roybal, R. Bauer, B. To, H. C. Yuan, A. Duda, and Y. F. Yan, Conference Record of the IEEE Photovoltaic Specialists Conference (2008).

[34] K. Masuko, M. Shigematsu, T. Hashiguchi, D. Fujishima, M. Kai, N. Yoshimura, T. Yamaguchi, Y. Ichihashi, T. Mishima, N. Matsubara, T. Yamanishi, T. Takahama, M. Taguchi, E. Maruyama, and S. Okamoto, IEEE Journal of Photovoltaics **4**, 1433 (2014).

[35] M. Bivour, S. Schröer, and M. Hermle, Energy Procedia **38**, 658 (2013).

[36] M. Bivour, S. Schröer, M. Hermle, and S. W. Glunz, Solar Energy Materials and Solar Cells **122**, 120 (2014).

[37] D. Adachi, J. L. Hernández, and K. Yamamoto, Applied Physics Letters **107**, 22 (2015).

[38] LONGi, At 26.81solar cells, 2022.

[39] A. Kanevce and W. K. Metzger, Journal of Applied Physics **105** (2009).

[40] W. G. Van sark, F. Roca, and L. Korte, *Physics and technology of amorphous-crystalline heteronstrutures sillicon solar cells.*, 2012.

[41] M. Bivour, *SILICON HETEROJUNCTION SOLAR CELLS : Fraunhofer Institute for Solar Energy Systems ISE Silicon Heterojunction Solar Cells : Analysis and Basic Understanding*, PhD thesis, University of Freiburg, 2015.

[42] E. Maruyama, A. Terakawa, M. Taguchi, Y. Yoshimine, D. Ide, T. Baba, M. Shima, H. Sakata, and M. Tanaka, Conference Record of the 2006 IEEE 4th World Conference on Photovoltaic Energy Conversion, WCPEC-4 **2**, 1455 (2006).

[43] C. A. Deline, S. Ayala Pelaez, W. F. Marion, W. R. Sekulic, M. A. Woodhouse, and J. Stein.

[44] Y. Tawada, K. Tsuge, M. Kondo, H. Okamoto, and Y. Hamakawa, Shinku **25**, 448 (1982).

[45] S. T. Pantelides, Physical Review B **36**, 3479 (1987).

[46] D. L. Staebler and C. R. Wronski, Journal of Applied Physics **51**, 3262 (1980).

[47] S. W. Glunz, S. Rein, J. Y. Lee, and W. Warta, Journal of Applied Physics **90**, 2397 (2001).

[48] A. V. Shah, J. Meier, E. Vallat-Sauvain, N. Wyrsch, U. Kroll, C. Droz, and U. Graf, Solar Energy Materials and Solar Cells **78**, 469 (2003).

[49] P. Roca i Cabarrocas, Physica Status Solidi (C) **1**, 1115 (2004).

[50] S. Kirner, L. Mazzarella, L. Korte, B. Stannowski, B. Rech, and R. Schlatmann, 2015 IEEE 42nd Photovoltaic Specialist Conference, PVSC 2015 **5**, 1601 (2015).

[51] O. Vetterl, F. Finger, R. Carius, P. Hapke, L. Houben, O. Kluth, A. Lambertz, A. Mück, B. Rech, and H. Wagner, Solar Energy Materials and Solar Cells **62**, 97 (2000).

[52] B. Delley and E. F. Steigmeier, Physical Review B **47**, 1397 (1993).

[53] S. Usui and M. Kikuchi, Journal of Non-Crystalline Solids **34**, 1 (1979).

[54] S. Guha, J. Yang, P. Nath, and M. Hack, Applied Physics Letters **49**, 218 (1986).

[55] P. Sichanugrist, T. Yoshida, Y. Ichikawa, and H. Sakai, Journal of Non-Crystalline Solids **164-166**, 1081 (1993).

[56] K. Y. Chan, D. Knipp, A. Gordijn, and H. Stiebig, Journal of Applied Physics **104**, 1 (2008).

[57] T. Kilper, W. Beyer, G. Bräuer, T. Bronger, R. Carius, M. N. Van Den Donker, D. Hrunski, A. Lambertz, T. Merdzhanova, A. Mück, B. Rech, W. Reetz, R. Schmitz, U. Zastrow, and A. Gordijn, Journal of Applied Physics **105** (2009).

[58] A. Lambertz, *Development of Doped Microcrystalline Silicon Oxide and its Application to Thin-Film Silicon Solar Cells Ontwikkeling van gedoteerd microkristallijn siliciumoxide en de toepassing in dunne film zonnecellen Proefschrift Andreas Lambertz*, Dissertation, University Utrecht, 2015.

[59] A. Lambertz, T. Grundler, and F. Finger, Journal of Applied Physics **109**, 113109 (2011).

[60] A. Lambertz, V. Smirnov, T. Merdzhanova, K. Ding, S. Haas, G. Jost, R. E. Schropp, F. Finger, and U. Rau, Solar Energy Materials and Solar Cells **119**, 134 (2013).

[61] X. Wang and Z. M. Wang, *High-efficiency solar cells: Physics, materials, and devices*, volume 190, 2014.

[62] P. Sichanugrist, T. Sasaki, A. Asano, Y. Ichikawa, and H. Sakai, Solar Energy Materials and Solar Cells , 415 (1994).

[63] K. Yamamoto, M. Yoshimi, Y. Tawada, S. Fukuda, T. Sawada, T. Meguro, H. Takata, T. Suezaki, Y. Koi, K. Hayashi, T. Suzuki, M. Ichikawa, and A. Nakajima, Solar Energy Materials and Solar Cells **74**, 449 (2002).

[64] F. Finger, R. Carius, T. Dylla, S. Klein, S. Okur, and M. Günes, IEE Proc.-Circuits Devices Syst **150**, 300 (2003).

[65] D. Dominé, P. Buehlmann, J. Bailat, A. Billet, A. Feltrin, and C. Ballif, Physica Status Solidi - Rapid Research Letters **2**, 163 (2008).

[66] C. Banerjee, J. Sritharathikhun, A. Yamada, and M. Konagai, Journal of Physics D: Applied Physics **41** (2008).

[67] J. Sritharathikhun, H. Yamamoto, S. Miyajima, A. Yamada, and M. Konagai, Japanese Journal of Applied Physics **47**, 8452 (2008).

[68] M. A. Lieberman, *Principles of plasma discharges and materials processing*, John Wiley Sons, Inc., 1994.

[69] Safa Kasap and P. Capper, *Electronic and Photonic Materials*, 2017.

[70] J. Perrin, O. Leroy, and M. C. Bordage, Contributions to Plasma Physics **36**, 3 (1996).

[71] J. W. McConkey, C. P. Malone, P. V. Johnson, C. Winstead, V. McKoy, and I. Kanik, Physics Reports **466**, 1 (2008).

[72] A. Matsuda, Journal of Non-Crystalline Solids **59-60**, 767 (1983).

[73] C. C. Tsai, G. B. Anderson, R. Thompson, and B. Wacker, Journal of Non-Crystalline Solids **114**, 151 (1989).

[74] K. Nakamura, K. Yoshino, S. Takeoka, and I. Shimizu, Japanese Journal of Applied Physics **34**, 442 (1995).

[75] A. Matsuda, Thin Solid Films **337**, 1 (1999).

[76] H. Fujiwara, M. Kondo, and A. Matsuda, Journal of Applied Physics **91**, 4181 (2002).

[77] K. Nakamura, K. Yoshino, S. Takeoka, and I. Shimizu, Japanese Journal of Applied Physics **34**, 442 (1995).

[78] S. Kirner, O. Gabriel, B. Stannowski, B. Rech, and R. Schlatmann, Applied Physics Letters **102** (2013).

[79] P. Cuony, D. T. Alexander, I. Perez-Wurfl, M. Despeisse, G. Bugnon, M. Boccard, T. Söderström, A. Hessler-Wyser, C. Hébert, and C. Ballif, Advanced Materials **24**, 1182 (2012).

[80] N. Layadi, P. Roca I Cabarrocas, and B. Drevillon, Physical Review B **52**, 5136 (1995).

[81] L. Mazzarella, S. Kirner, O. Gabriel, S. S. Schmidt, L. Korte, B. Stannowski, B. Rech, and R. Schlatmann, Physica Status Solidi (A) Applications and Materials Science **214** (2017).

[82] N. Pellaton Vaucher, B. Rech, D. Fischer, S. Dubail, M. Goetz, H. Keppner, N. Wyrsch, C. Beneking, O. Hadjadj, V. Shklover, and A. Shah, Solar Energy Materials and Solar Cells **49**, 27 (1997).

[83] Y. Zhao, L. Mazzarella, P. Procel, C. Han, G. Yang, A. Weeber, M. Zeman, and O. Isabella, Progress in Photovoltaics: Research and Applications **28**, 425 (2020).

[84] G. Bugnon, G. Parascandolo, S. Hänni, M. Stuckelberger, M. Charrière, M. Despeisse, F. Meillaud, and C. Ballif, Solar Energy Materials and Solar Cells **120**, 143 (2014).

[85] J. P. Seif, A. Descoeudres, G. Nogay, S. Hanni, S. M. De Nicolas, N. Holm, J. Geissbuhler, A. Hessler-Wyser, M. Duchamp, R. E. Dunin-Borkowski, M. Ledinsky, S. De Wolf, and C. Ballif, IEEE Journal of Photovoltaics **6**, 1132 (2016).

[86] Y. Djeridane, A. Abramov, and P. Roca i Cabarrocas, Thin Solid Films **515**, 7451 (2007).

[87] J. T. Gudmundsson, Plasma Sources Science and Technology **29** (2020).

[88] D. Chen, L. Zhao, H. Diao, W. Zhang, G. Wang, and W. Wang, Journal of Alloys and Compounds **618**, 357 (2015).

[89] C. V. Raman and K. S. Krishnan, Nature **121**, 501 (1928).

[90] N. B. Colthup, L. H. Daly, and S. E. Wiberley, *Introduction to infrared and raman spectroscopy*, 1975.

[91] Z. Iqbal, S. Vepek, A. P. Webb, and P. Capezzuto, Solid State Communications **37**, 993 (1981).

[92] A. Achiq, R. Rizk, F. Gourbilleau, R. Madelon, B. Garrido, A. Pérez-Rodríguez, and J. R. Morante, Journal of Applied Physics **83**, 5797 (1998).

[93] B. Langford, A.A; Fleet, M.L.; Nelson, Physical Review B **45** (1992).

[94] L. He, T. Inokuma, Y. Kurata, and S. Hasegawa, Journal of Non-Crystalline Solids **185**, 249 (1995).

[95] L. N. He, D. M. Wang, and S. Hasegawa, Journal of Non-Crystalline Solids **261**, 67 (2000).

[96] D. V. Tsu, G. Lucovsky, and B. N. Davidson, Physical Review B **40**, 1795 (1989).

[97] S. Curtins, H; Veprek, Solid State Communications **57**, 215 (1986).

[98] H. Wagner and W. Beyer, Solid State Communications **48**, 585 (1983).

[99] G. Lucovsky, J. Yang, S. S. Chao, J. E. Tyler, and W. Czubatyj, Physical Review B **28**, 3225 (1983).

[100] A. Richter, *Nanocrystalline silicon oxide in silicon heterojunction solar cells*, Diss, RWTH Aachen University, 2018.

[101] D. M. Goldie and S. K. Persheyev, Journal of Materials Science **41**, 5287 (2006).

[102] T. Kaneko, D. Nemoto, A. Horiguchi, and N. Miyakawa, Journal of Crystal Growth **275**, 1097 (2005).

[103] E. Bhattacharya and A. H. Mahan, Applied Physics Letters **52**, 1587 (1988).

[104] K. Ding, U. Aeberhard, O. Astakhov, U. Breuer, M. Beigmohamadi, S. Suckow, B. Berghoff, W. Beyer, F. Finger, R. Carius, and U. Rau, Journal of Non-Crystalline Solids **358**, 2145 (2012).

[105] T. Ambridge and M. M. Faktor, Journal of Applied Electrochemistry **5**, 319 (1975).

[106] P. Blood, Semiconductor Science and Technology **1**, 7 (1986).

[107] M. Pawlik, R. Groves, R. Kubiak, W. Leong, and E. Parker, A comparative study of carrier concentration profiling techniques in silicon: spreading resistance and electrochemical cv, in *Emerging Semiconductor Technology*, ASTM International, 1987.

[108] T. Cherng, Manual Wafer Profiler CVP21 System: Standard Operating Procedure, 2016.

[109] J. W. Rabalais, *Principles of Ultraviolet Photoelectron spectroscopy*, Wiley, 1977.

[110] H. Bubert, H; Jenett, Electron Detection, in *Surface and Thin Film Analysis: Principles, Instrumentation, Applications*, volume 4, chapter 2, pages 32–50, 2002.

[111] A. C. Beer, Solid State Electronics **9**, 339 (1966).

[112] S. Eriksson, Electronics Letters **21**, 1044 (1985).

[113] L. J. V. D. PAUW, A method of measuring the resistivity and Hall coefficient

on lamellae of arbitrary shape, 1958.

[114] R. Smith, *Semiconductors*, 1959.

[115] Y. Hishikawa, N. Nakamura, S. Tsuda, S. Nakano, Y. Kishi, and Y. Kuwano, Japanese Journal of Applied Physics **30**, 1008 (1991).

[116] R. Azzam and N. Bashara, Nature **269**, 270 (1977).

[117] H. Tompkins, *A User's Guide to Ellipsometry*, Dover Civil and Mechanical Engineering, Dover Publications, 2006.

[118] A. Fontcuberta i Morral, P. Roca i Cabarrocas, and C. Clerc, Physical Review B - Condensed Matter and Materials Physics **69**, 1 (2004).

[119] A. Hadjadj, N. Pham, P. Roca I Cabarrocas, O. Jbara, and G. Djellouli, Journal of Applied Physics **107** (2010).

[120] R. W. Collins, A. S. Ferlauto, G. M. Ferreira, C. Chen, J. Koh, R. J. Koval, Y. Lee, J. M. Pearce, and C. R. Wronski, Solar Energy Materials and Solar Cells **78**, 143 (2003).

[121] V. Kanneboina, R. Madaka, and P. Agarwal, Materials Today Communications **15**, 18 (2018).

[122] B. Drevillon and C. Godet, Journal of Applied Physics **64**, 145 (1988).

[123] D. Aspnes, A. Studna, and E. Kinsbron, Physical Review B **29**, 768 (1984).

[124] E. Edelberg, S. Bergh, R. Naone, M. Hall, and E. S. Aydil, Journal of Applied Physics **81**, 2410 (1997).

[125] A. Richter, S. W. Glunz, F. Werner, J. Schmidt, and A. Cuevas, Physical Review B - Condensed Matter and Materials Physics **86**, 1 (2012).

[126] A. Cuevas and D. Macdonald, Solar Energy **76**, 255 (2004).

[127] D. E. Kane and R. M. Swanson, Measurement of the emitter saturation current by a contactless photoconductivity decay method, 1985.

[128] R. A. Sinton and A. Cuevas, 16th European Photovoltaic Solar Energy Conference , 1 (2000).

[129] F. Einsele, W. Beyer, and U. Rau, physica status solidi c **7**, 1021 (2010).

[130] K. Ramspeck, S. Reissenweber, J. Schmidt, K. Bothe, and R. Brendel, Applied

Physics Letters **93**, 1 (2008).

[131] K. Ramspeck, K. Bothe, J. Schmidt, and R. Brendel, Journal of Applied Physics **106** (2009).

[132] S. Herlufsen, K. Ramspeck, D. Hinken, A. Schmidt, J. Müller, K. Bothe, J. Schmidt, and R. Brendel, Physica Status Solidi - Rapid Research Letters **5**, 25 (2010).

[133] S. Herlufsen, K. Bothe, J. Schmidt, R. Brendel, and S. Siegmund, Solar Energy Materials and Solar Cells **106**, 42 (2012).

[134] S. M. Sze and K. K. Ng, *Physics of Semiconductor Devices*, Wiley, 2006.

[135] I. Martil and G. Gonzalez Diaz, European Journal of Physics **13**, 193 (1992).

[136] O. Breitenstein, Opto-electronics Review **21**, 259 (2013).

[137] C. T. Sah, R. N. Noyce, and W. Shockley, Proceedings of the IRE **45**, 1228 (1957).

[138] K. R. McIntosh, PhD thesis University of New South Wales (2001).

[139] S. Steingrube, O. Breitenstein, K. Ramspeck, S. Glunz, A. Schenk, and P. P. Altermatt, Journal of Applied Physics **110** (2011).

[140] O. Breitenstein, J. P. Rakotoniaina, M. H. Al Rifai, and M. Werner, Progress in Photovoltaics: Research and Applications **12**, 529 (2004).

[141] M. A. Green, *Solar cells : operating principles, technology, and system applications / Martin A. Green*, Prentice-Hall Englewood Cliffs, N.J, 1982.

[142] M. Wolf and H. Rauschenbach, Advanced Energy Conversion **3**, 455 (1963).

[143] H. H. Berger, Journal of The Electrochemical Society **119**, 507 (1969).

[144] D. Qiu, W. Duan, A. Lambertz, Z. Wu, K. Bittkau, K. Qiu, Z. Yao, U. Rau, and K. Ding, ACS Applied Energy Materials **4**, 7544 (2021).

[145] S. Grover, *Effect of Transmission Line Measurement (TLM) Geometry on Specific Contact Resistivity Determination*, PhD thesis, Rochester Institute of Technology, 2016.

[146] K. R. McIntosh and S. C. Baker-Finch, Conference Record of the IEEE Photovoltaic Specialists Conference , 265 (2012).

[147] S. C. Baker-Finch and K. R. McIntosh, Conference Record of the IEEE Photovoltaic Specialists Conference , 2184 (2010).

[148] S. C. Baker-Finch and K. R. Mclntosh, Progress in Photovoltaics: Research and Applications **19**, 406 (2011).

[149] S. C. Baker-Finch, K. R. McIntosh, and M. L. Terry, IEEE Journal of Photovoltaics **2**, 457 (2012).

[150] S. C. Baker-Finch and K. R. Mclntosh, Progress in Photovoltaics: Research and Applications **20**, 51 (2012).

[151] A. Fell, IEEE Transactions on Electron Devices **60**, 733 (2013).

[152] R. Brendel, Progress in Photovoltaics: Research and Applications **20**, 31 (2012).

[153] A. Fell, J. Schön, M. C. Schubert, and S. W. Glunz, Solar Energy Materials and Solar Cells **173**, 128 (2017).

[154] A. Fell and P. P. Altermatt, IEEE Journal of Photovoltaics **8**, 1443 (2018).

[155] A. Fell, K. R. McIntosh, and K. C. Fong, IEEE Journal of Photovoltaics **6**, 611 (2016).

[156] A. Fell, K. R. McIntosh, P. P. Altermatt, G. J. M. Janssen, R. Stangl, A. Ho-Baillie, H. Steinkemper, J. Greulich, M. Müller, B. Min, K. C. Fong, M. Hermle, I. G. Romijn, and M. D. Abbott, IEEE Journal of Photovoltaics **5**, 1250 (2015).

[157] A. Froitzheim, R. Stangl, L. Elstner, M. Kriegel, and W. Fuhs, Proceedings of the 3rd World Conference on Photovoltaic Energy Conversion **A**, 279 (2003).

[158] R. Stangl and C. Leendertz, *General Principles of Solar Cell Simulation and Introduction to AFORS-HET*, pages 445–458, Springer Berlin Heidelberg, Berlin, Heidelberg, 2012.

[159] R. Ambrosio, M. Moreno, A. Torres, A. Carrillo, I. Vivaldo, I. Cosme, and A. Heredia, Journal of Alloys and Compounds **643**, S27 (2015).

[160] S. N. Agbo and P. E. Ugwuoke, International Journal of Physical Sciences **7**, 5559 (2013).

[161] G. B. Tong, M. R. Muhamad, and S. A. Rahman, Optical Materials **34**, 1282

(2012).

[162] A. Matsuda, Journal of Non-Crystalline Solids **338-340**, 1 (2004).

[163] B. Chapman, *Glow Discharge Processes: Sputtering and Plasma Etching*, John Wiley Sons, Inc., 1st edition, 2008.

[164] A. Sarker, C. Banerjee, and A. K. Barua, Journal of Physics D: Applied Physics **35**, 1205 (2002).

[165] W. Li, D. Xia, H. Wang, and X. Zhao, Journal of Non-Crystalline Solids **356**, 2552 (2010).

[166] A. H. Mahan, R. Biswas, L. M. Gedvilas, D. L. Williamson, and B. C. Pan, Journal of Applied Physics **96**, 3818 (2004).

[167] F. Chaibi, R. Jemai, H. Aguas, H. Khemakhem, and K. Khirouni, Journal of Materials Science **53**, 3672 (2018).

[168] A. Cremona, L. Laguardia, E. Vassallo, G. Ambrosone, U. Coscia, F. Orsini, and G. Poletti, Journal of Applied Physics **97** (2005).

[169] P. Kumar and B. Schroeder, Thin Solid Films **516**, 580 (2008).

[170] D. Das, S. Mandal, and A. K. Barua, Journal of Materials Science Letters **17**, 2097 (1998).

[171] O. Gabriel, S. Kirner, M. Klingsporn, F. Friedrich, B. Stannowski, and R. Schlatmann, Plasma Processes and Polymers **12**, 82 (2014).

[172] T. Kamei and T. Wada, Journal of Applied Physics **96**, 2087 (2004).

[173] S. M. Iftiquar, Journal of Physics D: Applied Physics **31**, 1630 (1998).

[174] L. V. Mercaldo, P. Delli Veneri, I. Usatii, and T. Polichetti, Solar Energy Materials and Solar Cells **112**, 163 (2013).

[175] M. Kondo, M. Fukawa, L. Guo, and A. Matsuda, Journal of Non-Crystalline Solids **266-269 A**, 84 (2000).

[176] Y. Mai, S. Klein, R. Carius, J. Wolff, A. Lambertz, F. Finger, and X. Geng, Journal of Applied Physics **97**, 1 (2005).

[177] L. Guo, M. Kondo, M. Fukawa, K. Saitoh, and A. Matsuda, Japanese Journal of Applied Physics, Part 2: Letters **37**, 2 (1998).

[178] L. Zhang, W. Liu, W. Guo, J. Bao, X. Zhang, J. Liu, D. Wang, F. Meng, and Z. Liu, IEEE Journal of Photovoltaics **6**, 604 (2015).

[179] A. Sassella, Physical Review B **48**, 208 (1993).

[180] R. K. Janev and D. Reiter, Contributions to Plasma Physics **43**, 401 (2003).

[181] R. K. Janev, D. Reiter, and U. Samm, *Collision Processes in Low-Temperature Hydrogen Plasmas*, PhD thesis, Macedonian Academy of Sciences and Arts, 2003.

[182] J. Shi, M. Boccard, and Z. Holman, Applied Physics Letters **109** (2016).

[183] S. Kim, J. Park, P. D. Phong, C. Shin, S. M. Iftiquar, and J. Yi, Scientific Reports **8**, 1 (2018).

[184] C. Shin, S. M. Iftiquar, J. Park, S. Ahn, S. Kim, J. Jung, S. Bong, and J. Yi, Materials Chemistry and Physics **159**, 64 (2015).

[185] J. You, L. Zhao, H. Diao, and W. Wang, Journal of Materials Science: Materials in Electronics **32**, 2814 (2021).

[186] H. Overhof, M. Otte, M. Schmidtke, U. Backhausen, and R. Carius, Journal of Non-Crystalline Solids **227-230**, 992 (1998).

[187] K. Shimakawa, Journal of Non-Crystalline Solids **266-269 A**, 223 (2000).

[188] K. Hübner, Physica Status Solidi (a) **65**, 271 (1981).

[189] K. Mui and F. W. Smith, Physical Review B **38**, 10623 (1988).

[190] R. Temkin, Journal of Non-Crystalline Solids **17**, 215 (1975).

[191] H. Watanabe, K. Haga, and T. Lohner, Journal of Non-Crystalline Solids **164-166**, 1085 (1993).

[192] K. Nakada, S. Miyajima, and M. Konagai, Japanese Journal of Applied Physics **54** (2015).

[193] J. Schmidt, R. Peibst, and R. Brendel, Solar Energy Materials and Solar Cells **187**, 39 (2018).

[194] L. Mazzarella, A. B. Morales-Vilches, M. Hendrichs, S. Kirner, L. Korte, R. Schlatmann, and B. Stannowski, IEEE Journal of Photovoltaics **8**, 70 (2018).

[195] A. Stapf, C. Gondek, E. Kroke, and G. Roewer, *Wafer Cleaning, Etching, and Texturization*, pages 1–47, Springer Berlin Heidelberg, Berlin, Heidelberg, 2018.

[196] W. Duan, K. Bittkau, A. Lambertz, K. Qiu, Z. Yao, P. Steuter, D. Qiu, U. Rau, and K. Ding, **2000576** (2021).

[197] L. Korte, A. Laades, and M. Schmidt, Journal of Non-Crystalline Solids **352**, 1217 (2006).

[198] M. Faver, H. Curtins, and A. Shah, Journal of Non-crystalline Solids **9798**, 731 (1987).

[199] M. Kondo, S. De Wolf, and H. Fujiwara, Materials Research Society Symposium Proceedings **1066**, 49 (2008).

[200] D. Deligiannis, V. Marioleas, R. Vasudevan, and C. C. G. Visser, **235307** (2016).

[201] H. Fujiwara and M. Kondo, Applied Physics Letters **86**, 1 (2005).

[202] L. Korte and M. Schmidt, Journal of Applied Physics **109** (2011).

[203] F. Einsele, P. J. Rostan, M. B. Schubert, and U. Rau, Journal of Applied Physics **102** (2007).

[204] C. G. Van de Walle and L. H. Yang, Journal of Vacuum Science and Technology B: Microelectronics and Nanometer Structures **13**, 1635 (1995).

[205] T. F. Schulze, L. Korte, F. Ruske, and B. Rech, Physical Review B - Condensed Matter and Materials Physics **83**, 1 (2011).

[206] T. Konishi and K. Ohdaira, Thin Solid Films **635**, 73 (2017).

[207] S. De Wolf and M. Kondo, Journal of Applied Physics **105**, 1 (2009).

[208] L. Korte and M. Schmidt, Journal of Non-Crystalline Solids **354**, 2138 (2008).

[209] B. Demaurex, S. De Wolf, A. Descoeudres, Z. Charles Holman, and C. Ballif, Applied Physics Letters **101** (2012).

[210] H. Plagwitz, B. Terheiden, and R. Brendel, Journal of Applied Physics **103** (2008).

[211] T. F. Schulze, H. N. Beushausen, C. Leendertz, A. Dobrich, B. Rech, and

L. Korte, Applied Physics Letters **96** (2010).

[212] W. Liu, L. Zhang, R. Chen, F. Meng, W. Guo, J. Bao, and Z. Liu, Journal of Applied Physics **120** (2016).

[213] R. Biron, C. Pahud, F. J. Haug, and C. Ballif, Journal of Non-Crystalline Solids **358**, 1958 (2012).

[214] R. Brendel, S. Dreissigacker, N. P. Harder, and P. P. Altermatt, Applied Physics Letters **93**, 2006 (2008).

[215] B. Strahm, A. A. Howling, L. Sansonnens, and C. Hollenstein, Plasma Sources Science and Technology **16**, 80 (2007).

[216] P. Roca i Cabarrocas, A. Fontcuberta i Morral, B. Kalache, and S. Kasouit, Solid State Phenomena **93**, 257 (2003).

[217] P. Roca i Cabarrocas, N. Layadi, T. Heitz, B. Drévillon, and I. Solomon, Applied Physics Letters **66**, 3603 (1995).

[218] L. Mazzarella, S. Kirner, O. Gabriel, L. Korte, B. Stannowski, B. Rech, and R. Schlatmann, Energy Procedia **77**, 304 (2015).

[219] D. P. Pham, S. Kim, S. Kim, S. Lee, A. H. T. Le, J. Park, and J. Yi, Materials Science in Semiconductor Processing **96**, 1 (2019).

[220] T. Watahiki, T. Furuhata, T. Matsuura, T. Shinagawa, Y. Shirayanagi, T. Morioka, T. Hayashida, Y. Yuda, S. Kano, Y. Sakai, H. Tokioka, Y. Kusakabe, and H. Fuchigami, Applied Physics Express **8**, 021402 (2015).

[221] L. Mazzarella, A. B. Morales-Vilches, L. Korte, R. Schlatmann, and B. Stannowski, Solar Energy Materials and Solar Cells **179**, 386 (2018).

[222] Y. Zhao, P. Procel, C. Han, L. Mazzarella, G. Yang, A. Weeber, M. Zeman, and O. Isabella, Solar Energy Materials and Solar Cells **219** (2021).

[223] R. Varache, C. Leendertz, M. E. Gueunier-Farret, J. Haschke, D. Muñoz, and L. Korte, Solar Energy Materials and Solar Cells **141**, 14 (2015).

[224] R. Biron, C. Pahud, F. J. Haug, J. Escarré, K. Söderström, and C. Ballif, Journal of Applied Physics **110** (2011).

[225] M. Klingsporn, S. Kirner, C. Villringer, D. Abou-Ras, I. Costina, M. Lehmann, and B. Stannowski, Journal of Applied Physics **119** (2016).

[226] A. B. Morales-Vilches, L. Mazzarella, M. Hendrichs, L. Korte, R. Schlatmann, and B. Stannowski, 33rd European Photovoltaic Solar Energy Conference and Exhibition , 715 (2017).

[227] R. Carius, R. Fischer, E. Holzenkämpfer, and J. Stuke, Journal of Applied Physics **52**, 4241 (1981).

[228] A. Descoeudres, L. Barraud, S. De Wolf, B. Strahm, D. Lachenal, C. Guérin, Z. C. Holman, F. Zicarelli, B. Demaurex, J. Seif, J. Holovsky, and C. Ballif, Applied Physics Letters **99**, 99 (2011).

[229] A. Khanna, T. Mueller, R. A. Stangl, B. Hoex, P. K. Basu, and A. G. Aberle, IEEE Journal of Photovoltaics **3**, 1170 (2013).

[230] R. Dingle, The London, Edinburgh, and Dublin Philosophical Magazine and Journal of Science **46**, 831 (1955).

[231] T. Koida, H. Fujiwara, and M. Kondo, Solar Energy Materials and Solar Cells **93**, 851 (2009).

[232] M. F. Van Hest, M. S. Dabney, J. D. Perkins, D. S. Ginley, and M. P. Taylor, Applied Physics Letters **87**, 2003 (2005).

[233] Y. Meng, X.-l. Yang, H.-x. Chen, J. Shen, Y.-m. Jiang, Z.-j. Zhang, and Z.-y. Hua, Journal of Vacuum Science Technology A: Vacuum, Surfaces, and Films **20**, 288 (2002).

[234] B. Grew, J. W. Bowers, F. Lisco, N. Arnou, J. M. Walls, and H. M. Upadhyaya, Energy Procedia **60**, 148 (2014).

[235] M. Frenzel, C. Mikolajczak, M. A. Reuter, and J. Gutzmer, Resources Policy **52**, 327 (2017).

[236] T. Minami, Thin Solid Films **516**, 1314 (2008).

[237] T. Koida, H. Fujiwara, and M. Kondo, Solar Energy Materials and Solar Cells **93**, 851 (2009).

[238] P. P. Altermatt, G. Heiser, and M. A. Green, Progress in Photovoltaics: Research and Applications **4**, 355 (1996).

[239] M. D. Abbott, J. E. Cotter, T. Trupke, and R. A. Bardos, Applied Physics Letters **88**, 3 (2006).

[240] K. R. Mcintosh and C. B. Honsberg, 16th PVSEC , 1651 (2000).

[241] A. Luque and I. Tobías, Journal of Applied Physics **73**, 4042 (1993).

[242] K. C. Fong, M. Padilla, A. Fell, E. Franklin, K. R. Mcintosh, T. C. Kho, A. W. Blakers, Y. Nebel-Jacobsen, and S. R. Surve, IEEE Journal of Photovoltaics **6**, 244 (2016).

[243] I. G. P. Espinet-González*, I. Rey-Stolle, M. Ochoa, C. Algora and E. Barrigón, Progress in Photovoltaics: Research and Applications **23**, 874 (2015).

[244] C. Chan, M. Abbott, B. Hallam, M. Juhl, D. Lin, Z. Li, Y. Li, J. Rodriguez, and S. Wenham, Solar Energy Materials and Solar Cells **132**, 535 (2015).

[245] F. Haase, S. Schäfer, C. Klamt, F. Kiefer, J. Krügener, R. Brendel, and R. Peibst, IEEE Journal of Photovoltaics **8**, 23 (2018).

[246] A. Cruz, D. Erfurt, P. Wagner, A. B. Morales-Vilches, F. Ruske, R. Schlatmann, and B. Stannowski, Solar Energy Materials and Solar Cells **236**, 111493 (2022).

[247] M. Hermle, F. Granek, O. Schultz, and S. W. Glunz, Journal of Applied Physics **103** (2008).

[248] M. Stutzmann, W. B. Jackson, and C. C. Tsai, Physical Review B **32**, 23 (1985).

[249] P. Mahtani, R. Varache, B. Jovet, C. Longeaud, J. P. Kleider, and N. P. Kherani, Journal of Applied Physics **114** (2013).

[250] K. Eriguchi, Japanese Journal of Applied Physics **56** (2017).

[251] S. De Wolf, B. Demaurex, A. Descoeudres, and C. Ballif, Physical Review B - Condensed Matter and Materials Physics **83**, 1 (2011).

[252] Z. Wu, W. Duan, A. Lambertz, D. Qiu, M. Pomaska, Z. Yao, U. Rau, L. Zhang, Z. Liu, and K. Ding, Applied Surface Science **542**, 16 (2021).

[253] J. Müllerová, P. Šutta, G. van Elzakker, M. Zeman, and M. Mikula, Applied Surface Science **254**, 3690 (2008).

[254] M. Fecioru-Morariu, B. Mereu, J. Kalas, J. Hoetzel, P. A. Losio, M. Kupich, O. Kluth, and T. Eisenhammer, EU-PVSEC proc. , 2947 (2010).

[255] M. Stuckelberger, R. Biron, N. Wyrsch, F. J. Haug, and C. Ballif, Renewable

and Sustainable Energy Reviews **76**, 1497 (2017).

[256] D. Qiu, W. Duan, A. Lambertz, K. Bittkau, K. Qiu, and K. Ding, Conference Record of the IEEE Photovoltaic Specialists Conference , 806 (2021).

[257] S. Nunomura, I. Sakata, and K. Matsubara, Physical Review Applied **10**, 1 (2018).

[258] A. Illiberi, P. Kudlacek, A. H. Smets, M. Creatore, and M. C. Van De Sanden, Applied Physics Letters **98**, 10 (2011).

[259] A. H. T. Le, V. A. Dao, D. P. Pham, S. Kim, S. Dutta, C. P. Thi Nguyen, Y. Lee, Y. Kim, and J. Yi, Solar Energy Materials and Solar Cells **192**, 36 (2019).

[260] L. Tutsch, M. Bivour, W. Wolke, M. Hermle, and J. Rentsch, 33rd European PV Solar Energy Conference and Exhibition (2017).

[261] B. Demaurex, S. De Wolf, A. Descoeudres, Z. Charles Holman, and C. Ballif, Applied Physics Letters **101** (2012).

[262] H. B. Profijt, P. Kudlacek, M. C. M. van de Sanden, and W. M. M. Kessels, Journal of The Electrochemical Society **158**, G88 (2011).

[263] T. Welzel and K. Ellmer, Vakuum in Forschung und Praxis **25**, 52 (2013).

[264] H. D. Hagstrum, Phys.ReV **96**, 336 (1954).

[265] C. Böhm, J. Perrin, and P. Roca I Cabarrocas, Journal of Applied Physics **73**, 2578 (1993).

[266] J. Dubeau, L. Hamel, and T. Pochet, Physical Review B - Condensed Matter and Materials Physics **53**, 10740 (1996).

[267] Y. Kuang, B. Macco, B. Karasulu, C. K. Ande, P. C. Bronsveld, M. A. Verheijen, Y. Wu, W. M. Kessels, and R. E. Schropp, Solar Energy Materials and Solar Cells **163**, 43 (2017).

[268] D. Qiu, W. Duan, A. Lambertz, K. Bittkau, K. Qiu, U. Rau, and K. Ding, Solar Energy **231**, 578 (2022).

[269] A. H. Smets, W. M. Kessels, and M. C. Van De Sanden, Journal of Applied Physics **102** (2007).

[270] J. F. Ziegler, M. D. Ziegler, and J. P. Biersack, Nuclear Instruments and

Methods in Physics Research, Section B: Beam Interactions with Materials and Atoms **268**, 1818 (2010).

[271] J. F. Ziegler, J. P. Biersack, and M. D. Ziegler, Energy , 8.2 (2008).

[272] Y. Wang, H. Liu, and W. Shen, Nanoscale Research Letters **13** (2018).

[273] S. Ray and S. Mukhopadhyay, Philosophical Magazine **89**, 2573 (2009).

[274] C. Lei, C. W. Peng, J. Zhong, H. Li, M. Yang, K. Zheng, X. Qu, L. Wu, C. Yu, Y. Li, and X. Xu, Solar Energy Materials and Solar Cells **209**, 110439 (2020).

[275] P. Procel, G. Yang, O. Isabella, and M. Zeman, Solar Energy Materials and Solar Cells **186**, 66 (2018).

[276] E. Kobayashi, S. De Wolf, J. Levrat, A. Descoeudres, M. Despeisse, F. J. Haug, and C. Ballif, Solar Energy Materials and Solar Cells **173**, 43 (2017).

[277] E. Kobayashi, S. De Wolf, J. Levrat, G. Christmann, A. Descoeudres, S. Nicolay, M. Despeisse, Y. Watabe, and C. Ballif, Applied Physics Letters **109**, 1 (2016).

[278] S. De Wolf, C. Ballif, and M. Kondo, Physical Review B - Condensed Matter and Materials Physics **85**, 2 (2012).

[279] S. De Wolf, S. Olibet, and C. Ballif, Applied Physics Letters **93**, 2 (2008).

[280] K. Onishi, Y. Hara, T. Nishihara, H. Kanai, T. Kamioka, Y. Ohshita, A. Ogura, and A. Ogura, Japanese Journal of Applied Physics **59** (2020).

[281] Z. Zhou, Y. Zhang, X. Chen, S. Li, Y. Zhao, and X. Zhang, ACS Applied Energy Materials **3**, 1574 (2020).

[282] J. Shi, L. Shen, F. Meng, and Z. Liu, Materials Letters **182**, 32 (2016).

[283] B. Macco, D. Deligiannis, S. Smit, R. A. Van Swaaij, M. Zeman, and W. M. Kessels, Semiconductor Science and Technology **29** (2014).

[284] Y. Kuang, B. Macco, B. Karasulu, C. K. Ande, P. C. Bronsveld, M. A. Verheijen, Y. Wu, W. M. Kessels, and R. E. Schropp, Solar Energy Materials and Solar Cells **163**, 43 (2017).

[285] F. Finger, P. Hapke, M. Luysberg, R. Carius, H. Wagner, and M. Scheib, Applied Physics Letters **65**, 2588 (1994).

[286] Y. Mai, S. Klein, X. Geng, and F. Finger, Applied Physics Letters **85**, 2839 (2004).

[287] M. Fukawa, S. Suzuki, L. Guo, M. Kondo, and A. Matsuda, Solar Energy Materials and Solar Cells **66**, 217 (2001).

[288] M. Yan and W. J. Goedheer, IEEE Transactions on Plasma Science **27**, 1399 (1999).

[289] U. Graf, J. Meier, U. Kroll, J. Bailat, C. Droz, E. Vallat-Sauvain, and A. Shah, Thin Solid Films **427**, 37 (2003).

[290] E. BELLINI, Helmholtz Center achieves 29.80tandem solar cell, 2021.

Acknowledgments

I would like to express my great thanks to the following people for their contribution to this work:

- Prof. Dr. Uwe Rau for the supervision and examination of this thesis, for providing me the opportunity to be part of IEK-5.
- Dr. Kaining Ding for being an excellent supervisor, for the knowledge, advice and inspiring guidance he provided. He always encourage critical thinking and taught me how to think in a scientific way and balance the work and the life.
- Dr. Andreas Lambertz for sharing his expertise on the deposition of silicon thin films, for countless and enlightening discussions on the experiment results and their interpretation, for his professionalism and enthusiasm to work.
- Dr. Weiyuan Duan for being my daily supervisor, for her contribution to my professional growing and for many fruitful and meaningful discussions on the SHJ solar cell development. Her continuous encouragement, help and kindness were precious for me in the good and the bad times.
- Dr. Karsten Bittkau for the supports to spectroscopy ellipsometry measurement, for always being available for discussion and sharing thoughts, for the assistance to OPAL2 and Quokka3 simulations.
- The many for the inspiring and fruitful discussions: Dr. Annabel Mikosch, Dr. Shenghao Li and Dr. Zhirong Yao on the contact issues of nc-SiO$_x$:H/TCO; Dr. Jürgen Hüpkes, Alexandar Eberst, and Dr. Timo Dittmar on the passivation degradation associated with ITO sputtering process; Dr. Bart Pieters and Paul Steuter on the perimeter recombination in small size solar cells; Dr. Kaifu Qiu on the loss analysis mechanism of SHJ solar cells; Dr. Yong Liu on AFORS-HET simulation of a SHJ solar cells, Dr. Zhuopeng Wu on the characterization

of nc-SiO_x:H via FTIR and SE; Dr. Thomas Riessle and Dr. Sergiu Sas from WEP on the eCV measurement for nc-SiO_x:H(n) and nc-Si:H(n) layers.

- The many who assisted sample preparation: Alain Doumit, Dr. Alaaelding Gad and Henrike Gattermann for wafer arrangement, texturing and cleaning; Andreas Mück, Volker Lauterbach and Silke Lynen for their kindly support on the PECVD system; Hildegard Siekmann and Dr. Andrei Salavei for TCO sputtering depositions; Dr. Manuel Pomaska, Iris Caspers, Henrike Gattermann and Klaus Wambach for the screen printing; Silke Lynen for the deposition of MgF_2.
- The many who supported the sample characterization: Dr. Uwe Breuer from ZEA-3 FZJ for the SIMS measurement; Patric Bernardy and Thomas Wolf from HNF for eCV measurement; Oliver Thimm for PDS measurement; Elmar Neumann from HNF for FIB fabrication; Xinchen Zhang and Dr. Pengfei Cao for TEM; Dr. Benjamin Klingebiel for the UPS measurement.
- Brigitte Zwaygardt and the whole Laser Group for the professional support to the wafer laser cutting and labeling.
- Andreas Schmalen, Johannes Wolff, Sven Schiffer, Joachim Kirchhoff, Wilfried Reetz, Christoph Zahren and Daniel Weigand for the kind and timely technical assistance.
- HITEC team for the organization of many interesting, meaningful and helpful events.
- The whole IEK-5 and especially the SHJ department. It is a very interesting and awesome family.
- All my lovely friends, office mates and flatmates whom i met in the passed four years and shared happiness, sadness and exciting moments with.

My last words go to the people i owe the most. I would like to express my deepest thanks to my parents, my parents in law and siblings for the emotional support and the encouragement in the good and the bad times. Finally, my greatest gratitude goes to my wife, Haodan Zheng. Thank you for your love, trust and accompanying. I cannot reach this PhD without your support. I love you!

Band / Volume 606
**Examining transport in the Upper Troposphere –
Lower Stratosphere with the infrared limb imager GLORIA**
L. Krasauskas (2023), v, 107 pp
ISBN: 978-3-95806-691-5

Band / Volume 607
**Sustainable Fabrication of Ceramic Solid Electrolytes
for Solid-State Lithium Batteries**
R. Ye (2023), vi, 119 pp
ISBN: 978-3-95806-694-6

Band / Volume 608
**Improving Nitrogen Retention in Soils Treated with Pig and Cattle Slurry
Through the Use of Organic Soil Amendments**
X. Cao (2023), XVI, 119 pp
ISBN: 978-3-95806-696-0

Band / Volume 609
**Mechanisches Verhalten von Polymer-Elektrolyt-Membran-
Elektrolysezellen und -Stacks**
S. Holtwerth (2023), x, 251 pp
ISBN: 978-3-95806-697-7

Band / Volume 610
Membrane Reactor Concepts for Power-to-Fuel Processes
H. Huang (2023), VI, 197 pp
ISBN: 978-3-95806-703-5

Band / Volume 611
**Deployment of Fuel Cell Vehicles in Road Transport and the
Expansion of the Hydrogen Refueling Station Network: 2023 Update**
R. C. Samsun, M. Rex (2023), i, 39 pp
ISBN: 978-3-95806-704-2

Band / Volume 612
**Behavior/performance of tungsten as a wall material
for fusion reactors**
M. Gago (2023), X, 120 pp
ISBN: 978-3-95806-707-3

Band / Volume 613
**Strategieentwicklung zur Umsetzung der Klimaschutzziele im
Verkehrssektor mit dem Fokus Kraftstoffe**
M. Decker (2023), ix, 243 pp
ISBN: 978-3-95806-714-1

Schriften des Forschungszentrums Jülich
Reihe Energie & Umwelt / Energy & Environment

Band / Volume 614
Joining of tungsten and steel for the first wall of a future fusion reactor
V. Ganesh (2023), xxx, 142, a-v pp
ISBN: 978-3-95806-715-8

Band / Volume 615
Polluter group specific emission optimisation for regional air quality analyses using four-dimensional variational data assimilation
P. M. Backes (2023), xxi, 115 pp
ISBN: 978-3-95806-717-2

Band / Volume 616
Effect of organic soil amendments on increasing soil N retention and reducing N losses from agricultural soils
Z. Li (2023), XI, 134 pp
ISBN: 978-3-95806-721-9

Band / Volume 617
Radiolytic Stability of BTBP-, BTPhen- and DGA-based Ligands for the Selective Actinide Separation by Solvent Extraction
H. Schmidt (2023), ca. 200 pp
ISBN: 978-3-95806-723-3

Band / Volume 618
$Na_5YSi_4O_{12}$-type Na^+ superionic conductors for solid-state batteries
A. Yang (2023), X, 150 pp
ISBN: 978-3-95806-731-8

Band / Volume 619
Development of industry-scalable processes for nanocrystalline silicon oxide in silicon heterojunction solar cells
D. Qiu (2023), 202 pp
ISBN: 978-3-95806-734-9

Weitere ***Schriften des Verlags im Forschungszentrum Jülich*** unter
http://wwwzb1.fz-juelich.de/verlagextern1/index.asp

Energie & Umwelt / Energy & Environment
Band / Volume 619
ISBN 978-3-95806-734-9

Mitglied der Helmholtz-Gemeinschaft

JÜLICH
Forschungszentrum